Furthering Transmission Electron Microscopy of Covalent Organic Frameworks

BENJAMIN LUKE WEARE, MSCI

THESIS SUBMITTED TO THE UNIVERSITY OF NOTTINGHAM FOR THE DEGREE OF
DOCTOR OF PHILOSOPHY.

APRIL 2023

Abstract

The transmission electron microscope (TEM) is a powerful instrument capable of a range of imaging, crystallographic, and spectroscopic measurements. As a result it has seen application to covalent organic frameworks (COFs), a class of polymer characterised by their porosity, high surface area, and tunable structures. However, examining the literature found a systematic low uptake of TEM for investigating COFs despite TEMs ability to provide nanoscale structural and elemental characterisation. Therefore to characterise COFs this thesis applies a range of TEM techniques including bright-field TEM (BF-TEM) imaging, selected area electron diffraction (SAED), electron energy loss spectroscopy (EELS), and energy dispersive X-ray spectroscopy (EDX). BF-TEM in particular was found to be invaluable for establishing crystallinity in samples with poor powder diffraction patterns. Two COFs, the novel cHBC-BDA-COF and the literature COF-5 were synthesised as a powder and as hybrids with a range of nanocarbon supports to facilitate investigation of COFs with TEM. In addition, matrix-assisted laser desorption ionisation mass spectrometry (MALDI MS) was applied as an analytical tool to COFs for the first time in order to investigate their structure and confirm that polymerisation had occurred. In order to put the TEM investigations of COFs on a firm theoretical footing a coarse-grained graph theoretical model was developed that predicts the TEM projections of COFs based on their fundamental topology: this gave rise to face-on (FO), side-on (SO), armchair (AC), and zigzag (ZZ) projections that were later experimentally confirmed in COF-5 and cHBC-BDA-COF. A stochastic graph model was made to investigate the presence of these features in more realistic structures and to investigate how to define when a crystalline structure has become amorphous. The experimental e-beam stability of cHBC-COF, pyrene-COF, and the non-COF polymer Bet-P-1 was investigated using this methodology. Overall this thesis develops a powerful holistic methodology combining modelling, TEM, and bulk measurements to investigate the structure and synthesis of COFs.

List of Publications

The following articles were published by or submitted to peer-reviewed journals in the course of this research.

- Imaging and analysis of covalent organic framework crystallites on a carbon surface: a nanocrystalline scaly COF/nanotube hybrid. B. L. Weare, R. W. Lodge, N. Zyk, A. Weilhard, C. L. Housley, K. Strutyński, M. Melle-Franco, A. Mateo-Alonso, and A. N. Khlobystov. *Nanoscale*, 2021, **13**, 6834-6845, DOI: 10.1039/D0NR08973G.
- A Crystalline 1D Dynamic Covalent Polymer. E. De Bolós, M. Martínez-Abadia, F. Hernández-Culebras, A. Haymaker, K. Swain, K. Strutyński, B. L. Weare, J. Castells-Gil, N. M. Padial, C. Marti-Gastaldo, A. N. Khlobystov, A. Saeki, M. Melle-Franco, B. L. Nannengam and A. Matero-Alonso. *J. Am. Chem. Soc.*, 2022, **144**, 15443-15450, DOI: 10.1021/jacs.2c06446.
- Reactions of polyaromatic molecules in crystals under electron beam of the transmission electron microscope. K. L.-Y. Fung, B. L. Weare, M. W. Fay, S. P. Argent, A. N. Khlobystov, *Micron*, 2023, **165**, 103395, DOI: 10.1016/j.micron.2022.103395.
- Covalent Organic Frameworks: Challenges and Opportunities of Transmission Electron Microscopy. B L. Weare, M. W. Fay, and A. N. Khlobystov, *Chem. Soc. Rev.*, 2022, *Submitted.*
- Direct measurement of single-molecule dynamics and reaction kinetics in confinement using time-resolved transmission electron microscopy. K. L. Y. Fung, S. T. Skowron, R. Hayter, S. E. Mason, B. L. Weare, N. A. Besley, Q. M. Ramasse, C. S. Allen, and A. N. Khlobystov, *PCCP*, 2023. DOI: 10.1039/d2cp05183d.
- Quantitative 3-Dimensional Spatial Sensing of Paramagnetic Nanoparticles Using Quantum Defects in Diamond on a Transmission Electron Microscopy Finder Grid. B. Flinn, R. Valentin, F. Michael, A. Tyler, J. Pitcairn, M. Cliffe, B. L. Weare, C. Stoppiello, M. Mather, and A. N. Khlobystov, *Nanoscale Advances*, 2023, *Submitted.*

Acknowledgements

In no particular order, thanks to all the people who were instrumental: M. P. Weare; D. A. Weare; A. J. Weare; K. L. Y. Fung; R. W. Lodge; M. Astle; C. Stoppiello; L. Norman; J. Jordan; I. Cardillo-Zallo; E. Norman; W. Cull; W. Townsend; J. Pitcairn; R. S. Z. Whitehead; C. L. Housley; A. Weilhard; M. W. Fay, T. Lemercier; H. Bhogal; H. Osmond; B. Flynn; T. Burwell; C. Parmenter; M. Cliffe; S. Argent; B. Pointer-Gleadhill; A. N. Khlobystov; C. Clark; J. Watts; Q. M. Ramasse; and anyone I might have missed.

Contents

List of Abbreviations

Abbreviation	**Full**
1D	One dimensional
2D	Two dimensional
3D	Three dimensional
AC	Armchair
AFM	Atomic Force Microscopy
ATR	Attenuated Total Reflectance
BET	Brauner-Emmett-Teller
BDA	Benzenediboronic acid
BFTEM	Bright-field TEM
CBED	Convergent Beam Electron Diffraction
cHBC	cata-Hexabenzocoronene
CNT	Carbon nanotube
COF	Covalent organic framework
CTF	Covalent triazine framework
DCC	Dynamic covalent chemistry
DFTEM	Dark-field TEM
DSC	Differential scanning calorimetry
EDS	Energy dispersive X-ray spectroscopy
EDX	Energy dispersive X-ray spectroscopy
EELS	Electron energy loss spectroscopy
ELNES	Energy loss near edge structure
EO	Edge-on
EXELFS	Extended energy loss fine structure
FO	Face-on
FT	Fourier transform
FTIR	Fourier transform IR

Abbreviation	**Full**
GNF	Graphitised nanofibre
HAADF	High-angle annular dark field
HHTP	Hexahydroxytriphenylene
HREELS	High resolution EELS
HRTEM	High resolution TEM
IR	Infrared
IUPAC	Internation Union of Pure and Applied Chemists
KBr	Potassium Bromide
KraKro	Kramers-Kronig
MALDI	Matrix-assisted laser desorption ionisation
MOF	Metal organic framework
MS	Mass spectrometry
MWNT	Multi-walled carbon nanotube
NA	Numerical aperture
NMR	Nuclear magnetic resonance
PBA	Phenylboronic acid
PCTEM	Phase-contrast TEM
PSD	Plural scattering distribution
PXRD	Powder X-ray diffraction
SAED	Selected area electron diffraction
SCXRD	Single-crystal X-ray diffraction
SiONP	Silica nanoparticle
SO	Side-on
SSD	Single scattering distribution
STEM	Scanning transmission electron microscopy
SWNT	Single-walled nanotube
TBB	Hexamethoxytribenzylbenzene

Abbreviation	**Full**
TEM	Transmission electron microscopy
TGA	Thermogravimetric analysis
TGA	Thermal gravimetric analysis
TOF	Time of flight
UV	Ultraviolet
UV-Vis	Ultraviolet-visible
XRD	X-ray diffraction
ZLP	Zero-loss peak
ZZ	Zigzag

Selected Physical and Mathematical Constants

Constant	**Symbol**	**Value**
Absolute zero	-	273.15 °C
Avogadro constant	N_A	6.022×10^{23} mol^{-1}
Copper Kα radiation	Cu(Kα)	1.402 Å
Elementary charge	Q_e	1.602×10^{-19}
Euler's number	e	2.718
Ideal gas constant	R	8.314 J K^{-1} mol^{-1}
Pi	π	3.142
Planck constant	h	6.626×10^{-34}J s
Electron rest mass	m_e	9.109×10^{-31} kg
Speed of light	c	2.998×10^{8} m s^{-1}

1 Introduction

1.1 Foreword

Before Frank Herbert wrote the sci-fi epic *Dune*, he reputably distilled the core sentiment into a haiku. Following this example:

Covalent framework
in electron microscope,
analysis blooms.

The main goal of this work is to further the fundamental understanding of growth and morphology of crystalline polymers, chiefly covalent organic frameworks, via transmission electron microscopy; at the same time, this thesis seeks to enhance the current application of transmission electron microscopy to covalent organic frameworks. To do this, inspiration was drawn from several discrete fields; reticular chemistry, classical polymer chemistry, solid-state materials chemistry, chemical graph theory, and electron microscopy. This is partially a response to the clustering of science into highly specialised sub-fields,[1] but also to gain insight into the chemical systems discussed by viewing them through a new lens. The work in this thesis is primarily an effort towards fundamental science and method development, and will hopefully explain to the reader why one would want to research covalent organic frameworks as well as what they are useful for. I hope that at some stage the information contained within will allow better design of crystalline polymers and facilitate scalable industrial synthesis of useful COFs.

1.2 Covalent Organic Frameworks

1.2.1 Introduction to Covalent Organic Frameworks

Covalent organic frameworks (COFs) are porous framework polymers made from organic monomers joined by covalent bonds. The design methodology has been dubbed "reticular chemistry", which is concerned with making open frameworks from molecular building-blocks. COFs first entered the literature in 2005 from Cótê *et al.*, who published COF-1 and COF-5.[3] From there the number of COF publications per year has continued to increase as researchers develop new COFs and exploit the properties of COFs for useful societal applications.[4]

COFs monomers are joined by chemical bonds into a framework structure (Figure 1a). These bonds are often referred to in the literature as linkers or linkages. Typically these are formed via condensation-hydrolysis equilibria as this is a straightforward way of forming a thermally /mechanically strong bond at the cost of the structure being susceptible to hydrolysis. Classic COF bonds are boroxine (COF-1) or boronate ester (COF-5), but a large variety of functional groups have been used. Linkers can be categorised by the atoms present in the functional groups; boron (boroxine,[3] boronate ester,[3] spiroborate,[5] borosilicate,[6] aminoborane, polycubane);[7] nitrogen (imine,[8] hydrazone,[9] amide,[10] triazine,[11] borazine,[12] urea,[13] phenazine,[14] carbamate,[15] azodioxy[16]); oxygen (dioxin);[17] carbon-only (olefin).[18] Boron and nitrogen containing COFs are the most common and most diverse.

The crystal structure of COFs derives from how the monomers fit together and arrange themselves in space; and is therefore intrinsically linked to the symmetry of the monomers (Figure 1b). For example, COF-1 is made from the self-condensation of benzenediboronic acid (BDA) monomers where three BDA monomers form a planar 6-membered boroxine ring. This means the BDA monomers are separated by 120° so the COF forms as flat sheets containing hexagonal pores and a *P6mmm* unit cell. This is an example of a 2D COF; covalent bonds join monomers into a sheet in the x-y plane, and intermolecular forces hold the sheets together in the z-direction (analogous to the structure of graphite). In a 3D COF, the covalent bonds hold the monomers together in all three cartesian directions. 3D COFs are less common in the literature than 2D COFs and the majority of the work in this thesis is not concerned with them. 2D COFs have a wide range of pore shapes; C3 monomers such as hexahydroxytriphenylene create hexago-

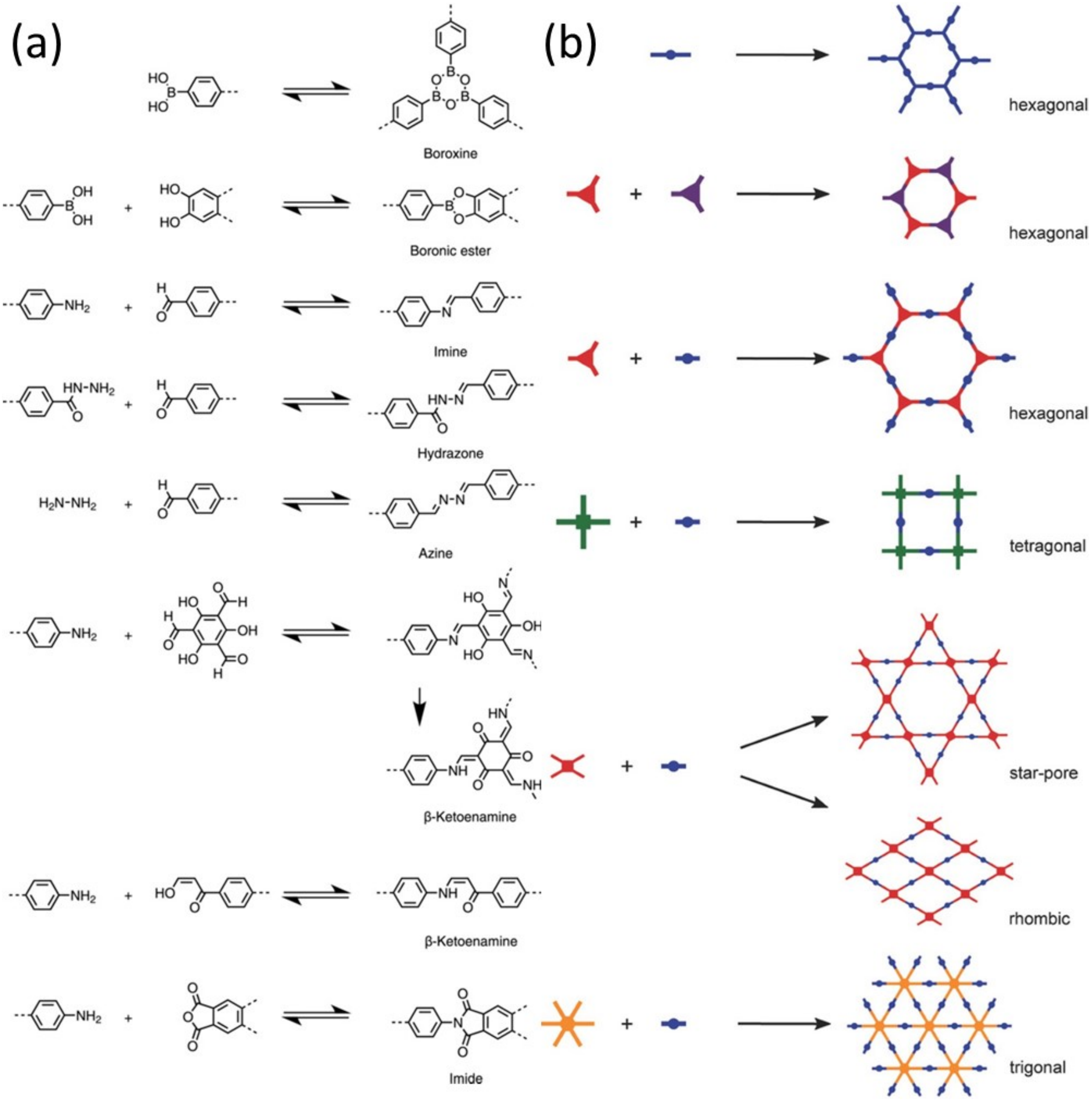

Figure 1: (a) Typical COF polymerisation reactions, showing formation of boroxine, boronate ester, imine, hydrazone, azine, β-ketoenamine and imide functional groups as used in COF polymer synthesis. Adapted with permission from ref [2]. Copyright 2018 John Wiley and Sons. (b) Typical COF pore geometry. Hexagonal pores can be formed by condensation of C3 monomers, co-condensation of two different C3 monomers, or co-condensation of C3 and C2 monomers. C4 monomers are used to give tetragonal (square), star (kagome) or rhombic pores. C6 monomers can give trigonal pores. Adapted with permission from ref [2]. Copyright 2018 John Wiley and Sons.

nal, triangular or kagome lattices; C4 monomers such as porphyrins create square or diamond lattices; and C2 monomers can be used control the size of the pore. 2D-COFs are more common because most COF monomers are aromatic organic molecules composed of sp^2 hybridised carbon which impart their trigonal planar nature to the synthesis product. 3D-COFs are less common as they require more novel chemistry in their design,[19] but some examples are COF-300 and cage-COF-1.[20,21] The shape of COF pores is predefined by the monomer geometry and the reaction conditions under which they combine.

It has been identified by Sasmal *et al.* that COFs form with a variety of morphologies. The authors divide COFs into categories based on the dimensionality: 0D (e.g. nanoparticles),[22] 1D (e.g. nanotubes), 2D (nanosheets),[23,24] and 3D (bulk materials). They further recognise that these categories can each contain distinct morphologies such as "foamy" structures[25] or single crystals.[26] The authors explain that the structure of the COF derives from both the chemistry of the COF monomers and the reaction conditions used. For example, boronate ester COFs can be foamy 3-D structures or crystalline colloids depending on the reaction conditions. They further clarify that high COF monomer concentration leads to smaller polymer crystallites due to rapid formation of amorphous phases. Haase and Lotsch identify "the COF trilemma" where framework stability, crystallinity, and complexity are in competition. They then outline the existing methodologies used to make COFs:[27] using reversible covalent bonds; prearranging monomers into a lattice before they react; or using monomers that have little conformational freedom so can only form a crystalline material.

1.2.2 Comparison to Metal Organic Frameworks

COFs are often compared to metal organic frameworks (MOFs) in publications (Figure 2), typically in introductions when defining a COF. This is because MOFs and COFs were both first publicised as reticular solids rather than polymers, and COF researchers typically have a background in reticular chemistry instead of polymer science. There also exist a number of high profile papers from the Yaghi group that reinforce the perception that these classes of compound are closely related, typically by grouping both under the umbrella of reticular chemistry.[4,25,28–32] Indeed the origin of the term reticular chemistry appears to be an attempt to differentiate MOFs and COFs from existing polymer research, seen in O'Keeffe *et al.* in reference to MOFs: "Although these materials are sometimes referred to as coordination polymers, we prefer to differentiate them, because MOFs are based on strong linkages that yield robust frameworks."[28] This is further clarified by Gropp *et al.* in the context of supramolecular chemistry: "In contrast, MOFs and COFs are held together by strong bonds between metal ions and charged linkers, and covalent bonds between light elements (e.g., B, C, N, O), respectively."[4] These definitions imply that the defining characteristic of a MOF or COF compared to other self-assembled materials is the presence of "strong bonds". The first use of reticular chemistry in the literature the author could find is from Yaghi *et al.*, where they introduce the term to describe their methodology for designing crystalline solids.[33] It is therefore useful to examine the comparison between MOFs and COFs critically and decide how much utility there is in grouping the two materials under the umbrella of reticular chemistry.

There exist a number of review articles that discuss MOFs and COFs together.[4,34,35] MOFs are made using reticular chemistry principles and are typically assembled in the solution phase from a mixture of monomers, but they are held together using coordinate bonds between organic ligands and metal centres. In contrast COFs use covalent bonds to join monomers. This means MOFs contain much more labile bonds so can crystallise more easily, and single-crystal MOFs are much more common than single-crystal COFs. Traditional crystallisation and recrystallisation techniques are also highly applicable to MOFs due to their labile nature. For example, MOFs can often be induced to crystallise via layering saturated solutions or addition of antisolvents. These techniques are typically absent in the COF literature, or are only applied in limited cases. In contrast, efforts to increase COF crystallinity have focussed on controlling the activity of the monomers, such as use of pyridine to protect boronate ester bonds from hydrolysis,[36] or the use of modulators to interfere with the reaction kinetics.[37–42] The difference in approach to MOF and COF synthesis reveal a different underlying methodology in how researchers tackle synthesising these materials, with COFs being made more reliably when using polymer chemistry techniques.

Using the nomenclature of the COF literature, typical MOFs would be considered 3D as their lattice is not composed of stacked 2D sheets. In contrast, typical COFs are 2D. This arises from the monomers used to make these materials. MOFs rely on coordination bonds, so have access

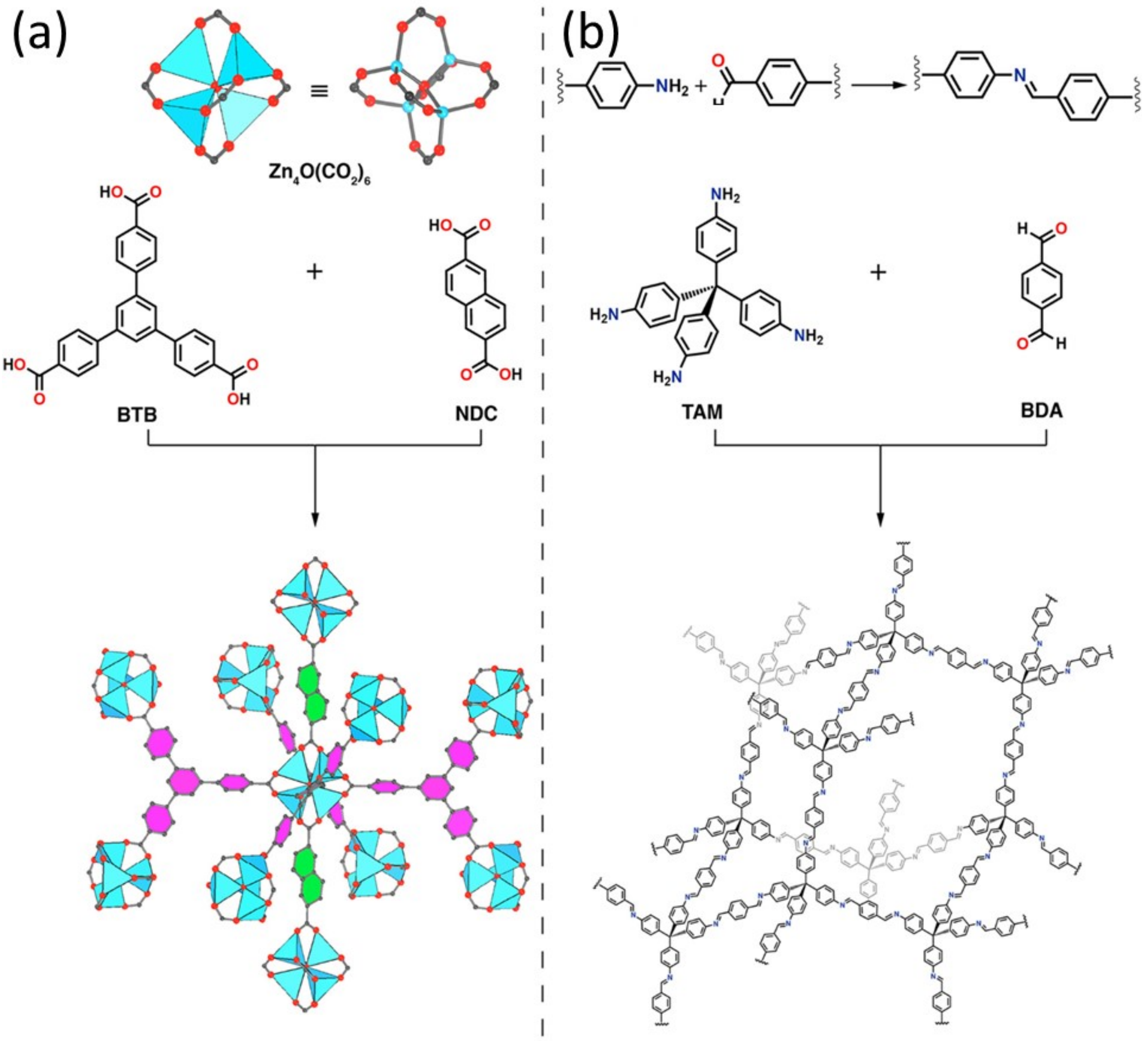

Figure 2: (a) MOF-205, (b) COF-300, and the monomers that make these two materials. These structures demonstrate that different chemistry and functionality can give rise to superficially similar structures, e.g. 3D porous networks. Adapted with permission from ref [4]. Copyright 2020 American Chemical Society.

to a variety of metal centre geometries such as octahedral and tetrahedral that allow easy design of 3D structures. COFs do not include coordination centres in their framework, and it has been found in the COF literature that the most accessible bonds are planar or sp^2 hybridised. COFs with interpenetrated frameworks are also published less often.[43]

The physical properties of MOFs and COFs tend to be similar, as described by reviews such as Freund *at al.*[34] Both are porous structures with large surface areas and low density compared to traditional materials. The pore chemistry is also tunable via selection of the monomers used in synthesis. MOFs have been shown to undergo metal ion/ligand exchange in solution, which is not currently known for COFs. The similarity in MOF and COF properties is best demonstrated by researchers targeting similar applications for both classes of material, such as gas sorption or catalysis.

Therefore while MOFs and COFs have some similar properties, the underlying chemistry can be very different. COFs are essentially a specific sub-category of classical polymers which requires crystallinity and a porous framework structure; however, the underlying chemistry is often that of step-growth polymerisation. MOFs by contrast are coordination polymers. In reality MOFs, COFs, and polymers are continuous fields that blur together at the edges. Therefore when studying COFs it is more useful to understand their properties using the lens of MOF chemistry, but more useful to understand their synthesis via classical polymer chemistry. As a result this text uses monomer/polymer terminology to emphasises the polymeric nature of COFs, which has literature precedence.[44] With regards to the term reticular chemistry, it is valid to classify compounds as related based on shared properties such as bond strength, but the author considers that the term "reticular chemistry" to be a high-level classification similar to calling polyethylene and deoxyribonucleic acid "polymers" - accurate but not always useful. Indeed the IUPAC defintion of "polymer molecule" is very broad: "Molecule of high molecular mass, the structure of which essentially comprises the multiple repetition of units derived, actually or conceptually, from molecules of low molecular mass."[45] However, the author thinks it is important to bear in mind that a COF can be both a polymer and a reticular solid, and that the best use of nomenclature is whichever is most useful at the present moment. Further discussion on this topic veers dangerously close to semantics.

1.2.3 COF Nomenclature

On the topic of semantics there is currently no universally adopted systematic naming procedure for new COFs. Typical naming practices include sequential numerical naming (so-called trivial names),[4] e.g. COF-1 and COF-5. This is hindered by the lack of a centralised audited database of all COFs, and relies on researchers naming their COFs sequentially. For example, the first two published COFs were COF-1 and COF-5, with no reason given for missing COFs -2, -3, and -4.

An alternative approach is a descriptive name. The name of each COF takes a characteristic of the COF,[46] or the name of the researcher,[47] and uses this to create a unique name. This is useful for giving each COF a specific identifier that is relevant to their properties, but is not systematic. This appears to be causing some confusion in the literature: da Silva *et al.* reported that TpPa-COF was also known as COF-LZU-1,[48] despite these two COFs being made of different monomers.[49,50] There is also both COF-MF and MF-COF-1 in the literature,[46,51] despite these two materials being unrelated.

Gropp *et al.* outlined naming procedures for COFs, where they suggest using a "reticular formula" alongside chemical formulae, molecular formulae, and trivial names.[4] COFs can also be named using the rules outlined in the IUPAC Colour Books. The IUPAC Compendium of Polymer Terminology and Nomenclature, a. k. a. the Purple Book, recommends naming polymers based on their structure and the ratio of monomers in them.[45] This is highly suitable for COFs as it generates a unique, descriptive name for each COF, and is analogous to the reticular formulae suggested by Gropp *et al.* In light of these points, in this thesis each COF will be referred to by the name given to them in the most relevant publication, typically a trivial name such as COF-300 or COF-5.

1.2.4 Synthesis of COFs

COFs are commonly made via solvothermal synthesis, in which the COF monomers are dissolved or dispersed in solvent and heated in a sealed reaction vessel under inert atmosphere. The archetypical synthesis is that of COF-1, where benzene-1,4-diboronic acid is heated at 120 °C for 72 hours in a 1:1 mixture of mestiylene/dioxane under inert atmosphere.[3] This is a versatile synthetic method as the solvent system and temperature can be tailored to the chosen monomers to maximise crystallinity or select a desired COF morphology. For example, Castano *et al.* have shown that inclusion of nitrile co-solvents is key to forming nanoparticles of boron-based COFs.[52] However, solvothermal syntheses typically take 1-3 days to complete and involve elevated temperatures and pressures. Furthermore, the solvothermal COFs are typically micro- or nanocrystalline powders, which have proven difficult to incorporate into real-world devices.[34] Equilibrium reactions are targeted by researchers as they are relatively easy to control by changing the reaction conditions to promote the forward or reverse reactions. COFs that are formed in equilibrium reactions can be considered as step-growth polymers.

Equilibrium reactions also allow so-called *error-checking*, which is the process of converting from an amorphous lattice to a crystalline lattice.[53] The mechanisms by which this occurs are that under suitable conditions, COFs can undergo rearrangement processes that drive the COF to a lower energy structure. This can include covalent bonds breaking and reforming, or lower energy transformations such as changes in conformation. The exact processes occurring will depend on the energy available and the chemical system; a low-temperature reaction may have a very low rate of covalent bond breaking/reforming, but still have enough energy for a significant rate of conformational change to occur.

Error-checking may be rate-limited; it was shown by Smith *et al.* that dilute reaction mixtures lead to more crystalline COFs,[22] which can be partially attributed to a slow rate of COF growth giving more time for error-checking to occur. In the case of rapid COF growth there is a danger that a structure may become trapped in an amorphous state. For example, introduction of new monomers could cause the lattice to be conformationally locked in an acrystalline arrangement. Another powerful method to limit COF growth rates is via modulators; Castano *et al.* included a mono-functional monomer that competes with the bi-functional benzenediboronic acid in COF-5 formation, and blocks addition of more monomers to the growing polymer. Under equilibrium condition, the modulator later leaves the polymer and allows benzenediboronic acid to take add to the structure, at which point the polymer can continue to grow. This was shown to cause slower growth of COF crystals, leading to larger crystals at the end of synthesis.[52] Another methodology is slow monomer addition, such that one monomer is always in excess. Evans *et al.* showed that this led to formation of fewer, larger COF crystals due to reduced rate of polymer growth.[44] This methodology presumes that acrystalline COFs are kinetic products, and that the crystal product is the thermodynamic product.[38] It has been suggested that COFs can form directly as crystals, or via an initial amorphous phase that rearranges into a crystal phase.[54]

To the author's knowledge, error-checking has not been rigorously proven to occur during COF formation beyond imine COFs. An early reference to error-checking in the literature was found in Rowan *et al.* in 2002,[55] where they use it to describe how dynamic covalent chemistry (DCC, a precursor/alternate term to reticular chemistry) gives rise to crystalline materials. The oldest reference that could be found was by Lindsey in 1991 which discusses biological self-assembly of proteins, viruses, and structures such as crystals or monolayers.[56] COFs typically follow the "strict self-assembly" pathway described by Lindsey where the final product forms spontaneously under the correct conditions, the assembly process is reversible, and the product is stable at thermodynamic equilibrium. Lindsey also highlights that crystallisation is a self-assembly process allowing rapid formation of 3D long-range ordered structures. Several other pathways are described, and the conceptual framework of biological self-assembled could likely be adapted easily and usefully for describing COF formation. The seeds of these ideas are found in the biology literature as early as Caspar and Klug in 1962, which discusses self-assembly of tobacco mosaic virus.[57] They make the key point that "self-assembly is a process akin to crystallisation and is governed by the laws of statistical mechanics," which underpins much of the current understanding of COF growth pathways.

It can be seen that error-checking is based on well-grounded ideas and assumptions, and is a small part of self-assembly of solids. A mechanistic study to determine the exact self-assembly/error-checking pathways taking place would be useful, but for the present error-checking remains a useful concept to understand COF formation. In practice single-crystal COFs are challenging to produce and most COFs remain as nano- or microcrystalline powders. Currently the main theory of COF polymerisation mechanism is the nucleation-elongation model,[23] where a "seed" crystal forms in solution from monomers to which further monomers add to grow the crystal. A seeded growth method exploiting this mechanism was used by Evans *et al.* to grow single-crystal COFs suitable for single-crystal X-ray diffraction (SC-XRD).[26] As most publications target crystalline COFs, accurate data on amorphous COF polymers is difficult to find.

Ionothermal synthesis is a solvothermal variant where the solvent is an ionic liquid or molten salt.[58] The energy source for the polymerisation reaction remains thermal. Ionothermal is less common than solvothermal synthesis, but is used to produce covalent triazine frameworks such as CTF-1.[11] CTFs are a subcategory of organic framework polymers in which the linkage is a triazine. Ionothermal synthesis has the same drawbacks as solvothermal synthesis, but remains a useful technique for monomers that are more soluble in ionic reaction media.

Microwave synthesis provides energy directly to the monomers in solution by microwave irradiation.[59] This shares the advantage of tailoring solvent systems to monomers, and is also typically much faster than thermal synthesis with reactions taking hours or minutes. COF-5 was synthesised by heating at 200 W for 20 mins,[60] which is 216 times faster than the original 72 hour solvothermal synthesis.[3] As for solvothermal synthesis, the COFs produced are typically crystalline powders.

Some less commonly used techniques include sonochemical synthesis,[61] which supplies energy to the reaction mixture through ultrasonication of the monomers in solution. This causes local heating via acoustic cavitation, allowing rapid heating and cooling. Yang *et al.* produced COF-1 and COF-5 as crystalline powders in 1-2 hours, comparable to microwave synthesis.[62] Photochemical synthesis uses typically ultra-violet (UV) light as the energy source for the polymerisation reaction, such as CTC-COF made via UV irradiation over 48 hours by Liang *et al*.[63] Photochemistry may be more efficient than thermal chemistry as the energy of the radiation can be tailored to the specific wavelength needed to initiate the reaction. The products are typically crystalline COF powders. Mechanochemical synthesis involves thorough grinding of monomers as dry powders or in slurry. This both mixes the monomers and provides the energy for the reaction. For example Biswal *et al.* used mechanochemical synthesis to produce three imine COFs, by grinding the monomers as dry powders at room temperature to form crystalline powder products.[64]

Interface synthesis[65] was developed to provide thin films of crystalline COFs that could be studied more easily by techniques like atomic force microscopy (AFM) and transmission electron microscopy (TEM). Synthesis of thin films avoids the issues associated with integration of powder products into applications. Here the COF polymerisation reaction takes place at the interface between two phases, often between two immiscible solutions containing COF monomers or the interface between solution and gas phase. Another form of interface synthesis is to form a COF at the surface of a solid nanosupport. The COF assembles at the interface, which restricts how large the COF can grow into either solution due to limited diffuse of monomers across the phase boundary. This has been used to produce very thin films of crystalline COF. Thin-film synthesis is a subset of interface synthesis where the COF formation takes place on a solid surface.[66] The COF may be peeled off or studied on the support substrate. The main drawback of interface synthesis is the amount of product is small compared to synthesis of COF powders, and thin films of COF can tear or be damaged during transfer procedures.

1.2.5 Properties and Applications of COFs

There have been a number of reviews discussing the useful properties of COFs and efforts to develop these for specific applications in the past decade.[2,34,67–71] COFs have been trialled for many applications, but at the time of writing all are at the research level and there has not been a successful commercialisation of COFs (dear future readers, please write the names of commercialised COFs in the margin). In general, the properties of COFs derive from the monomers used to make them, such as the topography of the COF lattice or the hydrophilicity of COF pores. Typically COFs are thermally stable as they are made of strong covalent bonds. Chemical stability of COFs depends on the reactivity of the functional groups joining monomers and the environment in which the COF is used; for example a boroxine COF will be susceptible to hydrolysis.[72] This is not an issue if it used in a dry environment, or it can be modified with pyridine to increase stability to hydrolysis.[36] Functionality can be introduced to the COF via monomer design, or post-synthetically by chemical modification of the COF.

COFs attract interest for gas sorption and storage applications because they have a high surface area to volume ratio, and low density. This theoretically allows the production of materials that can store more gas per unit mass than established materials in this field. This is largely spurred by the desire to develop alternative environmentally friendly fuels, such as hydrogen or methane, which are difficult to transport and store due to being gases. COFs are promising due to their low density and high porosity, leading to theoretical high fuel storage per unit mass. The ability to change the pore chemistry has also been identified as an advantage for COFs.[34] For example, COF membranes have been found to be highly effective at separating hydrogen from gaseous mixtures,[73] and COFs have been shown to be suitable for carbon dioxide storage.[74]

COFs have been trialled in the field of energy materials.[67] Ding *et al.* produced a low-density cathode from a 2D imine COF,[75] while Yang *et al.* used a 2D porphyrin-based COF as an anode to give over 600 mAh g^{-1} reversible capacity.[76] Shinde *et al.* used a mechanochemically synthesised 2D imine COF as a solid proton-conductive electrolyte.[77] Li *et al.* used a 2D azine COF as a fluorescent copper ions sensor.[78] Catalysis has been identified as a critically important field in the modern world. As such COFs have been trialled as both catalyst and catalyst support.[79] Ou *et al.* used COF-5 on the surface of a layered material to perform photo-catalytic carbon dioxide reduction.[80] COFs have been trialled for several biomedical applications, such as biosensing and bioimaging phototherapy, and biocatalysis.[81] As an example, 2D imine-based PI-3-COF was tested for drug delivery applications; it was found to be biocompatible, water-stable, and showed controlled release of a range of drugs including 5-flurouracil and ibuprofen.[82]

1.2.6 COF/Nanosupport Composites

Development of COF applications is limited by the crystallisation problem. It was mentioned earlier that many common COF synthesis techniques yield a powder product. These can be difficult to process into a form suitable for applications. Their low-density and small particle size means they can easily become airborne, making mass-transport considerations difficult. Further if processed into pellets or films these materials often have poor mechanical properties and will easily crumble or break. Indeed the applications in the previous section generally rely on thin-film COF, micro-crystalline COF, or COF/nanosupports. Production of COF/nanosupport hybrid materials is a powerful solution to this problem, as synergy between the COF and nanosupport properties can be very powerful.

For the purposes of this text, nanomaterials are materials with at least one dimension less than 1000 nm,[83] and a nanosupport is a nanomaterial with another material attached to its surface or encapsulated within it. This is of interest to COF synthesis as nanosupports have been used for applications, such as integration into devices, and promote the formation of thin layer COF material on their surface via interface synthesis. It should be noted that the opposite of a nanomaterial will be referred to as a *bulk* material - this is in contrast to convention in other parts of the literature where the *bulk* is in contrast to the *surface* of a material. For nanomaterials, the surface-area to volume ratio is typically very high so a large proportion of a nanosupport is its surface.

Nanosupports have diverse composition and properties. Two of relevance to this work are silica nanoparticles and carbon nanotubes. Silica nanoparticles, produced via the Stöber process, are nanoscale spheres of silica. They have a different band-gap compared to bulk amorphous silica,[84] have good thermal/chemical stability to a range of conditions, and are electrical insulators. As such they have been used as supports for COFs.[85] Another nanosupport used for COFs are carbon nanotubes (CNTs) (Figure 3). CNTs are a nanoscale allotrope of carbon consisting of a hollow cylinder of sp^2 hydrbidised carbon atoms. A single-walled carbon nanotube (SWNT) is composed of one cylinder of carbon atoms, a double-walled carbon nanotube (DWNT) contains one cylinder nested within another, and multiwalled carbon nanotubes (MWNTs) have more than two layers of carbon atoms. Especially large MWNTs are known as graphitised nanofibres (GNFs),[86] where the side-wall is made of many layers of carbon atoms which contain unique internal corregated morphology known as step-edges (or nano-folds). The length and diameter of a CNT varies, and the strain from p-orbital misalignment in the structure is inversely proportional to the CNTs diameter. CNTs may be metallic or semiconducting, depending on the chirality of the nanotube.[87] Several methods to produce CNTs exist, including arc-discharge[88] and chemical vapour deposition.[89] Nanotubes are terminated with fullerene-like hemispheres of carbon (end-caps) that must be removed by chemical or thermal treatment to access the interior cavity of the nanotube.[90] End-caps can be selectively oxidised over nanotube side-walls, called nanotube opening. This is because end-caps have higher strain than side walls due to greater p-orbital misalignment, caused by their hemispherical geometry. Opening allows material to be introduced into the nanotube cavity,[91] which is attractive as it gives access to nanoscale composite materials and facilitates the study of materials on the single molecule scale.[92] Some nanotubes have to be chemically cleaned to remove trace amounts of catalyst leftover from synthesis prior to use as supports.

COF/nanosupport hybrids give a material with the useful properties of a COF and the mechanical/electrical properties of the nanosupport. Chen *et al.* made COF-10@CNT for use as an anode in potassium-ion batteries, levering the potassium storage capabilities of COF-10 and the conductivity of the CNTs. The product was a powder that could easily be processed into an electrode via mixing. COF-10 was formed as a thin layer on the CNTs via direct condensation, leading to enhanced surface area compared to a bulk COF.[93] Wang *et al.* made a COF@CNT composite for electrochemical sensing of ascorbic acid. This gave the COF as crystalline thin

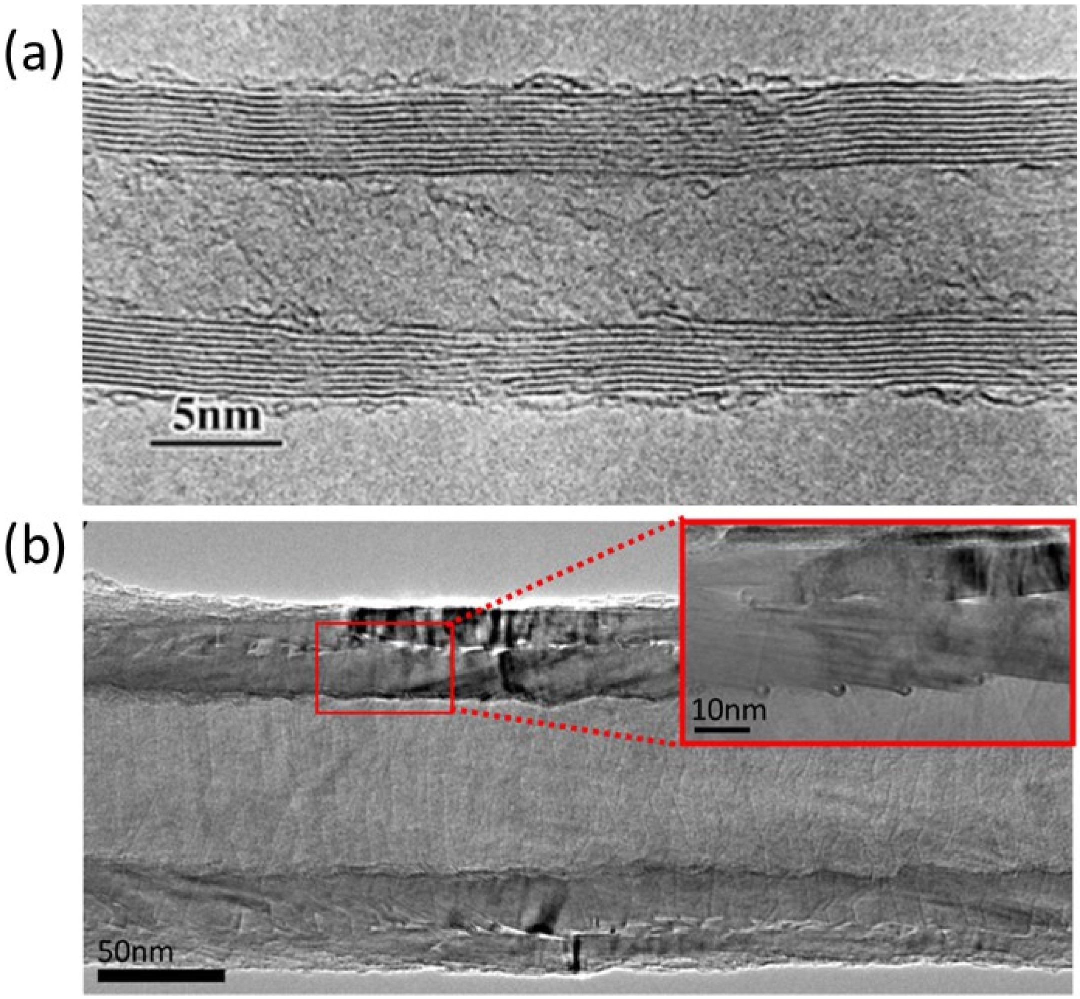

Figure 3: (a) Bright-field transmission electron microscopy (BF-TEM) image of a multiwalled carbon nanotube (MWNT). The MWNT has several side walls and a large internal cavity. Amorphous material can be seen attached to the outside surface of the MWNT. Adapted with permission from ref. [87]. Copyright 2001 Elsevier. (b) BF-TEM image of a graphitised nanofibre (GNF). The GNF has a much larger diameter than the MWNT and many more layers in it's side walls. Insert: GNF step-edges, which increase the interior surface area of the GNF and provide a preferential attachment site for species such as metal nanoparticles. Adapted with permission from ref [86]. Copyright 2020 American Chemical Society.

layer on the CNTs, again enhancing COF surface area and taking advantage of CNT conductivity. The composite was easily incorporated onto a glassy carbon electrode via drop-casting from solution.[94] Xu *et al.* leveraged the mechanical properties of CNTs to make their COF@CNT hybird into a flexible paper. The COF condensed as a layer on the surface of the CNT, then the reaction mixture made into a paper via vacuum filtration. CNTs are amenable to preparation as a paper as they consist of long fibres. The authors were then able to use a mask to prepare the paper in a predefined shape for use as a flexible component in an electronic circuit.[95] Wang *et al.* used the thermal stability of CNTs to make a COF/CNT composite for use in lithium sulphur batteries. The material was able to retain perfomance between -10 and 50 °C over 500 cycles.[96] CNTs would be stable up to hundreds of degrees, meaning the COF/CNT composite would not limit the upper operating temperature of the battery. Further COF/CNT composites have been successfully created using SWNTs,[97–99] MWNTs,[61,100–102] and GNFs.[103–106] Xu *et al.* prepared COF-rLZU1 on the surface of silica nanoparticles for use as the stationary phase in liquid chromatography. The COF was formed as a thin layer on the surface of the nanoparticles, then the bulk powder packed into a chromatography column and used to separate a mixture of organics. The advantage of this method is the nanoparticles lead to uniform thin COF of a well-defined morphology, and the COF could be tailored to match different mixtures for efficient separation. Silica nanoparticles provide a chemically inert support structure that are easy to prepare and handle.[85]

These examples show that COF/nanosupport hybrid materials can be applied usefully, and overcome the limitations associated with forming bulk COFs as powders. The above examples may not have been possible without the presence of nanosupports, or would have required substantial changes to how the COF was integrated into an application. Both bulk COFs and COF/nanosupports share the requirement for effective post-synthetic characterisation, with COF /nanosupport in particular requiring investigation of micro- and nanoscale morphology. Effective characterisation allows smart choices to be made about how to integrate materials into applications to make the best use of their properties.

1.3 Bulk Spectroscopy and Crystallography of Covalent Organic Frameworks

There are several techniques that have become established as standard practice for COF analysis, with one publication going as far as to lay out "gold-standards" for their use.[4] The choice of techniques used is the result of both scientific and socio-economic factors. It is expected that scientific concerns are the major motivator for choice of research technique; the technique must yield useful information that contributes to answering the research question at hand. For example diffraction techniques are only relevant if that sample produces detectable Bragg diffraction. Further, if techniques like X-ray diffraction can be used effectively to characterise a material this may sideline the need for electron diffraction techniques. Therefore the choice of analytical tool depends on the nature of the sample and the effectiveness of the available techniques. This said, it has been shown that researchers will tend to use the techniques they are familiar with or that are already established in their fields, and there is a financial cost and risk depending on the techniques used.[1] It has also been highlighted that so-called "signature pedagogies" can develop within a teaching environment, which are characteristic forms of teaching and learning that can define specific ways professionals think about and approach problems in their field of expertise.[107] As discussed above COFs are often considered more similar to MOFs than classical polymers, so most of the techniques used in the COF literature are derived from best-practices for MOFs. The techniques relevant to this thesis are outlined below.

1.3.1 X-ray Diffraction

X-ray diffraction (XRD) is a classic technique for solid-state materials science (Figure 4a).[110] It is used to find out information about the crystal structure of materials based on Bragg's Law; crystal planes separated by distance d will cause specular diffraction of X-rays at angle θ:

$$n\lambda = 2d\sin(\theta) \tag{1}$$

Where n is an integer and λ is the wavelength of the incident X-rays. Typically Cu($K_{\alpha1}$) X-rays are used. XRD is used extensively in the COF literature. Where COFs are formed as single

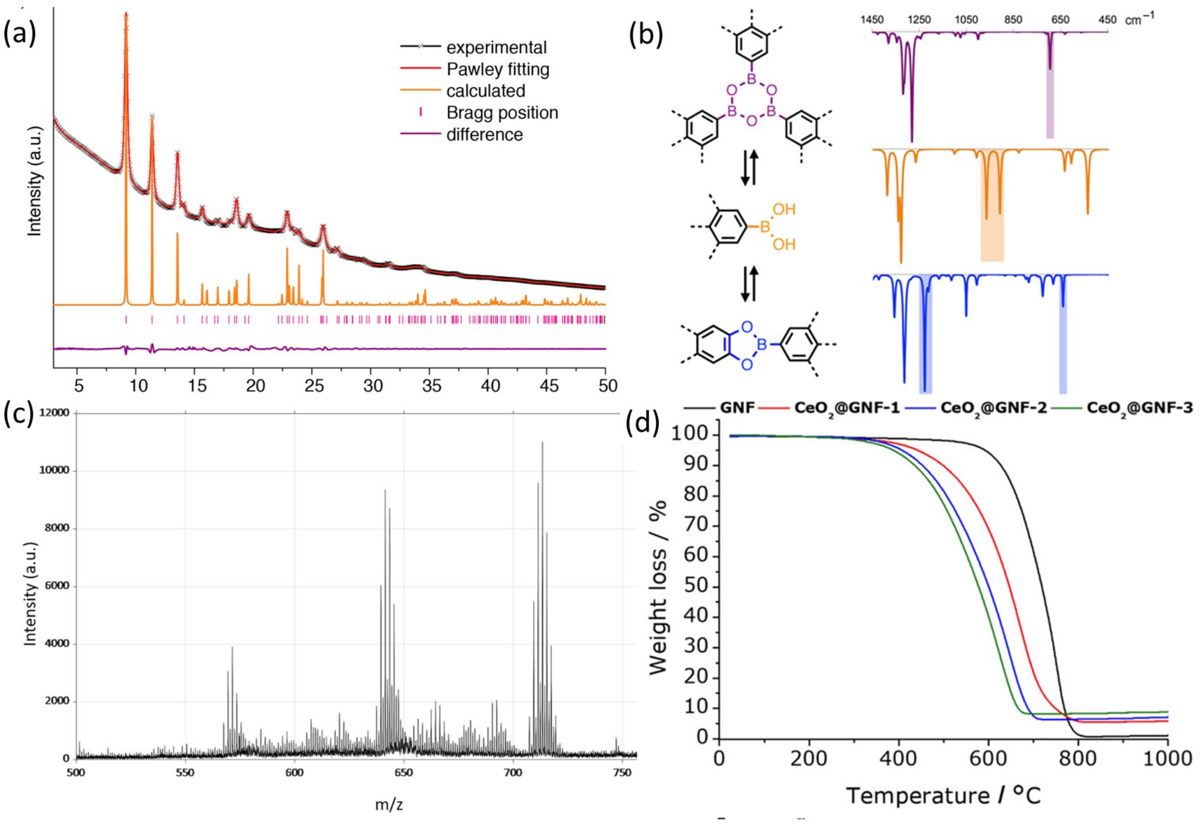

Figure 4: (a) Experimental and calculated PXRD pattern for COF-112. Typical COF powder patterns contain several high-intensity reflections between $0-20^\circ\ 2\theta$. Adapted with permission from ref. [4]. Copyright 2020 American Chemical Society. (b) IR spectra of COF boroxine, boronate ester, and boronic acid functionalities. The highlighted vibrations can be used to identify the presence of these functional groups in the IR spectra of boronate ester COFs. Adapted with permission from [108]. Copyright 2014 American Chemical Society. (c) MALDI-TOF spectrum of perchlorocoronene (PCC). The spectrum contains clear isotope and fragmentation patterns. Adapted with permission from ref. [109]. Copyright 2021 Royal Society of Chemistry. (d) TGA thermogram of cerium oxide nanoparticles on a GNF support. Residual weight is visible at 1000°. Adapted with permission from ref. [86]. Copyright 2020 American Chemical Society.

crystals, SC-XRD can be used to find the unit cell of the COF based on the symmetry of the pattern, then the atomic positions based on the intensity of the diffraction spots in the pattern. In X-ray crystallography *resolution* of a diffraction pattern refers to the d-spacing of the peak furthest from the centre of the diffraction pattern and is usually quoted in Å.

Typically COFs are polycrystalline powders and powder X-ray diffraction (PXRD) is used. PXRD gives a 1D powder pattern that shows intensity of reflection as a function of the angle between the X-ray source and the detector. Powder patterns may be subjected to Pawley or Le Bail fitting, where the whole pattern is fitted without a structural model. Peak positions are constrained based on size and symmetries of potential unit cells, which gives a "best fit" for how well the pattern matches a given unit cell and space group. The specifics of the Pawley and Le Bail methods differ.[111] For many COFs it is common to model unit cells using electronic structure methods such as density functional theory (DFT) then simulate powder patterns from the model.[4,112] This simulated pattern can then be compared to the experimental powder pattern. Once a structural model has been arrived at, Rietveld refinement can be used to match peak position, peak shape, and peak intensity to a given structure model.[113]

In some cases it has been noted that COFs yield a PXRD powder pattern with broad peaks despite exhibiting nanoscale crystallinity via TEM.[114] This is a key limitation of diffraction techniques. As shown by the Scherrer equation peak broadening correlates with crystal domain size.[115,116] In extreme cases such as for very small crystals or for nanosheets, this can make make a nanocrystalline sample appear to be amorphous by PXRD.[117] This has been identified as affecting COFs as the aforementioned crystallisation problem leads to many small, randomly oriented crystals that can appear amorphous; this is due to low intensity of diffraction from individual crystals coupled with random orientation of each crystal.[118] If a material forms as multiple phases, this can also lead to powder patterns that are difficult to interpret. In these cases, supplementary analytical techniques such as microscopy are often needed to determine the crystal structure of the sample.

1.3.2 Infrared Spectroscopy

Infrared spectroscopy (IR) is based on the principle that chemical bonds vibrate when they absorb specific wavelengths of light (Figure 4b). A useful introduction to the technique is found in *Fundamentals of Fourier Transform Infrared Spectroscopy*, which was used to furnish details for this section.[119]

Modern instruments use Fourier transform IR (FTIR). An IR beam containing multiple frequencies is passed through a sample, where the sample will absorb frequencies that cause bond vibrations. An interferometer is then used to create an interference pattern; the source beam is split into two beams with a different path length controlled by a moveable mirror, then recombined and passed through the sample. The moveable mirror means that for a given frequency the light wave will oscillate between constructive and destructive interference as a function of mirror distance. The frequency of oscillation depends on the frequency of the light, as each frequency of light will have a different optical path length that results in constructive/destructive interference. The resulting signal reaching the detector is known as an interferogram, and is formed of the sum of wave intensity versus mirror position for each wavelength in the spectrometer. This is measured as intensity versus mirror position (in centimetres). A Fourier transform converts the interferogram into a spectrum (in wavenumbers). The final IR spectrum of a sample is then the log ratio of a background spectrum and the spectrum of the sample. The background spectrum is comprised of atmospheric gases and any contributions from the detector, which are removed from the final spectrum by taking the above ratio.

IR is typically recorded as an absorbance spectrum, but can be converted to transmission:

$$A = \log(I_0/I) \tag{2}$$

$$T = 10^{-A} \tag{3}$$

Where A is the absorbance, I_0 is the intensity of the background spectrum, I is the intensity of the sample spectrum, and T is the transmission. The current practice in the COF literature is to report transmission spectra. The Beer-Lambert law then allows concentration c of a functional group to be calculated if the path length l and molar extinction coefficient ϵ are known:

$$A = \epsilon c l \tag{4}$$

Relevant sample preparation techniques for solid COFs are attenuated total reflectance (ATR) and pellet. ATR uses a solid crystal with a high refractive index through which IR radiation is passed. Diamond is often used due to its mechanical properties and high refractive index, with the downside being the strong diamond vibrations between 2200 and 2000 cm^{-1}. Total internal reflection of the radiation forms an evanescent wave at the surface of the crystal, against which the sample has been pressed into close mechanical contact via an anvil. The evanescent wave penetrates a limited distance into the sample on the order of micrometres, where absorption of IR by the sample occurs. This attenuates the IR beam. The main downside to ATR IR is that as the penetration depth of the evanescent wave varies with wavenumber, the relative intensities of peaks in an ATR spectrum will be different to those of a non-ATR spectrum. This also complicates calculating the concentration from an ATR spectrum. Penetration depth also depends on the refractive index of the crystal, so it is possible to create a depth profile of a sample if several crystals are available for the same spectrometer. This will show composition changes as a function of penetration depth. The position of an IR stretch will be essentially the same between ATR and non-ATR techniques.

In contrast, the pellet method creates a dispersion of the compound within an IR transparent material such as potassium bromide (KBr). KBr pellets are chemically inert and IR transparent above 400 cm^{-1}, but will absorb atmospheric water. The sample is first ground to a fine power, then mixed with KBr powder and pressed into a pellet. IR radiation is transmitted directly through the pellet; for this method peak intensity is concentration dependant and will not vary with wavenumber. An advantage of KBr pellets are that they allows less sample to be used, as roughly only 1 - 10 % of the pellet needs to be sample with the remainder being KBr. The key disadvantage is the time commitment required compared to ATR IR, and the brittleness of KBr pellets that causes them to crack easily.

Smith *et al.* provide an invaluable study of COFs via IR spectroscopy,[108] where they conduct an in-depth study of the fingerprint region vibrations for boronic acids, boroxine rings, and boronate ester rings. This allows fast and precise identification of these stretches in other

COFs. For COFs, IR is used to observe the appearance of vibrations caused by the polymer and attenuation of vibrations caused by the monomers.

1.3.3 Mass Spectrometry

In-depth details on mass spectrometry (MS) are available in textbooks such as *Mass Spectrometry* by Gross.[120] MS separates ions based on their mass (Figure 4c). The ionisation process causes molecules to fragment in predictable ways, such that each molecule has a specific mass spectrum that can be used to identify the molecular formula of the compound and which gives clues about the structure of the molecule. Mass spectra also contain isotope patterns, based on the abundance of elements on Earth. This allows exact determination of the identity of ions, as although two ions could have nearly the same mass the isotope pattern will be different depending on which elements are included in the ion.

Many MS ionisation techniques are not suitable for solids. Matrix-assisted laser desorption ionisation (MALDI) MS can be performed on dry powders, and works by desorbing and ionising a sample using laser irradiation. MALDI can be applied to COFs but is not widespread. Other MS techniques are often less useful for COF polymers, as many techniques require the compound to be dissolved, but these techniques can be used to gain mass spectra of COF monomers. One example is electrospray ionisation, where the substrate is ionised as a result of a high voltage being applied to the solvent to make an aerosol.

At the start of this body of research (October 2019), the only examples of MALDI of COFs in the literature used COFs as a matrix. Feng *et al.* used COF TpBD as a matrix to aid in detection of fatty acids and amino acids positive ions, and reported COF ions in the matrix only at high COF concentration.[121] Hu *et al.* used boric acid functionalised COFs as a selective absorbent and MALDI matrix for *cis*-diols, and reported no interference of the COF in the mass spectrum.[122] Since then Ouyang *et al.* and Sun *et al.* have also explored COFs as a MALDI matrix,[123,124] but the author found no examples of using MALDI to investigate COF structure or synthesis.

1.3.4 Thermogravimetric Analysis and Differential Scanning Calorimetry

Thermogravimetric analysis (TGA) measures to a high degree of precision the mass of a sample while it is heated, allowing mass changes at specific temperatures to be investigated (Figure 4d). This can be used to interrogate a range of thermal processes such as combustion temperature, pyrolysis temperature, or loss of solvent from COF pores. In essence TGA gives a measure of thermal stability, and as such is often applied to COFs or their monomers to evaluate the "strong covalent bonds" that make up their framework.[4] For nanocomposites TGA can be used to find the "loading" of a nanomaterial on a nanosupport, i.e. the relative amounts of each material in the sample.[86]

The related technique differential scanning calorimetry (DSC) measures heat required to increase the temperature of sample. This allows detection of physical transitions such as phase changes, where the sample will use absorbed heat to undergo a physical process rather than increase temperature. DSC is used widely in traditional polymer chemistry, but has not seen wide uptake by the COF community. This may be that as crystalline polymers, COFs do not have glass transition temperatures or cannot melt, or that at the current state of COF technology COF researchers are not concerned with these properties of COFs.

1.3.5 Nuclear Magnetic Resonance Spectroscopy

Nuclear magnetic resonance (NMR) spectroscopy is of course a staple technique for chemists.[125,126] Details can be found in a number of textbooks.[127,128] Atomic nuclei have an associated spin quantum number (I_s) that is either an integer or a half-integer. Nuclei have a number of spin orientations given by $2I_s + 1$, so if I_s is greater than 0 then the nuclei will have multiple possible spin orientations. These typically are of degenerate energy, but the presence of a strong external magnetic field will separate them into different energy levels. For the case of $I_s = 1/2$, such as hydrogen, a strong magnetic field will give an upper and lower spin state where the upper state is aligned against the external field and the lower is aligned with the external field. The magnitude of the energy difference between the two states is proportional to the strength of the applied magnetic field. Nuclei can be promoted from the lower to the upper spin orientation by application of radio waves that have the same energy as the difference between the upper and lower spin orientation. Both orientations will have similar populations at room temperature.

In an NMR experiment a solution-phase sample is rapidly rotated in a strong magnetic field, then a range of radio frequencies are applied to the sample in short pulses. Between pulses the excited nuclei undergo relaxation and emit radio frequencies corresponding to the energy difference between the spin orientations. These are detected as a function of time, then a Fourier transform is used to recover the frequencies emitted by the sample. This is then calibrated onto a scale of parts per million relative to a standard such as chloroform or tetramethyl silane. The chemical shift of the nucleus is affected by its chemical environment due to shielding. Briefly, the electron density creates an electromagnetic field that opposes the applied magnetic field from the spectrometer. This means the nucleus experiences an effective magnetic field that is relative to the chemical environment of the nucleus. A functional group containing electronegative atoms will reduce the shielding at the nucleus and lead to a larger chemical shift. Nuclei in identical chemical environments have the same chemical shift.

Spin-spin coupling occurs between adjacent nuclei with different chemical environments. Taking the case of proton NMR, this causes peaks to be split into multiplets that based on the number of adjacent protons. This is a through-bond effect and is strongest for protons separated by three bonds (protons on adjacent carbon atoms). The splitting is given by $2nI_s + 1$ where n is the number of coupling nuclei, which for protons simplifies to $n + 1$. For a CH_2 next to a CH_3 for example, the spectrum would contain a triplet from the CH_3 and a quartet from the CH_2. The distance between the peaks within a multiplet is called the coupling constant. Long-range coupling may also occur through 4 or more bonds and causes extra splitting within a multiplet. For example a double may appear to be a quartet; closer inspection will reveal two coupling constants within the multiplet, indicating the presence of long-range coupling. Roofing may be observed as the chemical shift between two multiplets approaches the coupling constant. This causes the multiplets to become distorted; in an extreme case two nearby doublets could appear to be a quartet. Spin-decoupling removes these effects, and ^{13}C-NMR is often recorded with spin-decoupling. In proton NMR the integrated area under a multiplet is proportional to the number of protons in that environment. The ratio of integrals for each peak in the spectrum can then be used to work out which environments contain more protons.

Of relevance to this work are solution state ^{1}H-NMR (proton NMR) and ^{13}C-NMR, but there are a wide range of other nuclei that are spin-active (e.g. ^{19}F, ^{11}B, ^{10}B) and NMR can also be performed in the solid state. Proton NMR and ^{13}C-NMR are very relevant to covalent organic frameworks, as the majority of the atoms in the organic monomers are often carbon or hydrogen. Both are spin $\frac{1}{2}$ so have straightforward splitting patterns. For COFs, NMR is typically confined to analysing the COF monomers prior to polymer synthesis. This is because conventional NMR requires a solution-phase analyte. Solution-phase NMR has been employed to show successful COF synthesis by digesting a COF solid (e.g. with acid) to yield a solution of COF monomers. This is used to accurately measure the ratio of monomers in the COF.[4] Solid-state NMR has been reported in the COF literature to analyse COF polymers but is less common,[129] possibly due to solid-state NMR being less widely available.

1.4 Electron Microscopy of Covalent Organic Frameworks

1.4.1 Scanning Electron Microscopy

Details of scanning electron microscopy (SEM) were taken from *The Springer Handbook of Microscopy.*[130] SEM uses a beam of electrons to form an image of the surface of a sample. The electron beam is converged to a point at the sample, then rastered over the sample to build up an image line by line (pixel by pixel). SEM is a surface technique, but the beam penetrates a limited distance into the sample depending on the beam energy and sample composition (the interaction volume). Beam-sample interaction causes backscattered electrons (BSE) and secondary electrons/secondary ions (SESI) signals to be emitted from the sample which can be used to form an image of the sample. Increasing the accelerating voltage increases the interaction volume, and for some nanomaterials the interaction volume can be similar to the nanomaterial thickness. These images contain depth information and are not flat projections. The SEM resolution is governed by the spot size at the sample, and the speed at which the beam is scanned over the sample. Slower scan speeds yield higher resolution but cause greater beam damage, and the image will be blurry if the sample moves during the time taken to scan the beam over the entire sample. SEM is used extensively in COF publications to investigate the microscale COF morphology and topography. SEM-EDX and SEM-EDX mapping are also used to find out the elemental composition of COFs.

1.4.2 Transmission Electron Microscopy

There are several good texts for a comprehensive understanding of transmission electron microscopy (TEM); for an overview there is *The Springer Handbook of Microscopy*[130] or *Transmission Electron Microscopy: a textbook for materials science*;[131] details of electron crystallography can be found in *Electron Crystallography: Electron Microscopy and Electron Diffraction*;[132] and electron energy loss spectroscopy has been covered in *Electron Energy Loss Spectroscopy*[133] and *Electron Energy-Loss Spectroscopy in the Electron Microscope*.[134] More generally, *Optics* contains a good foundation for microscopy.[135] These texts provide most of the information in this section.

The general concept of TEM is that it is a microscopy technique which uses a beam of electrons to form magnified images of an object with greater resolution than a conventional light microscope can furnish. TEM was developed during the 1930's, and since then has become a staple technique for material science as it allows a wide range of information to be gleaned from a sample;[136] a modern TEM can be used for imaging, diffraction, and spectroscopy of a sample during a single operating session. It is important to note that TEM is a local-probe method which is used to example sub-mg quantities of a sample under non-standard conditions, and therefore care must be taken to ensure image analysis is representative of the sample. Being a local-probe method, TEM is a powerful tool for analysing the structure of COF/nanosupport materials at the nanoscale. As TEM is a central technique to this thesis, it will be explained in a higher level of detail below.

Accelerating voltage controls the energy and wavelength of the electron beam (e-beam) in the TEM; electron energy is thus typically quoted in kilo electron volts (keV). Electron beam wavelength is given via the de Broglie equation with a relativistic correction as the electron velocity at the typical operating voltages of TEM is a significant fraction of the speed of light. Accelerating voltage can often be controlled by the microscopist and is typically between 80 - 300 kV for conventional TEM, and as a rule the electron wavelength is an order of magnitude shorter than that of Cu(Kα) radiation (1.54 Å). For example, an electron accelerated to 100 keV would have a wavelength of 0.037 Å. When discussing e-beam irradiation it is useful to distinguish between electron *flux* or *dose-rate* (electrons per area per time) and electron *fluence* or *dose* (electrons per area, or time-integrated flux). It is common in the TEM community to use the terms fluence and dose interchangeably, and it should be made clear that in this context that dose does not refer to energy absorbed from radiation per unit mass. This thesis will use flux/fluence nomenclature.

Resolution in a TEM image is defined as the smallest distance between two points in the object (the sample being imaged) which can be seen as two separate points in the image. If the two points were any closer together in the object, they could not be distinguished as separate in the image. The resolution is inversely proportional to the wavelength of the radiation used in the image forming process. This is essentially the result of imperfect lenses focussing rays from a point on the object as a disc in the image, known as an Airy disc. The radius of the smallest possible Airy disc is the resolution of the microscope in TEM, and the diameter is the resolution in SEM and STEM, given by Abbe's equation:

$$r = \frac{1.22\lambda}{n\sin(\theta)} \tag{5}$$

Where r is the radius, λ is the wavelength, n is the refractive index and θ is the semi-angle of collection for the lens through which the electrons pass. The quantity $n\sin(\theta)$ is also known as the numerical aperture (NA). NA can be thought of as the ability of a lens to collect radiation, and defines the maximum scattering angle of radiation that a lens can collect. As an aside, Hecht writes that NA was developed by Ernst Abbe while working at the Zeiss microscope workshops. The shortest wavelength of visible light is 380 nm, so no structures smaller than this can be resolved using a conventional light microscope. The wavelength of electrons is given by the de Broglie equation:

$$\lambda_e = \frac{h}{\sqrt{2m_e eV}} \tag{6}$$

Where the wavelength (λ_e) is the quotient of Planck's constant (h) and the momentum ($\sqrt{2m_e eV}$); m_e is the rest mass of the electron, e is elementary charge, and V is the accelerating voltage. For relativistic electrons, a correction is applied:

$$\lambda_e = \frac{h}{\sqrt{2m_e eV(1 + \frac{eV}{2m_e c^2})}} \tag{7}$$

Where c is the speed of light. The electron wavelength decreases as the electron velocity increases. Increasing the accelerating voltage leads to lower contrast in TEM and STEM images due to the scattering cross-section being inversely proportional to electron speed; slower electrons are more likely to interact with the sample. Higher accelerating voltages allow beam penetration through thicker regions of the sample. Another concept that is useful to refer to is numerical aperture (NA, given by Snell's law) which describes the range of angles an optical system can accept rays:

Resolution in the TEM is limited by optical aberrations:[135]

- Defocus, where the focus point is translated above or below the detection surface. This causes a blurry image with a thick outline. For low-contrast materials, deliberate defocus is often used to help visualise the sample.
- Comatic aberration (coma), where magnification changes as distance from the optical access increases so off-axis images are slightly displaced from each other, which causes a spot to be spread out into a line like a comet.
- Chromatic aberration, where different wavelengths are bought to a focus at different points. This may be different points in an x-y plane (line abberation) or different points in the z-direction (depth abberation).
- Spatial aberration, where electrons are emitted from different parts of the source so the beam is not infinitely thin.
- Spherical aberration, where focussing power changes as distance from optical axis increases which causes spots to appear as discs in the image.
- Astigmatism, where perpendicular lens directions have different focussing power. Causes a spot in an image to be focussed as an oval.

- Distortion, when a straight line in the object is curved in the image. Barrel and pincushion distortion are common radially symmetric types.
- Field curvature, which is caused by the image plane being an arc in reality which cannot be perfectly focussed on a flat detector, so the outside of the image is blurry. This is rarely an issue in TEM.

From a practical viewpoint these should be minimised by correct alignment of the TEM; any residual aberration will lead to a loss of resolution (and therefore information) in the TEM images. It is also worth noting resolution can be limited by factors such as voltage instability, environment vibrations, and sample thickness; and that in TEM spectroscopy resolution can refer to the spatial resolution as above, or the energy resolution of the spectrum.

To briefly elucidate electron scattering; electrons may scatter coherently or incoherently depending on the phase relationship of the electron waves, analogous to scattering of electromagnetic waves. Electrons are then said to scatter elastically or inelastically, where inelastically scattered electrons have a measurable change in energy before and after a scattering event while elastically scattered electrons do not. Elastic scattering is typically coherent, while inelastic scattering is typically incoherent. As electrons interact strongly with matter, electrons may undergo more than one scattering event as they pass through a sample. Electrons may be unscattered, single-scattered, or multiple-scattered. Some texts draw a distinction between plural scattering (more than one and less than twenty scattering events) and multiple scattering (more than twenty scattering events). Finally, electrons scattered less than 90° are termed as forward-scattered, and electrons scattered more than 90° are back-scattered.

TEM image formation can be compared to light microscopy. The end result is a 2D parallel projection caused by interference of the electron wave within and after the sample. The images formed contain contrast caused by difference in brightness between different areas of the image, where brightness is a measure of the electron wave intensity at that point in the image. Brightness is thus controlled by changing the electron flux. Contrast mechanisms are amplitude contrast, where regions of the sample scatter the e-beam more strongly out of the angle captured by the detector, and phase contrast, where coherent electron-waves interfere post-sample. Amplitude contrast can be further broken down into mass/thickness contrast (i.e. due to variations in sample thickness, density, or atomic number) and Bragg diffraction contrast. Note that some authors use the term Z-contrast to refer to contrast caused by scattering from individual atoms in high spatial resolution images, while other authors use terms interchangeably. Mass/thickness contrast is a form of incoherent electron scattering, while phase and Bragg contrast are examples of coherent electron scattering. Contrast in coherent scattering can be more prone to significant contrast changes with variations in specimen thickness, orientation, or defocus, which may make interpretation more complex.

Several contrast mechanisms can occur at once, for example a crystalline material imaged at a low collection angle would typically have significant contrast contributions from both Bragg contrast and mass/thickness contrast. These contrast formation mechanisms mean that TEM images should not be interpreted directly as containing 3D information without due care - a higher contrast region in an image may be due to local thickness or local density variations, and determining which is the cause may require careful inquiry. Bright-field (BF) TEM images are formed using the direct beam, which is the central part of the electron beam containing unscattered electrons or those scattered through small angles (mrad), up to a larger angle defined by any apertures in use beyond which electrons are excluded. As the sample scatters the electron beam, it appears as dark contrast against a light background, with any vacuum in the TEM images being the brightest region. The atomic number contrast in BF-TEM image scales approximately to the square-root of the atomic number of the image. Darkfield (DF) TEM images exclude the direct beam, so only electrons scattered at higher angles contribute to the image formation, leading to the sample appearing as bright contrast against a dark background. This leads to thicker or higher atomic number regions of the sample appearing the brightest in the image. These kinds of TEM images are sometimes referred to as conventional TEM.

High-resolution TEM (HRTEM) or phase contrast TEM (PCTEM) images are based on phase contrast caused by interference between electron waves post-sample. This leads to lattice fringes (also known as d-spacing) to be present in the images, which are caused by the periodic arrangement of the atomic planes in the sample leading to coherent electron waves. Unlike amplitude contrast images, HRTEM images typically require image simulation for full understanding as the bright and dark contrast caused by phase contrast does not always arise from atomic positions and may arise from the interference of the electron waves. For example a bright feature in a HRTEM image may correspond to an atom, while the intuition from conventional TEM would lead one to think that bright contrast would be due to the absence of an atom. HRTEM allows images of greater resolution than is possible with conventional TEM, and can be used for crystallographic analysis of a COF sample.

Crystallographic data in TEM comes from either HRTEM images or electron diffraction patterns, from which the unit cell and atomic positions in the sample can in principle be determined. In HRTEM, crystallographic structure factors can be directly recovered from images by direct measurement of intensity of Fourier transforms (FT). By using the optics of the TEM to form a diffraction pattern rather than an image, diffraction patterns are collected as single-crystal patterns, spotty ring patterns, or ring patterns, depending on the number of individual crystals the data is acquired from. Electrons interact with the electron density in the sample as well as the atomic nucleus, and are more strongly scattered than X-rays. Electron crystallography can be used to collect single-crystal diffraction patterns from smaller volumes than X-ray diffraction, and is a good complementary technique to TEM direct-space imaging. Difficulties in electron diffraction arise from multiple or plural electron scattering causing changes in diffraction spot intensities or the appearance of forbidden reflections in the diffraction pattern. The diffraction may be performed with a parallel e-beam (selected area electron diffraction, SAED), or a condensed beam (convergent beam electron diffraction, CBED). Other useful information such as Kikuchi lines (diffusely scattered electrons that are then Bragg scattered giving rise to bright and dark lines in the diffraction pattern) may also be present in the diffraction pattern.

Finally, TEM can be used to obtain spectroscopic data: energy dispersive X-ray (EDX) spectroscopy and electron energy loss spectroscopy (EELS). Inelastic scattering gives rise to EELS in TEM. This technique separates the direct beam using a magnetic prism to create a spectrum of electron energies where the unscattered or elastically scattered electrons form the zero-loss peak and the background is formed of electrons that have lost variable amounts of energy up to the beam energy. EELS allows elemental analysis because the beam electrons can ionise core-shell electrons from elements. This leads to a specific energy loss for these electrons, giving rise to an edge in the spectrum. Electrons are also scattered at a characteristic angle (θ_E):

$$\theta_E = \frac{E_{edge}}{2E_o} \tag{8}$$

Where E_{edge} is the energy at which the edge occurs in the EEL spectrum and E_o is the initial energy of the electron beam.

EELS can also be used to identify hybridisation of elements, and is most useful for light elements such as boron, carbon and oxygen. EELS is a powerful technique which can be used to deliver a range of information about a sample. The low-loss EEL spectrum (less than 50 eV) is dominated by the zero-loss peak (ZLP) and plasmon peaks that can be used to give a range of information including sample thickness, band gap determination, reflectance, and other optical data, and can often be compared directly to optical measurements. The core-loss EEL spectrum (greater than 50 eV) gives elemental analysis from edge location, and hybridisation states from the energy loss near edge structure (ELNES) and extended energy loss fine structure (EXELFS), and is analogous to the fine structure in an X-ray spectrum. High resolution EELS (HREELS) allows vibrational spectroscopy to be performed at the sub-nanoscale. While EELS typically has lower energy resolution than comparable optical techniques, EELS is able to collect information from a wide range of the optical spectrum at the same time and with much greater spatial resolution. For reference, the EELS spectrum up to 7 eV covers the entire UV-Vis region and lower frequency radiation, while above 7 eV can collect data analogous to hard UV and soft X-ray radiation.

EDX spectroscopy, also known in the literature as EDS, is complementary to EELS. The atoms ionised by the beam electrons undergo relaxation processes where higher core and valence electrons relax into the ionised orbital. This releases energy that either stimulated emission of an Auger electron or emission of an X-ray photon. The photons emitted have energy equal to that of the gap between orbitals in the source atom, so is also useful for elemental analysis. The number of Auger electrons versus X-ray photons produced is the fluorescence yield of the element, which practically means that EDX is best suited to identify heavier elements. The background in EDX is composed of bremsstrahlung radiation, X-rays emitted by beam electrons that are slowed from interactions with atomic orbitals and nuclei as they pass through the sample. Bremsstrahlung can be of any energy up to the beam energy, but are more likely to be lower. An electron losing a large amount of energy is less likely that losing a small amount of energy in a single scattering event. EDX can give accurate elemental analysis and ratios of elements in a sample, and is suitable for nearly the full range of elements in the periodic table with reduced counts for elements emitting X-rays of less than 1 keV. Quantitative EDX analysis requires knowledge of the sample thickness and density and allows quantification of the amount of each element contributing to the spectrum. EDX spectrum simulation can also be a useful tool for confirming the identity of experimental data.

Transmission electron microscopy therefore represents a powerful suite of techniques that can be used to study the morphology/topography of COFs, their crystal structure, and provide elemental analysis, and is complementary to the other techniques mentioned so far. However, EM has certain limitations. TEM cannot get data on every type of sample; the sample must be electron-transparent (typically less than 100 nm thick). Each technique is low throughput, as it can take hours to prepare and image the sample. Beam damage can make an area imaged unrepresentative of the rest of the sample. TEM grids are typically 3 mm diameter of which only a small area can be imaged in detail, so the assumption must be made that the sample seen in the microscope is representative of the bulk material. The specimen chamber must be evacuated to 10^{-5} mbar so the electron beam does not interact with gas before the sample, and to prevent arcing that could damage the instrument, so samples must be stable in vacuum. Samples that might out-gas or that are fragile such as cells must be flash-frozen, which can create a film of water ice on the sample during imaging. If the ice does not form as an amorphous layer, this will affect the usability of diffraction techniques.

1.4.3 Scanning Transmission Electron Microcopy

Scanning transmission electron microscopy (STEM) adheres to the above principles, but makes use of a different image forming system. Rather than a spread parallel beam, the e-beam is converged to a point and rastered over the sample. This builds up an image line-by-line, and often the ability to stop the beam at specific pixels in the image to perform electron energy loss spectroscopy (EELS), energy dispersive X-ray spectroscopy (EDX), or convergent beam electron diffraction (CBED) on small areas of the sample. EDX- or EELS- mapping can also be performed, by taking a spectrum at each pixel in the STEM image and making a colour-coded map of which elements are detected at each pixel. One widely used mode is high-angle annular dark field STEM (HAADF-STEM), which uses very large angle scattered electrons to form the image, forming what is commonly called a Z-contrast image (where Z is the atomic number of the element causing scattering). Z-contrast scattering scales roughly to the square of the atomic number (Z), and typically the approximation $Z^{1.8}$ is used. In STEM the beam is transmitted through the sample to create a 2D image where contrast is formed from scattering of the beam electrons; STEMs are typically equipped to detect BF and DF electrons.

1.4.4 Electron Beam Damage

Irradiation of a sample with high energy electrons causes damage to the sample (Figure 5). The accelerating voltage of the microscope defines the e-beam energy, while the electron flux affects the rate of energy transfer to the sample. Damage processes may not occur below a certain threshold voltage; at a particular voltage above the threshold voltage the electron flux will affect the rate of e-beam damage, at that voltage. Researchers usually try to minimise beam damage as it makes the area imaged unrepresentative of the entire sample, but there is a body of research that uses the electron-sample interaction as a source of energy for chemical reactions.

There are multiple competing mechanisms of beam damage. Atoms may displaced from their original position, or sputtered from the surface of the sample.[138] Energy transfer as heat leads to phase change (melting) or bond breaking.[139] Radiolysis involves breaking of bonds via electron-electron interactions, which can lead to breaking and reforming of weak forces such as van der Waals bonds or strong bonds such as covalent bonds.[140] Electrostatic charging involves ionisation of the sample by the electron beam, leading to a localised charge accumulation that can cause strain in the sample. Thin samples will be ionised to cations by the beam as it is unlikely fast electrons will be captured by atomic orbitals, whereas in thick samples beam electrons can be deposited into the material to create an anion.[141] Direct knock-on damage is caused by the energy transferred from the interaction of a beam electron and an atomic nucleus, and is particularly relevant for samples containing C-H bonds below 100 kV accelerating voltage. The profile for direct-knock on damage is not a step-function, rather at low energies the rate is negligible.[142]

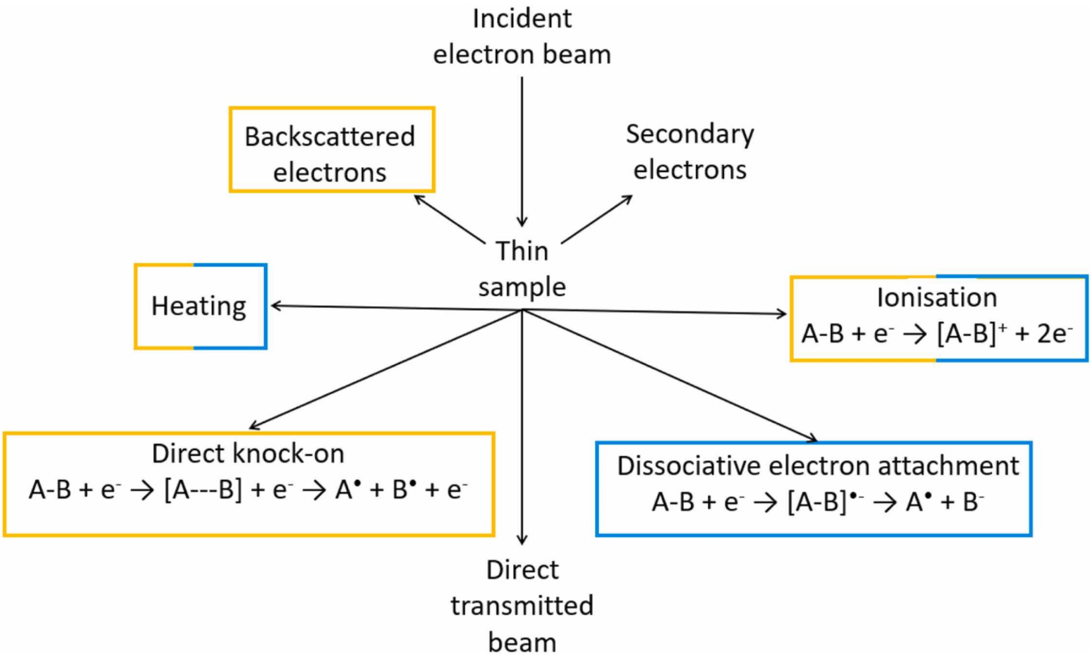

Figure 5: Diagram illustrating the types of beam damage on a thin sample, where yellow boxes indicate primary electron effects, blue boxes indicate secondary electron effects, and yellow/blue boxes indicate effects caused by both primary and secondary electrons. Reproduced with permission from ref. [137]. Copyright 2022 Elsevier.

Putting aside the precise damage mechanisms, the effects of these beam damages are sputtering atoms, breaking chemical bonds, and movement of atoms from their original positions.[140,143] This can be seen in the TEM as diffraction patterns fading over time due to changes in the crystal structure of the sample, elemental composition changing over time, or sample morphology changing over time. Beam damage tends to increase as a function of increasing sample thickness, decreasing thermal/electrical conductivity, and increasing electron flux. The effect of electron beam energy on molecular materials is further complicated due to the cross-section for direct-knock on damage for C-H bonds increasing below 100 kV; for most bonds, e.g. C-C, direct-knock on damage is at a minimum below 100 kV. Strategies to minimise beam damage have been described by Egerton:[138] thinner samples, using electrically/thermally conductive sample, putting the sample in contact with an electrical/thermal conductor, cooling the sample, selecting an accelerating voltage to reduce specific damage pathways, and reducing beam flux and/or total fluence. For example making a material as a hybrid with carbon nanotubes may reduce the effects of secondary electrons on the sample by making the sample much thinner.[142]

At the time of writing there has not been published an in-depth study on electron beam damage pathways of COFs. It is reasonable to assume that COFs will have similar electron-beam stability to molecular crystals, due to the similar types of C-H bonds, similar types of bonding and interactions (covalent bonds, $\pi - \pi$ stacking), and similar geometry of the constituents (e.g. typically aromatic organic molecules).[92,109] The main differences to consider are that the molecules in molecular crystals are held together by intermolecular forces rather than covalent bonds and molecular crystals will be higher density than COFs. It has been shown that a lower effective molecular occupancy, or volume of space occupied by a molecule in a crystal, leads to decreased stability.[144] Molecules in molecular crystals will also be more easily able to undergo beam-induced reactions with nearby molecules, whereas in COFs the rigid separation of monomers by the framework structure could help reduce these reactions. Therefore, it is expected that COFs will be marginally more stable in the electron beam than molecular crystals. For thin-layer COFs, it is expected that direct knock-on effect will play a major role in e-beam damage of COFs due to the high number of carbon-hydrogen bonds present in typical COF lattices. COFs are typically semi-conductors or insulators, so compared to metals they are at greater risk of thermal damage, and build-up of charge due to ionisation. Due to the low density of COFs secondary electron and sputtering mechanisms may play a reduced role in e-beam damage, although they will become more important as the sample thickness increases. For thin layer COFs selecting an accelerating voltage to minimise direct knock-on damage is vital, while for thick COFs the electron flux is likely more important.

1.5 Literature Review: TEM of COFs

At the time of writing much of the content of this section is in the process of being developed for publication as a review paper. An abridged version has been included here. The goal of this review was to perform a critical analysis of how different TEM techniques are currently being used for COF analysis, in order to find out what is being missed, what could be improved upon, and to highlight best practice.

The aim was to review all papers using at least 1 TEM technique on a COF; this relied on papers self-reporting their material as COFs, with similar materials such as MOFs, CMPs, or CTFs not included. Web of Science was the main search engine used, but SciFinder and Google

Scholar were consulted. In effect, this limits the review to papers indexed by Clarivate or CAS. The publications also had to written in English or translated to English. TEM techniques were defined as: BF-TEM, DF-TEM, HR-TEM, STEM, EDX (including STEM-EDX), EELS (including STEM-EELS), SAED, and CBED. The search terms "covalent organic framework" and "transmission electron microscope" (with the relevant conjugations) were used as the primary search, and "covalent organic framework" with each of the above TEM techniques was searched to check for any publications that may have been missed. For relevant publications, their citations and the papers citing them were checked for more unique publications. This gave 144 unique publications.

1.5.1 Bright-field TEM Imaging

BF-TEM is often used to study the morphology of COFs and typically appears alongside SEM or AFM. Nishiyabu *et al.* used SEM to show that the 3D morphology of their boronate ester COF was microspheres, followed by BF-TEM images of the COF spheres at higher magnification to provide a second confirmation of the morphology of the COF (Figure 6b).[145] This is a good example of how BF-TEM is typically integrated alongside other techniques to show the morphology of the COF, and is also representative of publications typically not performing statistical analysis of measurements taken from BF-TEM images. While the authors produced a size distribution of the COF spheres from the SEM, this was not included for the BF-TEM images.

3D information can be extracted from 2D BF-TEM images using tomography, where the sample is tilted between images. Martinez-Abadia *et al.* applied BF-TEM tomography to boronate-ester linked 2D-wavy Marta-COF-1 in order to show that by tilting over 70° the projection of the COF changes from dark fringes into hexagonal pores which was effectively linked to the computational model of this material (Figure 6a).[47] Surprisingly, TEM tomography is not used more often by COF researchers which might be a symptom of the electron-beam instability of COFs meaning they degrade before a full tomographic image series can be acquired.

TEM can also be used to study COF morphology during growth, or before and after reactions. Smith *et al.* studied a series of boronate ester COF-5 colloids using variable temperature liquid cell (VT-LC) TEM and showed the formation of boronate-ester linked COF-5 nanoparticles at

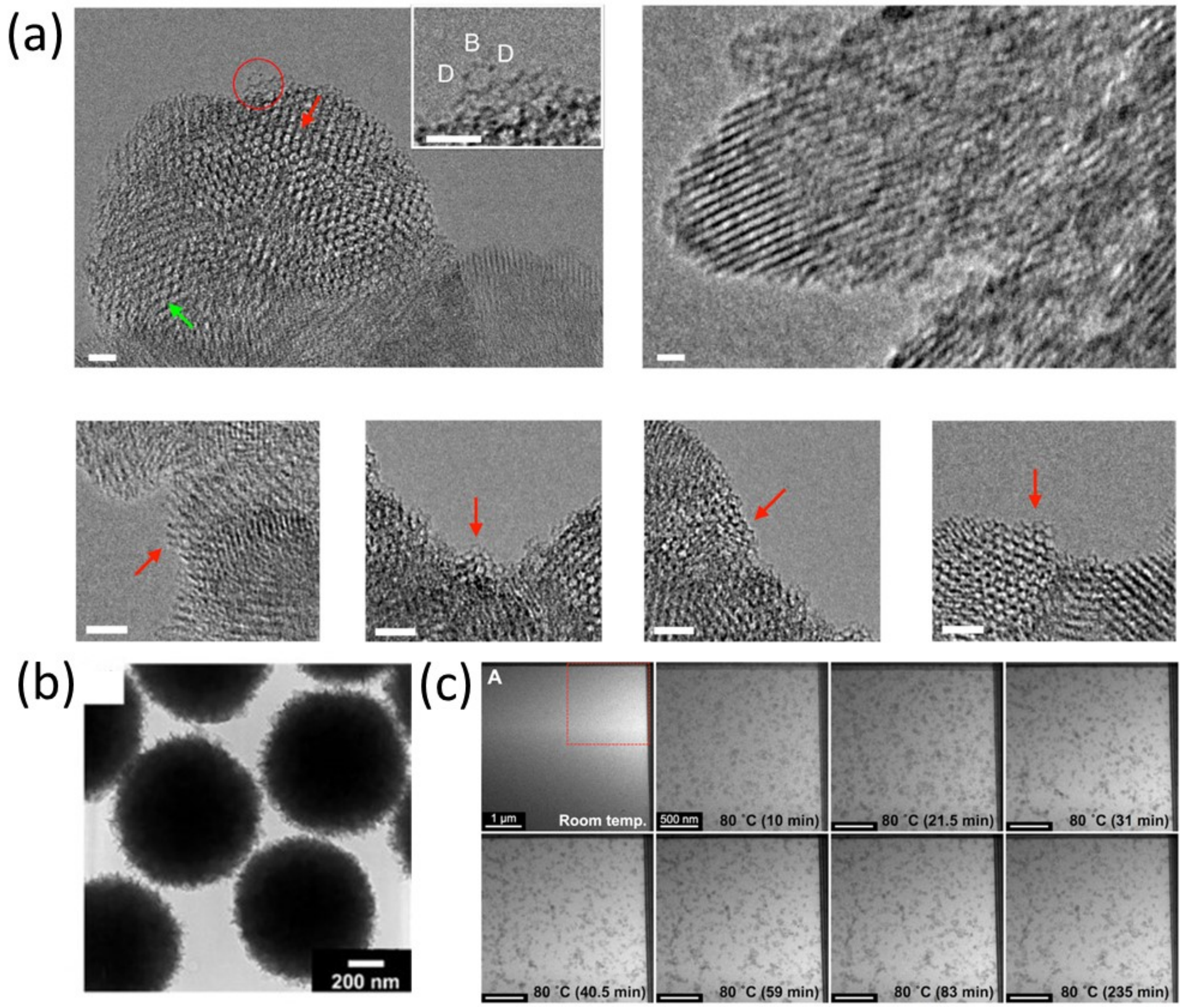

Figure 6: (a) Example of BF-TEM to study nanoscale morphology, BF-TEM tomography revealing how COF lattice projections change from hexagons to lines during a tilt. Adapted with permission from ref. [47] Copyright 2019 American Chemical Society. (b) Low-magnification BF-TEM showing morphology of COF spheres. Of note is that the majority of the microstructure is electron-opaque, leaving a small area at the edges that can be usefully studied at high magnification. Adapted with permission from ref.[145] Copyright 2012 John Wiley and Sons. (c) Variable temperature liquid cell TEM time series showing COF particle formation in-situ. Adapted from ref.[22]. Copyright 2017 American Chemical Society.

80 °C in solution (Figure 6c). This was quantified using a particle size range with error. Lei *et al.* used BF-TEM to study changes to the structure of their imine-linked COF@multi-walled carbon nanotube composite anode as a result of cycling.[104] They found that a solid electrolyte interphase (SEI) formed on their hybrid after cycling, and suggested that the COF was able to store lithium within its structure. Wang *et al.* used Fourier transforms (FTs) of their imine hexagonal 2D COF to appraise d-spacing variation.[38]

In summary, BF-TEM imaging of COFs is ubiquitous in the COF-TEM literature. It is typically used to study or illustrate the morphology of COFs. Currently it is not standard practice to include tabulated or distributed measurements taken from BF TEM images in publications.

1.5.2 Scanning Transmission Electron Microscopy

STEM was typically used alongside BF-TEM imaging as STEM-EDX mapping. Liu *et al.*[146] and Lu *et al.*[147] show a typical STEM-EDX analysis of a COF. DF-STEM images were acquired for regions of interest and a series of STEM-EDX maps showing the distribution of elements within that region. Liu *et al.* used the mapping to probe "single Fe/Co atoms" coordinated to nitrogen sites within the pthalocyanine-based 2D COF structure, and applied AC STEM imaging to show that there were no lattice fringes within their structure indicating that it is an amorphous COF. This is a powerful illustration of the high-end capabilities of STEM-EDX, provided that the spatial resolution of the STEM probe is small enough to detect individual atoms, and provided that the low Z-number elements yield enough signal to be detected against the background of other elements and Bremsstrahlung radiation. Lu *et al.* also used HAADF-STEM images to confirm the location of higher atomic number features in the imine-linked 2D COF, in this case palladium nanoparticles.[147] STEM-EDX showed palladium throughout the COF structure. Using STEM and STEM-EDX to locate high atomic number elements such as metals is an effective use of the technique, but it is worth bearing in mind the spatial resolution of the EDX maps when interpreting the data.

Guntern *et al.* used HAADF-STEM imaging to convincingly show successful synthesis of a series of nanocrystals encapsulated by imine-linked COF-LZU-1, where a COF shell forms around a nanoparticle core including gold, tungsten oxide, and iron oxide. They used measure-

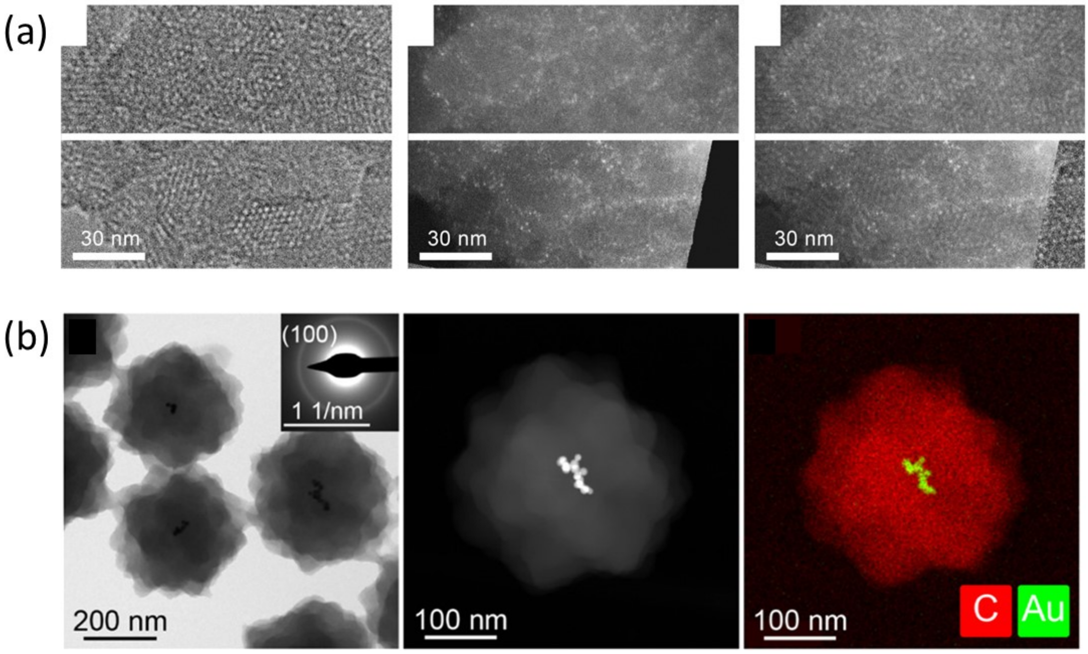

Figure 7: (a) BF-TEM (left) and HAADF-STEM images (centre, right) showing the accumulation of irrdium stain at grain boundaries. Adapted with permission from ref.[41] Copyright 2016 American Chemical Society. (b) BF-TEM, HAADF-STEM and STEM-EDX map showing the location of higher atomic number elements in the COF superstructure. Adapted with permission from ref. [148]. Copyright 2021 American Chemical Society.

ments of COF shell thickness to show that control of reaction conditions led to a thicker COF shell, followed by STEM-EDX mapping to show that the high contrast region in the centre of the composite material contained elements corresponding to the nanoparticles.[148]

Zhang *et al.* used both BF-STEM and HAADF-STEM to image two imine-linked COFs, COF-LZU-1 and COF-Naph.[149] COF-LZU-1 was claimed to consist of hollow spherical particles containing rod-shaped crystallites. The thickness of the COF spheres was then measured from HAADF-STEM images.

Calik *et al.* used both TEM and HAADF-STEM imaging to show that an iridium stain accumulated mostly at the grain boundaries in the sulphur functionalised COF-5 analogue, which the authors showed is due to the presence of a sulphur-containing modulator mostly at grain boundaries in the COF (Figure 7a).[41] HAADF-STEM is a highly suitable technique for this study, as the images are formed using scattered electron beams. As iridium is the highest atomic number element in the COF structure, it will scatter the incident electron beam the most and appear brightest in the HAADF images. EDX spectra were not reported.

1.5.3 High-Resolution Transmission Electron Microscopy

Like BF-TEM, HRTEM was typically used to study sample morphology. A good example is from Wang *et al*, who used HRTEM to resolve the pore channels in thin COF sheets and accurately measure the pore diameter using intensity profiles for their Schiff-base linked V2DP COF film (Figure 8a).[150] The authors were also able to establish the size of the crystal domains via HRTEM and SAED. Use of HRTEM to map grain boundaries in COFs was also explored by Castano *et al.* (Figure 8c).[151] The authors first used HRTEM to image a series of four boronate ester COFs to confirm that they were crystalline thin films. Images of COF film were then processed using Fourier-mapping process that was able to identify different grains within the sample. The authors choice of HRTEM over DF-TEM or SAED was explained as the COFs being beam-sensitive and would degrade under a high electron flux, with HRTEM being able to provide the lowest flux out of these techniques.

HRTEM is more suited for studying crystalline samples than BF-TEM, which is reflected by the number of papers that use HRTEM specifically to image crystalline regions. A number of the papers reviewed used HRTEM to show evidence of crystallinity. Veber et al (Figure 8b)[152], used a multi-technique approach to show crystallinity of their thin-film imine-linked COF, combining HRTEM images of lattice fringes and comparison to modelled structures. The authors also make use of Fourier transforms of lattice fringes to confirm results of direct space imaging.

1.5.4 Electron Diffraction

Neither CBED or 4D-STEM has been reported used on COFs at the time of writing. Therefore this section focussed on selected area electron diffraction (SAED) of COFs.

The most straightforward use of SAED was to display the SAED pattern of a region of interest and use this to draw conclusions about the crystallinity of the sample (Figure 9a). A number of authors compared a SAED pattern without diffraction spots to a PXRD pattern containing no sharp peaks and concluded that the 2D boronate-ester COF did not contain crystals large enough to provide detectable diffraction patterns.[146,153,154] Liu *et al.* utilised SAED to show that the porphyrin-based 2D COF particles generated a spotty ring pattern indicative of many small randomly oriented microcrystals which were linked to lattice fringes in their TEM images.[146]

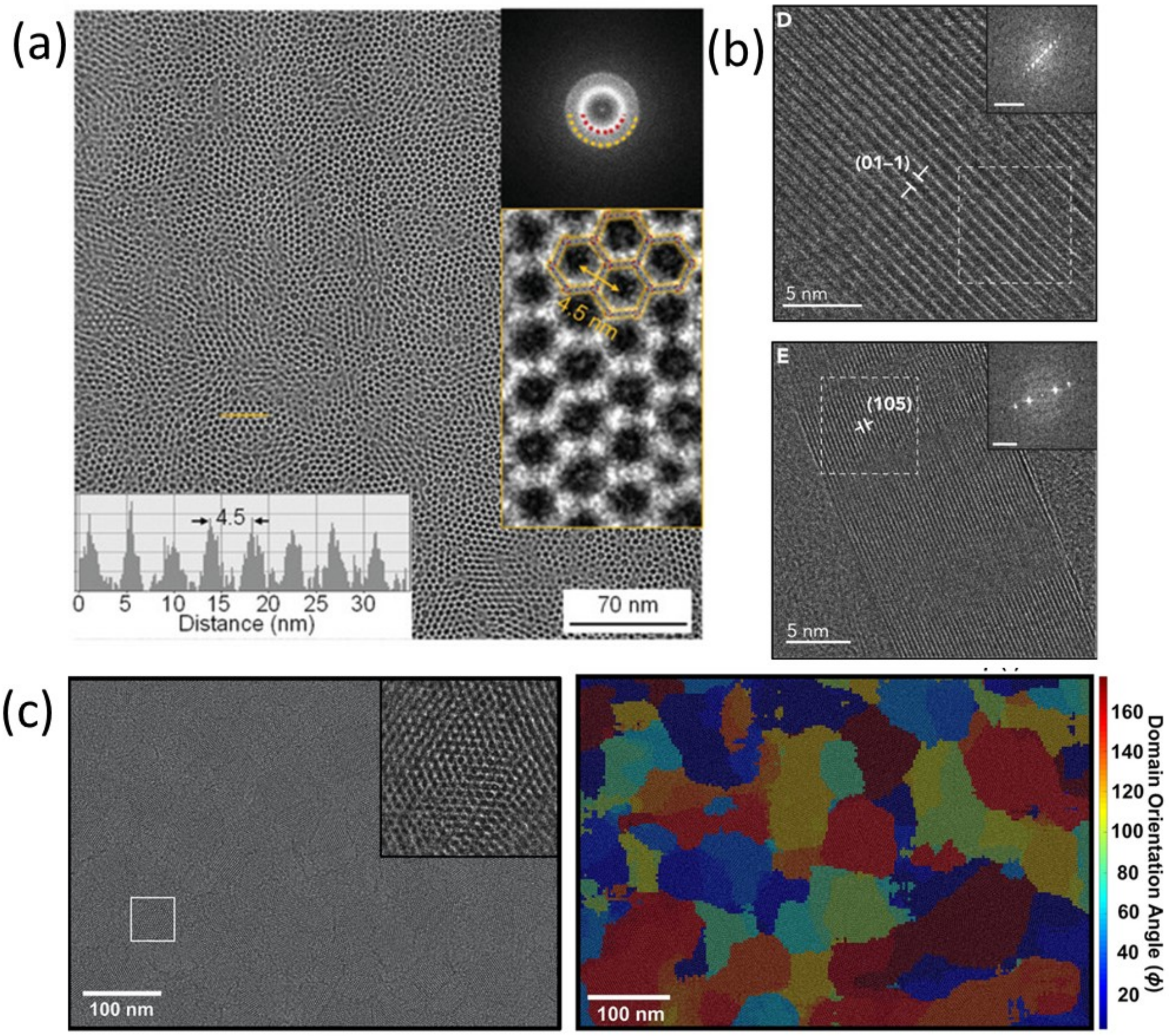

Figure 8: (a) HRTEM image showing atomic-scale hexagonal COF pores at low and high magnifications (insert), along with the intensity profile across a series of COF pores (yellow line) and the FFT of the image. Adapted with permission from ref.[150] Copyright 2021 John Wiley and Sons. (b) HRTEM showing COF lattice projections and FFTs displaying the crystallinity of the sample. Adapted with permission from ref.[152] Copyright 2020 Elsevier. (c) HRTEM showing atomic-resolution COF pores (top) and colour-coded COF grains (bottom), achieved via an automated mapping process involving FFTs. Adapted with permission from ref.[151]. Copyright 2021 American Chemical Society.

SAED was used in similar ways by several authors of publications reviewed, as acquiring both SAED and BF or HRTEM images then correlating lattice spacings obtained in reciprocal and direct space which is both straightforward and generally useful.[147,155–159]

More advanced applications of SAED were developed by Cheng *et al.*, who showed that modifications to the linker through a series of four imine-linked COF made the SAED pattern change from rings to sharp spots, indicating larger crystalline domains.[160] Li *et al.* used SAED to provide evidence of polycrystallinity from ring patterns and demonstrated control of reaction conditions achieving sharp spot patterns instead of ring patterns for porphyrin-based imine COF-366.[161]

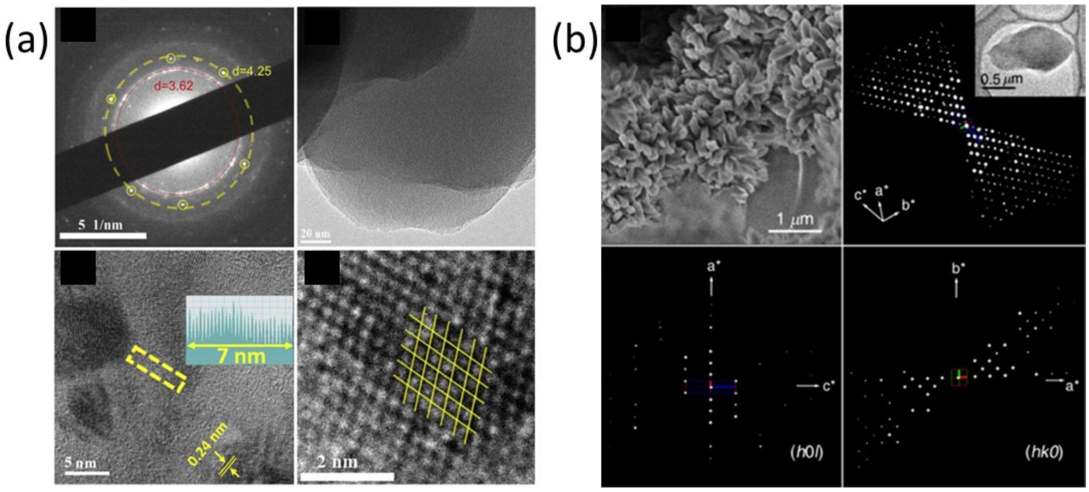

Figure 9: (a) Example of SAED spotty ring pattern and corresponding region of sample pattern was recorded from. The rings in the SAED can be matched to the features observed by BF-TEM. Adapted with permission from ref. [162]. Copyright 2021 Elsevier. (b) Reconstructed 3DED diffraction pattern and COF microstructure the data was recorded from (insert), from which the single-crystal structure of the COF was solved. Adapted with permission from ref. [163]. Copyright 2013 American Chemical Society.

Three-dimensional electron diffraction (3DED), or continuous rotation electron diffraction (CRED), is a powerful technique that allowed the crystal structure of nanoscale and sub-micron particles to be solved by using a TEM as a single-crystal diffractometer. This requires triply a beam stable single-crystal sample, an instrument capable of performing ED over a very large tilt range, and the ability to collect high crystallographic resolution data. The only current example of CRED applied to COFs is from Zhang *et al.* (Figure 9b).[163] The single-crystal structure of imine-linked 3D COF-320 was found by collecting two datasets at 298 K and at 89 K, to reduce beam damage. At 89 K, the data was collected from -34.19° to $+38.33^\circ$ with a 0.20° step width for a total of 396 individual diffraction patterns over 21 minutes. This allowed reconstruction of the reciprocal lattice, with 570 unique reflections and 1.5 Å crystallographic resolution. It was found that the crystal structures were different at the two temperatures. Fewer atoms were found for the 298 K dataset, which was attributed to beam damage reducing the crystallographic resolution of the dataset. The authors also found that the highly interpenetrated crystal structure made it difficult to solve the crystal structure of COF-320 from PXRD and computer modelling without single crystal data from CRED.

In summary, SAED is often used in conjunction with PXRD to probe crystallinity of COF particles. Few attempts to extract unit cell parameters or space group information from SAED are reported in the literature, with authors opting to use computational modelling and PXRD instead of SAED to derive this information.

1.5.5 Energy Dispersive X-ray Spectroscopy

Most publications used either SEM-EDX, or STEM-EDX mapping, with a total of four examples of TEM-EDX found. This is unsurprising, as STEM-EDX gives more information than EDX and is suitable for most samples. Vargheese *et al.* used EDX to confirm the presence of carbon, nitrogen, oxygen, and manganese in the porous-carbon/manganese oxide hybrid made by thermally annealing a triazine linked COF (Figure 10a).[164] The TEM grids were carbon coated copper, so the presence of carbon in the EDX spectrum is not indicative of the composition of the material. Furthermore, the nitrogen and oxygen peaks in the published spectrum overlap with the carbon peak making this analysis difficult, however, the manganese peak is observed clearly. Gao *et al.* used EDX to show the presence of carbon, oxygen, nitrogen, boron and iron in the imine-linked 2D COF.[165] for which they quantify weight‰ and atomic‰ of the elements in the EDX spectrum. Stoppiello *et al.* used EDX to show the presence of carbon, boron, and nitrogen in the sample of COF-5,[166] with the boron peak in the EDX spectrum being very low intensity and overlapping with the carbon peak. Additionally the elemental abundances in the EDX spectrum was not quantified, although the EDX spectrum of Aza-CMP in the same publication was quantified.

In summary, EDX of COFs has been used successfully to show qualitatively the presence of specific elements in COF materials. However, often no quantification of the EDX spectrum

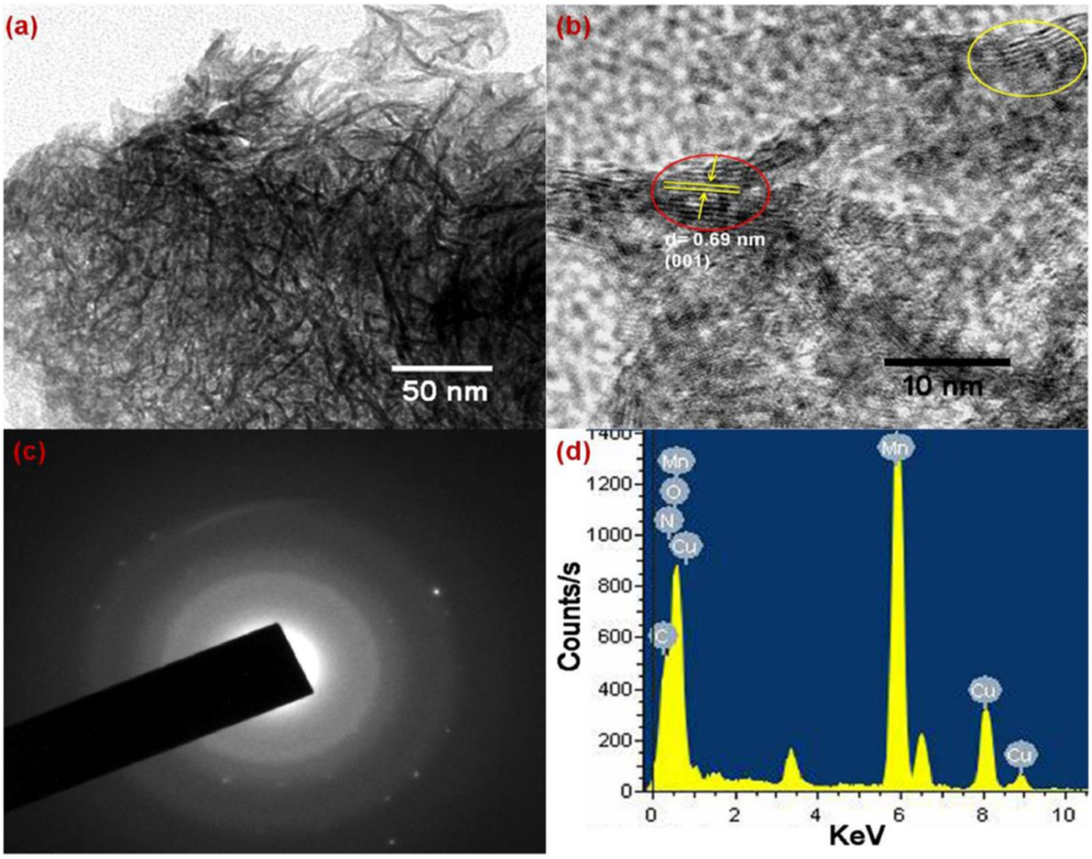

Figure 10: Typical EDX analysis of a COF. (a, b) An area of sample shown in the BF-TEM image, with the corresponding (c) SAED pattern and (d) EDX spectrum. A large manganese peak is clearly visible in the EDX spectrum due to the presence of manganese in the COF structure. The overlapping carbon, oxygen, and nitrogen peaks illustrate the challenge in detecting these elements via EDX. Adapted with permission from ref.[164]. Copyright 2020 Elsevier.

is undertaken, which is presumably because effective thickness and density of the sample is unknown so any quantification would be only semi-quantitative. In the case of STEM-EDX maps it is routine to not report the sum spectrum despite this being very useful for the reader. EDX peaks of light elements (B,N,O) overlapping with the ubiquitous carbon peak create a hurdle for the accurate elemental analysis of COF materials via EDX.

1.5.6 Electron Energy Loss Spectroscopy

Four examples of EELS were found in the publications reviewed, including one example of STEM-EELS. Berlanga *et al.* used EELS for elemental analysis to confirm that the boronate-ester linked 2D COF-8 contained carbon and boron (Figure 11a).[167] This was demonstrated very convincingly using the EELS spectrum range that includes both the carbon and boron K-edges, but a corresponding TEM or STEM image of the area EELS was acquired from was not included. Krishnaraj e*t al.* reported that they analysed the shape of the carbon K-edge to find that the majority of the carbon in the triazine-linked 2D COF sample sample was amorphous.[168] However, they did not include the EELS spectrum or TEM image of the area EELS was performed on in their publication. This is presumably an oversight, but does not inspire confidence. Stoppiello *et al.* used EELS for elemental analysis of COF-5,[166] revealing a clear carbon K edge and no boron edge, despite the authors claiming EELS confirms the presence of boron. This is likely due to the large amount of noise in the spectrum. None of the publications indicated that they had used any peak fitting algorithms to de-convolute their spectra.

Kim and Choi used STEM-EELS mapping to provide elemental analysis of the imine-linked 2D hcc-COF (Figure 11b).[169] Their photochemically synthesised imine-COF was rich in carbon and nitrogen, reflected by EELS mapping showing that there was an even distribution of nitrogen and carbon, further supported using STEM-EDX mapping. No sum EELS spectrum was seen in the paper or supporting information, and no discussion was made of the hybridisation of the carbon and nitrogen in the sample.

In summary, the uptake of EELS in the COF literature is currently low and is lacking in depth of analysis. Sum EELS spectra are often missing and discussion of edge hybridisation in COF materials requires attention. For an effective EELS analysis, the entire spectrum, inserts of

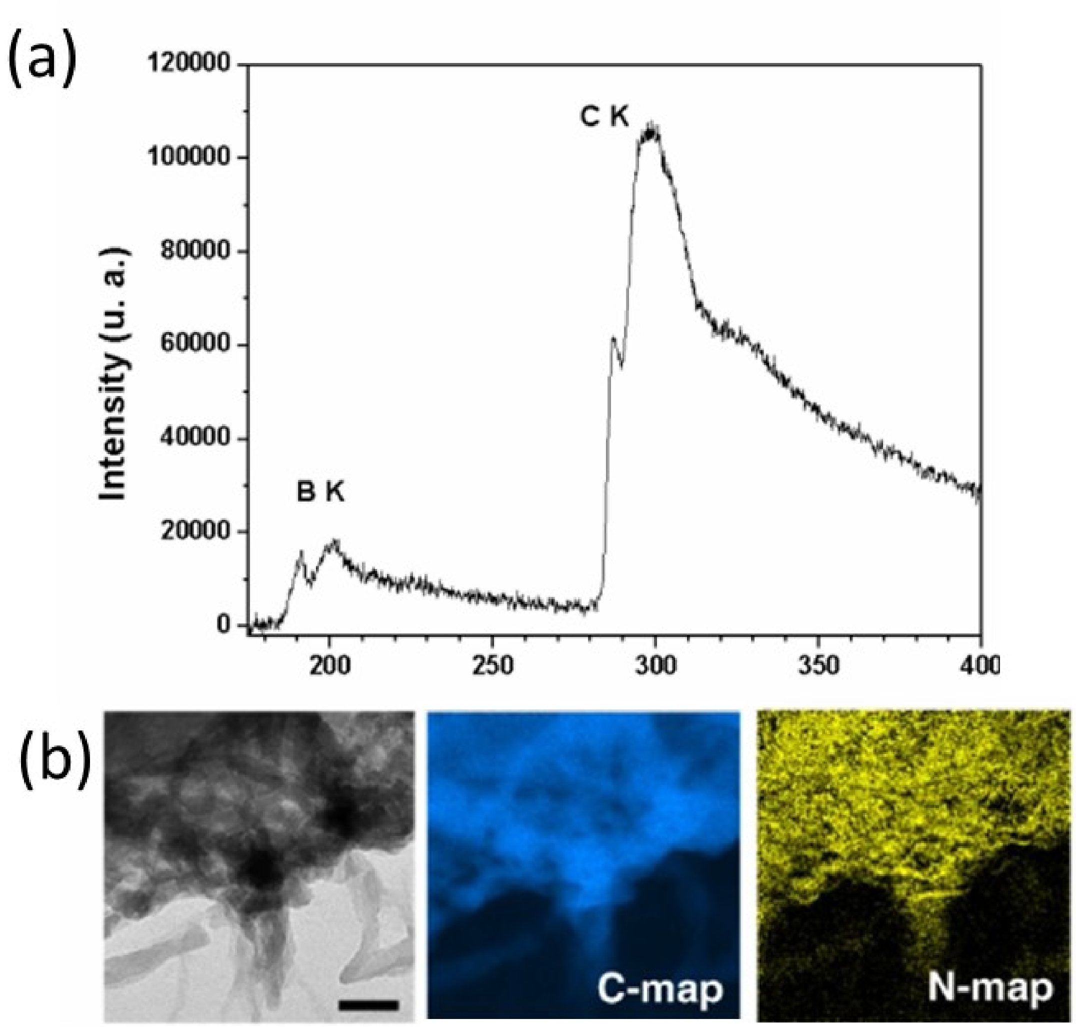

Figure 11: (a) Example EELS spectrum showing sp^2 B(K) and C(K) edges, typical of boronate ester COFs. Adapted with permission from ref.[167]. Copyright 2011 John Wiley and Sons. (b) An example of STEM-EELS mapping, with corresponding BF image, N(K) edge map and C(K) edge map showing that the N and C edges arise from the same regions of sample. Adapted from ref.[169] under creative commons CC-BY-4.0.

the relevant edges, and an image of the area the spectrum was taken from would be very useful to enhance the depth of scientific information. Edge fitting procedures to fit and subtract the background signal in EELS spectra would be very useful for more accurate quantification of low-intensity edges.[170]

1.5.7 Operating Conditions and General Trends

The type of TEM grid was often reported, as were the material deposition onto grid process which typically involve drop-casting suspensions of COF particles in solvent onto a TEM grid. An alternative method is introduction of the dry powder onto a TEM grid by mechanical contact. Sample deposition on TEM grids is expected to vary in accordance with the sample, so neither technique is superior as long as sample preparation effect on morphology is taken into account during experiment design stage. Very few published examples of non-standard sample holder were found, and typically the type of holder was not mentioned. Non-standard holders are typically used to probe very specific scientific questions or processes; Sun *et al.* used cryo-TEM to investigate the effect of temperature on the electron diffraction pattern of imine-linked COF-320,[171] and Smith *et al.* used variable-temperature liquid-cell TEM to study the in-situ formation of COF-5 colloids in solution heated to 80°C.[22]

TEM analysis of COF materials was reported at different accelerating voltages, from 80 to 300 kV, with some publications reporting use of multiple accelerating voltages (Figure 12a). However, 51 % of the papers reviewed did not explicitly report the accelerating voltage used. In order of most common; 200 kV (26 %),300 kV (10 %), 120 kV (4.7 %), 100 kV (3.9 %), 80 kV (3.1 %). Due to formatting issues, the full list of publications sorted by accelerating voltage is available in the Appendix.

It is expect that accelerating voltage, TEM sample holder, sample preparation, and TEM grid choice may often represent the in-house standard setup for TEM. Consideration of the effects of these variables on TEM imaging of COFs does not have to be very detailed as long as the images are acquired rapidly enough that they are representative of the COF. For example, consideration of the precise accelerating voltage to give the best contrast and lowest beam damage is probably unnecessary if images are taken before beam damage makes the area imaged unrepresentative of the sample as a whole.

All papers reviewed used BF-TEM imaging. For 49 % of reviewed papers BF TEM was the only TEM technique reported. The remaining 51 % used BF TEM and at least 1 other TEM technique. The remaining techniques were used in the proportion: HRTEM (23 %), DF-TEM (1 %); EDX (2 %); STEM-EDX mapping (6 %); EELS (2 %); SAED (11 %); STEM (4 %) (Figure 12b).

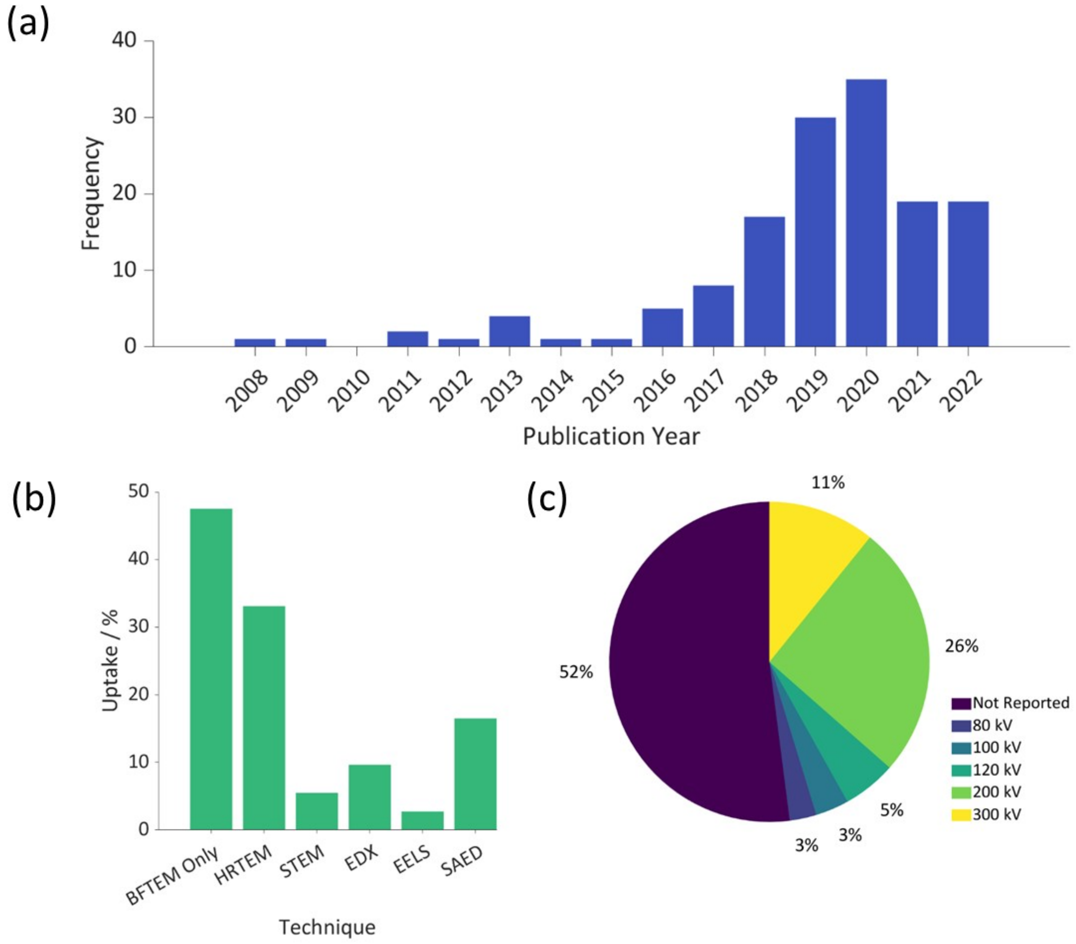

Figure 12: (a) Distribution of 144 reviewed papers showing an increase in the number of COF papers utilising TEM since 2015. (b) Techniques reported in reviewed publications; only BF TEM (50 %); HRTEM (32 %); STEM (5.5 %); EDX (9.7 %); EELS (2.8 %); SAED (16.6 %). All reviewed papers used BF TEM, with 50 % using at least one other TEM technique. STEM-EDX and STEM-EELS mapping are included in EDX and EELS percentages. (c) Reported accelerating voltages. The majority did not explicitly report the accelerating voltage of TEM, then in order of most common: 200 kV, 300 kV, 120 kV, 100 kV, 80 kV.

BF imaging can be considered the default TEM operation mode which is why all papers reviewed contain BF TEM images. Other TEM techniques are published less frequently as they may involve a higher electron flux or higher total fluence, destroying the sample before useful data can be acquired, or because other techniques are used in addition to TEM (such as PXRD to provide crystal structure information). TEM is often used to study the morphology of COF particles at the nanoscale, which is reflected by 49 % of papers using only BF imaging. Further, few studies focus on TEM as a central methodology and usually include it as a supporting technique.

As COF synthesis typically targets crystalline product, it was expected that SAED would make up a higher percentage of the techniques applied to COFs. Publications typically include PXRD patterns as evidence of crystallinity which may be the reason SAED is neglected during TEM studies. Additionally, it is likely that many COFs are too electron-beam sensitive for effective SAED studies.

Most surprising was the low uptake of EDX and EELS for COF characterisation. Both techniques provide local-probe elemental analysis from sub-mg quantities of material deposited onto TEM grids. EELS in particular gives the oxidation state and hybridisation and is very suitable for light elements such as carbon, boron, nitrogen, and oxygen, which are the elements typically found in COFs. It is currently unclear if low uptake of EDX and EELS is due to lack of awareness of these methods in the COF research community, or lack of EDX and EELS spectrometers on TEM instruments.

1.6 Summary

This chapter has introduced the class of compounds known as covalent organic frameworks (COFs), which are a broad category of crystalline polymers with diverse structural features and chemical functionality. It was discussed that COFs are distinct entities from metal organic frameworks (MOFs) despite their similar historical origins, and that the nomenclature of COFs is currently not well standardised. The common synthesis pathways of COFs were discussed, including the assumption that error-checking is a fundamental part of COF formation and that COFs represent a form of step-growth polymer. The concept of nanosupports was introduced, with particular reference to carbon nanotubes. It was highlighted that COF/nanosupport hybrids can be a useful way to develop COFs for useful applications. The properties and applications of COFs were discussed briefly, and while COFs have promise for gas sorption and storage (amongst other fields) there has yet to be a successfully commercialised COF. The common bulk analysis techniques that are used to interrogate COFs were described, namely X-ray diffraction, infrared spectroscopy, mass spectrometry, thermogravimetric analysis, and nuclear magnetic resonance spectroscopy. MALDI-MS was identified as potentially useful technique for COF analysis, that has not yet been applied to this class of materials.

The operating principles of TEM were described, with a brief mention of STEM and SEM. Aspects such as resolution, optical aberrations, and electron beam damage were covered. Finally a literature review was presented covering the current state-of-the-art of TEM of COFs. It was found that while most publications involving TEM of COFs include bright-field TEM imaging, many do not fully utilise the diffraction, spectroscopy, and imaging techniques available on modern TEMs. Of particular note is the low uptake of EELS to COFs, which was expected to be a major technique as it allows nanoscale spatial resolution elemental analysis.

Overall while many aspects of COF research have developed significantly since their inception, there is scope to systematically develop the application of TEM techniques to COFs in order to more effectively characterise COFs at the nanoscale.

1.7 Aims and Objectives

This thesis will attempt to develop the application of TEM to COFs so that researchers will have a powerful tool in their arsenal for future investigations of COFs. In particular, this will allow effective and facile characterisation of nanoscale COF materials such as nanoparticles, thin films, or COF/nanosupport hybrids. Underused bulk-scale techniques such as TGA and MALDI-MS will also be applied to uncover information about the chemistry and structure of COFs. Individual aims and objects are outlined in each chapter, but the overall goals of this thesis are as follows:

- Develop the application of TEM to COFs, by taking established TEM techniques and applying them broadly to COFs, with an emphasis on TEM spectroscopy and advanced bright-field imaging techniques/data analysis.
- Creation of a novel modelling method for understanding and predicting TEM projections

of COFs.

- Synthesis of a range of novel and extant COFs for TEM analysis, both as polymers and polymer-support composites.
- Investigate the effect nanosupports have on COF formation and morphology via TEM and bulk-scale techniques.
- Extension of TGA and MALDI-TOF MS to COF polymers to evaluate the usefulness of these techniques in COF investigations for uncovering structural and chemical information.

References

(1) J. G. Foster, A. Rzhetsky and J. A. Evans, *American Sociological Review*, 2015, **80**, 875–908.

(2) M. S. Lohse and T. Bein, *Advanced Functional Materials*, 2018, **28**, 1705553.

(3) A. P. Cótê, A. I. Benin, N. W. Ockwig, M. O'Keeffe, A. J. Matzger and O. M. Yaghi, *Science*, 2005, **310**, 6.

(4) C. Gropp, S. Canossa, S. Wuttke, F. Gándara, Q. Li, L. Gagliardi and O. M. Yaghi, *ACS Central Science*, 2020, **6**, 1255–1273.

(5) Y. Du, H. Yang, J. M. Whiteley, S. Wan, Y. Jin, S.-H. H. Lee and W. Zhang, *Angewandte Chemie*, 2016, **128**, 1769–1773.

(6) J. R. Hunt, C. J. Doonan, J. D. LeVangie, A. P. Clôté and O. M. Yaghi, *Journal of the American Chemical Society*, 2008, **130**, 11872–11873.

(7) C. Gropp, T. Ma, N. Hanikel and O. M. Yaghi, *Science*, 2020, **370**, 1255–1273.

(8) F. J. Uribe-Romo, J. R. Hunt, H. Furukawa, C. Klöck, M. O'Keeffe and O. M. Yaghi, *Journal of the American Chemical Society*, 2009, **131**, 4570–4571.

(9) F. J. Uribe-Romo, C. J. Doonan, H. Furukawa, K. Oisaki and O. M. Yaghi, *Journal of the American Chemical Society*, 2011, **133**, 11478–11481.

(10) P. J. Waller, S. J. Lyle, T. M. Osborn Popp, C. S. Diercks, J. A. Reimer and O. M. Yaghi, *Journal of the American Chemical Society*, 2016, **138**, 15519–15522.

(11) P. Kuhn, M. Antonietti and A. Thomas, *Angewandte Chemie - International Edition*, 2008, **47**, 3450–3453.

(12) K. T. Jackson, T. E. Reich and H. M. El-Kaderi, *Chemical Communications*, 2012, **48**, 8823–8825.

(13) C. Zhao, C. S. Diercks, C. Zhu, N. Hanikel, X. Pei and O. M. Yaghi, *Journal of the American Chemical Society*, 2018, **140**, 16438–16441.

(14) J. Guo, Y. Xu, S. Jin, L. Chen, T. Kaji, Y. Honsho, M. A. Addicoat, J. Kim, A. Saeki, H. Ihee, S. Seki, S. Irle, M. Hiramoto, J. Gao and D. Jiang, *Nature Communications*, 2013, **4**, 2736.

(15) S. J. Lyle, T. M. Osborn Popp, P. J. Waller, X. Pei, J. A. Reimer and O. M. Yaghi, *Journal of the American Chemical Society*, 2019, **141**, 11253–11258.

(16) B. Nath, W. H. Li, J. H. Huang, G. E. Wang, Z. H. Fu, M. S. Yao and G. Xu, *CrystEngComm*, 2016, **18**, 4259–4263.

(17) B. Zhang, M. Wei, H. Mao, X. Pei, S. A. Alshmimri, J. A. Reimer and O. M. Yaghi, *Journal of the American Chemical Society*, 2018, **140**, 12715–12719.

(18) H. Lyu, C. S. Diercks, C. Zhu and O. M. Yaghi, *Journal of the American Chemical Society*, 2019, **141**, 6848–6852.

(19) A. Nagai, in *Covalent Organic Frameworks*, Jenny Stanford Publishing, 1st edn., 2020, pp. 10–11.

(20) Z. Li, H. Y. Zhou, F. L. Zhao, T. X. Wang, X. Ding, B. H. Han and W. Feng, *Chinese Journal of Polymer Science (English Edition)*, 2020, **38**, 550–557.

(21) J. X. Ma, J. Li, Y. F. Chen, R. Ning, Y. F. Ao, J. M. Liu, J. Sun, D. X. Wang and Q. Q. Wang, *Journal of the American Chemical Society*, 2019, **141**, 3843–3848.

(22) B. J. Smith, L. R. Parent, A. C. Overholts, P. A. Beaucage, R. P. Bisbey, A. D. Chavez, N. Hwang, C. Park, A. M. Evans, N. C. Gianneschi and W. R. Dichtel, *ACS Central Science*, 2017, **3**, 58–65.

(23) H. Li, A. M. Evans, I. Castano, M. J. Strauss, W. R. Dichtel and J. L. Bredas, *Journal of the American Chemical Society*, 2020, **142**, 1367–1374.

(24) S. W. Park, Z. Liao, B. Ibarlucea, H. Qi, H. H. Lin, D. Becker, J. Melidonie, T. Zhang, H. Sahabudeen, L. Baraban, C. K. Baek, Z. Zheng, E. Zschech, A. Fery, T. Heine, U. Kaiser, G. Cuniberti, R. Dong and X. Feng, *Angewandte Chemie - International Edition*, 2020, **59**, 8218–8224.

(25) H. L. Nguyen, N. Hanikel, S. J. Lyle, C. Zhu, D. M. Proserpio and O. M. Yaghi, *Journal of the American Chemical Society*, 2020, **142**, 2218–2221.

(26) A. M. Evans, I. Castano, A. Brumberg, L. R. Parent, A. R. Corcos, R. L. Li, N. C. Flanders, D. J. Gosztola, N. C. Gianneschi, R. D. Schaller and W. R. Dichtel, *Journal of the American Chemical Society*, 2019, **141**, 19728–19735.

(27) F. Haase and B. V. Lotsch, *Chemical Society Reviews*, 2020, **49**, 8469–8500.

(28) M. O'Keeffe, M. A. Peskov, S. J. Ramsden and O. M. Yaghi, *Accounts of Chemical Research*, 2008, **41**, 1782–1789.

(29) C. S. Diercks and O. M. Yaghi, *Science*, 2017, **355**, 1585.

(30) P. J. Waller, F. Gándara and O. M. Yaghi, *Accounts of Chemical Research*, 2015, **48**, 3053–3063.

(31) A. P. Côté, H. M. El-Kaderi, H. Furukawa, J. R. Hunt and O. M. Yaghi, *Journal of the American Chemical Society*, 2007, **129**, 12914–12915.

(32) H. Lyu, Z. Ji, S. Wuttke and O. M. Yaghi, *Chem*, 2020, **6**, 2219–2241.

(33) O. M. Yaghi, M. O'Keeffe, N. W. Ockwig, H. K. Chae, M. Eddaoudi and J. Kim, *Nature*, 2003, **423**, 705–714.

(34) R. Freund, O. Zaremba, G. Arnauts, R. Ameloot, G. Skorupskii, M. Dincă, A. Bavykina, J. Gascon, A. Ejsmont, J. Goscianska, M. Kalmutzki, U. Lächelt, E. Ploetz, C. S. Diercks and S. Wuttke, *Angewandte Chemie International Edition*, 2021, **60**, 23975–24001.

(35) C. Zheng, J. Zhu, C. Yang, C. Lu, Z. Chen and X. Zhuang, *Science China Chemistry*, 2019, **62**, 1145–1193.

(36) Y. Du, K. Mao, P. Kamakoti, B. Wooler, S. Cundy, Q. Li, P. Ravikovitch and D. Calabro, *Journal of Materials Chemistry A*, 2013, **1**, 13171–13178.

(37) Z. Li, Z.-W. Liu, Z. Li, T.-X. Wang, F. Zhao, X. Ding, W. Feng and B.-H. Han, *Advanced Functional Materials*, 2020, **30**, 1909267.

(38) S. Wang, Z. Zhang, H. Zhang, A. G. Rajan, N. Xu, Y. Yang, Y. Zeng, P. Liu, X. Zhang, Q. Mao, Y. He, J. Zhao, B.-G. Li, M. S. Strano and W.-J. Wang, *Matter*, 2019, **1**, 1592–1605.

(39) R. L. Li, N. C. Flanders, A. M. Evans, W. Ji, I. Castano, L. X. Chen, N. C. Gianneschi and W. R. Dichtel, *Chemical Science*, 2019, **10**, 3796–3801.

(40) H. Guo, N. Song, D. Wang, J. Ma and Q. Jia, *Talanta*, 2019, **198**, 277–283.

(41) M. Calik, T. Sick, M. Dogru, M. Döblinger, S. Datz, H. Budde, A. Hartschuh, F. Auras and T. Bein, *Journal of the American Chemical Society*, 2016, **138**, 1234–1239.

(42) S. D. Brucks, D. N. Bunck and W. R. Dichtel, *Polymer*, 2014, **55**, 330–334.

(43) T. Ma, J. Li, J. Niu, L. Zhang, A. S. Etman, C. Lin, D. Shi, P. Chen, L.-H. Li, X. Du, J. Sun and W. Wang, *Journal of the American Chemical Society*, 2018, **140**, 6763–6766.

(44) A. M. Evans, L. R. Parent, N. C. Flanders, R. P. Bisbey, E. Vitaku, M. S. Kirschner, R. D. Schaller, L. X. Chen, N. C. Gianneschi and W. R. Dichtel, *Science*, 2018, **361**, 6.

(45) *Compendium of polymer terminology and nomenclature: IUPAC recommendations, 2008*, ed. R. G. Jones, RSC Pub. : IUPAC, Cambridge, 2009, 443 pp.

(46) X. Hu, J. Jian, Z. Fang, L. Zhong, Z. Yuan, M. Yang, S. Ren, Q. Zhang, X. Chen and D. Yu, *Energy Storage Materials*, 2019, **22**, 40–47.

(47) M. Martínez-Abadía, C. T. Stoppiello, K. Strutynski, B. Lerma-Berlanga, C. Martí-Gastaldo, A. Saeki, M. Melle-Franco, A. N. Khlobystov and A. Mateo-Alonso, *Journal of the American Chemical Society*, 2019, **141**, 14403–14410.

(48) V. da Silva, K. Zalewska, Z. Petrovski, C. Buarque, L. Branco and P. Esteves, *Materials Today Sustainability*, 2023, **21**, 100279.

(49) R. Wang, X. Shi, A. Xiao, W. Zhou and Y. Wang, *Journal of Membrane Science*, 2018, **566**, 197–204.

(50) S.-Y. Ding, J. Gao, Q. Wang, Y. Zhang, W.-G. Song, C.-Y. Su and W. Wang, *Journal of the American Chemical Society*, 2011, **133**, 19816–19822.

(51) D. Rodríguez-San-Miguel, A. Abrishamkar, J. A. R. Navarro, R. Rodriguez-Trujillo, D. B. Amabilino, R. Mas-Ballesté, F. Zamora and J. Puigmartí-Luis, *Chemical Communications*, 2016, **52**, 9212–9215.

(52) I. Castano, A. M. Evans, H. Li, E. Vitaku, M. J. Strauss, J.-L. Brédas, N. C. Gianneschi and W. R. Dichtel, *ACS Central Science*, 2019, **5**, 1892–1899.

(53) J. Hu, S. K. Gupta, J. Ozdemir and M. H. Beyzavi, *ACS Applied Nano Materials*, 2020, **3**, 6239–6269.

(54) H. S. Sasmal, A. K. Mahato, P. Majumder and R. Banerjee, *Journal of the American Chemical Society*, 2022, **144**, 17.

(55) S. J. Rowan, S. J. Cantrill, G. R. L. Cousins, J. K. M. Sanders and J. F. Stoddart, *Angewandte Chemie International Edition*, 2002, **41**, 898–952.

(56) J. S. Lindsey, *New journal of chemistry*, 1991, **15**, 153–180.

(57) D. L. D. Caspar and A. Klug, *Cold Spring Harbor Symposia on Quantitative Biology*, 1962, **27**, 1–24.

(58) T. Zhang, F. Hu, C. Song, S. Li, W. Shao, S. Liu, H. Peng, S. Hu and X. Jian, *Chemical Engineering Journal*, 2021, **407**, 127141.

(59) W. Ji, Y.-S. Guo, H.-M. Xie, X. Wang, X. Jiang and D.-S. Guo, *Journal of Hazardous Materials*, 2020, **397**, 122793.

(60) N. L. Campbell, R. Clowes, L. K. Ritchie and A. I. Cooper, *Chemistry of Materials*, 2009, **21**, 204–206.

(61) J. Yoo, S. Lee, S. Hirata, C. Kim, C. K. Lee, T. Shiraki, N. Nakashima and J. K. Shim, *Chemistry Letters*, 2015, **44**, 560–562.

(62) S. T. Yang, J. Kim, H. Y. Cho, S. Kim and W. S. Ahn, *RSC Advances*, 2012, **2**, 10179–10181.

(63) R. Liang, Y. Hu and G. Li, *Journal of Chromatography A*, 2020, **1618**, 460867.

(64) B. P. Biswal, S. Chandra, S. Kandambeth, B. Lukose, T. Heine and R. Banerjee, *Journal of the American Chemical Society*, 2013, **135**, 5328–5331.

(65) H. Qi, H. Sahabudeen, B. Liang, M. Položij, M. A. Addicoat, T. E. Gorelik, M. Hambsch, M. Mundszinger, S. W. Park, B. V. Lotsch, S. C. Mannsfeld, Z. Zheng, R. Dong, T. Heine, X. Feng and U. Kaiser, *Science Advances*, 2020, **6**, 1–9.

(66) N. Turangan, Y. Xu, H. Spratt, L. Rintoul, S. Bottle and J. MacLeod, *Nanotechnology*, 2021, **32**, 075604.

(67) K. Zhang, K. O. Kirlikovali, R. S. Varma, Z. Jin, H. W. Jang, O. K. Farha and M. Shokouhimehr, *ACS Applied Materials and Interfaces*, 2020, **12**, 27821–27852.

(68) R. K. Sharma, P. Yadav, M. Yadav, R. Gupta, P. Rana, A. Srivastava, R. Zbořil, R. S. Varma, M. Antonietti and M. B. Gawande, *Materials Horizons*, 2020, **7**, 411–454.

(69) Y. Liu, W. Zhou, W. L. Teo, K. Wang, L. Zhang, Y. Zeng and Y. Zhao, *Chem*, 2020, **6**, 3172–3202.

(70) W. Zhao, L. Xia and X. Liu, *CrystEngComm*, 2018, **20**, 1613–1634.

(71) S.-Y. Ding and W. Wang, *Chem. Soc. Rev.*, 2013, **42**, 548–568.

(72) L. M. Lanni, R. W. Tilford, M. Bharathy and J. J. Lavigne, *Journal of the American Chemical Society*, 2011, **133**, 13975–13983.

(73) H. Fan, A. Mundstock, A. Feldhoff, A. Knebel, J. Gu, H. Meng and J. Caro, *Journal of the American Chemical Society*, 2018, **140**, 10094–10098.

(74) Z. Li, Y. Zhi, X. Feng, X. Ding, Y. Zou, X. Liu and Y. Mu, *Chemistry - A European Journal*, 2015, **21**, 12079–12084.

(75) H. Ding, Y. Li, H. Hu, Y. Sun, J. Wang, C. Wang, C. Wang, G. Zhang, B. Wang, W. Xu and D. Zhang, *Chemistry – A European Journal*, 2014, **20**, 14614–14618.

(76) H. Yang, S. Zhang, L. Han, Z. Zhang, Z. Xue, J. Gao, Y. Li, C. Huang, Y. Yi, H. Liu and Y. Li, *ACS Applied Materials & Interfaces*, 2016, **8**, 5366–5375.

(77) D. B. Shinde, H. B. Aiyappa, M. Bhadra, B. P. Biswal, P. Wadge, S. Kandambeth, B. Garai, T. Kundu, S. Kurungot and R. Banerjee, *Journal of Materials Chemistry A*, 2016, **4**, 2682–2690.

(78) Z. Li, Y. Zhang, H. Xia, Y. Mu and X. Liu, *Chemical Communications*, 2016, **52**, 6613–6616.

(79) H.-Y. Cheng and T. Wang, *Advanced Synthesis & Catalysis*, 2021, **363**, 144–193.

(80) S. Ou, M. Zhou, W. Chen, Y. Zhang and Y. Liu, *ChemSusChem*, 2022, **15**, e202200184.

(81) S. Bhunia, K. A. Deo and A. K. Gaharwar, *Advanced Functional Materials*, 2020, **30**, 2002046.

(82) L. Bai, S. Z. F. Phua, W. Q. Lim, A. Jana, Z. Luo, H. P. Tham, L. Zhao, Q. Gao and Y. Zhao, *Chemical Communications*, 2016, **52**, 4128–4131.

(83) C. Buzea, I. I. Pacheco and K. Robbie, *Biointerphases*, 2007, **2**, MR17–MR71.

(84) X.-D. Wang, Z.-X. Shen, T. Sang, X.-B. Cheng, M.-F. Li, L.-Y. Chen and Z.-S. Wang, *Journal of Colloid and Interface Science*, 2010, **341**, 23–29.

(85) S. Xu, Z. Li, L. Zhang, W. Zhang and D. Li, *Talanta*, 2021, **221**, 121612.

(86) N. Agasti, M. A. Astle, G. A. Rance, J. Alves Fernandes, J. Dupont and A. N. Khlobystov, *Nano Letters*, 2020, **20**, 1161–1171.

(87) E. T. Thostenson, Z. Ren and T.-W. Chou, *Composites Science and Technology*, 2001, **61**, 1899–1912.

(88) T. W. Ebbesen and P. M. Ajayan, *Nature*, 1992, **358**, 220–222.

(89) A. M. Cassell, J. A. Raymakers, J. Kong and H. Dai, *The Journal of Physical Chemistry B*, 1999, **103**, 6484–6492.

(90) S. C. Tsang, Y. K. Chen, P. J. F. Harris and M. L. H. Green, *Nature*, 1994, **372**, 159–162.

(91) D. Ugarte, T. Stöckli, J. Bonard, A. Châtelain and W. de Heer, *Applied Physics A: Materials Science & Processing*, 1998, **67**, 101–105.

(92) T. W. Chamberlain, J. Biskupek, S. T. Skowron, A. V. Markevich, S. Kurasch, O. Reimer, K. E. Walker, G. A. Rance, X. Feng, K. Müllen, A. Turchanin, M. A. Lebedeva, A. G. Majouga, V. G. Nenajdenko, U. Kaiser, E. Besley and A. N. Khlobystov, *ACS Nano*, 2017, **11**, 2509–2520.

(93) X. Chen, H. Zhang, C. Ci, W. Sun and Y. Wang, *ACS Nano*, 2019, **13**, 3600–3607.

(94) L. Wang, Y. Xie, Y. Yang, H. Liang, L. Wang and Y. Song, *ACS Applied Nano Materials*, 2020, **3**, 1412–1419.

(95) J. Xu, Y. He, S. Bi, M. Wang, P. Yang, D. Wu, J. Wang and F. Zhang, *Angewandte Chemie - International Edition*, 2019, **58**, 12065–12069.

(96) J. Wang, W. Qin, X. Zhu and Y. Teng, *Energy*, 2020, **199**, 117372.

(97) E. P. Dillon, C. A. Crouse and A. R. Barron, *ACS Nano*, 2008, **2**, 156–164.

(98) Y. He, D. Gehrig, F. Zhang, C. Lu, C. Zhang, M. Cai, Y. Wang, F. Laquai, X. Zhuang and X. Feng, *Advanced Functional Materials*, 2016, **26**, 8255–8265.

(99) Y. Han, Q. Zhang, N. Hu, X. Zhang, Y. Mai, J. Liu, X. Hua and H. Wei, *Chinese Chemical Letters*, 2017, **28**, 2269–2273.

(100) F. Xu, S. Jin, H. Zhong, D. Wu, X. Yang, X. Chen, H. Wei, R. Fu and D. Jiang, *Scientific Reports*, 2015, **5**, 8225.

(101) J. Yoo, S.-J. Cho, G. Y. Jung, S. H. Kim, K.-H. Choi, J.-H. Kim, C. K. Lee, S. K. Kwak and S.-Y. Lee, *Nano Letters*, 2016, **16**, 3292–3300.

(102) X. Chen, Y. Xu, F.-H. Du and Y. Wang, *Small Methods*, 2019, **3**, 1900338.

(103) B. Sun, J. Liu, A. Cao, W. Song and D. Wang, *Chemical Communications*, 2017, **53**, 6303–6306.

(104) Z. Lei, Q. Yang, Y. Xu, S. Guo, W. Sun, H. Liu, L.-P. Lv, Y. Zhang and Y. Wang, *Nature Communications*, 2018, **9**, 576.

(105) Z. Xiao, D. Kong, Q. Song, S. Zhou, Y. Zhang, A. Badshah, J. Liang and L. Zhi, *Nano Energy*, 2018, **46**, 365–371.

(106) X. Zhang, Z. Wang, L. Yao, Y. Mai, J. Liu, X. Hua and H. Wei, *Materials Letters*, 2018, **213**, 143–147.

(107) L. S. Shulman, *Daedalus*, 2005, **134**, 52–59.

(108) M. K. Smith and B. H. Northrop, *Chemistry of Materials*, 2014, **26**, 3781–3795.

(109) K. L. Y. Fung, S. T. Skowron, C. S. Allen and A. N. Khlobystov, *Chemical Communications*, 2021, **57**, 10628–10631.

(110) N. Widjonarko, *Coatings*, 2016, **6**, 54.

(111) K. D. M. Harris and M. Tremayne, *Chemistry of Materials*, 1996, **8**, 2554–2570.

(112) Y. Jiang, L. Cao, X. Hu, Z. Ren, C. Zhang and C. Wang, *Inorganic Chemistry*, 2018, **57**, 15123–15132.

(113) L. B. McCusker, R. B. Von Dreele, D. E. Cox, D. Louër and P. Scardi, *Journal of Applied Crystallography*, 1999, **32**, 36–50.

(114) M. Martínez-Abadía, K. Strutyński, C. T. Stoppiello, B. Lerma Berlanga, C. Martí-Gastaldo, A. N. Khlobystov, A. Saeki, M. Melle-Franco and A. Mateo-Alonso, *Nanoscale*, 2021, **13**, 6829–6833.

(115) A. L. Patterson, *Physical Review*, 1939, **56**, 978–982.

(116) M. M. Harding, *Journal of Synchrotron Radiation*, 1996, **3**, 250–259.

(117) M. Gemmi, E. Mugnaioli, T. E. Gorelik, U. Kolb, L. Palatinus, P. Boullay, S. Hovmöller and J. P. Abrahams, *ACS Central Science*, 2019, **5**, 1315–1329.

(118) Z. Huang, E. S. Grape, J. Li, A. K. Inge and X. Zou, *Coordination Chemistry Reviews*, 2021, **427**, 213583.

(119) B. C. Smith, *Fundamentals of Fourier Transform Infrared Spectroscopy*, CRC Press, 1st edn., 2011.

(120) J. H. Gross, *Mass Spectrometry*, Springer International Publishing, Cham, 2017.

(121) D. Feng and Y. Xia, *Analytica Chimica Acta*, 2018, **1014**, 58–63.

(122) K. Hu, Y. Lv, F. Ye, T. Chen and S. Zhao, *Analytical Chemistry*, 2019, **91**, 6353–6362.

(123) D. Ouyang, K. Luo, W. Ma, J. Wu, J. Li, Y. He, Z. Cai and Z. Lin, *The Analyst*, 2020, **145**, 3125–3130.

(124) Q. Sun, C. Gao, W. Ma, Y. He, J. Wu, K. Luo, D. Ouyang, Z. Lin and Z. Cai, *Microchimica Acta*, 2020, **187**, 370.

(125) T. R. Hoye, P. R. Hanson and J. R. Vyvyan, *The Journal of Organic Chemistry*, 1994, **59**, 4096–4103.

(126) H. E. Gottlieb, V. Kotlyar and A. Nudelman, *The Journal of Organic Chemistry*, 1997, **62**, 7512–7515.

(127) P. W. Atkins and J. De Paula, *Atkins' Physical chemistry*, Oxford University Press, Oxford ; New York, Tenth edition, 2014, 1008 pp.

(128) J. Clayden, N. Greeves and S. G. Warren, *Organic chemistry*, Oxford University Press, Oxford ; New YorK, 2nd ed, 2012, 1234 pp.

(129) J. Ma, X.-B. Fu, Y. Li, T. Xia, L. Pan and Y.-F. Yao, *Microporous and Mesoporous Materials*, 2020, **305**, 110287.

(130) *Springer Handbook of Microscopy*, ed. P. W. Hawkes and J. C. H. Spence, Springer International Publishing, Cham, 2019.

(131) D. B. Williams and C. B. Carter, *Transmission electron microscopy: a textbook for materials science*, Springer, New York, 2nd ed, 2008.

(132) X. Zou, S. Hovmöller and P. Oleynikov, *Electron Crystallography: Electron Microscopy and Electron Nanodiffraction*, Oxford University Press, New York, 2012, vol. 1.

(133) R. Brydson, *Electron Energy-Loss Spectroscopy*, Taylor and Francis, Oxford, 2001.

(134) R. F. Egerton, *Electron Energy-Loss Spectroscopy in the Electron Microscope*, Springer New York, New York, 3rd edn.

(135) E. Hecht, *Optics*, Harlow: Pearson Education, 5th edn.

(136) P. Harris, *C*, 2018, **4**, 4.

(137) K. L. Fung, B. L. Weare, M. W. Fay, S. P. Argent and A. N. Khlobystov, *Micron*, 2023, **165**, 103395.

(138) R. Egerton, *Ultramicroscopy*, 2013, **127**, 100–108.

(139) J. Reyes-Gasga and R. Garcıía-Garcıía, *Radiation Physics and Chemistry*, 2002, **64**, 359–367.

(140) R. Egerton, *Microscopy Research and Technique*, 2012, **75**, 1550–1556.

(141) C. R. Arumainayagam, H.-L. Lee, R. B. Nelson, D. R. Haines and R. P. Gunawardane, *Surface Science Reports*, 2010, **65**, 1–44.

(142) S. T. Skowron, T. W. Chamberlain, J. Biskupek, U. Kaiser, E. Besley and A. N. Khlobystov, *Accounts of Chemical Research*, 2017, **50**, 1797–1807.

(143) R. Egerton, *Micron*, 2019, **119**, 72–87.

(144) M. Koshino, Y. H. Masunaga, T. Nemoto, H. Kurata and S. Isoda, *Micron*, 2005, **36**, 271–279.

(145) R. Nishiyabu, S. Teraoka, Y. Matsushima and Y. Kubo, *ChemPlusChem*, 2012, **77**, 201–209.

(146) W. Liu, C. Wang, L. Zhang, H. Pan, W. Liu, J. Chen, D. Yang, Y. Xiang, K. Wang, J. Jiang and X. Yao, *Journal of Materials Chemistry A*, 2019, **7**, 3112–3119.

(147) F. Lu, Y. Li, Q. Shi, C. Zhao, S. Li and S. Pang, *New Journal of Chemistry*, 2020, **44**, 15354–15361.

(148) Y. T. Guntern, J. Vávra, V. V. Karve, S. B. Varandili, O. Segura Lecina, C. Gadiyar and R. Buonsanti, *Chemistry of Materials*, 2021, **33**, 2646–2654.

(149) G. Zhang, M. Tsujimoto, D. Packwood, N. T. Duong, Y. Nishiyama, K. Kadota, S. Kitagawa and S. Horike, *Journal of the American Chemical Society*, 2018, **140**, 2602–2609.

(150) Z. Wang, X. Jia, P. Zhang, Y. Liu, H. Qi, P. Zhang, U. Kaiser, S. Reineke, R. Dong and X. Feng, *Advanced Materials*, 2021, **34**, 2106073.

(151) I. Castano, A. M. Evans, R. d. Reis, V. P. Dravid, N. C. Gianneschi and W. R. Dichtel, *Chemistry of Materials*, 2021, **33**, 1341–1352.

(152) G. Veber, C. S. Diercks, C. Rogers, W. S. Perkins, J. Ciston, K. Lee, J. P. Llinas, A. Liebman-Peláez, C. Zhu, J. Bokor and F. R. Fischer, *Chem*, 2020, **6**, 1125–1133.

(153) V. Rajagopal, N. Jothi Narayanan, M. Kathiresan, D. K. Pattanayak and V. Suryanarayanan, *Materials Today Chemistry*, 2021, **19**, 100408.

(154) W. Song, Y. Zhang, A. Varyambath and I. Kim, *ACS Nano*, 2019, **13**, 11753–11769.

(155) Z. Xiang, Y. Xue, D. Cao, L. Huang, J.-F. Chen and L. Dai, *Angewandte Chemie International Edition*, 2014, **53**, 2433–2437.

(156) K. Preet, G. Gupta, M. Kotal, S. K. Kansal, D. B. Salunke, H. K. Sharma, S. Chandra Sahoo, P. Van Der Voort and S. Roy, *Crystal Growth & Design*, 2019, **19**, 2525–2530.

(157) S. Kim and H. C. Choi, *ACS Omega*, 2020, **5**, 948–958.

(158) I. Gadwal, G. Sheng, R. L. Thankamony, Y. Liu, H. Li and Z. Lai, *ACS Applied Materials & Interfaces*, 2018, **10**, 12295–12299.

(159) W. Wang, Y. Zhang, L. Chen, H. Chen, S. Hu, Q. Li, H. Liu and S. Qiao, *Polymer Chemistry*, 2021, **12**, 650–659.

(160) Y. Cheng, S. K. Ravi, Y. Wang, J. Tao, Y. Gu, S. C. Tan and D. Zhao, *Chinese Chemical Letters*, 2018, **29**, 869–872.

(161) Y. Li, Z. Ou, B. Liang, J. Yang, R. Chen, H. Qi, U. Kaiser, W. Hong, X. Chen, L. Du, W. Liu and Z. Zheng, *Polymers*, 2021, **13**, 1561.

(162) Z. Liu, B. Zhang, Y. Huang, Y. Song, N. Dong, J. Wang and Y. Chen, *iScience*, 2021, **24**, 102526.

(163) Y.-B. Zhang, J. Su, H. Furukawa, Y. Yun, F. Glándara, A. Duong, X. Zou and O. M. Yaghi, *Journal of the American Chemical Society*, 2013, **135**, 16336–16339.

(164) S. Vargheese, D. Muthu, D. Pattappan, K. Kavya, R. R. Kumar and Y. Haldorai, *Electrochimica Acta*, 2020, **364**, 137291.

(165) C. Gao, J. Bai, Y. He, Q. Zheng, W. Ma and Z. Lin, *ACS Sustainable Chemistry & Engineering*, 2019, **7**, 18926–18934.

(166) C. T. Stoppiello, H. Isla, M. Martínez-Abadía, M. W. Fay, C. D. J. Parmenter, M. J. Roe, B. Lerma-Berlanga, C. Martí-Gastaldo, A. Mateo-Alonso and A. N. Khlobystov, *Nanoscale*, 2019, **11**, 2848–2854.

(167) I. Berlanga, M. L. Ruiz-González, J. M. González-Calbet, J. L. G. Fierro, R. Mas-Ballesté and F. Zamora, *Small*, 2011, **7**, 1207–1211.

(168) C. Krishnaraj, H. S. Jena, K. Leus, H. M. Freeman, L. G. Benning and P. Van Der Voort, *Journal of Materials Chemistry A*, 2019, **7**, 13188–13196.

(169) S. Kim and H. C. Choi, *Communications Chemistry*, 2019, **2**, 60.

(170) K. L. Fung, M. W. Fay, S. M. Collins, D. M. Kepaptsoglou, S. T. Skowron, Q. M. Ramasse and A. N. Khlobystov, *Ultramicroscopy*, 2020, **217**, 113052–113052.

(171) T. Sun, W. Lei, Y. Ma and Y.-B. Zhang, *Chinese Journal of Chemistry*, 2020, **38**, 1153–1166.

2 cHBC-BDA-COF

2.1 Aims and Objectives

In this chapter the formation of a novel COF as a powder and as a composite with nanosupports will be discussed, some of which has been published.[1] The COF chosen for this was cHBC-BDA-COF (Figure 13), also known in the literature as Marta-COF-2 due to research by the Mateo-Alonso group at the University of the Basque Country that took place separately from this Ph.D. research.[2] The results of both sets of research were intentionally published at the same time in the same journal.

cHBC-BDA-COF was chosen as the cata-hexabenzocoronene (cHBC) monomer was found to provide good TEM contrast and clear TEM projections in the related Marta-COF-1.[3] cHBC-derived COFs in general had at the time of writing received little attention in the literature with the full roster being: Marta-COF-1, cHBC-BDA-COF, Marta-COF-3,[4] Marta-COF-4,[4] and the confusingly named c-HBC-COF.[5] The materials have been found to have useful charge-transport properties via conductivity measurements, and Marta-COF-2 was found to have a Branauer-Emmett-Teller (BET) surface area of 1151 m^2 g^{-1} and a calculated band-gap of 2.6 - 2.8 eV.[2] However, in all cases the TEM analysis was limited to morphology characterisation via bright-field TEM. Therefore cHBC-BDA-COF represents an good test system to study the lattice projections of COFs while furthering the analysis of an emerging group of COFs. Synthesis of this COF on nanocarbon supports will allow comparative investigation to elucidate COF morphology and formation processes. The following objectives are defined:

- Develop a synthesis of cHBC-BDA-COF that gives a crystalline product, as a free COF and as a COF/nanosupport hybrid material.
- Characterise synthesis products using bulk analytical methods, including infrared spectroscopy and powder X-ray diffraction.
- Investigate the applicability of matrix-assisted laser desorption-ionisation mass spectrometry (MALDI MS) to COF polymers.

- Study the lattice projections of this cHBC-BDA-COF via TEM imaging and electron crystallography.
- Apply electron energy loss spectroscopy (EELS) to investigate the low-loss spectrum of cHBC-BDA-COF, with particular reference to plasmon measurements.

2.2 Synthesis of cHBC-BDA-COF

The cata-hexabenzocoronene (cHBC) monomer was first synthesised by a three step reaction pathway according to the literature procedure by collaborators at the University of Nottingham.[6] Briefly, successive Suzuki reactions yield hexamethoxytribenzylbenzene (TBB) from 1,3,5- tribromobenzene and phenylboronic acid (PBA). TBB then undergoes Friedl-Crafts acylations/Scholl reaction to give cHBC-OMe, which was deprotected by treating with boron tribromide to yield cHBC-OH. This was characterised by proton NMR spectroscopy, infrared (IR) spectroscopy, and mass spectrometry.

A number of COF syntheses were attempted (Figure 14a). The first synthesis 1 was an adaptation of the literature synthesis of Marta-COF-1; a 2:1 mixture of benzene diboronic acid (BDA)/cHBC was heated at 125°C for 72 hours under inert atmosphere in a 2:1 mixture of 1,4-dioxane/mesitylene. Graphitised nanofibres (GNFs) were introduced as it was hoped the GNF would act as a template for COF formation, thus promoting a thin layer of crystalline COF at the surface of the GNF. While IR spectroscopy showed the formation of boronate ester functional groups, no evidence of crystallinity was seen by powder X-ray diffraction (PXRD). BF-TEM imaging found that the COF was mostly amorphous material with infrequent nanocrystalline regions (Figure 14b). This result was unsurprising, as COFs typically form easily as amorphous solids and extensive optimisation is needed to yield crystalline products. Repeating this reaction over 7 days with and without GNFs gave the same results, and also suggests that the solvent system will be more important than the reaction temperature or time for achieving crystalline COF. This is because the synthesis is already relatively hot and solid formation occurred rapidly under the conditions used, implying the reaction system already has enough thermal energy and time to form a kinetic (amorphous) product. Further the review by Sasmal *et al.* suggests that COFs crystals typically form more readily in dilute solution, and the low reaction volume used

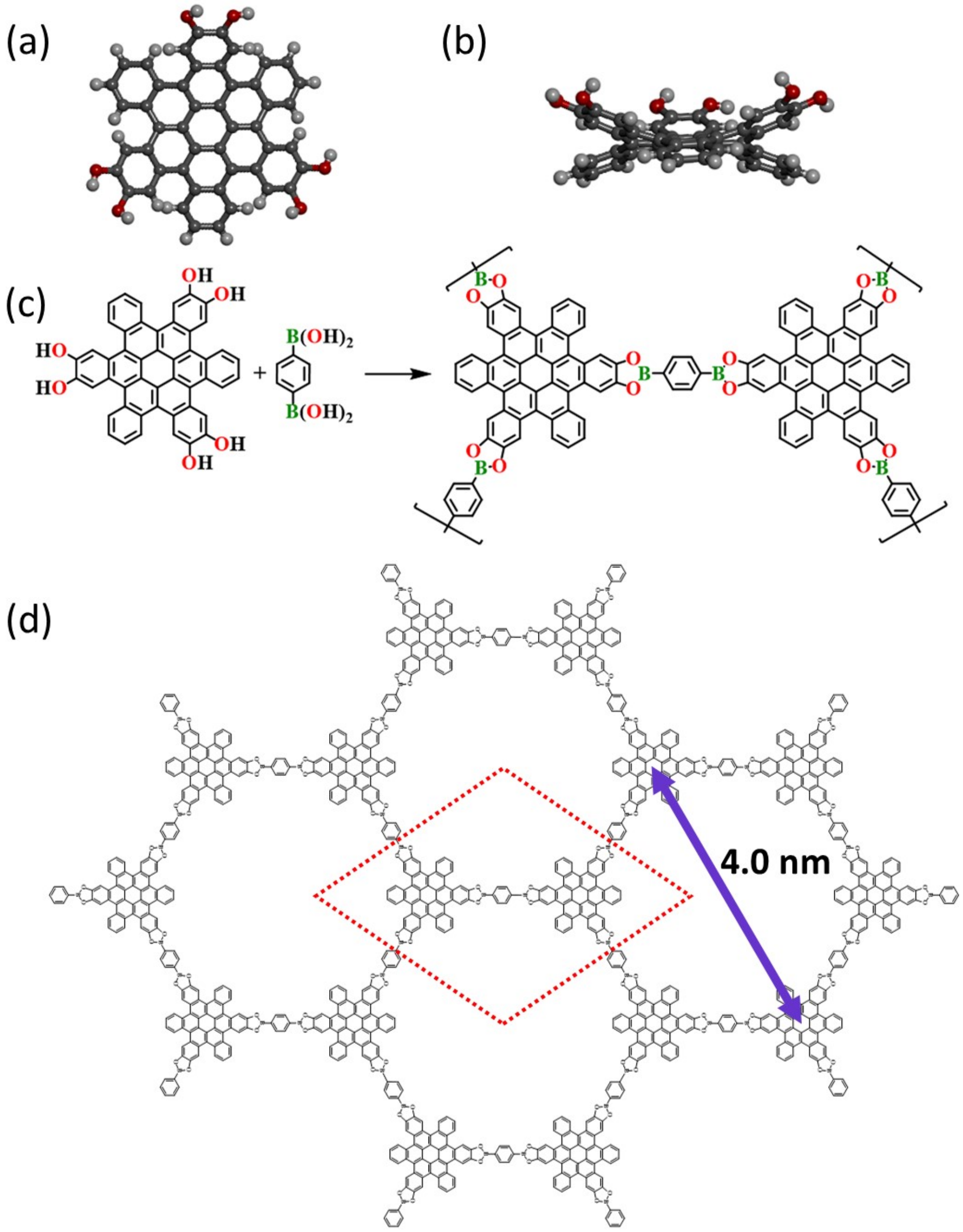

Figure 13: (a) Front and (b) side view of cHBC molecule illustrating its wavy geometry. (c) synthesis scheme for cHBC-COF. (d) 2D lattice of cHBC-COF, with the pore diameter and repeat unit highlighted.

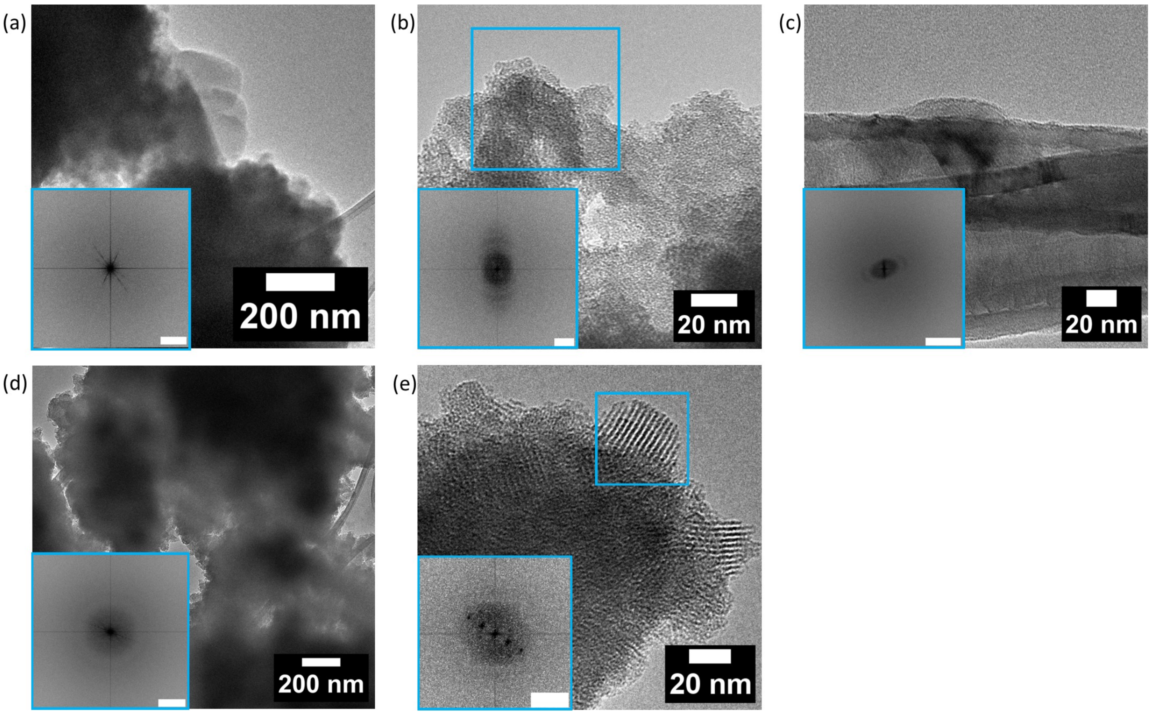

Figure 14: (a) Low magnification TEM image of synthesis 1, showing an amorphous COF product. Insert: FT, scale = 200 nm^{-1}. (b) High magnification TEM image of synthesis 1. No crystal planes can be seen in this image. Insert: Fourier transform (FT) of indicated region, scalebar = 2 nm^{-1}. (c) Bright-field TEM image of the product of synthesis 2, showing little accumulation of material at the GNF. The COF that is present is amorphous. Insert: FT of whole image, scalebar = 2 nm^{-1}. (d) Low magnification image of synthesis 3. The COF is only electron-beam transparent at it's thin edge. Insert: FT of whole image, 0.2 nm^{-1}. (e) High magnification image of synthesis 3, showing clear nanocrystalline regions. TEM has revealed that what appeared to be an amorphous powder was in fact crystalline. Insert: FT of indicated region, scale bar = 1 nm^{-1}. Fourier transforms have been cropped to the centre of the FT for readability.

here would drive the formation of an amorphous COF solid.[7]

The synthesis 2 attempted to localise BDA at a GNF prior to the addition of cHBC. The intent was that COF formation would only occur at the surface of the GNF where the BDA was localised, with the rate limited by the diffusion rate of the cHBC to the localised BDA. GNFs and BDA powder were heated to 350°C for 1 hour under inert atmosphere, which melted the BDA. Liquid substances have been shown to fill into nanotubes via capillary action,[8,9] and would give greater surface area of contact between the BDA and GNF than would be possible for a dry powder. No significant filling of the GNF or accumulation of material on the outside of the GNF was observed by BF TEM (Figure 14c) due to the thermal decomposition of BDA prior to melting, confirmed via thermogravimetric analysis (TGA) of BDA. Next, a solution of GNFs and BDA were stirred for 24 hours at 125°C prior to the addition of cHBC. This was unsuccessful in forming a crystalline COF and did not localise COF formation onto the GNF. This is likely because there is no obvious strong driving force for the accumulation of BDA and cHBC on the side-walls or step-edges of the GNF, and desorption of the monomers from the GNF into solution following Le Chatelier's principle. This is in contrast to the behaviour of small molecules filled into nanotubes that have a diameter similar to the size of the molecule, such as fullerenes filling into single-walled nanotubes, where there is a large energy gain from the molecule being inside the tube due strong Van der Waals forces surrounding the molecule.[10,11] For small molecules on GNFs, the diameter of the GNF is too large to provide the same driving force that would allow localisation of the monomers at the GNFs.

The third synthetic strategy was an adaptation of the method used in the synthesis of colloidal COF-5.[12] A 1:1.5 mixture of cHBC/BDA were reacted to give cHBC-BDA-COF, with acetonitrile as a cosolvent and phenylboronic acid (PBA) as a modulator. The monomers were heated in a solution of acetonitrile/1,4-dioxane/mesitylene (8:1.6:0.4) overnight, then filtered, washed and dried to give a solid COF power. Both nitrile cosolvents and modulators have been shown to improve the crystallinity of COFs. Nitrile solvents have been found to have a stabilising effect on boronate ester COF formation via coordination of the nitrile lone pair into the boron p-orbital. This is not strong enough to break the boron-oxygen bond, but also prevents nucleophilic attack from harder nucleophiles such as water that would break the bond. Modulators, also known as a chain-termination reagents, have seen limited use in COF chemistry[13–18] but are common in traditional polymer chemistry. The modulator is a competitive inhibitor that works by forming a boronate ester bond that terminates the COF polymer, but which can later undergo the reverse reaction to allow the chain to continue to grow. This slows the rate of reaction, helping the polymer to form as the thermodynamic crystalline product instead of the kinetic amorphous product. This synthesis was successful in producing nano-ordered COF (Figure 14d) and was taken forwards to use in a series of COF on nanosupport (COF/nanosupport) reactions, where the reaction was modified by inclusion of a solid nanosupport dispersed in solution for the COF to form on as a polymer layer. This allowed synthesis of: COF/graphite, COF/graphitised nanofibre (GNF), COF/multi-walled nanotube (MWNT), COF/single-walled nanotube (SWNT), and COF/silica nanoparticle (SiONP). The ratio of nanosupport:cHBC was be between 2:1 and 5:1 in mass/mass terms. The bulk properties of these materials were then investigated.

The next step for cHBC-BDA-COFs could be to examine the thermodynamics and kinetics of COF formation. The thermodynamics of cHBC-COF formation are currently unknown, so the exact way to drive to equilibrium crystalline product instead of amorphous kinetic product is unknown. A Hess cycle would be the go-to method for finding out the free energy change for COF synthesis, and kinetic studies could be conducted into finding out the rate of the forwards and reverse reactions for COF formation.

2.3 Bulk Measurements of cHBC-BDA-COF

2.3.1 Infrared Spectroscopy

The chosen methodology for infrared (IR) analysis of COFs was based on the study by Smith and Northrop, and involved precise identification of boronate ester vibrational bands within the COF spectrum.[19] COF samples were analysed using attenuated total reflectance (ATR) IR, but for samples containing nanocarbons transmission IR using a potassium bromide pellet was sometimes necessary; nanocarbons absorb strongly across the IR spectrum and cause a poor baseline due to Mie scattering,[20] but a usable spectrum can be recorded by diluting the nanocarbon with KBr. As discussed in Chapter 1, in a KBr spectrum the intensity of the vibrations is related to the concentration via the Beer-Lambert law, but KBr is hygroscopic so the O-H stretch intensity is often misleading. The intensity of stretches in an ATR spectrum cannot be necessarily compared with other spectra.[21]

IR spectroscopy was used to show the presence of characteristic boronate ester stretches in the materials (1393, 1333, 1235, 1079, 660, 601 and 541 cm^{-1}), as well as attenuation of the boronic acid/catechol O-H stretch (Figure 15). Boronic acid stretches are still present in the IR spectrum of COF, as the 2D COF lattice is terminated by unpolymerised boronic acid groups.[19] Boroxine stretches did not appear in the spectrum, indicating that COF-1, formed by self-condensation of BDA, did not form during the synthesis of COF. This is consistent with literature studies that found that boronate ester bonds were more thermodynamically favourable than boroxine bonds under certain COF formation conditions.[22] Comparing the COF IR spectra to the starting

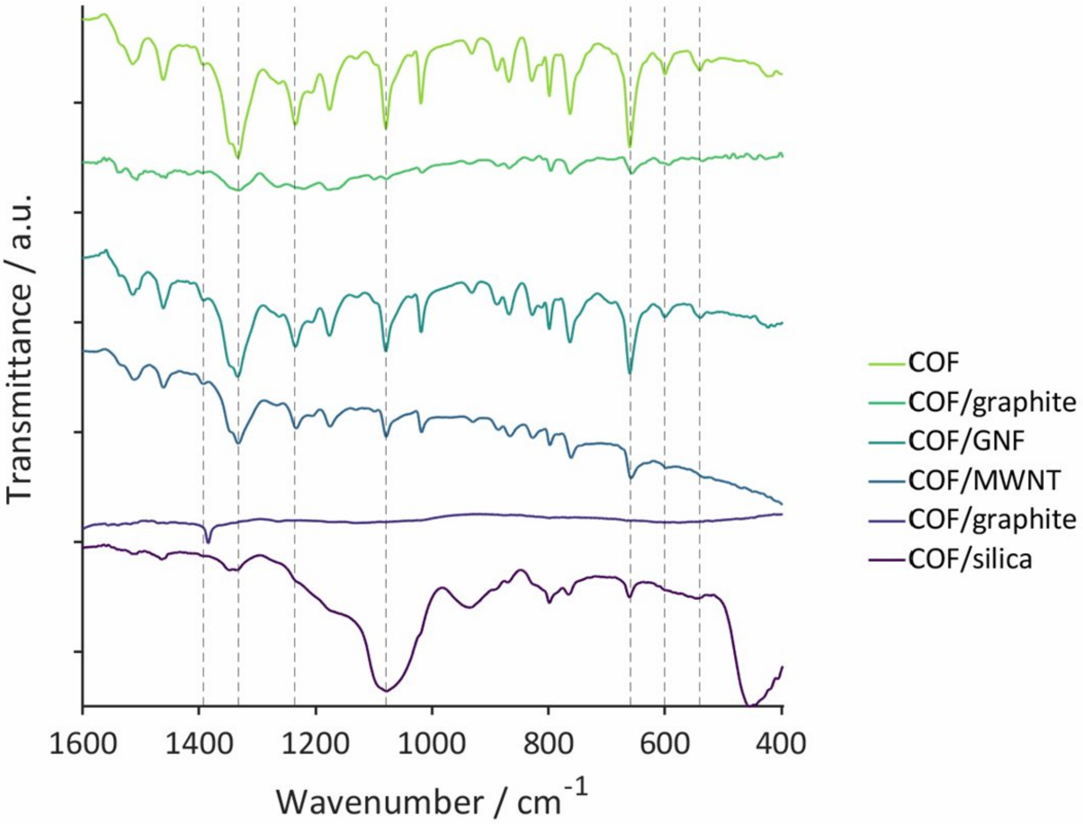

Figure 15: Infrared spectra of COF and COF/: graphite, GNF, MWNT, SWNT, and silica. Key COF vibrations at 1393, 1333, 1235, 1079, 660, 601 and 541 cm^{-1} have been indicated with dashed lines. For COF/graphite and COF/SWNT, the absorption from the nanocarbons effectively masks the COF vibrations, and these spectra were recorded using KBr pellets. For COF/silica, the silica vibrations overlap and mask some of the COF vibrations. The spectrum above 1600 cm^{-1} has been removed for clarity.

materials further confirms COF formation from the attenuation of boronic acid vibrations and the appearance of boronate ester vibrations. Of note is that IR of the amorphous COFs produced by syntheses 1 and 2 also contain characteristic COF vibrations, due to crystalline and acrystalline COFs containing the same functional groups.

2.3.2 MALDI-TOF MS

Matrix-assisted laser desorption ionisation time of flight mass spectrometry (MALDI-TOF MS) was used to investigate COF polymerisation and investigate COF polymer structure, for COF and COF/nanosupports (Figure 16). All spectra were recorded without a matrix, as the highly aromatic COF and monomers desorb and ionise readily under the laser wavelengths used. Comparing the polymer and monomer mass spectra, the base peak in the spectrum of cHBC is the molecular ion at 696 m/z, with lower peaks being fragments of cHBC and no peaks occurring above 696 m/z. The mass spectrum of COF has an essentially identical spectrum below the cHBC molecular ion, but contains several peaks at mz > 696. Isotope pattern modelling and structural modelling confirmed that peaks with m/z greater than 696 are due to cHBC and BDA molecules bound by boronate ester bonds. The empirical formulae of the ions were found (Appendix Table 23), and possible structures of some ions were rationalised (Appendix Figure 109). The mass spectra for COF/nanosupports are similar to that of pure COF, but have additional peaks in the spectrum with a different intensity distribution. This is due to the electron-rich nanocarbons acting as a matrix to help ionise the COF.[23] For MALDI of COF/nanocarbons, the MALDI contained a series of peaks separated by 24 m/z, likely C_2 units which is consistent with the MALDI of graphitic materials,[24] but was otherwise consistent with the MALDI of COF. Silica gives some low-mass MALDI peaks but does not impact the COF spectrum otherwise.

It was also found that a mechanical mixture of cHBC and BDA gives rise to a MALDI TOF spectrum similar to that of the COF (see Appedix Figure 108), which suggests that the MALDI laser is capable of causing the COF polymerisation reaction; it seems unlikely that the ions would be composed of physisorbed monomers. Therefore MALDI cannot be used to confirm COF polymerisation without support from other techniques such as IR or TEM. However as the ratio of ions in a mass spectrometry technique is due to the composition of the sample, MALDI could be used to establish the ratio of COF monomers in an unknown structure. For example 4:1, 2:1, and 1:1 mixtures of monomers could be prepared and used as a standard to compare to the mass spectrum of the COF in order to aid bulk structure analysis. This would essentially create a calibration curve for concentration of target ions, as has been used in MS of drug molecules.[25] This would also allow identification of ions that are only present at particular ratios of monomers. This would be useful for structures where the monomers can adopt more than one crystal structure, where each structure has a different ratio of monomers.[26]

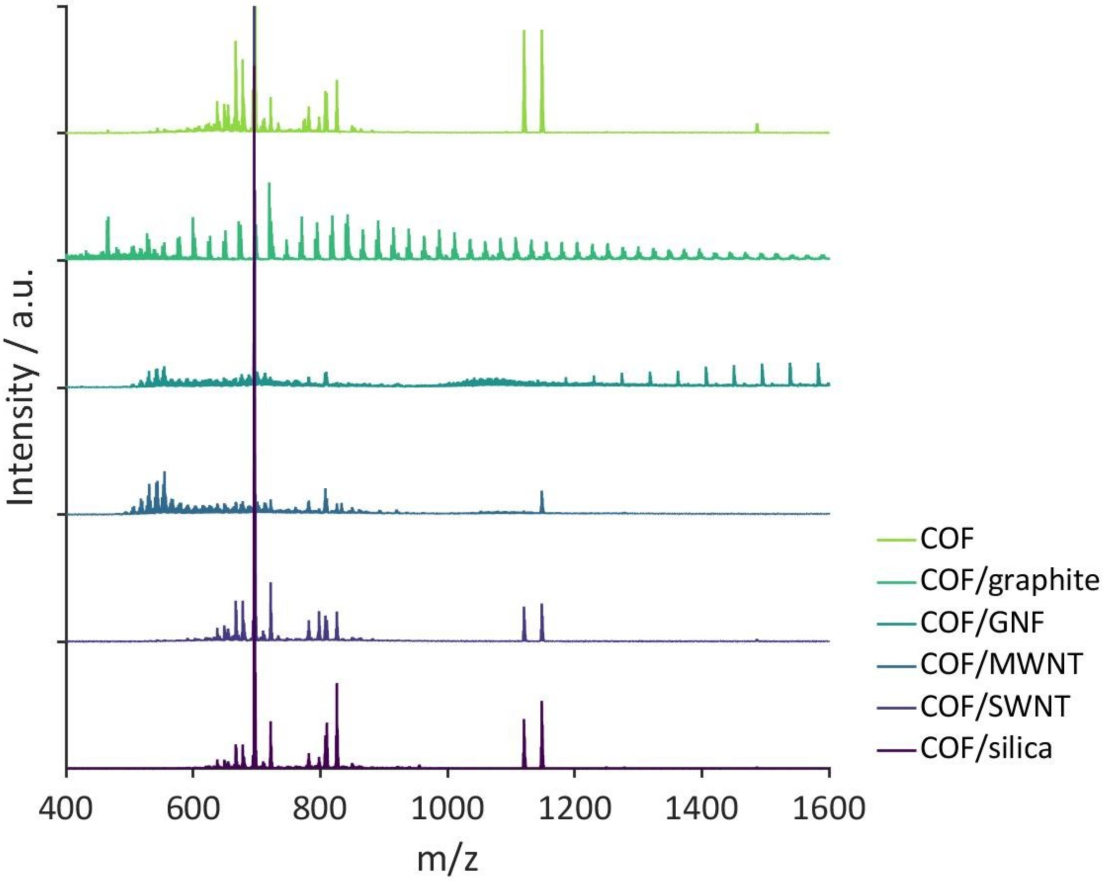

Figure 16: Positive ion MALDI-TOF spectra for cHBC-BDA-PBA COF and COF/: graphite, GNF, MWNT, SWNT, and silica. The base peak in each spectrum is due to the cHBC molecular ion. The spectra of COF/graphite and COF/GNF contain a series of periodic peaks that are due to fragmentation of the graphitic support. All ions below the base peak are due to fragmentation of cHBC, and above are due to fragments of the COF lattice.

2.3.3 Thermal Measurements

Thermogravimetric analysis (TGA) of COF and COF/nanosupport was undertaken to quantify their thermal decomposition temperature and products. This is useful to know in the context of industrial applications as safe disposal of product must be undertaken at the end of its lifespan, and the thermal decomposition temperature represents the maximum possible operating temperature of a device.

It was found that both COF and COF/nanosupport undergo complete combustion when heated under flow of compressed air between $497 - 539$°C. The combustion of COF occurs at a higher temperature than cHBC or BDA, indicating higher thermal stability. The onset temperature for combustion of COF was between $341 - 403$°C. It can be seen that the COF combustion

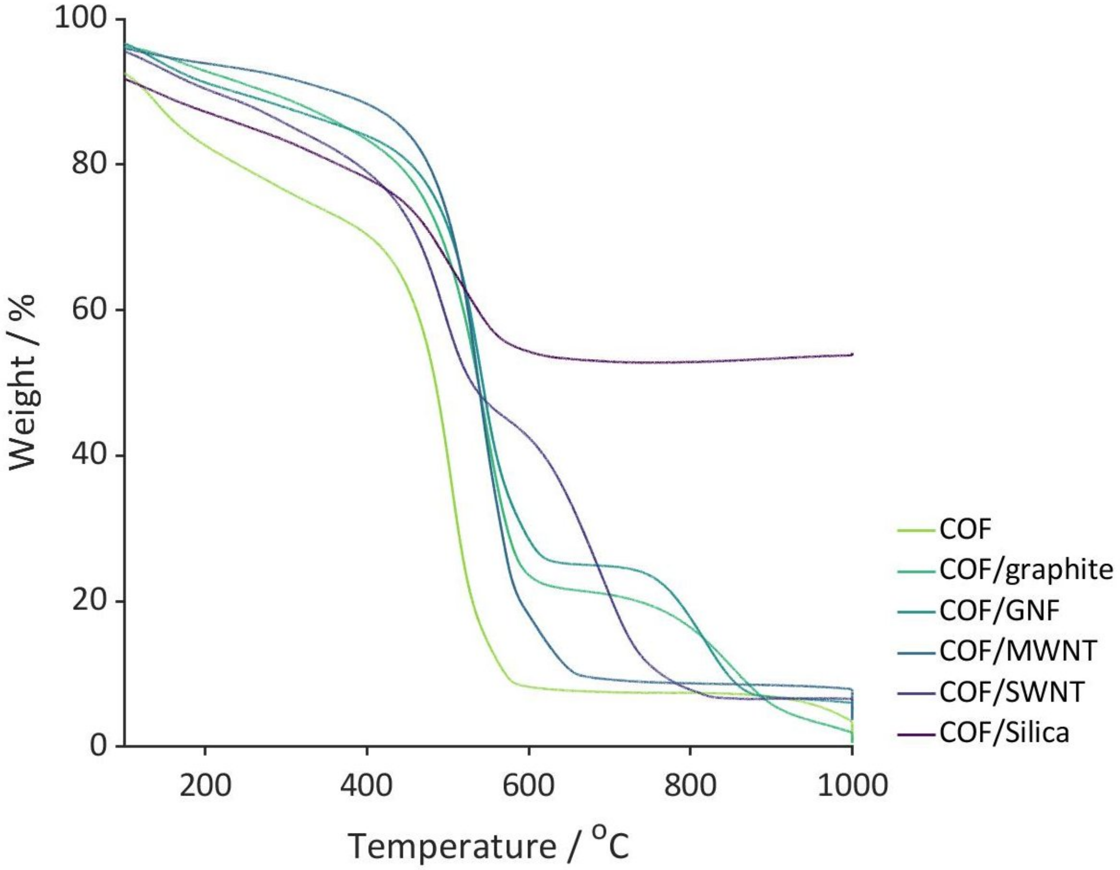

Figure 17: Thermograms for COF, and COF/: graphite, GNF, MWNT, SWNT, and silica. The sloping baselines are due to the small masses used in the thermograms. Residual mass in each thermogram is due to residual mass from nanosupport or boron oxide from COF combustion, and was measured at 1000 °C.

temperature decreases as the average diameter of the nanosupport decreases (Table 3). This could imply a thinner layer of COF formed on the surface of the nanosupport, but other factors such as COF morphology or nanosupport packing could also be involved. Nanocarbon supports underwent complete combustion between $613 - 847$°C, with larger nanosupports combusting at higher temperatures except for SWNTs. This can be explained by considering that combustion will occur more readily at the end of nanotubes and at defects in nanotubes, so compared to nanotubes with more layers SWNT have fewer points at which combustion can occur. Compared to unmodified nanosupports, the nanosupports in the hybrid materials combusted at a higher temperature but otherwise followed the same trend of smaller materials combusting at lower temperatures. Silica does not combust under these conditions (or at all), and contributes to the residual mass of the thermogram. The rest of the residual mass was made up of boron oxide, derived from the boronate ester and boronic acid groups in the COF structure, and a small amount

Material	**COF Combustion / °C**	**Residual / %**	**Support Combustion / °C**	**Residual / %**	**COF loading / %**
cHBC	515	4.5	-	-	-
BDA	200	50	-	-	-
COF	505	8.2	-	-	66
COF/graphite	548	22	847	4.0	28
COF/GNF	540	26	705	6.6	53
COF/MWNT	539	19	613	5.3	70
COF/SWNT	494	45	684	6.6	50
COF/silica	512	53	-	-	57
Graphite	-	-	774	0	-
GNF	-	-	713	0	-
MWNT	-	-	523	4	-
SWNT	-	-	562	6	-
SiONPs	-	87	-	-	-

Table 3: Combustion temperature and onset temperature, residual mass, and loading for COF, COF/nanosupport, nanosupports, and starting materials.

of impurities in the nanocarbons (residual catalyst from nanotube synthesis). Boron oxide formation was likely aided by the small amount of water present in the TGA compressed air source. The exact decomposition pathway is not known for COFs, but it likely involves formation of an amorphous carbon lattice[27] as boronate ester groups react with water or pyrolyse to eventually form boron oxide.[28] This may proceed via boric acid and metaboric acid (Figure 18).[28]

The residual mass of boron oxide was used to calculate the loading of COF on nanosupport (Table 3). The following relation was used to calculate the residual mass of boron oxide:

$$m_o = m_i \times p_r(1 - p_s) \tag{9}$$

Where m_o is the mass of boron oxide, m_i is the mass at the start of the thermogram, p_r is the residual percent mass of the thermogram, and p_s is the residual percent mass of the nanosupport thermogram. This relation is derived from a similar expression used to calculate the internal loading of carbon nanotubes.[29] In essence, we know how much residual mass a nanosupport will provide to a thermogram and use this to work out how much of the residual mass is from boron oxide; i.e., if a nanosupport gives 50 % residual mass and the residual mass of the sample thermogram is 50 %, the residual mass of boron oxide is 25 %. This elemental compostion of the residual mass was not tested experimentally, as the boron oxide melted into a thin layer on the TGA pans that could not be recovered without damaging the pans. It was made clear in no uncertain terms any procedure that might risk damage to the pans, made of thin platinum metal, was not allowed.

For combustion of boronate ester COFs one mole of boron oxide is yielded per mole of diboronic acid, which is then related to the stoichiometry of the COF via a balanced equation (Figure 18). This was tested using COF powder, which gave a "loading" of 66 %, corresponding to the COF after all solvents have left the structure. The accuracy of this method is limited by the assumption that all boronic acid in the TGA sample is in the form of boronate ester in a COF polymer, and does not account for unpolymerised boronic acid groups at the edge of the COF lattice. For the remaining COF/nanosupport materials, loading was found to range from 85 - 34 %, with smaller nanosupports tending to have higher loading. COF/MWNT had the largest loading, COF/silica and COF/GNF had comparable loading, and COF/graphite had the smallest loading. This likely reflects the greater available surface area for COF formation as the nanosupports get smaller.

Combustion and onset temperature are affected by particle size, surface area and packing. The decrease in COF combustion temperature and onset temperature is due to promotion of thinner COF materials by nanosupport templating. Onset temperature is harder to measure accurately for broad thermal features, so this value has a larger intrinsic error than the combustion temperatures.

These results show that the COF polymers formed are more thermally stable than the monomers, due to higher onset temperature and higher combustion temperature. This is due to the reactive catechol and boronic acid functionalities being protected by the polymerisation process into the more thermally stable boronate ester group. Nanosupports do not significantly change the combustion temperature of the materials, implying that the COF chemical structure is not being affected by the nanosupport and that they are held together by a physical interaction.

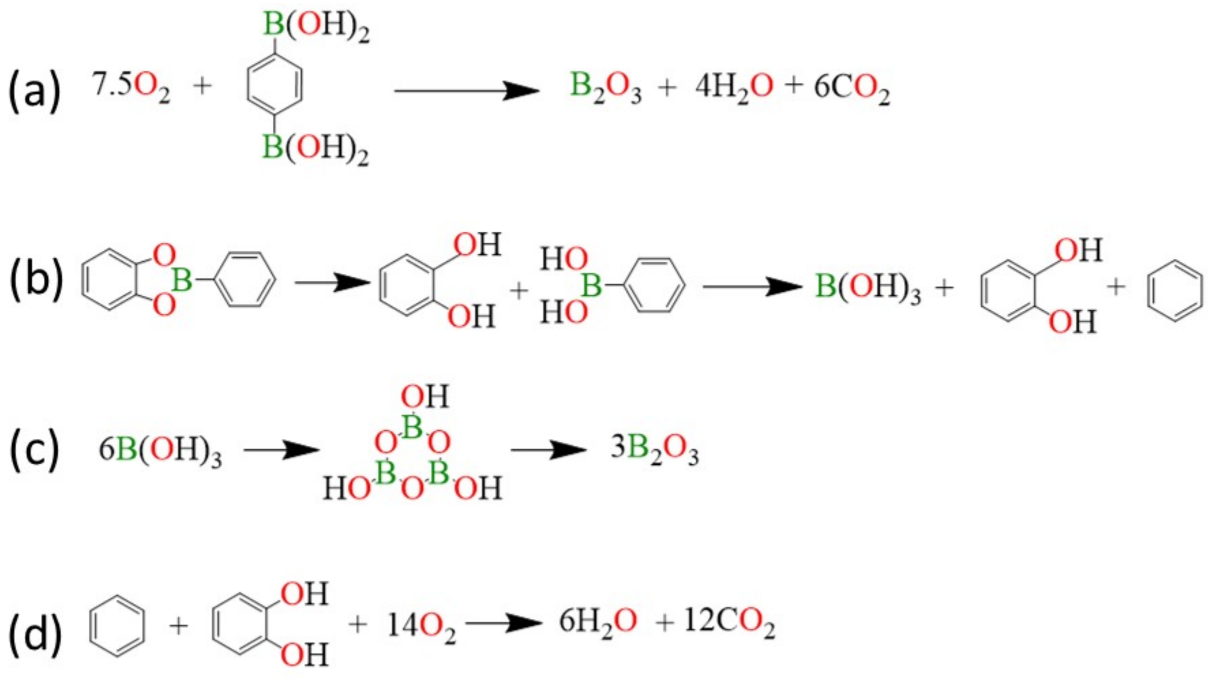

Figure 18: (a) Thermal decomposition of benzene diboronic acid. (b) Decomposition of boronate ester to boric acid. (c) Decomposition of boric acid to boron oxide via metaboric acid.[28] (d) Combustion of carbonacous materials in COF lattice. These pathways are not exact for a real COF material; benzene and catechol represent an amorphous carbonaceous lattice that would form as the boronate ester groups decompose.

2.3.4 Powder X-ray Diffraction

For each sample, a routine PXRD from $2 - 40°$ was performed. As COFs contain large internal pores, it is expected that the d-spacing will be large and therefore the reflections in PXRD will occur primarily at low angles. For example, a reflection arising from a 3.0 nm crystal plane (e.g. occurring across the COF pore channels, the (001) planes) would have a corresponding reflection at $2\theta = 2.94°$. By contrast nanocarbon supports would mostly have reflections occurring at larger values of 2θ due to their graphitic crystal planes. Therefore the small angle reflections are characteristic of COFs, confirmed by the simulated power pattern (Figure 19).

For cHBC-BDA-COF, it was found that the experimental powder pattern did not contain any sharp peaks, and the broad peaks present at $2\theta = 17.9°, 23.8°, 26.5°$ and $28.4°$ did not match to any theoretical d-spacing in this material. In order to detect reflections even from poorly crystalline samples, typically zero-background single-crystal silicon PXRD plates were used along with as much sample as possible. Furthermore, comparison to simulated powder patterns

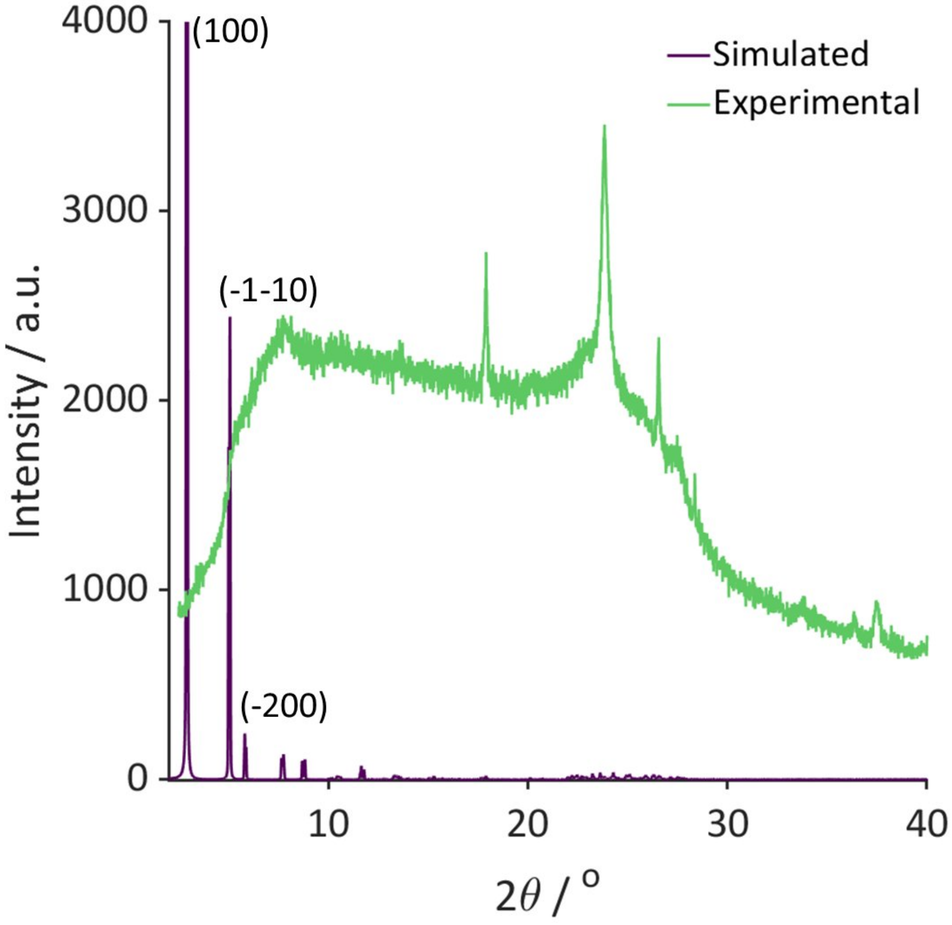

Figure 19: Simulated (purple) and experimental (green) PXRD patterns for COF. For the simulated powder pattern the three most intense reflections have been indexed, with many minor reflections present above 10°. The sharp peaks in the experimental COF powder pattern do not match to the simulated COF powder pattern or to the powder patterns of COF monomers. The experimental powder pattern has been scaled up to allow visualisation of the reflections.

of the starting materials did not match. This implies that the COF is amorphous or made up of small crystallites, rather than a mix of crystalline starting materials. Application of the Scherrer equation[30] showed that the crystallites would have to be very small to result in lines this broad. For the largest and smallest measured COF crystallites (59.9 nm and 12.9 nm) the predicted line broadening would be $6.8°$ and $1.8°$. Applying the Scherrer equation to the observed peak at $5.1°$ with a value of β = 7.26x10^{-3} rad gives a predicted crystallite size of 21.2 nm (using Cu(Kα_1)) radiation = 1.5046 Å (λ) and a shape factor (K) of 1 to predict line broadening (β). Given the large signal-to-noise ratio for these reflections, and that they do not match to any materials, these reflections are likely an artefact of signal processing or contamination and should be ignored.

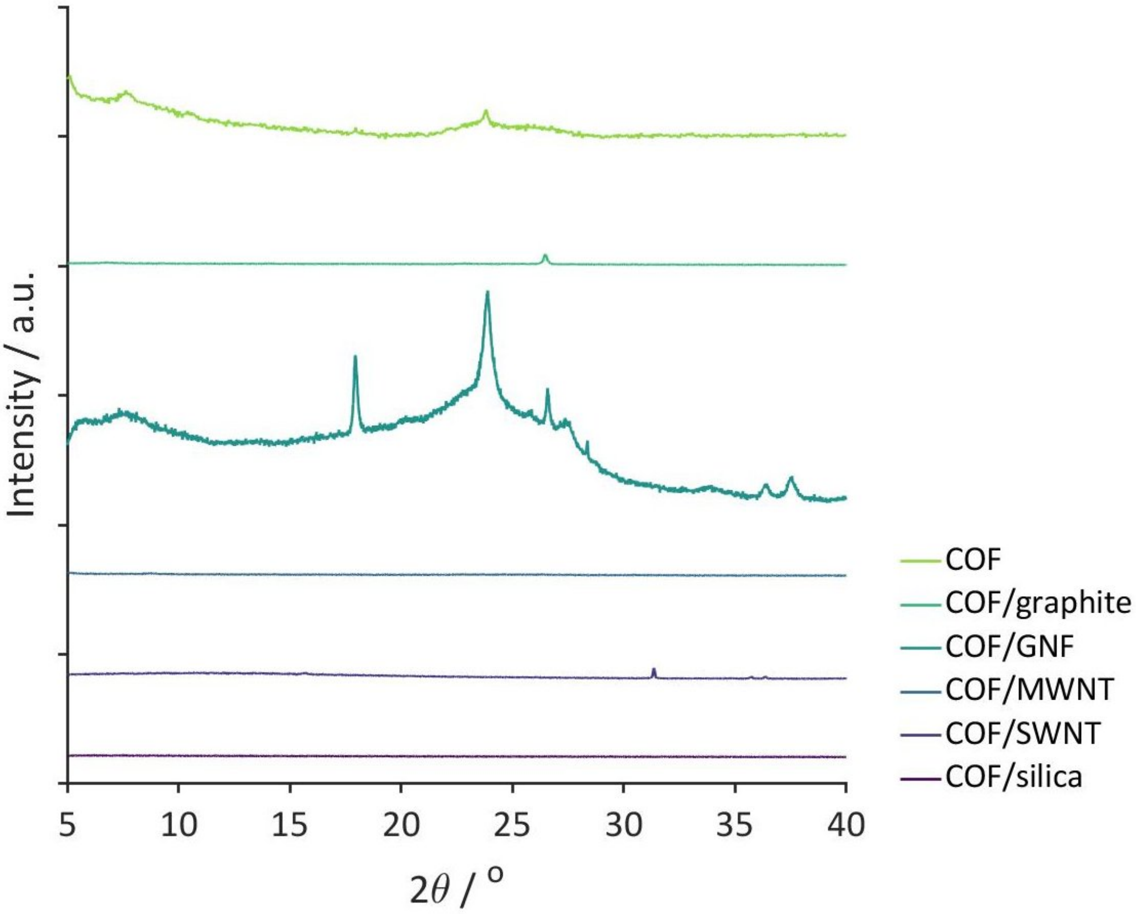

Figure 20: Powder X-ray diffraction (PXRD) patterns for cHBC-BDA-COF and COF/: graphite, GNF, MWNT, SWNT, and silica. The reflections in cHBC-BDA-COF/GNF, /graphite and /SWNT are due to graphitic reflections from the carbon supports.

For COF/nanosupport, the PXRD patterns contain no relfections arising from the COF. All reflections arise from nanocarbon supports. It can be therefore concluded that the nanosupports are not promoting formation of larger COF crystals that would give measureable reflections in the PXRD patterns. PXRD suggests either the formation of an amorphous COF, or the formation of a nanocrystalline material. Therefore, electron microscopy (EM) was applied to ascertain the structure of the COF.

2.4 Electron Microscopy of cHBC-BDA-COF

2.4.1 Scanning and Scanning Transmission Electron Microscopy

Scanning electron microscopy (SEM) and scanning transmission electron microscopy (STEM) were used as a supplement to TEM analysis, and to investigate sample morphology on the microscale. SEM imaging shows that the COF forms a "foamy" structure,[7] characterised by lack of defined crystal shapes such as plates or needles (Figure 21). This corroborates the PXRD data that showed no evidence of long-range crystallinity. The SEM analysis was not able to show whether COF foam was made up of large single pieces of foam, or whether the foam was made of agglomeration of several smaller pieces of COF foam. This is also true for COF/nanosupports; noteworthy is that SEM imaging shows that COF does not form selectively at the nanosupport surface. In all cases, both the COF/nanosupport and free COF can be found in the reaction mixture, as well as regions of nanosupport without significant COF formation. STEM of COF/silica was used to clearly visualise the boundary between COF and nanosupport (Figure 22), which could also be achieved by BF-TEM imaging.

2.4.2 TEM Image Processing and Automated Detection Methods

Image processing is important to consider for analysing and handling TEM data. For example the computer monitors used for making figures for this text display 8-bit colour while the Gatan Digitial Micrograph .dm3 and .dm4 format used to save TEM data is 32-bit, so it is theoretically possible to view the image at a greater colour depth to aid interpretation. TEM images are typically displayed in in an 8-bit greyscale colour palette, however the human eye is more sensitive to colour than intensity of light so it can be useful to apply false colour using a lookup table (LUT) to an image to aid interpretation (Figure 23a).[31]

One of the key goals in this work was to understand COF crystals, which involves processing images that contain visible lattice projections. While possible to detect lattice projections by eye, it would be faster and more repeatable to use an automated approach. To detect lattice projections in TEM an image processing technique based on the Fourier transform (FT) called Fourier filtering or Fourier masking was used (Figure 23b).[32,33] Briefly, straight lines in real space give spots in reciprocal space. It is therefore possible to use a FT to detect the presence

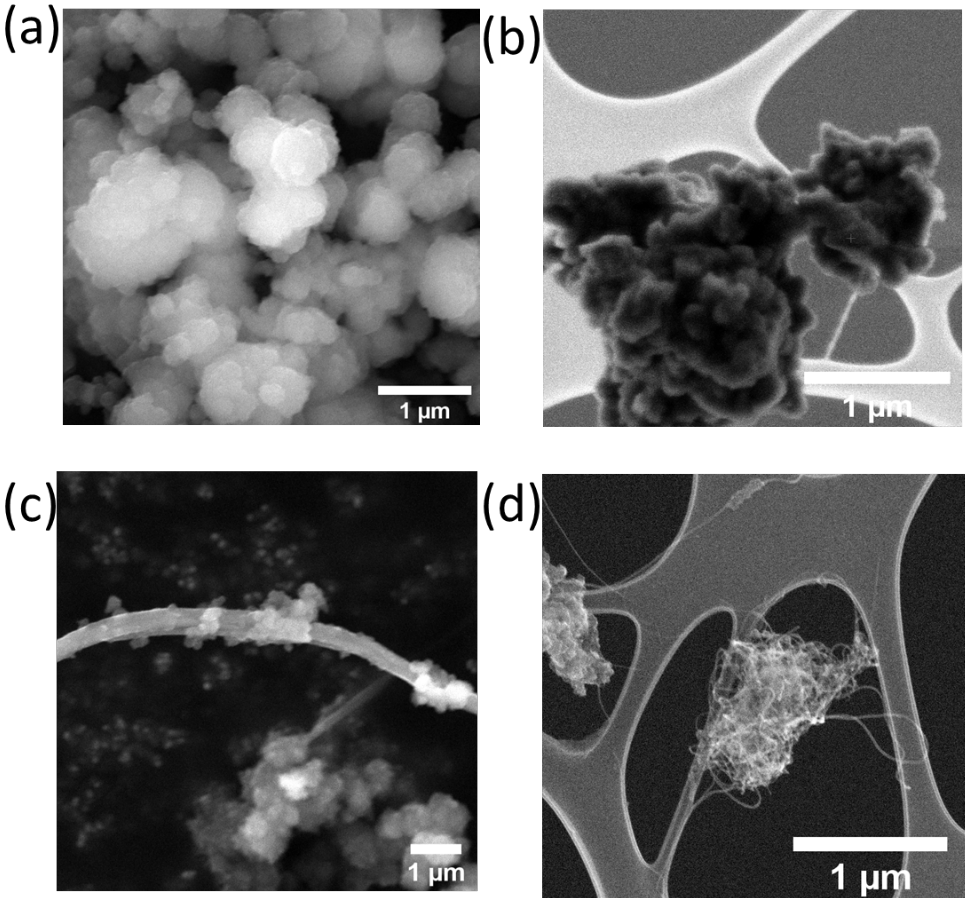

Figure 21: SEM images of (a) COF, (b) COF/graphite, (c) COF/GNF, (d) COF/MWNT. The COF exhibits a foamy morphology, as opposed nanoparticles or crystal shapes such as needles. SEM is a useful tool for low-magnification COF morphology characterisation.

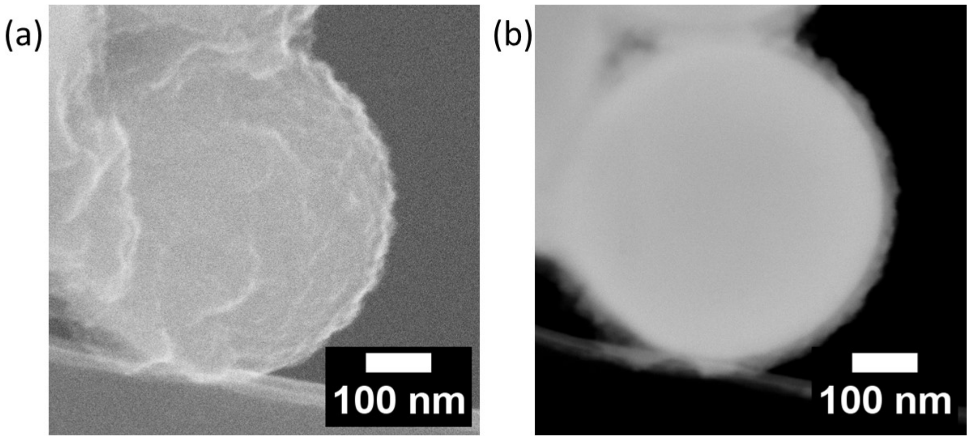

Figure 22: (a) SEM and (b) annular dark-field (ADF) STEM images of COF/SiONP. The dense silica core provides more contrast than the COF shell, which can be clearly seen in via ADF-STEM.

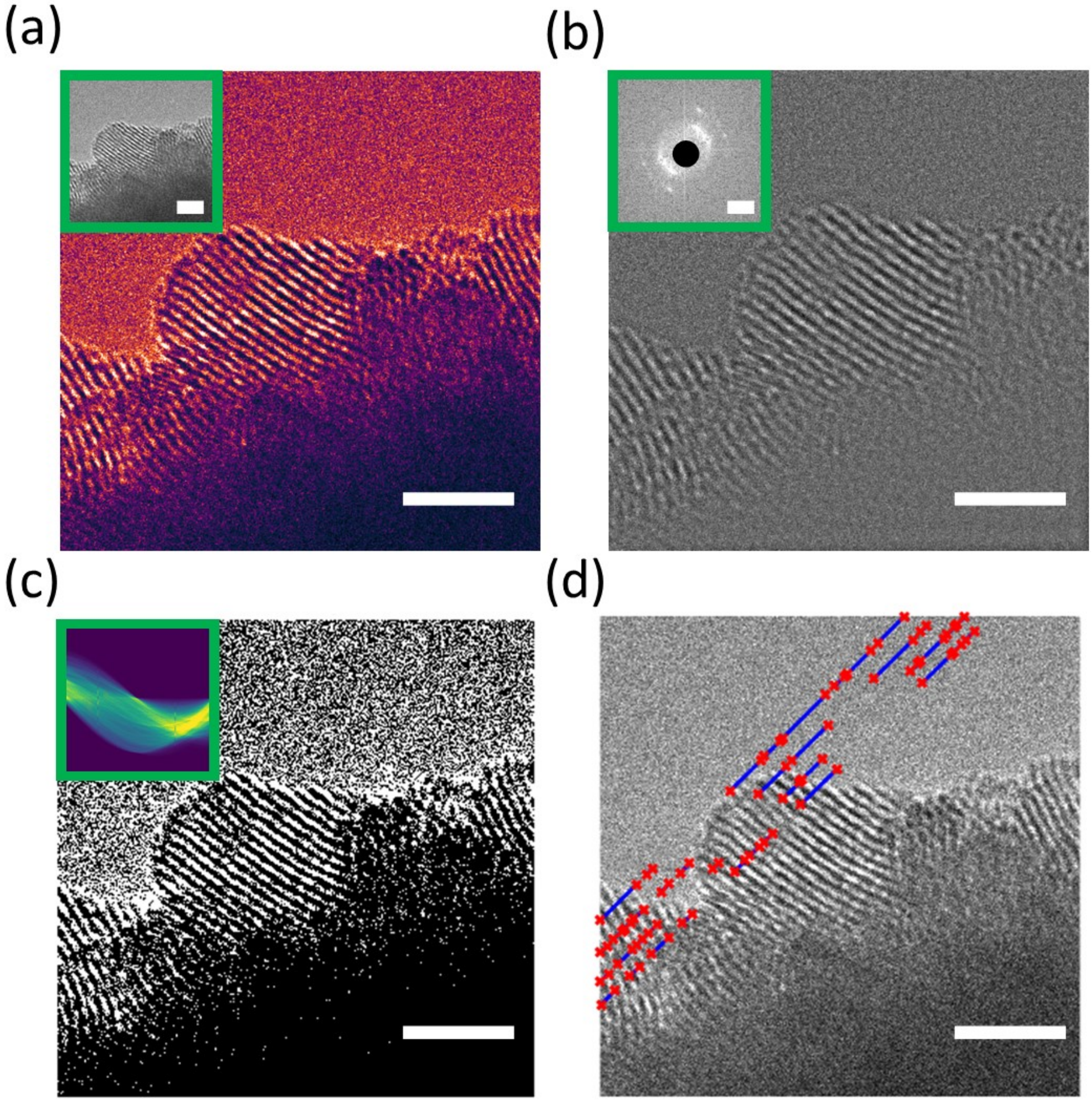

Figure 23: (a) False-colour TEM image of a cHBC-COF crystallite. Insert: Original 8-bit greyscale image. Scale bars = 50 nm. (b) Fourier filtered TEM image, which contains intensity only from the unmasked region of the FT. Scale bar = 50 nm. Insert: Fourier transform with mask over central spot. Scale bars = 0.2 nm^{-1}. (c) 1-bit binary image with Gaussian filtering for noise reduction. Scale bar = 50 nm. Insert: Hough transform sinogram. (d) Detected straight lines from 1-bit image drawn onto 8-bit greyscale image. It can be seen that the detected lines do not match to the visible lattice projections in the image. Scale bar = 50 nm.

of straight lines, and this also allows the inter-line spacing to be measured from the FT. Further it is possible to use masking to increase the intensity of lattice projections; a bright spot in the FT is selected, and the inverse FT is performed in this selected region of the image. This gives bright lattice projections and darker contrast in the rest of the image, and is analogous to dark field TEM image formation process. This was found to be useful for individual images, but automating this process was not undertaken due to time constraints.

An alternative approach is to detect the presence of straight lines was attempted based on the Hough transform. Hough transforms are a core part of computer vision and can be used for a variety of object detection, and have been used successfully to detect straight lines.[34] The Hough transform for straight-line detection works on the principle that a straight line can be described by an linear equation $y = mx + c$ where y and x are the variables, m is the gradient and c is the y-intercept. The Hough transform takes an image in x-y space and converts it into m-c space. As m and c are constants for a straight line, this creates a spot of local intensity in the Hough transform. This spot can then be detected and the corresponding straight line labelled in the source image. As lattice projections in TEM images present as bright and dark lines, it is theoretically possible to detect these with Hough transforms.

To detect straight lines, images were first imported as 16-bit TIFFs. Noise reduction was implemented by averaging pixels in an n by m area, or by using Gaussian filtering to a given number of standard deviations. Following this, the image was converted to 1-bit (black and white) with a user-defined threshold value. The resulting image was then Hough transformed, and the maxima on the sinogram used to detect straight-lines in the source image (Figure 23c). Maxima were found by defining an arbitrary detection factor and minimum line length. It was found that this process worked well with test images and high quality TEM images, but for most TEM images this method was not able to consistently identify lattice projections. This is attributed to the lattice projections often being faint and therefore not giving much intensity in the sinogram. Therefore changing the detection factor was not able to effectively find the lattice projections against the other features in the TEM image (Figure 23d), and further tweaking is needed for reliable lattice projection detection.

In summary, both Hough transforms and Fourier filtering are viable image processing techniques to enhance lattice projection detection and allow reproducible results. However, for the TEM images used in this thesis noise and lack of data can make this process more challenging. Likely the best approach for lattice projection detection would be to apply machine learning by training a convolutional neural network to detect the features of interest.[35]

2.4.3 Direct Space TEM Imaging of COF crystallites

For the synthesised COF powder, the effect of TEM accelerating voltage and TEM grid preparation were investigated. The COF samples were lightly ground then brought into mechanical contact with the TEM grid, and a second batch of samples was dispersed in isopropanol then drop-cast onto the TEM grid. No differences in morphology were detected via TEM imaging, indicating the COF is resilient to sample preparation techniques used. The COF was then imaged at 200 kV and 80 kV accelerating voltage. As expected, the higher accelerating voltage led to lower contrast TEM images. There was no detectable difference in sample stability between the two accelerating voltages: there was no noticeable differences in sample drift under the e-beam, and sample thinning was not observed at either voltage. Due to the lack of a detectable diffraction pattern, the effects on sample crystallinity could not be measured. It was elected to use 200 kV as the standard accelerating voltage.

Bright-field TEM (BF-TEM) revealed that the COF was in fact made up of many overlapping nanoscale crystallites, leading to no long-range crystallinity (Figure 24). This is despite the PXRD measurements that suggested the COF was entirely amorphous. The COF contained bright and dark fringes; these correspond to separate armchair (AC) and zigzag (ZZ) lattice projections of the 2D hexagonal COF lattice. These projections are formed by rotations of the COF lattice in projection, with either the AC or ZZ edges of the COF sheet aligned with the optical axis of the TEM. Image simulation shows that each projection has a characteristic lattice projection distance associated (Figure 24d). The theoretical AC lattice projection width was 3.0 nm, and ZZ was 1.9 nm. Distributing the lattice projection measurements showed that the dataset was bimodal, with a bimodality index (S) of 1.2, where each peak corresponds to the ZZ and AC projections. The ZZ mean was 1.73 ± 0.34 nm, and the AC mean was 2.95 ± 0.61 nm ($\mu \pm 2\sigma$). The overlap between these distributions is expected, as the AC and ZZ projections exist

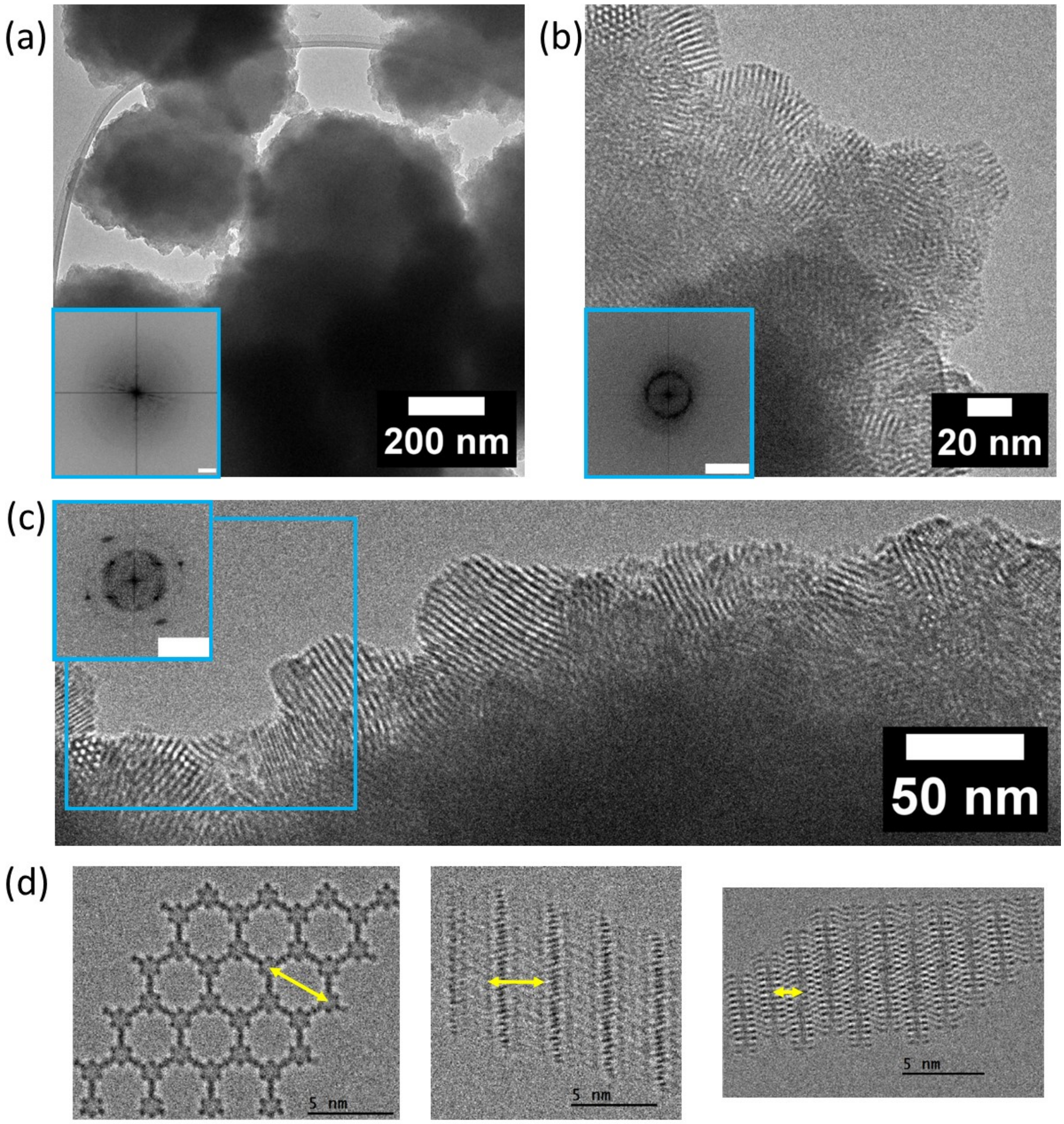

Face-On
(4.0 nm)

Armchair
(3.0 nm)

Zigzag
(1.9 nm)

Figure 24: cHBC-COF BF-TEM. (a) Low magnification BF-TEM image showing overall morphology of cHBC-BDA-COF particles. Insert: Fourier transform, scale bar = 0.2 nm^{-1}. and (b, c) high magnification images illustrating the lattice fringes visible at the edge of the COF particles. It can be seen that the COF is made up of many uncorrelated nanoscale crystallites with a variety of projections relative to the optical axis. The inserts show the Fourier transform of the image, for (c) the blue box indicates the region the Fourier transform was taken from. Scale bar = 1 nm^{-1}. (d) Image simulations of face-on (FO), armchair (AC) and zigzag (ZZ) COF lattice projections. The characteristic lattice projection distance has been indicated (yellow arrow); FO = 4.0 nm, AC = 3.0 nm, ZZ = 1.9 nm.

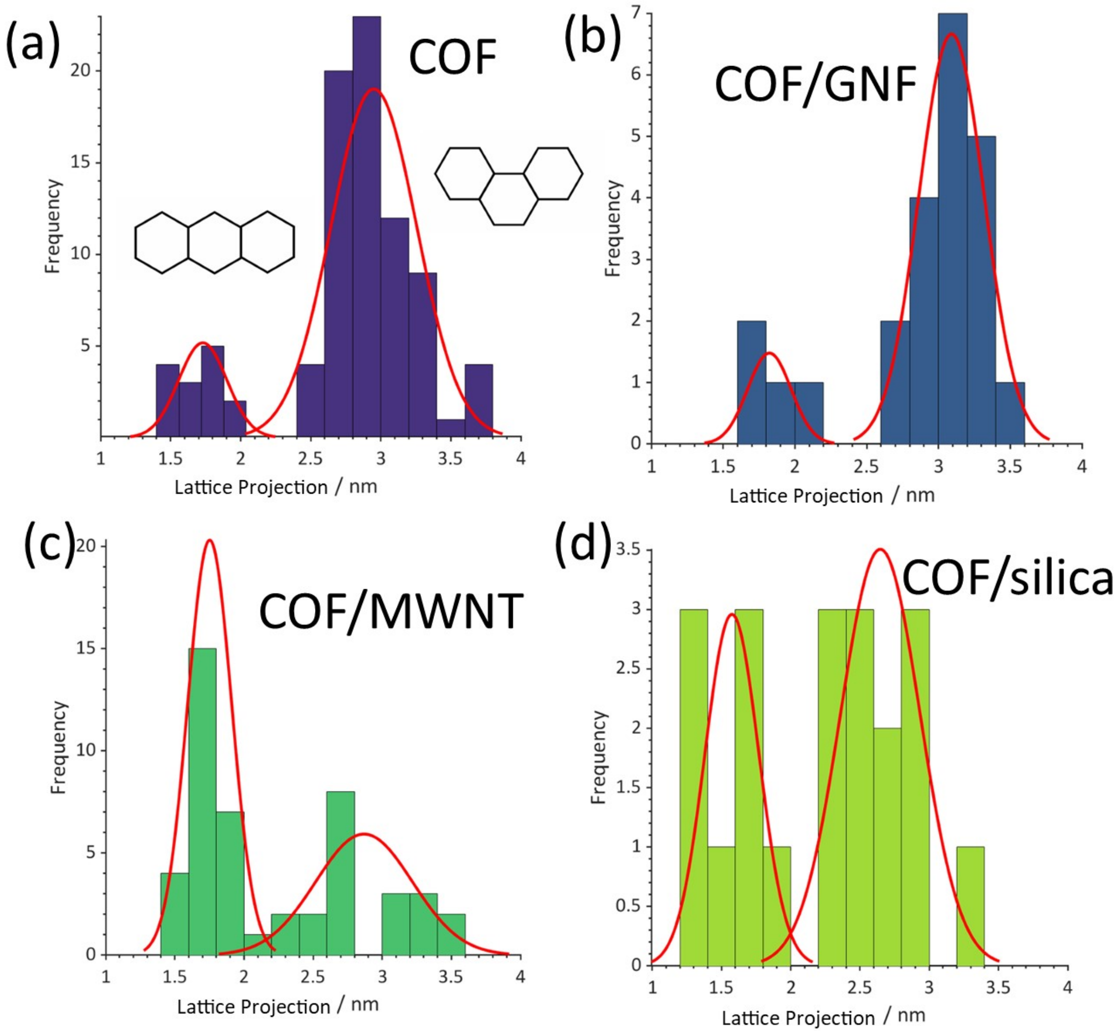

Figure 25: Histograms showing the lattice projection distribution for (a) COF, (b) COF/GNF, (c) COF/MWNT, and (d) COF/silica. The distribution for COF and COF/GNF best illustrate the bimodality arising from AC and ZZ projections in TEM images. The fits are normal distributions computed by the grouping the datasets into AC and ZZ by splitting at 2.02 nm, and are to help guide the eye.

on a continuum. The histogram binning method was equally distributed bins of 0.2 nm across the data range. This was chosen because using techniques such as Scott's Normal Reference Rule[36] or Sturges' Formula[37] would have given five or fewer bins across the data range, masking the bimodal distribution. The overall mean for the dataset was 2.75 ± 1.0 nm (Figure 25a). A tilt series of the COF reveals that the lattice fringes do in fact change as a function of angle (Figure 26).

COF/GNF was also found to contain lattice fringes (Figure 27). The fringes were found to extend away from the surface of the GNF between 52° - 89°, and were never observed parallel to

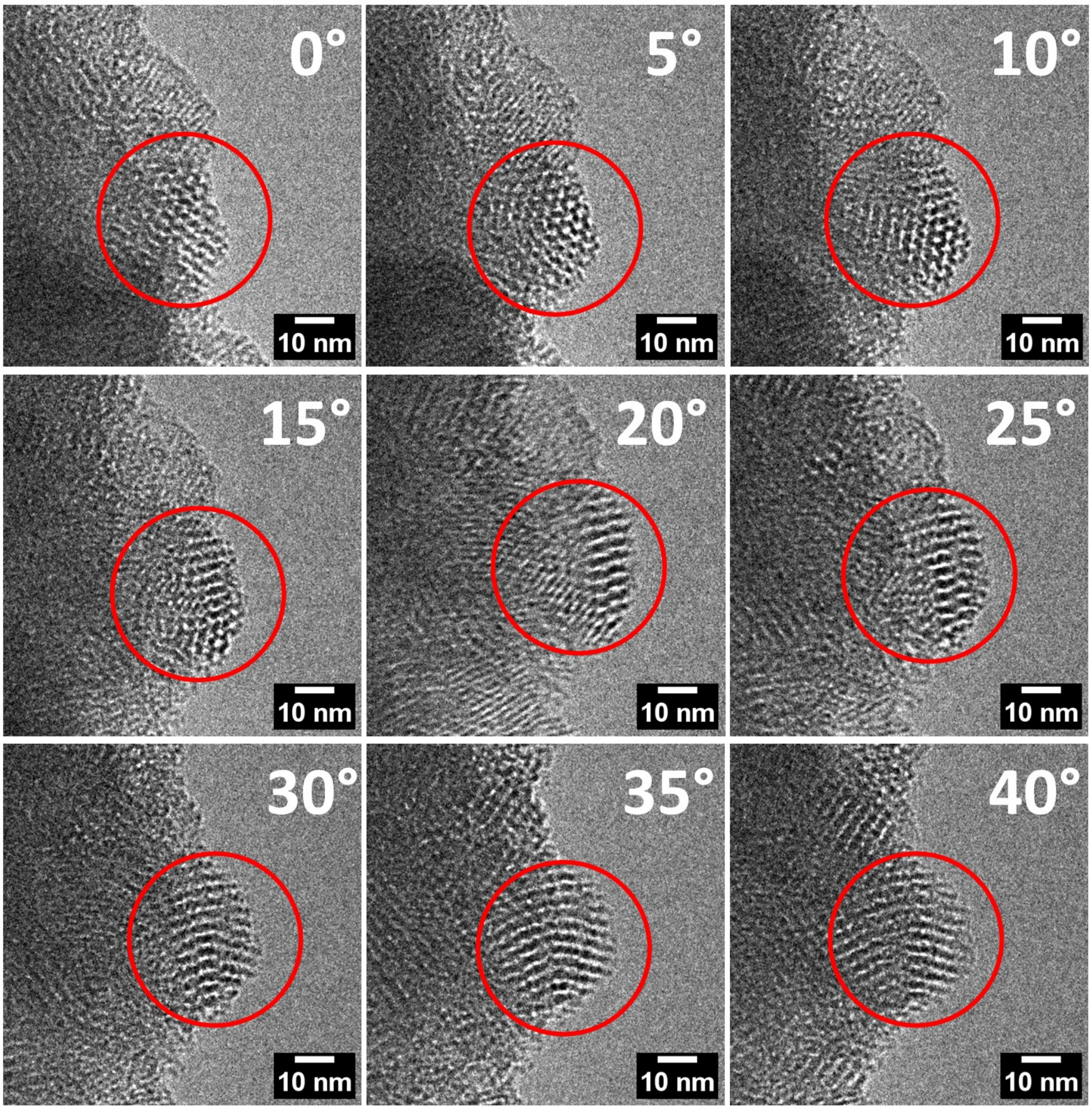

Figure 26: BF-TEM 40° tilt series for cHBC-BDA-COF. Red circles indicate a region of the sample with visible changes in lattice projections between images, from a hexagonal projection to bright and dark fringes. The lattice projection width in the final frame was 1.49 nm, indicating a ZZ projection.

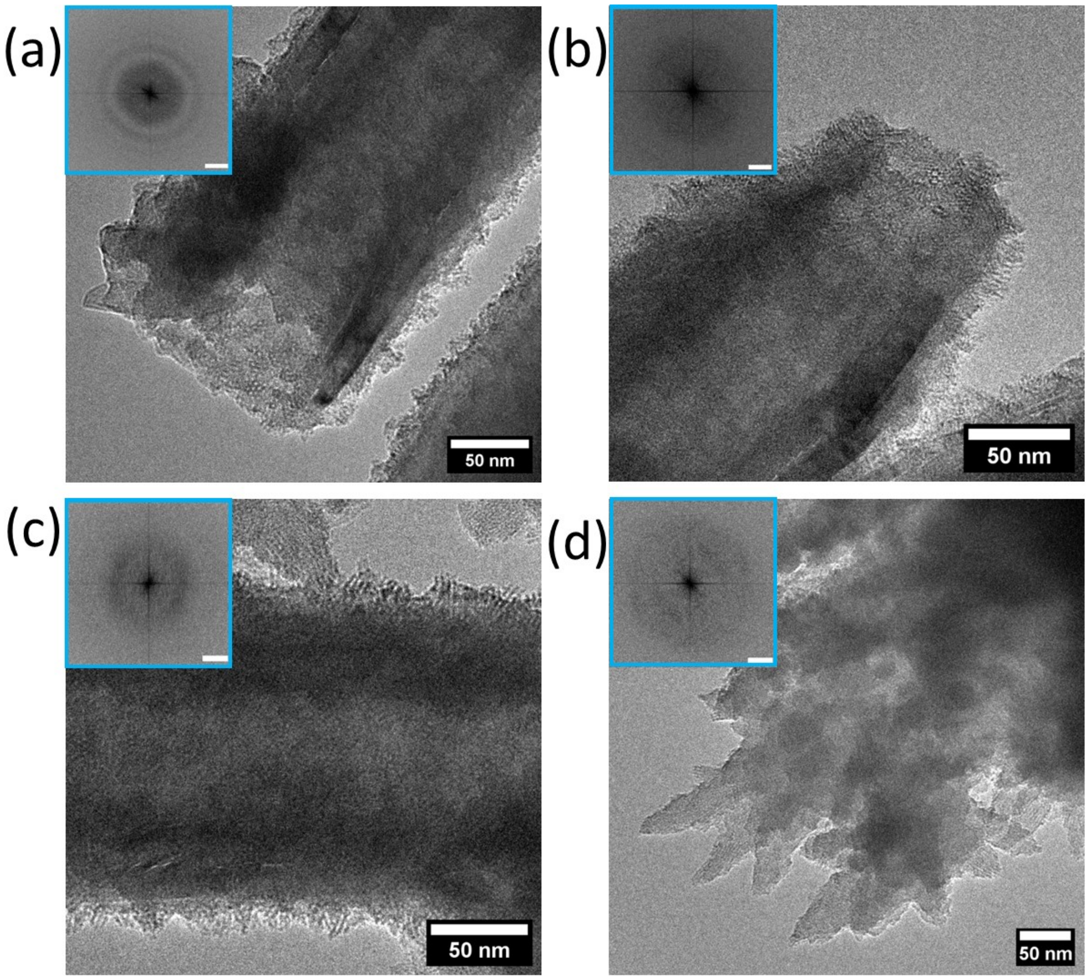

Figure 27: (a - c) BF-TEM of COF/GNF, showing how the COF forms an irregular layer on the surface of the GNF. (d) Example of COF not associated with GNF in the sample, indicating that GNF by themselves cannot cause selective growth on nanosupport surfaces. Inserts: FT, scale bar = 0.1 nm^{-1}.

the surface of the GNF. Distributing the lattice projection measurements gave a bimodal distribution where the peaks correspond to the mean AC (3.09 ± 0.45 nm) and ZZ (1.82 ± 0.30 nm), with a lower bimodality index (S = 0.83) than for COF indicating greater overlap (Figure 25b). The mean lattice projection for the entire dataset was 2.87 ± 1.1 nm. A tilt series shows that the COF forms an irregular layer around the GNF, agreeing with the SEM morphology (Figure 28). Overall, the COF forms a layer around 5-10 nm thick on the surface of the GNF.

The lattice projection distribution for COF/MWNT lattice fringes is clearly bimodal, with a bimodality index of 0.55 (Figure 25c). The two modes correspond to the mean AC and ZZ distances in the COF (2.87 ± 0.70 nm and 1.75 ± 0.32 nm). The overall mean is 2.22 ± 1.22 nm. Hexagonal projections of the face-on COF lattice were much more common in this system

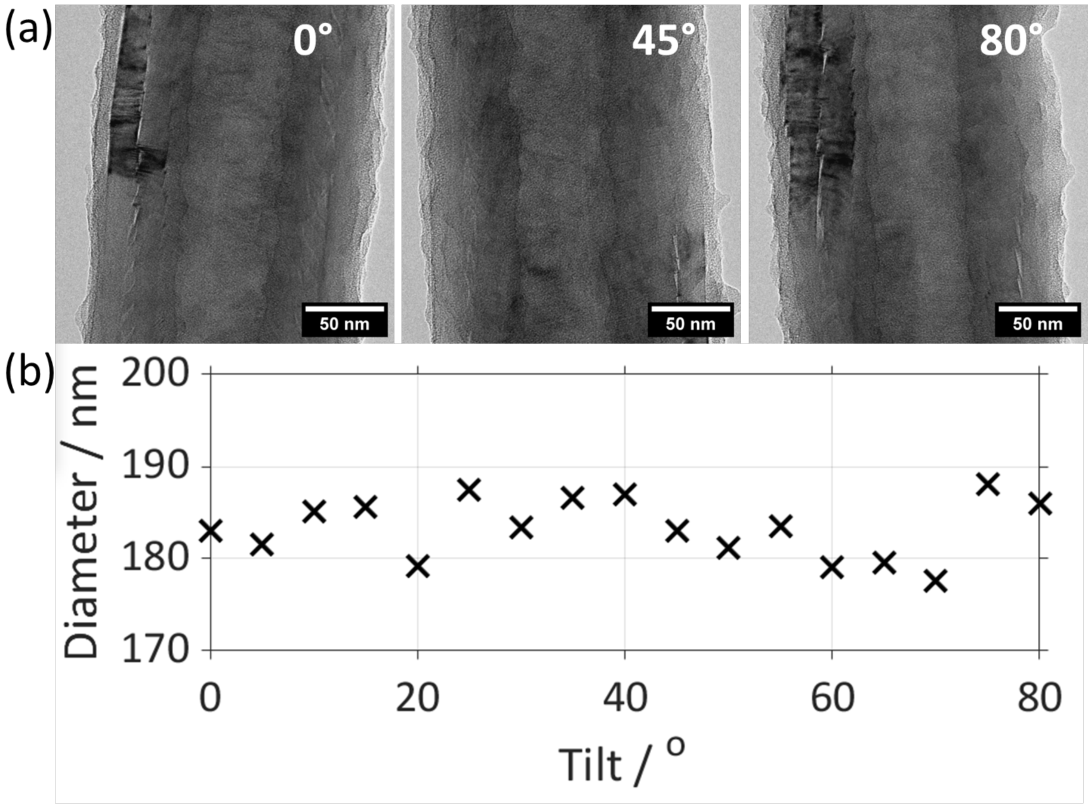

Figure 28: (a) Images of COF/GNF during a tilt series at 0°, 45°, and 80°. (b) Diameter measurements for COF/GNF during the tilt series, showing that while the thickness of the COF layer varies it is within a small range of 10 nm.

than the others (Figure 29), from which the measured COF pore diameter was 3.96 ± 0.53 nm which matches the theoretical pore diameter. The vertex diameter of the observed hexagons was 1.30 ± 0.39 nm, which matches to the theoretical diameter of cHBC (Table 4).

COF/SiONPs were made as a test system for the growth of COF on silica surfaces (Figure 30). After COF synthesis, it was observed that the reaction vessel would have a green tinge on the inside. This tinge was difficult to remove, and typically required treating with strong base. This observation implies that COF was forming directly onto the pyrex borosilicate glass. Silica nanoparticles were selected as "nano-glass" to approximate the pyrex glass surface, while allowing investigation by TEM. Crushing pyrex glassware was rejected as unsafe and having poor repeatability. Silica nanoparticles were made via the Stöber process, a facile method to create monodisperse nanoparticles with good control over the diameter. This involved basic hydrolysis of tetraethylorthosilicate to give silica, where the nanoparticle diameter is controlled by the ratio of reagents.[38] The silica nanoparticles were confirmed to have a diameter of 495 ± 8.7

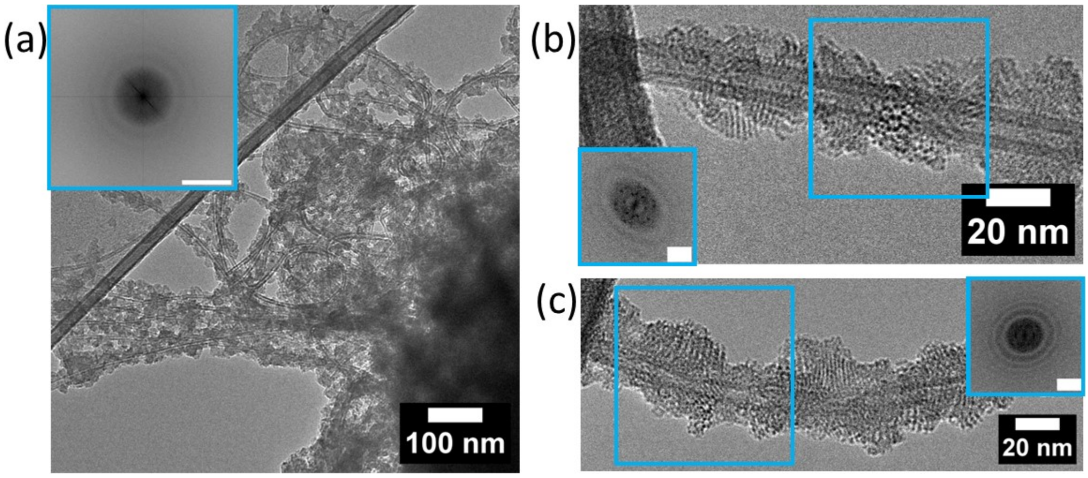

Figure 29: (a) Low-magnification COF-MWNT, which group into large bundles. Insert: FT, scale bar = 0.1 nm^{-1}. (b) COF/MWNT showing hexagonal COF pores. Insert: FT, scale bar = 0.5 nm^{-1}. (c) Examples of COF/MWNT, displaying irregular COF growth on the MWNT surface. The COF layer thickness varies even on the same nanotube. Insert: FT, scale bar = 1 nm^{-1}.

Sample	$\mu \pm 2\sigma$ **/ nm**	**n(total)**	**Theoretical / nm**
Hexagon diameter	3.96 ± 0.53	66	2.7 - 4.0
Hexagon side length	2.01 ± 0.41	102	2.0 - 3.3
Hexagon vertex diameter	1.30 ± 0.39	86	1.2 - 1.3

Table 4: Mean measurements of hexagonal projection diameter, side length and vertex diameter for COF/MWNT. Standard deviations are 2σ confidence interval. Hexagonal diameter was measured between pairs of opposite vertices (3 measurements per hexagon). Each side length was measured once, and was not remeasured if hexagons shared a side. Each vertex was measured once, and was not remeasured if hexagons shared a vertex. 22 individual hexagons were measured. The measured values match well to the modelled face-on projection.

nm by TEM and 445 ± 58 nm by dynamic light scattering (DLS).

For COF/SiONPs, the lattice projection distribution had a mean value of 2.22 ± 1.20 nm that could be readily split into AC and ZZ measurements (2.48 ± 0.72 nm and 1.54 ± 0.32 nm) (Figure 25d). The COF formed as a more uniform shell than for the other nanosupports, but contained some large protrusions. A measure of COF shell thickness without taking the protrusions into account was achieved using a TEM tilt series from -40 to + 40 ° of an isolated COF/SiONP which found the COF shell thickness was 37.7 ± 6.0 nm. Including COF spikes and measuring a range of nanoparticles found that the shell thickness was 47.2 ± 42 nm, with a larger standard deviation reflecting the irregular rough surface of the COF shell (Table 5).

For COF/GNF, COF/MWNT, and COF/SiONPs it was found that the fringes extend away from the support surface, which indicates that the polymer grows as a covalent sheet parallel

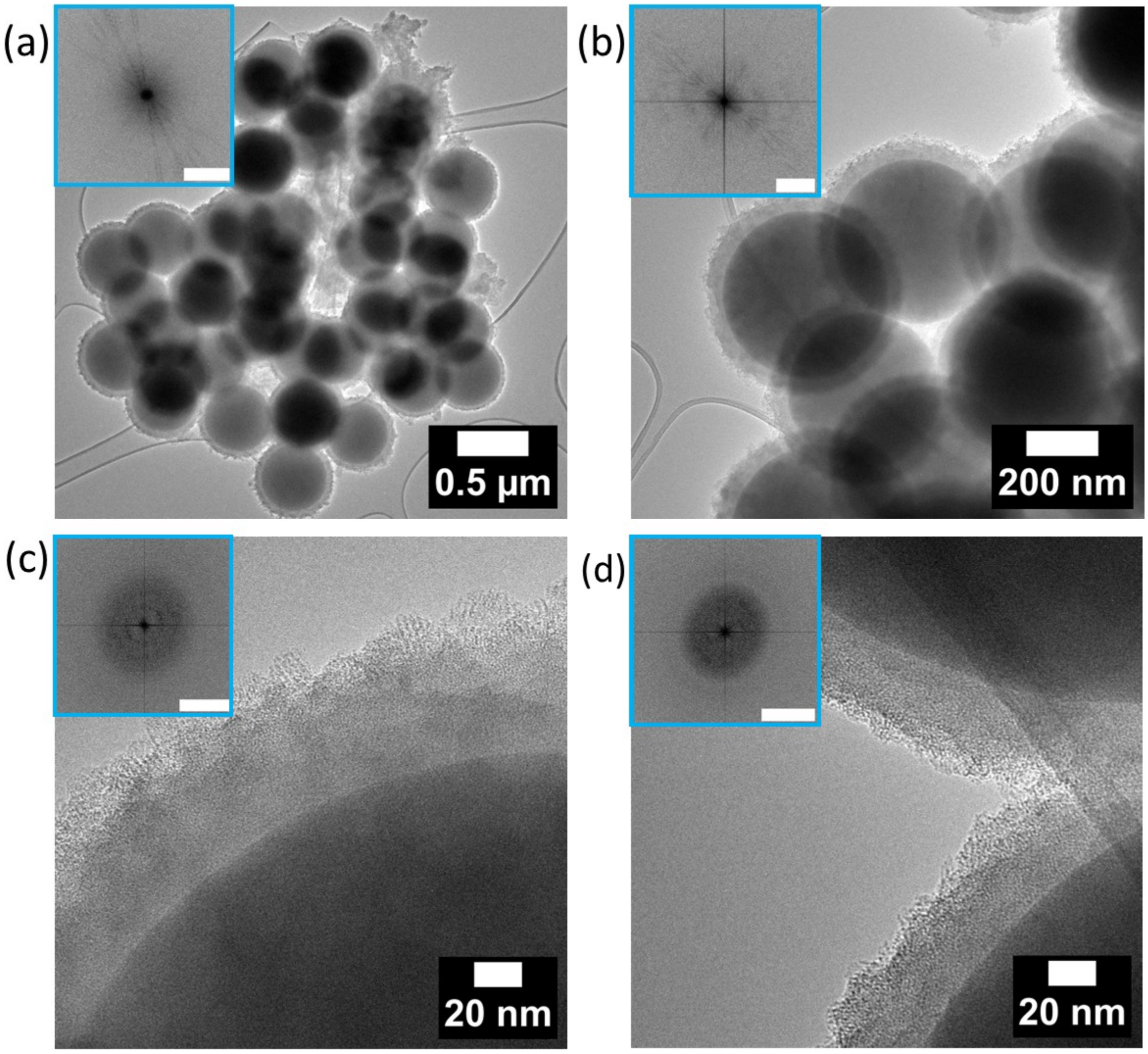

Figure 30: (a) Low magnification images COF/silica, showing how the nanoparticles cluster together on the microscale. Insert: FT, scale bar = 50 μm^{-1}. (b) Group of COF/SiONPs. The COF shell clearly has lighter contrast than the dense silica core. Insert: FT, scale bar = 1 nm^{-1}. (c, d) Examples of COF shell surrounding silica nanoparticle, with visible lattice projections at the thin edges. Inserts: FT, scale bar = 1 nm^{-1}.

to the support surface and grows by π - π stacking away from the support surface. The low-magnification TEM images of agree with the morphology given by SEM imaging.

For COF/SNWT and COF/graphite, no lattice fringes were observed (Figures 31 - 32). Graphite was the thickest support used, so lattice fringes are only visible at the very edge of the material where the COF can extend away from the graphite. For COF/SWNT, only a 1-2 nm thick layer of amorphous COF was observed on the surface of the SWNTs, indicating that the available support surface area was too large to allow formation of ordered crystal domains, instead promoting the formation of a very thin layer of amorphous COF.

It was assumed that the AC and ZZ edges would occur equally frequently in all samples, as the sample was drop-cast onto the TEM grid so the crystallites should be distributed in random orientations on the grid. It can be seen in the lattice projection distribution that the projections do not occur at the same frequency (Figure 25). To see if this is statistically significant, a binomial test was applied with the null hypothesis as equal numbers of ZZ and AC projections. It was decided that it was statistically significant if the results fell out of a 95 % confidence bound for the null hypothesis. A binomial test was selected over a z-test or t-test as mean and variance of the sample could not be meaningfully calculated.[39] The expected number of each projection was taken as half of the total number of projections for each sample (Table 6): AC = ZZ = 1/2(Total Observations). For COF and COF/GNF the binomial test results reject the null hypothesis. This suggests that the COF projections are not occurring randomly, and may be due to preferential deposition of the COF samples in a specific orientation. For COF/MWNT and COF/silica, the results do not reject the null hypothesis.

The difference between the samples can be rationalised by considering the effect of the support surface on the COF, and the conditions required for electron beam transmission. Greater surface area nanosupports will lead to thinner COFs; assuming the nucleation-elongation mechanism for COF scale growth there is proportionally more surface area for nucleation to occur on. This will lead to more, thinner, COF crystallites. In COF and COF/GNF, large regions of the sample are therefore too thick for electron beam transmission so many projections are not seen. The GNF itself also obscured projections of crystallites not at the edges of the side wall in transmission. In COF/MWNT, most of the sample is thin enough for COF projections to be seen, so it

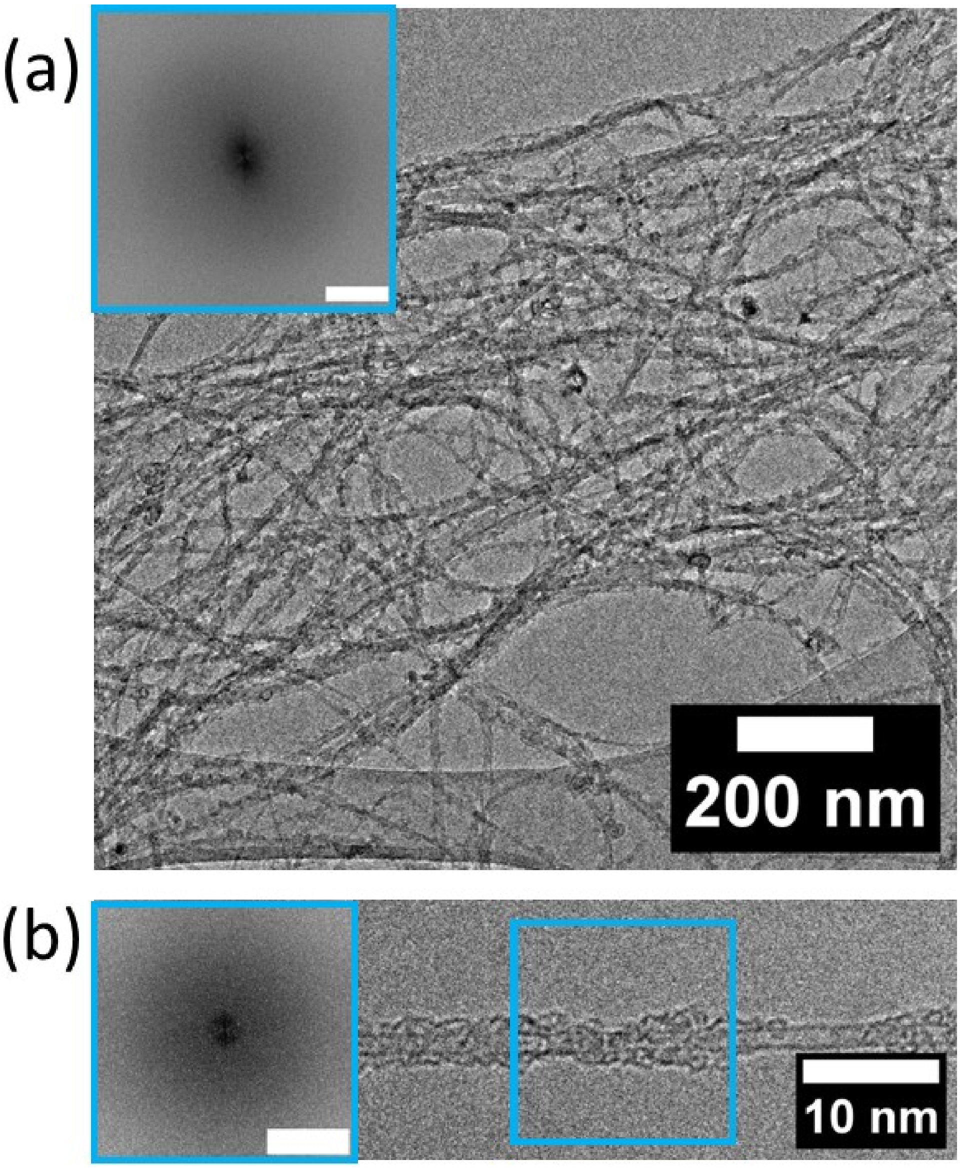

Figure 31: (a) Bundle of COF/SWNT, with visible material on the surface of the nanotubes. Insert: FT, scale bar = 200 nm^{-1}. (b) Single nanotube, illustrating that the material on the surface of the nanotube has no clear COF crystal projections and does not form a uniform layer. Insert: FT, scale bar = 10 nm^{-1}.

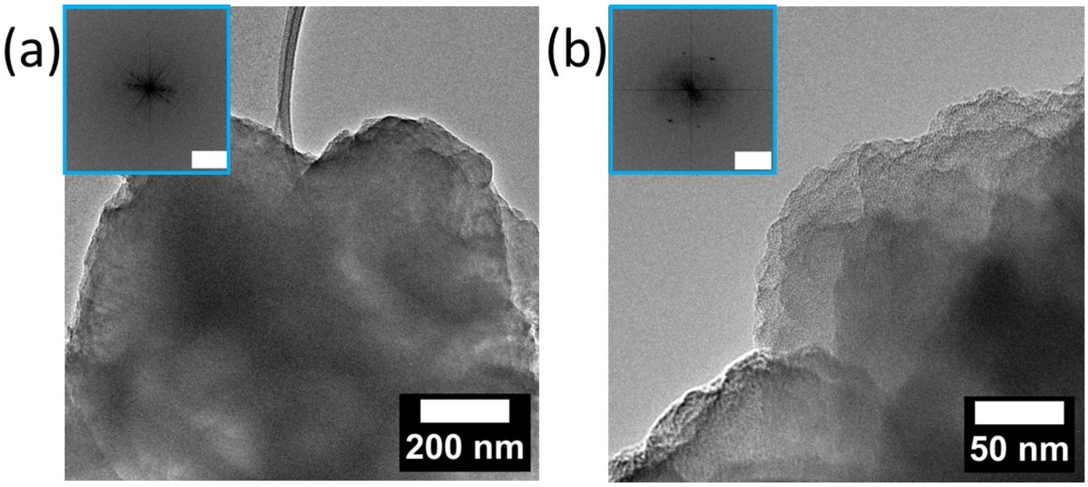

Figure 32: (a) Low magnification image of COF-graphite illustrating overall morphology. Unlike other samples, no COF lattice projections are visible. (b) COF/graphite, with lattice fringes corresponding to graphite crystal planes. No crystalline COF can be observed. Inserts: FT, scale bar = 0.1 nm^{-1}

gives a more representative picture of how frequent each projection is. For COF/SiONPs, while the silica spheres are thick enough to hide some projections, as they are spheres they have less of a preferred orientation. Therefore the new working hypothesis is that in thick COF samples you will see one projection more frequently, but in thin samples you will see each projection equally frequently. This leaves unanswered why AC was more frequent than ZZ. Either the samples measured happened to contain more AC than ZZ, or there truly are more AC than ZZ in the sample. This can be addressed by measuring more datasets; if it is random whether AC is more frequent than ZZ, it is expected that over a large number of datasets AC and ZZ will be in excess equally frequently. This again can be tested for using a binomial or z-test test and 95 % confidence bounds.

The size of COF crystallites was measured parallel and perpendicular to the lattice projections. The size of an object in projection depends on its rotation relative to the optical axis of the TEM, so this method does not necessarily give the absolute size of the COF crystallite in real space. However by aggregating this data the effect of random orientations should be reduced, allowing comparison between COF/nanosupport hybrids. This was performed for COF, COF/GNF, and COF/MWNT (Table 7); for COF/silica the overlap between the crystallites made the measurements unreliable. In general COF had the largest crystallites and the largest range of sizes, while COF/MWNT had the smallest. This suggests that the smaller diameter nanosupports encourage the growth of smaller COF crystallites. The large range for COF crystallite sizes could indicate that new crystallites are forming throughout synthesis, or that the rate of growth for different sized crystals is not equal. Each sample has a larger mean perpendicular to the lattice projection, which implies that the COF grows more rapidly by addition of monomers to an existing 2D sheet than by formation of new 2D sheets. However, further investigation is needed to establish whether the COF is growing via the nucleation-elongation mechanism suggested by Li *et al.*[40] This could be achieved via combination liquid-cell TEM, kinetic studies, and computer modelling of growth pathways for example.

Electronic structure modelling was performed by Karol Strutyński and Manuel Melle-Franco at the University of Aveiro of cHBC and COF on the surface of graphene, both with curved and flat geometry. A conformational search was done using tight binding methods with energies refined by DFT(PBE). Graphene is a suitable model for the surface of a GNF as over the diameter of a cHBC molecule, the surface of a GNF is essentially flat. This is not a good model for nanoparticles or for MWNTs as they have significant curvature over the diameter of the cHBC molecule adsorbed to the surface. The curvature of a GNF (taken as the reciprocal of the radius, Table 8) is negligible over short distances. A GNF of radius 75 nm would have a curvature of 0.013 nm^{-1}, while curvature of cHBC is 0.86 nm^{-1}. It was found that cHBC has a large binding energy to graphene (-2.14 eV) that is very close to the modelled binding energy of cHBC to cHBC (-2.07 eV). The binding energy to graphene of a COF fragment consisting of two cHBC units joined by a BDA linker (cHBC-BDA-cHBC) (-2.22 eV) was very close to the binding energy of cHBC. This was due to the corrugated geometry of the COF sheet that allowed only one cHBC unit to sit on the graphene surface. Modelling the extended COF structure on graphene found the binding energy of one COF layer on graphene (-2.20 eV) was less negative than the binding energy between two AA stacked COF sheets (-5.22 eV), indicating a single COF layer on a graphitic support surface is unlikely. Furthermore, it was found that by modelling COF as a planar structure (i.e. planar cHBC rather than concave), binding energy increased to a value comparable to AA stacking (-5.14 eV) due to increased contact area between the molecule and the graphene surface. Modelling the orientation of cHBC nodes in COF relative to the graphene surface found that pore channels would be 44° relative to the graphene surface.

	$\mu \pm 2\sigma$ / nm	No. measurements
Total diameter	533 ± 35.3	8
Core diameter	467 ± 20.4	8
Shell thickness	47.2 ± 42.4	31
Total diameter	567 ± 10.2	18
Core diameter	495 ± 8.71	18
Shell thickness	37.8 ± 5.97	18

Table 5: Top: Mean and standard deviation (2σ) for COF/silica-NP diameter, diameter of the silica-NP core, and thickness of the COF shell. Due to many silica-NPs overlapping in projection, fewer were suitable for full diameter measurement. The standard deviation for shell thickness is of similar magnitude to the mean because it takes into account large COF spikes that project from the surface of COF/silica-NP. Bottom: results of tilt series of isolated COF/silica-NP. An image was aquired every 5° from -40 to +40 °. This gives a measurements that do not take into account the effect of COF spikes.

Sample	n(total)	n(AC)	n(ZZ)	Expected	Bounds
COF	87	73	14	43.5	34, 53
COF/GNF	23	19	4	11.5	67, 16
COF/MWNT	47	20	27	23.5	17, 30
COF/silica	20	13	7	10	6, 15

Table 6: Results of binomial test for AC and ZZ projections. The null hypothesis was: n(AC) = n(ZZ) = $\frac{1}{2}$n(total), with 95% confidence bounds indicated. The null hypothesis was rejected if the measured n(AC) fell outside calculated bounds. COF and COF/GNF reject the null hypothesis, while COF/MWNT and COF/silica do not reject the null hypothesis.

Sample	Perpendicular Mean / nm	Perpendicular Range / nm	Parallel Mean / nm	Parallel Range / nm
COF	28.0 ± 20	10.1 - 59.9	18.4 ± 16	6.07 - 52.5
COF/GNF	21.9 ± 16.2	8.4 - 38	12.4 ± 7.2	5.5 - 23.2
COF/MWNT	14.5 ± 8.44	7.02 - 27.9	10.9 ± 9.13	4.41 - 22.3

Table 7: Crystallite size parallel and perpendicular to the COF lattice fringes for COF, COF/GNF, and COF/MWNT. Nanosupports appear to cause the formation of smaller COF crystallites, and nanosupports with greater surface area lead to smaller crystallites.

Sample	Radius / nm	Curvature / nm^{-1}
Graphene	-	0
Silica-NP	200	0.005
GNF	75	0.013
MWNT	5	0.2
cHBC	1.2	0.86
SWNT	0.65	1.5

Table 8: Radius and curvature for graphene, silica-NP, GNF, MWNTs, cHBC, and SWNTs. The radii were measured from TEM images, or calculated for cHBC.

2.4.4 Electron Crystallography

No specular diffraction arising from COF was found by selected area electron diffraction (SAED) for all samples. Many SAED patterns contained diffuse rings corresponding to diffraction from the amorphous carbon support film, and samples containing nanocarbons have diffraction rings caused by diffraction from the graphitic carbon layers (Figure 33). Convergent beam electron diffraction (CBED) was applied to COF/MWNT, which gave rise to diffraction spots from the MWNT but not from COF (Figure 33k).

Although the COF nanocrystallites are on the order of tens of nanometres, it would be expected that they cause some specular diffraction of either X-rays or of electrons. It is known that the intensity of diffraction spots is proportional to the square of the structure factor, and therefore is proportional to the number of unit cells causing scattering and the atomic form factors of the elements in the unit cell. While boron, carbon, and oxygen each have low atomic form factors compared to heavier elements, it is possible to collect single-crystal diffraction data from organic molecular crystals. This shows that a large number of unit cells are important for causing detectable diffraction, and implies that the COF crystals in this work are too small to give detectable diffraction on the instruments available.

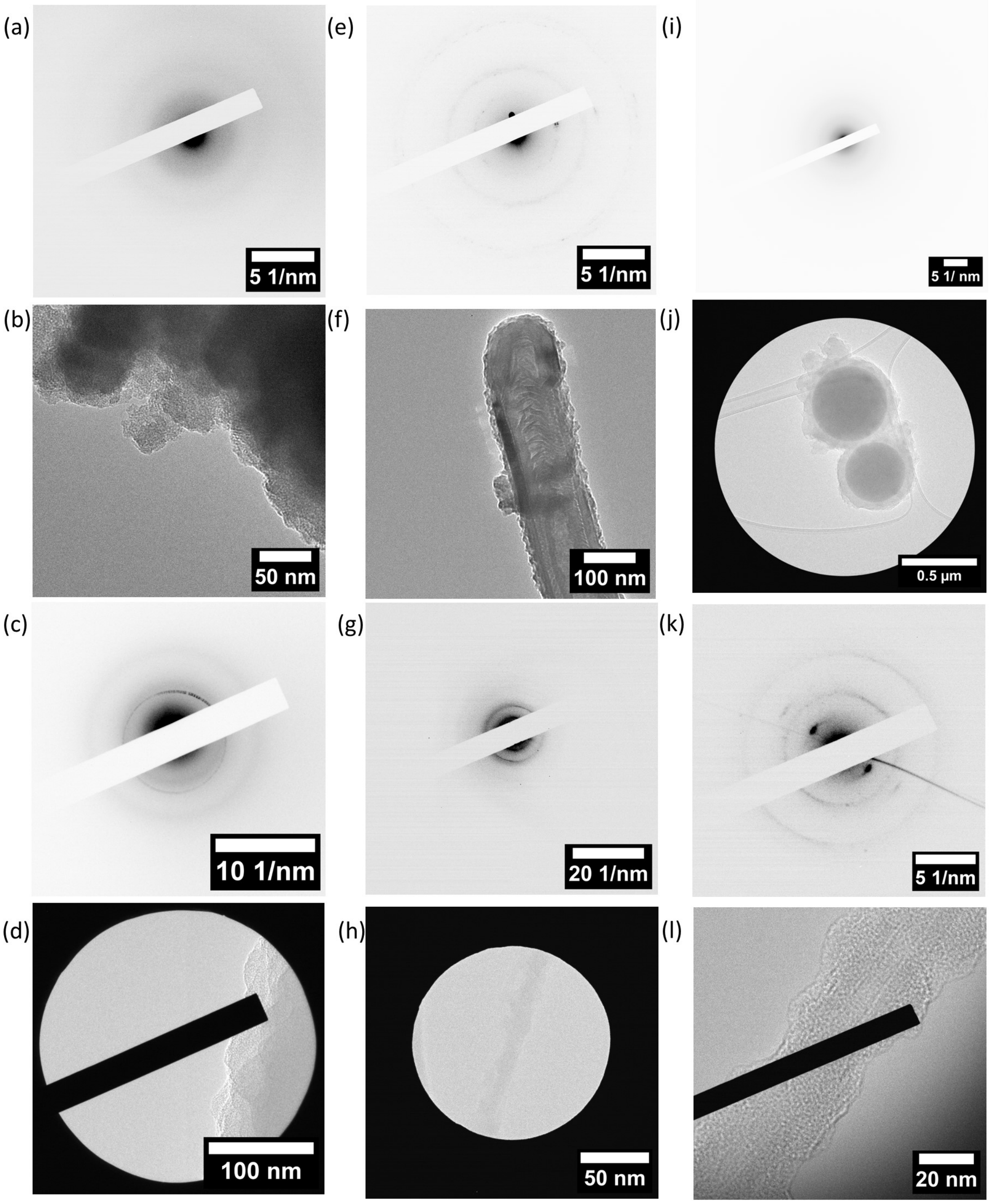

Figure 33: Selected are electron diffraction (SAED) of (a, b) cHBC-COF, (c, d) COF/GNF, (e, f) COF/GNF, (g, h) COF/SWNT, (i, j) COF/SiONP. (k, l) Convergent beam electron diffraction (CBED) of COF/MWNT. Each pair of images is the diffraction pattern and the area from which is was acquired; no reflections corresponding to the COF where observed. All specular diffraction is the result of the nanocarbon supports.

2.4.5 TEM Electron Energy Loss Spectroscopy

As discussed in Chapter 1, electron energy loss spectroscopy (EELS) is currently underused in TEM analysis of COFs. In particular, no examples were found of low-loss EELS analysis in the COF literature. Therefore an investigation into the applicability of EELS to cHBC-COF was undertaken. To begin, core-loss EEL spectra were acquired for all samples to provide elemental analysis. All spectra contain a sp^2 carbon edge (Figure 34a-c, 35a-c), which corresponds to either the aromatic monomers in the COF polymer or the nanocarbon support in the sample. Compared to amorphous carbon edges, sp^2 carbon edges have much more detail in the ELNES/EXELFS region of the carbon edge which allows effective fingerprinting of the carbon hybridisation state. For COF/silica, a silicon L edge was seen. Due to a low signal, the ELNES/EXELFS region of the edge could not be interrogated. However, silicon edges were not seen in other samples that did not contain silica nanoparticles. Of note is the difficulty detecting a boron K edge in all samples even at higher electron flux and long spectrum exposure time. As can be seen in the core-loss spectra, no boron K edge was detected in any sample (Figure 34d-f, 35d-f). The presence of sp^2 hybridised boron in the core-loss spectrum would be an ideal fingerprint. However, in this COF boron has a very low atomic abundance (3.3 %) compared to carbon (63 %) and oxygen (6.6 %) which leads to a low signal to noise ratio on the spectrometers available on the instruments used; i.e. carbon is 20 times more abundant than boron in the COF polymer so gives a more obvious signal. The core-loss spectra of COF/graphite, COF/GNF, and COF/MWNT did not contain a detectable oxygen K edge, while the other samples had a low-intensity oxygen K edge. This is due to the low atomic abundance of oxygen in the samples (Figure 34g-i, 34g-i). Core-loss EEL spectra are thus useful for characterisation of carbon, oxygen, and silicon in these materials but boron remains elusive via EELS for this COF. This has literature precedence for Marta-COF-1, as the published EELS spectrum also does not contain a detectable boron K edge.[41]

The lack of a boron K edge can be considered a limit of detection issue, and reliable detection will be dependant on sample composition. For samples that contain a low concentration of boron, use of a more sensitive detector would allow identification of the boron K edge. This could be enhanced by using an aperture to limit the collection angle for EELS electrons to the characteristic scattering angle for the boron K edge, in order to maximise edge intensity and while reducing noise from electrons scattered at higher angles. Practical implementation and calculation of scattering angles has been described by Egerton.[42]

Sample	***t*(KraKro) / nm**	**Plasmon peak / eV**	**Band gap / eV**
COF	23.0	22.8 ± 2.6	2.0 ± 2.6
COF/graphite	378	24.5 ± 2.7	0 ± 2.7
COF/GNF	128	27 ± 5.0	1.5 ± 5.0
COF/MWNT	26.4	23.5 ± 2.7	2.0 ± 2.7
COF/SWNT	10.8	24.3 ± 2.5	1.8 ± 2.5
COF/silica	136	24.8 ± 2.6	1.8 ± 2.6
Graphite	14.3	25.4 ± 2.0	0 ± 2.0
GNF	23.4	17.8 ± 2.5	0 ± 2.5
MWNT	3.1	20.3 ± 2.0	3.4 ± 2.0
SWNT	2.4	22.8 ± 2.0	3.3 ± 2.0
Silica	25.5	23 ± 2.5	2.0 ± 2.5

Table 9: Kramers-Kronig analysis of thickness (*t*), plasmon peaks, and band gaps measured from low-loss EELS. Plasmon peak energy varies due to the presence/absence of nanosupports. Due to the poor energy resolution and effects of deconvolution, band-gap values are not reliable.

The low-loss spectrum was also investigated for each sample. As there were no published examples of low-loss EELS analysis of COFs at the time of writing the techniques employed come from Egerton's textbook, which furnished methodology and software for analysis.[42] The spectra were first de-convoluted using a Fourier-log deconvolution method which removes plural scattering from the spectrum to give a single scattering distribution (SSD) (Figure 37 - 36). The mathematics of Fourier-log deconvolution is beyond the scope of this thesis. For all spectra the low-loss region was taken as 0-100 eV, as above this point the main contribution to the spectrum intensity is from edges. This also removed the zero-loss peak (ZLP) from the plasmon. Qualitatively the SSDs for thicker materials such as graphite silica nanoparticles are much less intense than the recorded plural scattering distribution (PSD), which confirms the necessity of deconvolution. For the thinner samples, the PSD and SSD are very similar. This can be explained with the approximate elastic mean free path of the materials ($\lambda_{elastic}$), which was found to be 500 nm at 200 keV accelerating voltage. A 20 nm thick sample would be 4 $\%$ of $\lambda_{elastic}$, meaning plural electron scattering is highly unlikely. The spectrum is therefore essentially only made up of singly scattered electrons.

The shape, intensity, and position of the SSD plasmon acts as a fingerprint for the material.

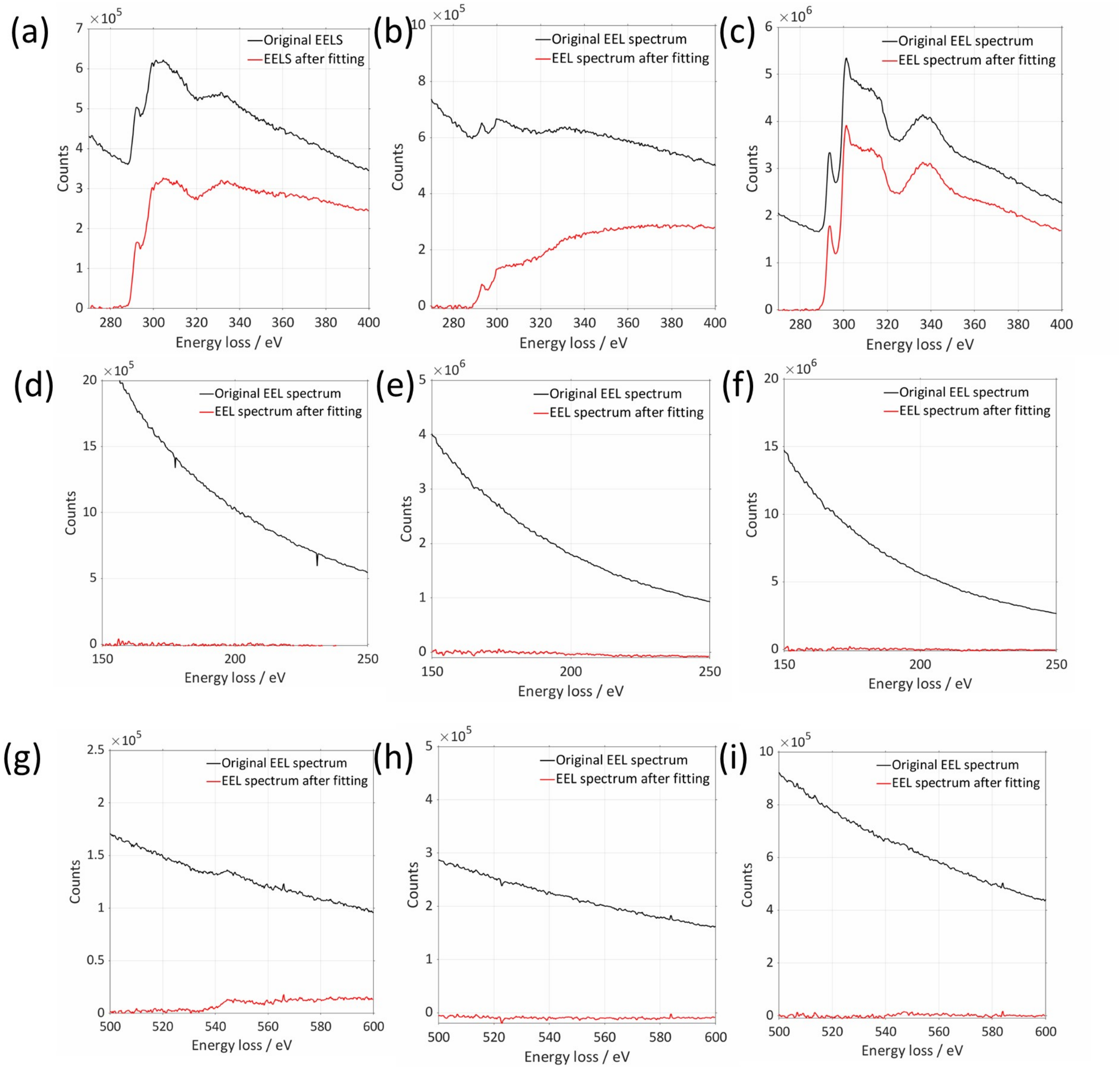

Figure 34: Core-loss EELS. Left to right columns correspond to: COF, COF/graphite, and COF/GNF. (a - c) Carbon K edges. (d - f) Boron K edge region. (g-i) Oxygen K edges. Boron K edges were difficult to detect due to the low concentration of boron in the COF and the limits of the experimental setup. Carbon K edges contain clear sp^2 hybridisation.

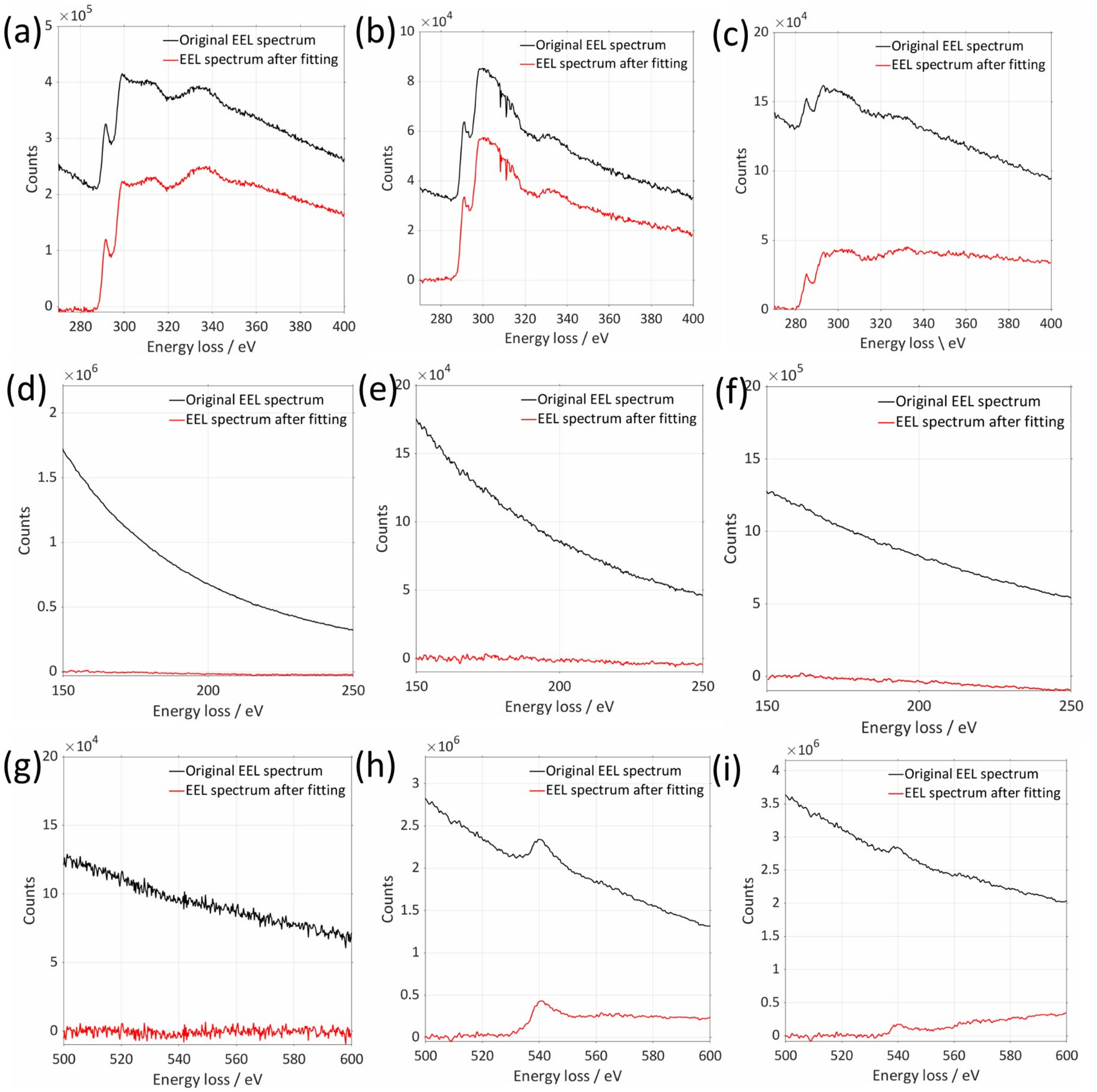

Figure 35: Core-loss EELS. Left to right columns correspond to: COF/MWNT, COF/SWNT, and COF/silica. (a - c) Carbon K edges. (d - f) Boron K edge region. (g-i) Oxygen K edges. Boron K edges were difficult to detect due to the low concentration of boron in the COF and the limits of the experimental setup. Carbon K edges contain clear sp^2 hybridisation.

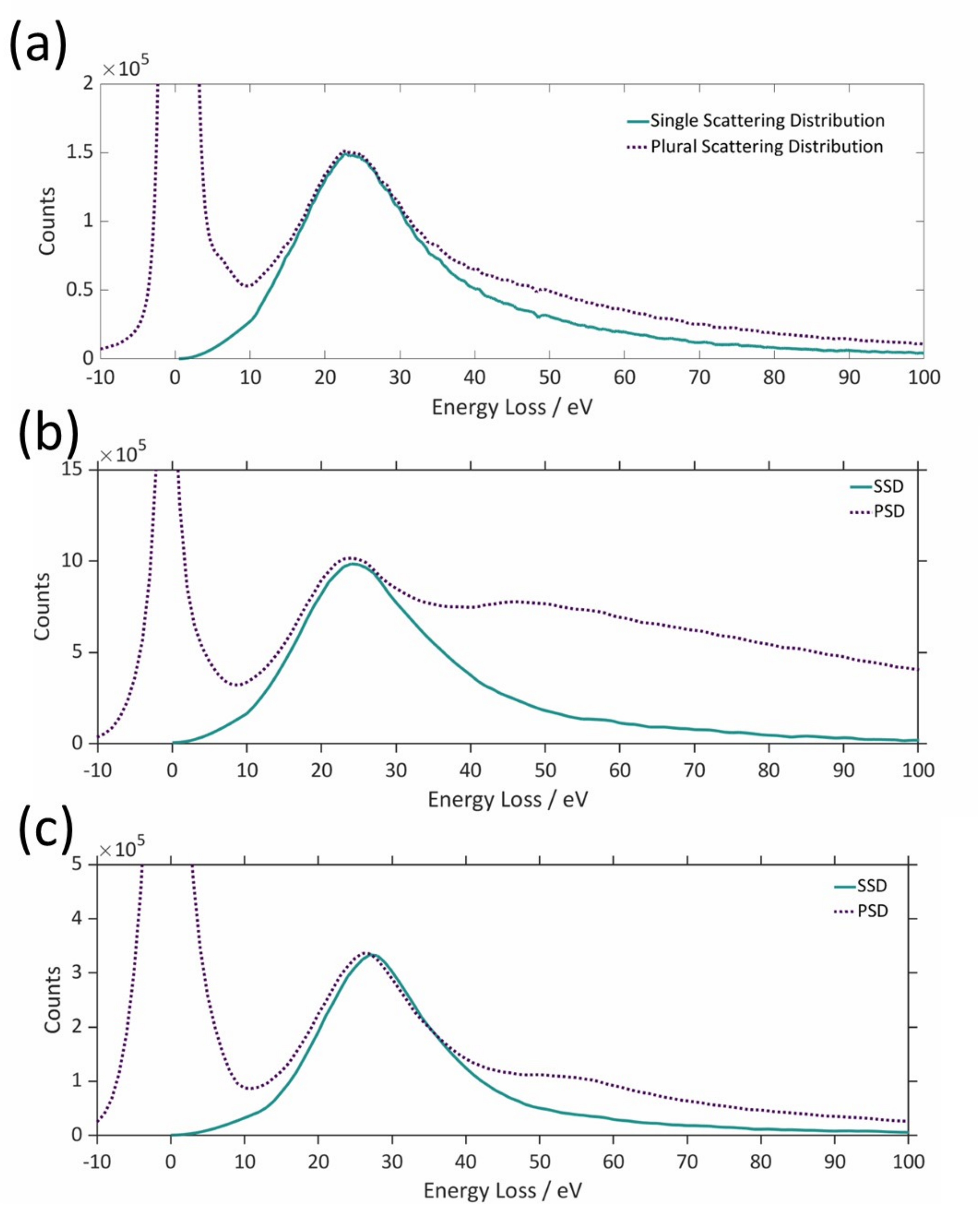

Figure 36: Low-loss EELS for: (a) COF, (b) COF/graphite, (c) COF/GNF. The ZLP has been truncated to allow better visualisation of the plasmon. The effect of deconvolution can be seen in the lower intesnity of the single-scattering distributions compared to the plural scattering distributions, and it can be seen that the plamon peak energy has not been affected.

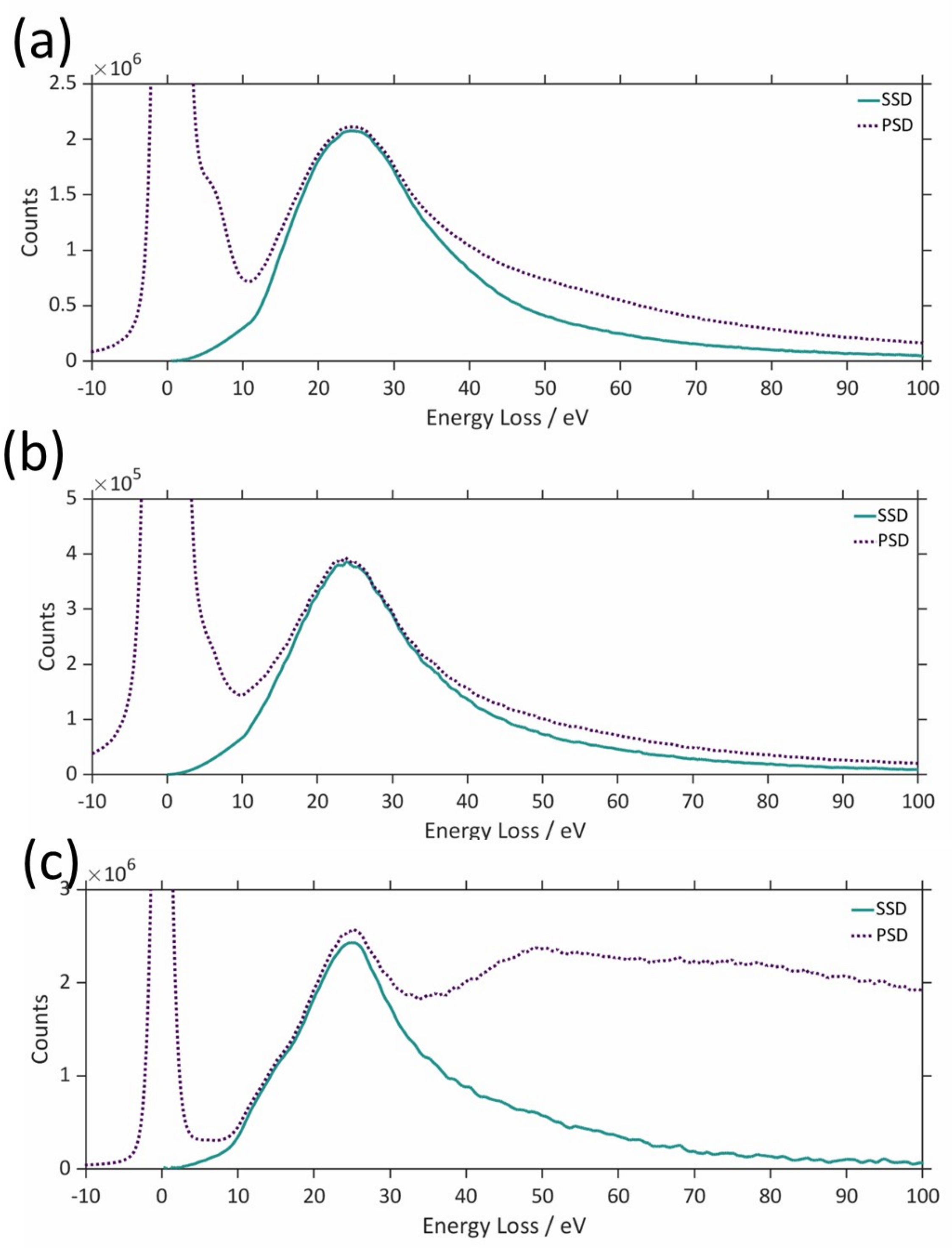

Figure 37: Low-loss EELS for: (a) COF/MWNT, (b) COF/SWNT, and (c) COF/silica. The ZLP has been truncated to allow better visualisation of the plasmon. The effect of deconvolution can be seen in the lower intesnity of the single-scattering distributions compared to the plural scattering distributions, and it can be seen that the plamon peak energy has not been affected.

The plasmon may also contain fine structure in the form of sharp peaks superimposed onto the smooth plasmon profile. For example, bonding-antibonding orbital transitions or interband transitions can be observed in organics and semiconductors.[43] Building a library of relevant EELS spectra would allow identification of new COFs by comparison of the low-loss spectrum, and give a tool for fast confirmation that a synthesis has yielded the target product.

The script for Fourier-log deconvolution identifies the ZLP as the first maximum of the y-axis data in the input file, then assumes that the ZLP is a symmetric Gaussian. It can be seen in some of the low-loss spectra (Figure 36a and Figure37a, b) that there is a small shoulder present on the right-hand side of the ZLP in the PSD. This is likely the $\pi - \pi^*$ transition that is commonly found in EEL spectra of aromatic systems, which would be expected in the π electron rich COF. As it is not present in the SSD, this implies that the deconvolution has removed it. Therefore, while deconvolution is necessary it precludes analysis of the region of the spectrum previously occupied by the ZLP. To investigate this region an EEL spectrum with a smaller energy resolution would be required, and deconvolution cannot be substituted for improved energy resolution.

Further, the current energy resolution prevents effective band-gap measurement. Fourier-log deconvolution allowed band-gap measurement directly from the low-loss spectrum.[42,44] The energy resolution of the EEL spectrum is the full-width half maximum of the ZLP,[42] which was around 2.5 eV, representing the typical energy resolution on the instruments available. Energy resolution is limited by a number of factors, including user alignment of the ZLP, choice of spectrum binning, and TEM aperture selection. The measured band gaps were typically 1-2 eV, judged by taking the derivative of the SSD and seeing when it deviates from the noise (Table 12). This indicates a region of the spectrum into which the beam electrons cannot lose energy, i.e. a band gap. COF/graphite had no discernible band gap, due to the conducting graphite. However, the uncertainty in the width of the band gap often exceeded the magnitude of the band gap; the values of the band gap derived are therefore entirely unreliable. This is compounded by the Fourier-log deconvolution that is likely distorting the profile of the pre-plasmon region of the spectrum, further rendering band-gap measurement unreliable. These results reinforce the idea that effective low-loss EELS requires a spectrometer with greater energy resolution. Once high energy-resolution EELS is recorded, the next step could be to compare this to optical band gap data, which has better energy resolution but a smaller energy range and worse spatial resolution. For COF/nanotube hybrids, optical band gap measurements may not be available due to the strong interaction of the nanosupport with the whole UV-Vis spectrum.

The SSD was then treated with Kramer-Kronig (KraKro) analysis to find the sample thickness and optical information. The process and underlying mathematics of the KraKro relation has been explained thoroughly in the literature, and is beyond the scope of this thesis.[42,44–46] KraKro analysis was chosen over the log-ratio method as theoretically it is more accurate; however, KraKro analysis requires knowledge of the optical refractive index of the sample. As this is unknown for these materials, the assumption was made that the refractive index was 2 (using a collection semi-angle of 100 mrad). Many solids have refractive indicies between 2.5 (diamond) and 1.5 (quartz),[47] and the assumed refractive index for COF is in the centre of this range. Accurate measurement of the refractive index of solid COFs was not undertaken, but the true value for refractive index is likely to be within the above range. In contrast, using the log-ratio method would require estimating the mean free path of electrons through the sample using the free electron formula; in essence, neither approach is perfect and thickness measurements are sensitive to the exact values used. It is also worth noting that the inaccuracy in refractive index and electron mean free path only affects the absolute thickness values calculated - relative sample thickness is given by the ratio of the ZLP integral to the plasmon integral and is reliable. The above assumptions may cast light on the limited use of EELS in the COF community; without accurate scattering cross-sections for inelastic processes in COFs, the utility of the low-loss spectrum is limited. The KraKro software used also assumes the sample has a smooth, unoxidised surface perpendicular to the electron beam. EELS sample thickness calculations tend to underestimate the sample thickness, especially if the region the spectrum is acquired from is not of uniform thickness.

KraKro absolute thickness measurements can be checked by observing the corresponding direct-space TEM image of the area from which the EELS measurement has been taken. In the case of uniform materials such as nanotubes, or crystal shapes such as needles, the thickness of the sample in the direction of the e-beam can be estimated by assuming the sample is as thick as it is wide. This gives an estimate of thickness to which the KraKro thickness should be similar. Taking GNF as an example, the corresponding BF-TEM shows that the GNF is 155 nm in diameter; while significantly larger than the KraKro thickness of 23 nm, the EEL spectrum was taken at the edge of the GNF. This means that the e-beam did not pass through the full thickness of the GNF, making the KraKro thickness estimation more reasonable. In addition much of the thickness of the GNF is the empty space of the internal cavity, with the side walls being 34 nm thick. The KraKro thickness thus correlates well with the e-beam passing though one of the side walls. Similar measurements can be made for other nanotubes. In the case of anisotropic thickness, such as for the foamy COFs in this thesis or crystal shapes such as plates, a TEM tilt-series or supplementary SEM imaging can be used to estimate the sample thickness in the beam direction. For example, BF-TEM imaging of COF showed that it tends to form crystals that were 10 - 59 nm wide; the KraKro thickness of 23 nm falls within the range and is therefore a reasonable value. If the thickness of a material was known to a high precision, performing KraKro over a range of values for refractive index would theoretically allow determination of the true refractive index by seeing when the calculated thickness matches the measured thickness. Overall, this is a powerful approach that helps extract 3D information from TEM and helps to establish the true shape of samples. This is expect to be most useful in situations where tilting of the TEM sample is limited and imaging cannot be used to confirm thickness of the sample.

KraKro analysis can also be used to estimate the dielectric function of a material.[46] The utility of this lies in the extraction of a complex refractive index, $n_c = n + i\kappa$, where κ is the energy-loss function and n is the refractive index. The energy-loss function is also known as the extinction coefficient, which is distinct from the molar extinct coefficient ϵ seen in the Beer-Lambert law. These can be used to compute a range of optical values for a material over a wide energy range, nominally infrared to X-ray but practically starting at the UV-Vis region.[42,44] For example, calculating the energy-loss function from a low-loss spectrum would allow the radiation penetration depth to be computed over a wide range of photon wavelengths; or the reflectance can be computed and a Tauc plot derived.[48] In practice this was limited by the low sampling frequency of the software (roughly every 5 eV), which was based on the eV/channel of the deconvoluted spectrum. It was possible to override this for finer sampling, but this may be oversampling the data due to the energy resolution of the spectrometer. Further, oversampling

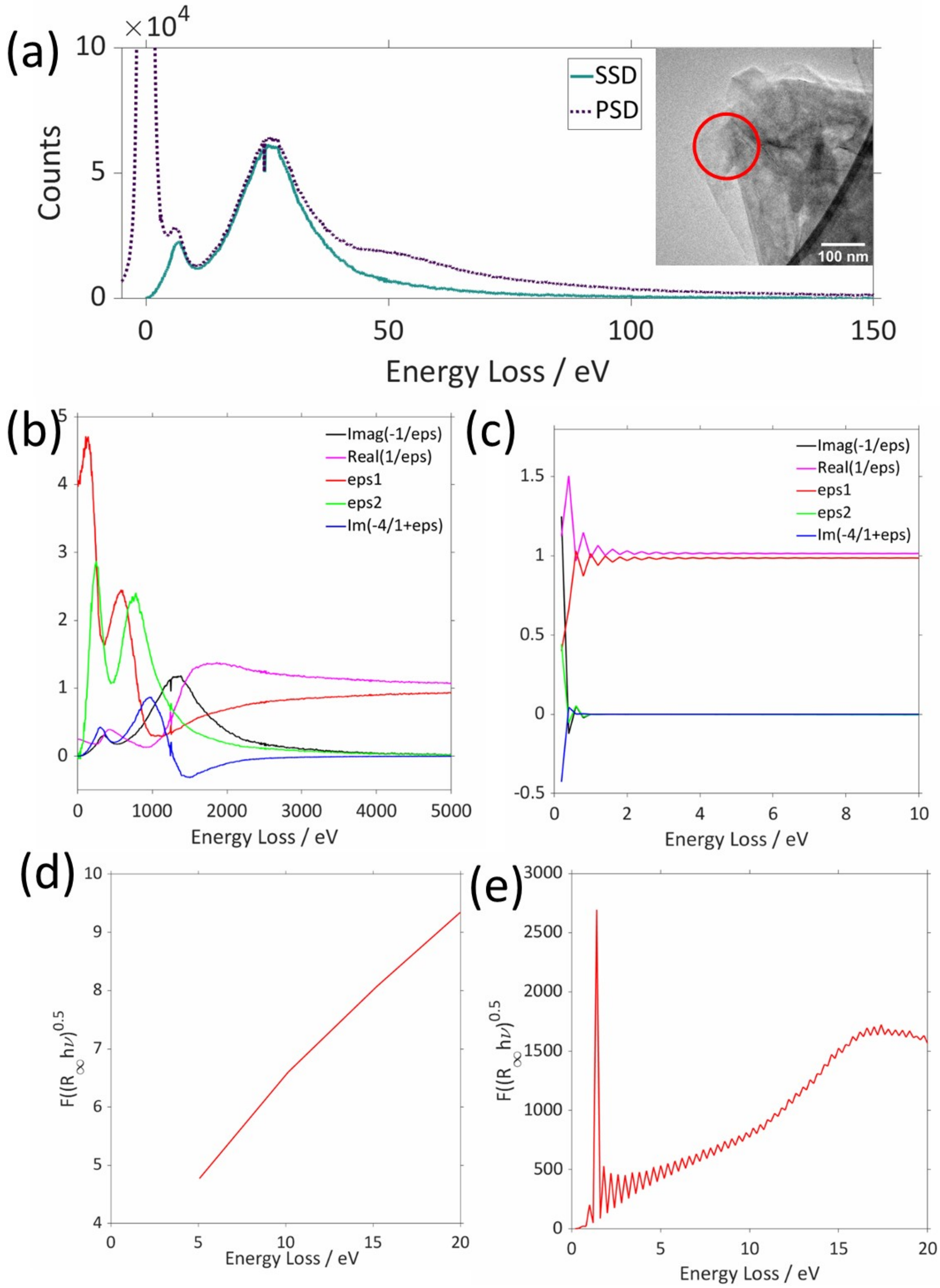

Figure 38: (a) Plural scattering distribution and Fourier-log deconvoluted single-scattering distribution. The feature on the plasmon peak is due to dead pixels on the EEL spectrometer. Insert: BF TEM image showing the approximate region the sample was recorded from highlighted in red. Note the varying thickness and vacuum contribution to the EEL spectrum. (b) Dielectric function and (c) oversampled dielectric function given by Kramers-Kronig analysis of the SSD. Oversampling used 0.2 eV between data points. (d) Tauc plot calculated using energy-loss function and (e) Tauc plot calculated using oversampled energy loss function. This demonstrates the difficulties caused by oversampling the EEL spectrum.

introduces a ripple into the data at low energy-loss values, seen in the KraKro analysis of graphite (Figure 38). This is also limited by the Fourier-log deconvolution changing the profile of the pre-plasmon region as discussed above, as this will affect the calculated energy-loss function. Kramers-Kronig analysis to yield optical data from EELS is likely very powerful in the right circumstances, but at present further work needs to be done to acquire higher energy resolution EELS from which a more useful KraKro analysis can be derived.

2.4.6 AC-STEM-EELS of COF/GNF

cHBC-BDA-COF/GNF was examined by aberration-corrected (AC) STEM-EELS. COF/GNF was selected as an initial test system which would allow investigation of both the COF on the outside of the GNF and of the nanosupport itself. The energy resolution of these spectra was 0.02 eV (20 meV), which is two powers of ten more precise than the TEM-EELS in the previous section. This allowed STEM-EELS mapping of a COF/GNF hybrid, which clearly shows that the boron is localised to the outside of the GNF (Figure 39a-c). This is consistent with the BF-TEM imaging earlier in this chapter. The corresponding EELS used to create the maps contains a boron K edge, and an sp^2 carbon K edge. The spectrum shows that the boron K edge is low intensity (less than 100 counts), which demonstrates why it was difficult to find conclusive evidence of a boron K edge by TEM-EELS with worse energy resolution in the previous section.

The low-loss spectrum was not able to furnish a band gap for the COF, due to the contribution of the conductive GNF effectively masking the presence of a COF band gap. Vibrational EELS (VEELS) data was obtained from the low-loss region, and comparing a region of COF with a region of GNF shows a clear difference in the vibrational spectrum (Figure 39e-f). The VEELS spectrum of COF has a weak band corresponding to an aromatic C-H stretch at 344 meV (2860 cm^{-1}) due to the organic monomers making up the COF, which is much weaker in the VEELS of GNF. The VEELS of GNF contains a sharp peak at 80 meV (655 cm^{-1}) which is the C-C stretch. Both spectra contain a peak at 168 meV (1398 cm^{-1}) which is caused by the radial breathing motion (RBM) of the GNF; this could also have contributions from the COF B-O vibration at 1393 cm^{-1}. These stretches are consistent with the IR spectra present earlier in the chapter, but with nanoscale spatial resolution.

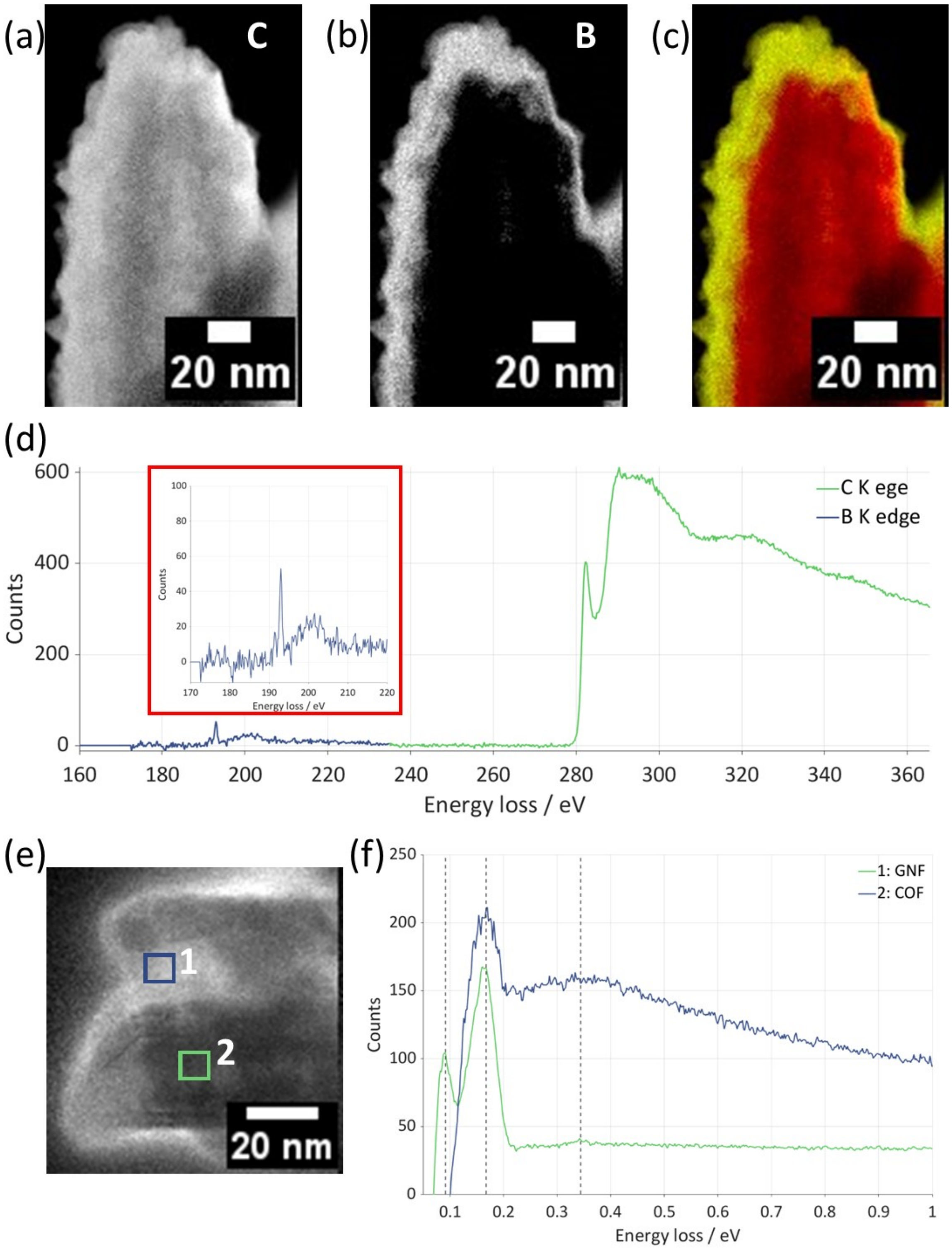

Figure 39: STEM-EELS mapping of (a) carbon, (b) boron, and (c) colourised map showing that boron is localised to the outside of the hybrid. (d) Corresponding edges used for mapping. Insert: magnified boron K edge. (e) STEM image showing regions of COF (1) and GNF (2) that were used for vibrational EELS. (f) Corresponding low-loss spectra. The spectrum of GNF contains vibrations at 80 meV and 168 meV, corresponding to a C-C stretch and the GNF radial breathing motion (RBM). The spectrum of COF has an attenuated RBM and the appearance of a broad C-H stretch at 344 meV indicating the presence of more organic material, i.e. COF.

Overall AC-STEM-EELS allowed precise determination of the physical location of the COF in the COF/GNF hybrid, as well as allowing the observation of a boron K edge that had previously been elusive by TEM-EELS. The VEEL spectrum also corroborates previous IR investigations of COF/GNF, and the spectrum changes depending on which region of the sample it is taken from.

2.4.7 Energy Dispersive X-ray Spectroscopy

Energy dispersive X-ray spectroscopy (EDX) spectra were simulated for an ideal cHBC-COF over vacuum (Appendix Figure 111a). This gave the somewhat trivial result of a carbon Kα peak and an oxygen Kα peak, but critically the boron Kα peak overlaps substantially with the carbon Kα peak and is much lower intensity. It was therefore expected that the boron peak will be difficult to detect in experimental EDX, which was borne out across all samples.

The main role of EDX here is qualitative determination of sample purity. Quantitative information is available from EDX, but requires knowing sample thickness and density in order to relate EDX peaks to elemental abundances. Further, carbon, oxygen and boron presence can be confirmed directly by IR, EELS, or mass spectrometry. EDX can detect the presence of other elements in the sample (Figure 40 - 41). Several elements appear in all EDX spectra: copper, iron, chromium, and gold are all part of the TEM and come from spurious X-rays. Several elements appear often in spectra: chlorine, calcium, silicon, aluminium, molybdenum, and sodium can be rationalised as common lab containments from glassware/sample handling, or contamination of the microscope column, and are safely ignored as long as they do not have large intensity in the spectrum (note: molybdenum would not be a contaminant in a typical lab, but is used extensively in the sample preparation lab and TEMs this work was carried out in and appears to have gotten into some odd places). Carbon and oxygen arise from the both sample and the support film on the TEM grid. Nickel is used for synthesis of carbon nanotubes and is difficult to remove entirely from the spectrum. The last element seen in the spectra is bromine, which is likely present in low concentrations as a salt arising from the deprotection of the COF monomers using boron tribromide. Overall EDX spectroscopy served to confirm that there were no unexpected elements in the material being examined, with all impurities rationalised.

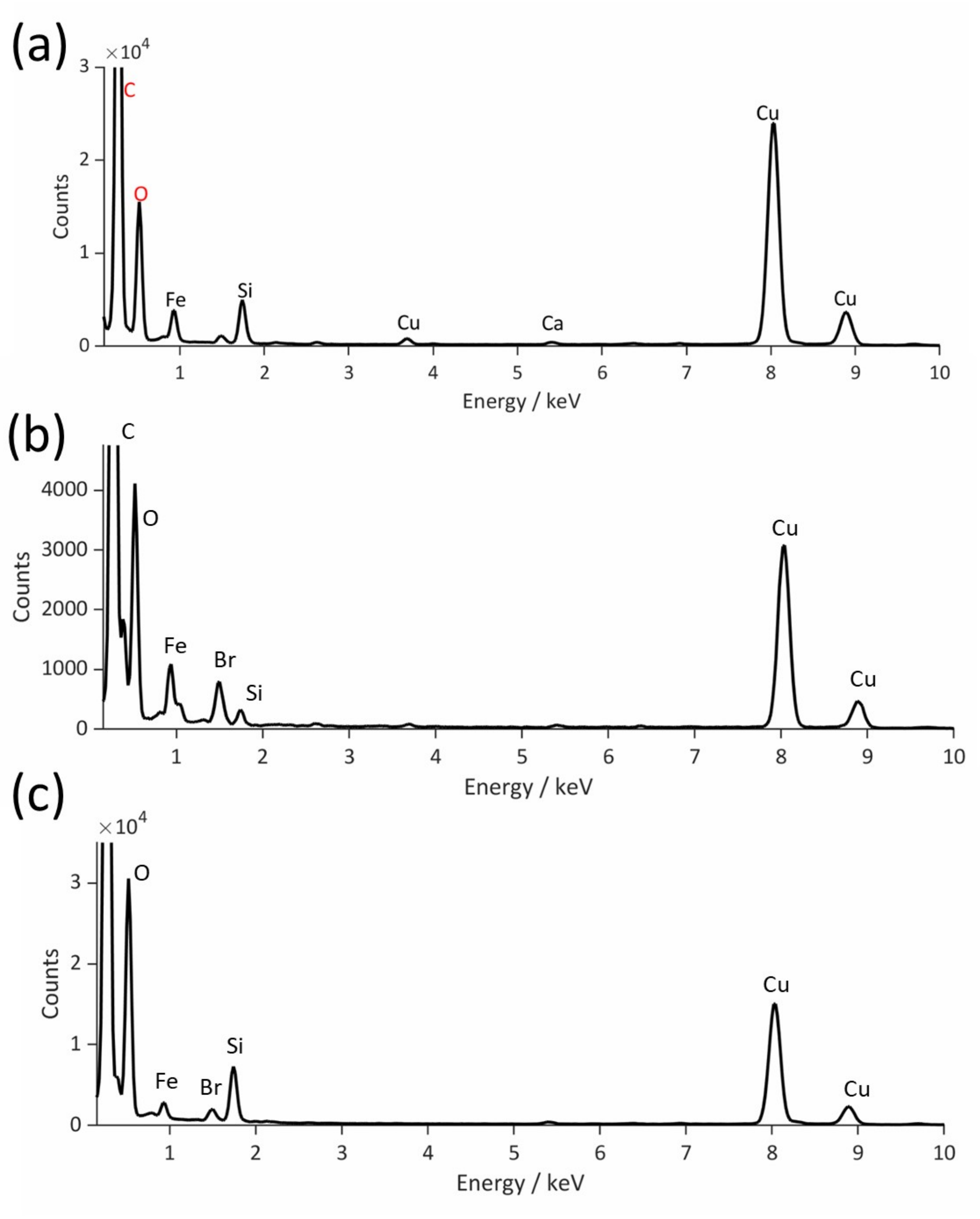

Figure 40: EDX spectra of (a) COF, (b) COF/graphite, and (d) COF/GNF. The spectra contains signals from both COF (carbon, oxygen) and common contaminents (iron, bromine, silicon, copper). No boron peak was seen, as this forms a small shoulder on the carbon peak that is often obscured.

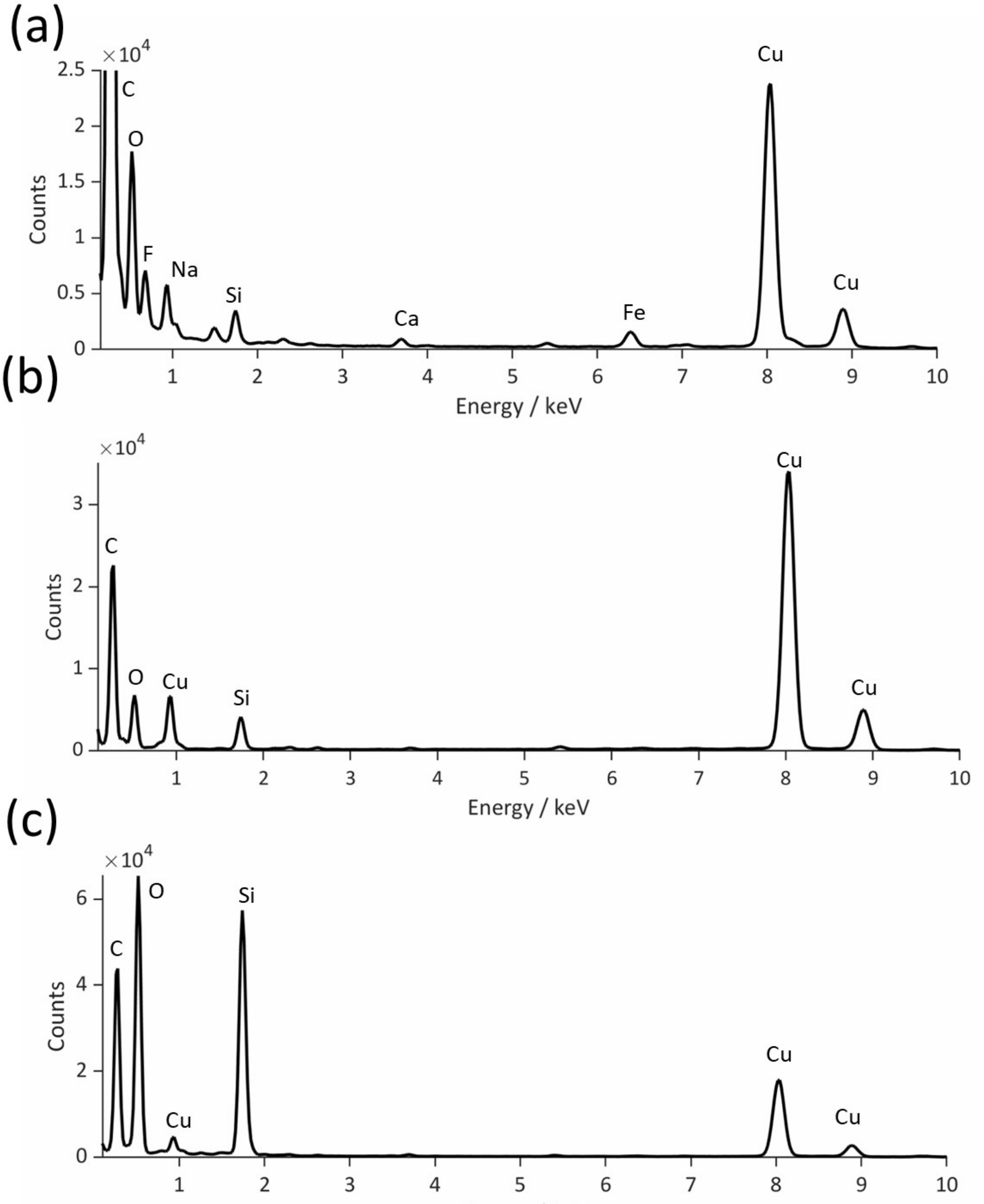

Figure 41: EDX spectra of (a) COF/MWNT, (b) COF/SWNT, and (d) COF/silica. The spectra contains signals from both COF (carbon, oxygen) and common contaminents (iron, bromine, silicon, copper, fluorine, sodium, calcium). For COF/silica, the high counts for the silicon peak are indicitive of the presence of silica nano particles. No boron peak was seen, as this forms a small shoulder on the carbon peak that is often obscured.

2.5 Summary

This chapter has developed a synthesis of a novel COF, cHBC-BDA-COF, as a nanocrystalline powder and as hybrid with nanosupports. Use of low concentration, nitrile solvents, and modulator were effective in providing conditions under which reversible reactions and error-checking could yield crystalline COF. Synthesis was investigated using infrared spectroscopy (IR) to confirm that polymerisation had occured. MALDI-TOF mass spectrometry found evidence of COF polymerisation via the presence of ions that could be rationalised as fragments of the 2D COF lattice, and it was suggested that MALDI could be used to discover the ratio of monomers in an unknown structure. Thermogravimetric analysis (TGA) was used to investigate the thermal stability of cHBC-BDA-COF, where it was found that the presence of nanosupports affected the combustion temperature of the COF, and a method of calculating how much COF was present in a TGA sample was derived. Scanning electron microscopy (SEM) was used to illustrate the sample morphology.

Powder X-ray diffraction was not able to resolve any Bragg reflections for the materials made. Bright-field TEM (BF-TEM) imaging was able to reveal that samples in many cases contained nanocrystals that were invisible to PXRD. This showed that TEM is a powerful way to reveal information about a sample that can be hidden if only bulk-scale techniques are applied. Qualitatively, BF-TEM showed that bulk-scale COF forms as a microscale foamy structure with thin electron-transparent edges. In COF/nanosupport the COF forms both as a layer on the nanosupport and as bulk COF not attached to nanosupports. This implies there is no strong driving force for COF to form selectively on the nanosupport surface. Tilt-series were used to show that the COF forms as an uneven layer on the surface of the nanosupport. Larger nanosupport surface areas correlate with thinner COF layers forming, and therefore formation of smaller COF crystals. In the case of thicker supports such as graphite, GNFs, and silica nanoparticles, the combined thickness of the COF/nanosupport hybrid was often too thick to resolve all of the COF lattice projections. In contrast, for COF/MWNT the thinner nanosupport allowed all of the material to be electron-beam transparent. COF/SWNT had such a large surface area that only very thin layers of amorphous COF formed on the SWNTs, all of which was electron-beam transparent.

BF-TEM images were then used to investigate the COF lattice projections. It was found that by distributing the lattice projection measurements that the results were bimodal, which was then used to test whether the AC and ZZ measurements occurred with equal frequency. It was found that for COF and COF/GNF AC and ZZ did not occur equally, which was rationalised as being due to the thickness of the material obscuring some lattice projections. COF/MWNT and COF/silica were found to have equally frequent AC and ZZ projections. Electron crystallography was unable to detect any specular diffraction, despite the presence of lattice projections in BF-TEM images. Tilt-series were used to show that COF lattice projections change as a function of orientation relative to the electron beam.

A detailed electron energy loss spectroscopy (EELS) analysis was undertaken to establish the plasmon profile of cHBC-BDA-COF and COF/nanosupport hybrids and both EELS and energy-dispersive X-ray (EDX) spectroscopy were used to provide elemental analysis. Calculated sample thickness from EELS data was shown to rationalise well with observed sample thickness in BF-TEM, giving information on the 3D shape of samples. Limited energy resolution and practicalities of spectrum deconvolution made band-gap measurement unreliable. TEM-EELS was unable to establish the presence of boron due to the limits of the available equipment, but repeating these measurements with a more advanced detector or by limiting the spectrum to the characteristic scattering angle of the boron K edge would likely lead to facile edge detection. STEM-EELS mapping and vibrational EELS (VEELS) were applied to COF/GNF, which confirmed that in the hybrid materials the COF forms a layer on the outside of the nanosupport.

Overall, this chapter has examined the structure of a novel COF using BF-TEM methodology. This approach was able to show that the sample consisted of nanocrystallites and link the TEM projections to the orientation of the COF relative to the optical axis. Bulk-scale methods detected some difference between samples, but TEM was required to understand their fundamental morphology. This work serves to demonstrate the TEM analysis of COFs is a valuable tool for interrogating their structure and properties.

2.6 Future Work

- Further optimisation of the synthesis conditions of cHBC-BDA-COF should be undertaken to facilitate it’s synthesis as single-crystals from which the crystal structure can be solved.

- cHBC-BDA-COF should be synthesised on a larger scale to allow application of more bulk characterisation methods.
- Other thermal measurement techniques such as differential scanning calorimetry should undertaken to see if these materials have useful thermal properties.
- Automated TEM lattice projection detection should be developed to enhance repeatability and allow faster data processing throughput.
- EELS with greater energy resolution should be undertaken to allow more precise band-gap determination, and to establish if the sample morphology affects the measured band-gap.

2.7 Experimental

General

Synthesis was carried out using standard laboratory practice with Pyrex glassware with reagents bought from Merck, Alfa-Aesar, Fischer Scientific or Acros Organics and used without further purification unless explicitly stated. All experimental work was done by the author unless otherwise indicated.

All ^{1}H and ^{13}C NMR spectroscopy was performed on a Bruker Ascend 400HD by B. Weare or Analytical Services. IR spectra were recorded on solids using a Bruker Alpha FTIR Spectrometer using a Bruker Platinum ATR attachment over the range 4000-400 cm^{-1}, or as a potassium bromide pellet with less than 1 mg of sample and 150 mg of potassium bromide.

Thermogravimetric analysis (TGA) was performed by the author or W. Cull with a TA Q500 Thermogravimetric Analyser. Measurements were performed using platinum pans and were run in air. The parameters for all experiments were ramp 10 °C from 20-1000 °C, then isothermal for 10 mins at 1000 °C. Air flow was 60 mL min^{-1}.

MALDI-ToF MS measurements were recorded using a Bruker ultraFlexIII (Bruker Daltonik, Bremen, Germany) by the author or Analytical Services (B. Pointer Gleadhill, T. Liu). Samples were dispersed in acetone or chloroform without a matrix unless otherwise indicated then drop-cast on a stainless steel target plate (type MTP384; Bruker Daltonik, Bremen, Germany). The sample was ionised using a pulsed solid-state UV laser (355 nm, 500 μJ, 66.7 Hz). The instrument was operated in linear mode. Data was acquired using the on-board flexControl software (v3, B185;Bruker Daltonik, Bremen, Germany) and processed using Bruker's flexAnalysis software (v3, B96;Bruker Daltonik, Bremen, Germany).

Powder X-ray diffraction measurements were made by the author, R. Lodge, or W. Cull with a PANalytical Xpert Pro using Cu(Kα_1) radiation (λ=1.5432 Å) from $2^\circ - 40^\circ$ 2θ on a zero-background silicon holder in Bragg-Brentano geometry. Powder patterns were simulated using VESTA (v. 3.4.8).[49]

Dynamic light scattering (DLS) measurements were performed by B. Flynn using a Zetasizer Nano ZS in water (pH 7) at room temperature. Solid silica nanoparticles were dispersed via sonication to give a concentration of 0.1 mg mL^{-1} that was used without further preparation.

Transmission electron microscopy (TEM) was performed using either a JEOL 2100F transmission electron microscope with an accelerating voltage of 200 kV or a JEOL 2100PLUS transmission electron microscope with an accelerating voltage of 80 kV or 200 kV, located at the University of Nottingham Nanoscale and Microscale Research Centre (nmRC). COF and COF/nanosupport samples were prepared via bringing a copper TEM grid coated with "lacey" carbon film (Agar Scientific UK) into contact with the dry powdered sample and gently agitating the sample against the grid for 1 minute, or by dispersing the dry sample in HPLC grade IPA and drop-casting on the TEM grid. Analysis was performed using Gatan Microscopy Suite 3 and ImageJ FIJI software.[50,51] Fourier-transforms of real-valued images are presented as the magnitude of the original complex-valued Fourier-transform. Energy-dispersive X-ray spectroscopy (EDX), electron energy loss spectroscopy (EELS) and selected-area electron diffraction (SAED) measurements were taken using the JEOL 2100PLUS transmission electron microscope. EELS background fitting was performed using the literature software.[52] EELS Fourier-log convolution and Kramers-Kronig analysis was performed using literature software.[42] EDX simulation was performed using NIST-DTSA-II Power Tools for Microanalysis "simulation alien", using the Monte Carlo model of a bulk homogeneous material. Simulations were performed using 200 kV accelerating voltage, 60 nAs probe dose, and 0 ° incident angle.[53]

Aberration-corrected scanning transmission electron microscopy (AC-STEM) imaging and EELS was performed by Q. Ramasse on a Nion UltraSTEM 100MC 'Hermes' with an accelerating voltage of 60 kV, located at SuperSTEM. EELS maps were made using Gatan Microscopy Suite 3.

Scanning electron microscopy (SEM) and scanning transmission electron microscopy (STEM) were aquired by the author or C. Parmenter using a Zeiss Crossbeam 550 FIB-SEM at an accelerating voltage of 30 kV at a working distance of 4.0 mm on a lacy carbon coated TEM grid. Supplementary SEM was acquired by C. Housley or Additional SEM images were taken using a JEOL 7100F field emission gun scanning electron microscope by C. Housley at 1 kV at 5.0 mm working distance on a 10 mm aluminium stub with an adhesive carbon tab. Analysis was performed using SmartTiff (v03.00.03) and ImageJ FIJI software.[50,51]

Electronic Structure Calculations

Electronic structure calculations was performed by Karol Strutyński and Manuel Melle-Franco at the University of Aviero.[1] Tight Binding (TB) calculations were used to explore different conformations and to preoptimise COF as well as to study in detail COF/graphene interfaces. The Matsci parameter set with attractive dispersion corrections from the OPLSAA force-field as implemented on the DFTB+ software was used.[54,55] The COF periodic structure was computed with DFT with the Fritz Haber Institute ab initio molecular simulations (FHI-aims) package with "light" numeric atomic orbitals, which approximately correspond to TZVP Gaussian type orbitals.[56–58] The PBE functional augmented with Many Body Dispersion (MBD) was used for geometry optimisation and energies.[59,60] 3D images of the modelled structures were prepared using CrystalMaker (ver 2.07).

Statistical Analysis

The sample standard deviation σ was calculated using the usual equation:

$$\sigma(x) = \sqrt{\frac{\Sigma(x-\mu)^2}{N-1}} \tag{10}$$

where μ is the mean and N is the number of measurements.[39,61] The bimodal separation index S was calculated via:

$$S = \frac{\mu_1 - \mu_2}{2(\sigma_1 + \sigma_2)} \tag{11}$$

where μ is the mean and σ is the standard deviation.[62]

Binomial tests were completed using the MATLAB binopdf function, which calculates a binomial probability density function using number of trials and probability of success.[63] This is computed using the following function:

$$y = \begin{pmatrix} n \\ x \end{pmatrix} p^x q^{n-z} I_{(0,1,\ldots,n)}(x) \tag{12}$$

where p is the probability of success in a trial, $q = 1-p$, and y is the probability of observing

x successes in n trials. The indicator value I means x only adopted values $(0, 1, ...n)$. MATLAB calculates the confidence intervals from the function using the Clopper-Pearson method.[63]

Nanotube preparation

P2 SNWT and PD30 MWNTs were processed according to the methods developed by K. Fung.[64]

PR19 graphitised nanofibres were used without further purification. IR (KBr) νmax cm^{-1}: 3449br, 2959s, 2924s, 2852s, 2362w, 1633br, 1383s, 1190br, 1132w, 1052w, 1011w, 835w, 689w, 584w.

PD30 multi-walled carbon nanotubes were (10 mg, 0.83 mmol) were heated at 530 °C for 2 minutes, then cooled to room temperature and washed with nitric acid (1 M, 10 mL), washed with aqueous sodium hydroxide (1 M, 10 mL), then washed with deionised water (10 mL) to give a black powder and a pale yellow filtrate. The black powder product was dried under reduced pressure overnight then used without further purification (7.6 mg, 0.63 mmol, 76 %). IR (KBr) νmax cm^{-1}: 3544, 3472, 3414, 2957, 2920, 2850, 2353, 1637, 1617, 1385, 1260, 1099, 802.4, 623.9, 474.1.

P2 single-walled carbon nanotubes (50 mg, 4.2 mmol) were refluxed in nitric acid (3 M, 50 mL) for 2 hours. The nanotubes were filtered off and washed with deionised water (50 mL). The resulting black powder was dried under reduced pressure overnight, then used without further purification (45.6 mg, 3.8 mmol, 90 %). IR (KBr) νmax cm^{-1}: 3437br, 2920s, 2852s, 1629br, 1578vs, 1385vs, 1132br, 607br.

Graphite was treated according to the literature procedure.[65] Black graphite powder (85.5 mg, 7.1 mmol) was emulsified with 4:1 deionised water/hexane (30 mL) by vigorous shaking then poured into a mixture of glass beads (21 g, diameter = 2 mm) and deionised water (75 mL). The solution was decanted from the beads, then then beads were washed 5 times with hexane (30 mL). The resulting metallic silver coloured beads were washed with acetone (30 mL) which was then decanted from the beads. The grey solid graphite product collected via filtration and dried under reduced pressure overnight. The metallic grey product was used without further purification (19.6 mg, 1.6 mmol, 23 %). IR (KBr) νmax cm^{-1}: 2351, 1432, 1093, 870.1.

Stober process for Silica Nanoparticles

Silica nanoparticles were made according to the literature procedure.[38] To a stirred mixture of isopropanol (10 mL) and ammonium hydroxide (0.36 M, 0.23 mL) was added dropwise tetraethylorthosilicate (1 mL, 4.5 mmol). The mixture was stirred at room temperature under atmosphere for 5 hours. The solution became cloudy white within 15 minutes, exhibiting the Tyndall effect. The silica nanoparticles were collected via centrifugation and dried at room temperature under reduced pressure overnight to give the final product as an opalescent white powder (26.82 mg, %). The prepared silica nanoparticles were used without further purification. MS (MALDI-ToF) m/z 747 (12.8), 647 (20.3), 619 (34.5), 591 (18.5), 522 (12.8), 427 (20.7), 399 (22.1), 381 (65.5), 353 (43.7), 334 (60.1), 323 (M^+, 100), 306 (41.5), 295 (66.9). IR (ATR) ν_{max} / cm^{-1}: 1100 (SiOSi), 946(SiOH), 800 (SiOSi), 462 (SiOSi).

cHBC synthesis

cHBC was synthesised by A. Weilhard and N. Zyk at the University of Nottingham, and used without further purification.

Suzuki coupling:[66] 3,4-dimethoxyphenylboronic acid (0.803 g, 4.41 mmol) and sodium carbonate (1.325 g, 12.5 mmol) were stirred under inert atmosphere in 1:1 acetone/water until a homogeneous phase formed. The reaction mixture was cooled on ice then 1,3,5- tris(bromomethyl) benzene (0.5405 g, 1.51 mmol) and palladium chloride (0.0303 g, 0.17 mmol) were added. The mixture was stirred at room temperature for 1 hour, then stirred at 38 °C for 72 hours. After, the reaction mixture was cooled to room temperature and acetone was removed under reduced pressure. The aqueous layer was extracted with diethyl ether, dried over magnesium sulphate, filtered, and ethyl acetate was removed under reduced pressure. The crude white product was purified via column chromatography using 2:1 pet ether/ethyl acetate, to give a while crystalline product (360 mg, 0.68 mmol, 45 %). ^{1}H NMR (($CDCl_3$, 400 MHz) δ 6.85 (Ar-H, s, 1H), 6.77 (Ar-H, d, 1H), 6.67 (Ar-H, d, 1H), 3.85 (Ar-OMe, s, 3H), 3.78 (CH2, s, 2H).

Friedel-Crafts acylation/Scholl:[66] Benzaldeyhde (0.40 mL) and acetic anhydride (1 mL) were dissolved in dichloromethane (350 mL) under inert atmosphere. Iron(III) chloride (69 mg) in nitromethane (1 mL) was added at room temperature, then 1,3,5-tris(3,4-dimethoxybenzyl)benzene

(346.5 mg) in DCM (30 mL) was added slowly. The reaction mixture was stirred overnight, then iron (III) chloride (1.126 g) in nitromethane (8 mL) was slowly added. The reaction mixture was stirred for a further 12 hours. The reaction mixture was quenched with methanol (50 mL) then poured into water (300 mL). The organic layer was separated, dried over magnesium sulphate, filtered, and the DCM removed under reduced pressure. The crude product was purified via column chromatography in 10:1 DCM/ethyl acetate, to give a yellow powder product (630 mg, 1.2 mmol, 42 %). ^{1}H NMR (($CDCl_3$, 400 MHz) δ 6.85, 6.79-6.76, 6.70-6.67, 3.78.

Deprotection:[67] c-HBC (50.1 mg, 0.064 mmol) was stirred in dichloromethane (5 mL) on ice. Boron tribromide (0.48 mL, mmol) in dichloromethane (5 mL) was slowly added, then then reaction mixture was stirred overnight at room temperature. Methanol (30 mL) was added, then the solvent was removed from the reaction mixture under reduced pressure. The product (40.0 mg, 0.057 mmol, 89 %) was a dark green powder. ^{1}H NMR ((DMSO-d_6, 400 MHz) δ 9.19 (6H, s,), 8.58 (6H), 7.87(6H, s,). MS (MALDI-ToF) m/z 774 (0.7 %), 709 (1) 696 (M^+ 100), 680 (2), 678 (4), 667 (4), 655 (3), 645 (2), 638 (2). IR (ATR) ν_{max} / cm^{-1}: 3156br (OH).

Synthesis of cHBC-BDA-PBA-COF

Cata-Hexahydroxyhexabenzocoronene (4.7 mg, 6.75x10^{-3} mmol), benzene-para-diboronic acid (1.76 mg, 1.06x10^{-2} mmol, 98.5 mol%) and phenylboronic acid (1.9 mg, 1x10^{-3} mmol, 1.5 mol%) were combined with a mixture of acetonitrile/dioxane/mesitylene (8 mL/1.6 mL/0.4 mL). The solids were dispersed by sonicating for 15 mins, then the mixture was syringe filtered (PTFE, 2.5 μm) and degassed via 3 freeze-pump-thaw cycles. The green reaction mixture was heated at 90 °C overnight. The solid green product was collected via filtering under reduced pressure, then was washed with THF (10 mL), then acetone (10 ml) and then hexane (10 mL). The dry green product was stored under reduced pressure in the presence of a desiccant (1.9 mg, 1x10^{-3} mmol, 16.8 %). MS (MALDI-ToF) m/z 1487 (0.7 %), 1149 (7.1), 1121 (7.1), 864.1 (0.3), 853.9 (0.4), 850.1 (0.55), 826.1 (3.7) 810.3 (2.8), 798.1 (1.2), 782.1 (1.9), 775.9 (1.0), 733.9 (0.75), 722.0 (2.5), 712.0 (1.1), 710 (0.89), 696.0 (M^+, 100), 693.9 (3.0), 677.9 (5.1), 666.8 (6.4), 655.1(2.0), 648.9 (2.0), 637.9 (2.2). IR (ATR)ν_{max} / cm^{-1}: 3501br (OH), 1393w (CO_2B), 1334s (BC), 1235s (CO), 1079vs (BO), 660.7vs (BO), 599.2w (CO2B), 539.7w (OH).

COF/nanosupport hybrid synthesis

A typical synthesis is given below.

COF/GNF: GNFs (1.9 mg, 0.158 mmol) were dried at 400 °C for 1 hour. cHBC (9.8 mg,0.0147 mmol), benzene-para-diboronic acid (3.4 mg,0.0205 mmol, 83.4 mol%) and phenylboronic acid (0.5 mg, 0.0041 mmol, 16.6 mol%) were combined with a mixture of acetonitrile/dioxane/mesitylene (8 mL/1.6 mL/0.4 mL). The solids were dissolved by sonicating for 15 mins, then the mixture was syringe filtered (PTFE, 2.5 μm), mixed with GNF, then degassed via 3 freeze-pump-thaw cycles. The green reaction mixture was heated at 90 °C overnight. The solid green product was collected via filtering under reduced pressure, then was washed with THF (10 mL), then acetone (10 mL) and then hexane (10 mL). The dry black product was stored under reduced pressure in the presence of a desiccant (10.9 mg). IR (ATR)ν_{max} / cm^{-1}: 3347br (OH), 1393w (CO_2B), 1334s (BC), 1235s (CO), 1079vs (BO), 660.7vs (BO), 601.2w (CO_2B), 539.7w (OH). MS (MALDI-ToF) m/z 1180 (7.1 %), 1149 (9.5), 1132 (6.5), 1111 (7.0), 936.2 (5.5), 912.2 (5.3), 891.2 (5.7). 867.2 (5.6), 833.5 (5.7), 826.2 (2.0), 819.1 (5.9), 808.2 (13.1), 798.1 (7.8), 750.1 (7.8), 734.0 (10), 722.0 (18), 714.1 (11), 696 (M^+, 100), 678 (18), 667 (23), 649 (17), 637.9 (26), 624.9 (18), 603 (17), 591 (20), 578.9 (20), 565.9 (23), 554.98 (53), 543.9 (67) 541.9 (67), 530.9 (82), 517.9 (60), 506.8 (42), 493.8 (25), 480.8 (14), 467.8 (7.4).

COF/graphite: cHBC (4.4 mg, 0.0063 mmol), BDA (1.89 mg, 0.012 mmol), PBA (0.0227 mg, 0.23 νmol), graphite (2.2 mg, 0.183 mmol). Product was a black powder (4 mg, 0.002 mmol, 37 %). IR (ATR)ν_{max} / cm^{-1}: 3240, 1506, 1333, 1266, 1218, 1175, 1097, 868.0, 796.4, 763.4, 656.7. MS (MALDI-ToF) m/z 1663 (87 %), 1638 (87), 1613 (87), 1591 (87), 1564 (87), 1517 (88), 1492 (88), 1468 (88), 1444 (88), 1419 (88), 1396 (89), 1372 (89), 1348 (89), 1324 (89), 1300 (89), 1275 (89), 1252 (90), 1228 (90), 1204 (90), 1180 (90), 1155 (90), 1132 (90), 1107 (91), 1083 (91), 1059 (90), 1036 (90), 1011 (92), 987.2 (92), 936.1 (92), 939.1 (92), 915.1 (92), 891.1 (94), 867.0 (92), 843.0 (95), 819.0 (94), 795.0 (93), 771.0 (94), 746.9 (90), 720.0 (100), 698.9 (M^+, 93), 671.8 (93), 650.8 (92), 627.0 (91), 599.7 (94), 578.8 (91), 554.8 (90), 527.7 (91), 466.8 (94).

COF/MWNT: cHBC (8.0 mg, 0.011 mmol), BDA (3.3 mg, 0.027 mmol), PD30 MWNT (1.7 mg, 0.142 mmol). Product was a black powder (9.5 mg, 0.005 mmol, 47 %). IR (ATR)ν_{max}

/ cm^{-1}: 3478, 2963, 2920, 2850, 2355, 1633, 1385, 1260, 1128, 574. MS (MALDI-ToF) m/z 1600 (2.3 %), 1148 (10), 920 (3.5), 894 (3.9), 861 (5.0), 833 (6.2), 826 (7.4), 808 (14), 782 (8.9), 722 (9.2), 714 (9.3), 696 (M^+, 100), 678 (12), 667 (12), 649 (12), 638 (13), 603 (9.7), 579 (12), 566 (13), 555 (31), 544 (32), 531 (30) 518 (19), 507 (12), 493 (5.9), 481 (3.0).

COF/SWNT: cHBC (10.6 mg, 0.015 mmol), BDA (3.52 mg, 0.034 mmol), PBA (0.075 mg, 0.002 mmol), SWNT (1.9 mg, 0.158 mmol). Product was a black powder (7.5, 0.004 mg, 29 %). IR (ATR)ν_{max} / cm^{-1}: 3499br (OH), 1390w (CO_2B), 1338s (BC), 1230s (CO), 1082vs (BO), 662.0vs (BO), 600.4w (CO2B), 539.7w (OH). MS (MALDI-ToF) m/z 1486 (14 %), 1148 (18), 1120 (17), 882.2 (14), 864.1 (14), 851.1 (14), 835.1 (14), 826.1 (17), 808.1 (17), 798.1 (17), 782.1 (16), 768.1 (14), 748.1 (14), 734.0 (15), 722.1 (20), 710.1 (15), 696.1 (M^+, 93), 678.1 (18), 667.1 (18), 655.2 (15), 649.1 (16), 638.1 (15), 603.1 (14), 591.1 (14), 555.0 (14), 544.0 (14).

COF/SiONPs: cHBC (10.3 mg, 0.015 mmol), BDA (3.53 mg, 0.021 mmol), PBA (0.147 mg, 1.2 νmol), silica (2.0 mg, 0.03 mmol). Product was a light green powder (2.4 mg, 0.001 mmol, 9.7 %). IR (ATR)ν_{max} / cm^{-1}: 3320, 1465, 1348, 1079, 933.7, 798.3, 765.4, 660.7, 547.9, 455.6. MS (MALDI-ToF) m/z 1600 (0.18 %), 1573 (0.18), 1486 (0.34), 1400 (0.34), 1400 (0.18), 1278 (0.35), 1250 (0.36), 1174 (0.22), 1148 (9.7), 1134 (0.22), 1120 (7.1), 956.2 (0.65), 940.4 (0.40), 922.4 (0.46), 882.2 (0.37), 861.1 (0.50), 850.1 (0.87), 836.3 (0.50), 826.1 (12), 810.4 (6.5), 798.1 (1.7), 782.1 (2.3), 762.1 (0.49), 750.1 (0.47), 734.0 (0.47), 722.1 (6.8), 710.1 (1.1), 696.1 (M^+, 100), 678.1 (3.5), 667.1 (3.5), 655.3 (1.1), 649.1 (1.3), 638.1 (1.4), 625.1 (0.51), 621.2 (0.47).

References

(1) B. L. Weare, R. W. Lodge, N. Zyk, A. Weilhard, C. L. Housley, K. Strutyński, M. Melle-Franco, A. Mateo-Alonso and A. N. Khlobystov, *Nanoscale*, 2021, **13**, 6834–6845.

(2) M. Martínez-Abadía, K. Strutyński, C. T. Stoppiello, B. Lerma Berlanga, C. Martí-Gastaldo, A. N. Khlobystov, A. Saeki, M. Melle-Franco and A. Mateo-Alonso, *Nanoscale*, 2021, **13**, 6829–6833.

(3) M. Martínez-Abadía, C. T. Stoppiello, K. Strutynski, B. Lerma-Berlanga, C. Martí-Gastaldo, A. Saeki, M. Melle-Franco, A. N. Khlobystov and A. Mateo-Alonso, *Journal of the American Chemical Society*, 2019, **141**, 14403–14410.

(4) M. Martínez-Abadía, K. Strutyński, B. Lerma-Berlanga, C. T. Stoppiello, A. N. Khlobystov, C. Martí-Gastaldo, A. Saeki, M. Melle-Franco and A. Mateo-Alonso, *Angewandte Chemie International Edition*, 2021, **60**, 9941–9946.

(5) G. Xing, W. Zheng, L. Gao, T. Zhang, X. Wu, S. Fu, X. Song, Z. Zhao, S. Osella, M. Martínez-Abadía, H. I. Wang, J. Cai, A. Mateo-Alonso and L. Chen, *Journal of the American Chemical Society*, 2022, **144**, 5042–5050.

(6) Q. Zhang, H. Peng, G. Zhang, Q. Lu, J. Chang, Y. Dong, X. Shi and J. Wei, *Journal of the American Chemical Society*, 2014, **136**, 5057–5064.

(7) H. S. Sasmal, A. K. Mahato, P. Majumder and R. Banerjee, *Journal of the American Chemical Society*, 2022, **144**, 17.

(8) H. Liu and G. Cao, *Scientific Reports*, 2016, **6**, 23936.

(9) D. Mattia and Y. Gogotsi, *Microfluidics and Nanofluidics*, 2008, **5**, 289–305.

(10) B. W. Smith, M. Monthioux and D. E. Luzzi, *Nature*, 1998, **396**, 323–324.

(11) B. W. Smith, M. Monthioux and D. E. Luzzi, *Chemical Physics Letters*, 1999, **315**, 31–36.

(12) B. J. Smith, L. R. Parent, A. C. Overholts, P. A. Beaucage, R. P. Bisbey, A. D. Chavez, N. Hwang, C. Park, A. M. Evans, N. C. Gianneschi and W. R. Dichtel, *ACS Central Science*, 2017, **3**, 58–65.

(13) Z. Li, Z.-W. Liu, Z. Li, T.-X. Wang, F. Zhao, X. Ding, W. Feng and B.-H. Han, *Advanced Functional Materials*, 2020, **30**, 1909267.

(14) S. Wang, Z. Zhang, H. Zhang, A. G. Rajan, N. Xu, Y. Yang, Y. Zeng, P. Liu, X. Zhang, Q. Mao, Y. He, J. Zhao, B.-G. Li, M. S. Strano and W.-J. Wang, *Matter*, 2019, **1**, 1592–1605.

(15) R. L. Li, N. C. Flanders, A. M. Evans, W. Ji, I. Castano, L. X. Chen, N. C. Gianneschi and W. R. Dichtel, *Chemical Science*, 2019, **10**, 3796–3801.

(16) H. Guo, N. Song, D. Wang, J. Ma and Q. Jia, *Talanta*, 2019, **198**, 277–283.

(17) M. Calik, T. Sick, M. Dogru, M. Döblinger, S. Datz, H. Budde, A. Hartschuh, F. Auras and T. Bein, *Journal of the American Chemical Society*, 2016, **138**, 1234–1239.

(18) S. D. Brucks, D. N. Bunck and W. R. Dichtel, *Polymer*, 2014, **55**, 330–334.

(19) M. K. Smith and B. H. Northrop, *Chemistry of Materials*, 2014, **26**, 3781–3795.

(20) J. Wang, Y. Chen and W. J. Blau, *Journal of Materials Chemistry*, 2009, **19**, 7425.

(21) B. C. Smith, *Fundamentals of Fourier Transform Infrared Spectroscopy*, CRC Press, 1st edn., 2011.

(22) E. L. Spitler, M. R. Giovino, S. L. White and W. R. Dichtel, *Chemical Science*, 2011, **2**, 1588–1593.

(23) C. Pan, S. Xu, L. Hu, X. Su, J. Ou, H. Zou, Z. Guo, Y. Zhang and B. Guo, *Journal of the American Society for Mass Spectrometry*, 2005, **16**, 883–892.

(24) R. K. E. Gover, Ph.D. Thesis, University of Nottingham, 2016.

(25) Y. Fu, W. Li and J. Flarakos, *Bioanalysis*, 2019, **11**, 1375–1377.

(26) E. De Bolós, M. Martínez-Abadía, F. Hernández-Culebras, A. Haymaker, K. Swain, K. Strutyński, B. L. Weare, J. Castells-Gil, N. M. Padial, C. Martí-Gastaldo, A. N. Khlobystov, A. Saeki, M. Melle-Franco, B. L. Nannenga and A. Mateo-Alonso, *Journal of the American Chemical Society*, 2022, **144**, 15443–15450.

(27) A. M. Evans, M. R. Ryder, W. Ji, M. J. Strauss, A. R. Corcos, E. Vitaku, N. C. Flanders, R. P. Bisbey and W. R. Dichtel, *Faraday Discussions*, 2021, **225**, 226–240.

(28) S. Kocakuşak, K. Akçay, T. Ayok, H. Koöroğlu, M. Koral, Ö. Savaşçi and R. Tolun, *Chemical Engineering and Processing: Process Intensification*, 1996, **35**, 311–317.

(29) B. Ballesteros, G. Tobias, M. A. H. Ward and M. L. H. Green, *The Journal of Physical Chemistry C*, 2009, **113**, 2653–2656.

(30) A. L. Patterson, *Physical Review*, 1939, **56**, 978–982.

(31) D. B. Williams and C. B. Carter, *Transmission electron microscopy: a textbook for materials science*, Springer, New York, 2nd ed, 2008.

(32) R. Kulkarni and P. Rastogi, *Optics and Lasers in Engineering*, 2020, **135**, 106190.

(33) Q. Kemao, *Optics and Lasers in Engineering*, 2015, **66**, 67–73.

(34) K. Zhao, Q. Han, C.-B. Zhang, J. Xu and M.-M. Cheng, *IEEE Transactions on Pattern Analysis and Machine Intelligence*, 2021, 1–1.

(35) D. M. Pelt and J. A. Sethian, *Proceedings of the National Academy of Sciences*, 2018, **115**, 254–259.

(36) D. W. Scott, *Biometrika*, 1979, **66**, 605–610.

(37) H. A. Sturges, *Journal of the American Statistical Association*, 1926, **21**, 65–66.

(38) X.-D. Wang, Z.-X. Shen, T. Sang, X.-B. Cheng, M.-F. Li, L.-Y. Chen and Z.-S. Wang, *Journal of Colloid and Interface Science*, 2010, **341**, 23–29.

(39) M. Bonamente, *Statistics and Analysis of Scientific Data*, Springer New York, New York, NY, 2017.

(40) H. Li, A. M. Evans, I. Castano, M. J. Strauss, W. R. Dichtel and J. L. Bredas, *Journal of the American Chemical Society*, 2020, **142**, 1367–1374.

(41) C. T. Stoppiello, H. Isla, M. Martínez-Abadía, M. W. Fay, C. D. J. Parmenter, M. J. Roe, B. Lerma-Berlanga, C. Martí-Gastaldo, A. Mateo-Alonso and A. N. Khlobystov, *Nanoscale*, 2019, **11**, 2848–2854.

(42) R. F. Egerton, *Electron Energy-Loss Spectroscopy in the Electron Microscope*, Springer New York, New York, 3rd edn.

(43) R. F. Egerton, *Reports on Progress in Physics*, 2009, **72**, 016502.

(44) M. Stöger-Pollach, *Micron*, 2008, **39**, 1092–1110.

(45) S. Korneychuk, G. Guzzinati and J. Verbeeck, *Physica Status Solidi A*, 2018, **215**, 1800318.

(46) H. R. Phillip and E. A. Taft, *Physical Review*, 1964, **136**, A1445–A1448.

(47) E. Hecht, *Optics*, Harlow: Pearson Education, 5th edn.

(48) R. Arenal, O. Stéphan, M. Kociak, D. Taverna, A. Loiseau and C. Colliex, *Microscopy and Microanalysis*, 2008, **14**, 274–282.

(49) K. Momma and F. Izumi, *J. Appl. Crystallogr., 44, 1272-1276 (2011).*, 2011, **44**, 1271–1276.

(50) J. Schindelin, I. Arganda-Carreras, E. Frise, V. Kaynig, M. Longair, T. Pietzsch, S. Preibisch, C. Rueden, S. Saalfeld, B. Schmid, J.-Y. Tinevez, D. J. White, V. Hartenstein, K. Eliceiri, P. Tomancak and A. Cardona, *Nature Methods*, 2012, **9**, 676–682.

(51) J. Schindelin, C. T. Rueden, M. C. Hiner and K. W. Eliceiri, *Molecular Reproduction and Development*, 2015, **82**, 518–529.

(52) K. L. Fung, M. W. Fay, S. M. Collins, D. M. Kepaptsoglou, S. T. Skowron, Q. M. Ramasse and A. N. Khlobystov, *Ultramicroscopy*, 2020, **217**, 113052–113052.

(53) *NIST DTSA-II*, NIST, `https://www.nist.gov/services-resources/software/nist-dtsa-ii` (visited on 02/27/2023).

(54) W. L. Jorgensen and J. Tirado-Rives, *J. Am. Chem. Soc.*, 1988, **110**, 1657–1666.

(55) W. L. Jorgensen, D. S. Maxwell and J. Tirado-Rives, *J. Am. Chem. Soc.*, 1996, **118**, 11225–11236.

(56) V. Blum, R. Gehrke, F. Hanke, P. Havu, V. Havu, X. Ren, K. Reuter and M. Scheffler, *Computer Physics Communications*, 2009, **180**, 2175–2196.

(57) A. Marek, V. Blum, F. Hanke, P. Havu, V. Havu, X. Ren, K. Reuter and M. Scheffler, *Journal of Physics: Condensed Matter*, 2014, **26**, 213201.

(58) V. W.-z. Yu, F. Corsetti, A. García, W. P. Huhn, M. Jacquelin, W. Jia, B. Lange, L. Lin, J. Lu, W. Mi, A. Seifitokaldani, A. Vázquez-Mayagoitia, C. Yang, H. Yang and V. Blum, *Computer Physics Communications*, 2018, **26**, 267–285.

(59) A. Tkatchenko, R. A. DiStasio, R. Car and M. Scheffler, *Physical Review Letters*, 2012, **108**, 236402.

(60) A. Ambrosetti, A. M. Reilly, R. A. DiStasio and A. Tkatchenko, *The Journal of Chemical Physics*, 2014, **140**, 18A508.

(61) L. Wasserman, *All of Statistics: A Concise Course in Statistical Inference*, Springer New York, New York, NY, 2004.

(62) C. Zhang, B. E. Mapes and B. J. Soden, *Quarterly Journal of the Royal Meteorological Society*, 2003, **129**, 2847–2866.

(63) *MathWorks Help Center*, MathWorks, 2023, `https://uk.mathworks.com/help/index.html?s_tid=CRUX_lftnav` (visited on 07/02/2023).

(64) K. L. Y. Fung, Ph.D. Thesis, University of Nottingham, Nottingham, 2021.

(65) M. Lotya, Y. Hernandez, P. J. King, R. J. Smith, V. Nicolosi, L. S. Karlsson, F. M. Blighe, S. De, Z. Wang, I. T. McGovern, G. S. Duesberg and J. N. Coleman, *Journal of the American Chemical Society*, 2009, **131**, 3611–3620.

(66) S. T. Yang, J. Kim, H. Y. Cho, S. Kim and W. S. Ahn, *RSC Advances*, 2012, **2**, 10179–10181.

(67) J. F. W. McOmie, M. L. Watts and D. E. West, *Tetrahedron*, 1968, **24**, 2289–2292.

3 Covalent Organic Framework 5

3.1 Aims and Objectives

Covalent organic framework 5 (COF-5) is a 2D hexagonal boronate ester COF, which was one of the first two polymers published under the name COF.[1] COF-5 has been well studied, and is known to consist of AA-stacked sheets with *P6mmm* symmetry[1] (although there is a counter-opinion that it is in fact a kagome AA lattice),[2] with a known X-ray powder pattern,[1,3] X-ray scattering pattern,[4] infrared spectrum,[1,5] UV-Vis spectrum,[4], thermogravimetric analysis thermogram,[6] gas adsorption isotherm,[1,3] and pore diameter (0.27 nm).[1] COF-5 has been synthesised under a variety of conditions, including microwave[3,7], sonochemical[5,8] and solvothermal heating;[1] and as a powder, microcrystals,[9] thin-film on support,[4,10] and hybrid material.[5,11] COF-5 has been used as a test system for understanding boronate ester COF growth mechanisms,[12–15] COF hydrolytic stability,[14] for carbon dioxide adsorption studies,[5] as a stationary phase for chromatography,[16], hydrogen gas storage,[17], and in energy technologies,[11] amongst others. Although there have been studies investigating the resilience of COF-5 to changing reaction conditions, focussing on water and nitrile co-solvents,[12,13] the literature tends to use dry solvents to make crystalline COF-5. Studies also do not discuss safe disposal of COF at the end of it's working lifetime.

For COF-5 there are a handful of noteable transmission electron microscopy (TEM) studies: Stoppiello *et al.* used TEM tomography combined with focussed ion beam (FIB) milling to visualise mesopores present in the COF structure;[18] Evans *et al.* used HRTEM to clearly visualise COF-5 crystal planes;[9] and Smith *et al.* used liquid-cell TEM to observe the formation of COF-5 crystallites *in situ*.[13] However, COF-5 suffers the same drawbacks in TEM analysis discussed in Chapter 1; namely low uptake of TEM spectroscopy, lack of depth of analysis, and TEM being used mainly as a secondary analytical technique.

With these points in mind, COF-5 is a highly suitable test system for expanding the TEM analysis techniques used in Chapter 3 to a different COF system, and confirming that the graph theoretical models in Chapter 2 are generalisable across 2D hexagonal boronate ester COFs. The HHTP nodes making up COF-5 provide good amplitude contrast in TEM, and there is a wealth of bulk characterisation data in the literature for comparison. Furthermore matrix-assisted laser desorption-ionisation mass spectrometry (MALDI MS) analysis has not yet been applied to COF-5. Finally an attempt to optimise existing COF-5 synthesis conditions, to give a rapid synthesis of crystalline COF that does not rely on dry solvents, can be attempted. To this end, the following goals are defined:

- Investigation of the effects of reaction conditions on COF-5 synthesis in order to produce COF-5 as a powder and as a hybrid with nanosupports, in particular the role of dry solvents.
- Application of novel techniques to COF-5 for analysis, such as MALDI MS and electron energy loss spectroscopy (EELS).
- Thermogravimetric analysis (TGA) investigations of COF-5 and COF-5/nanosupports hybrids, to find COF loading and investigate safe disposal of these materials.
- Heating COF-5 under anoxic conditions to investigate it's thermal stability, and as a possible disposal route for COF-5.
- Further develop the application of TEM imaging and spectroscopy to COFs, using the methods established as viable in Chapter 3.

3.2 Synthesis of COF-5

COF-5 has previously been synthesised using a variety of conditions. The first reported synthesis used a 1:1 mixture of 1,4-dioxane and mesitylene to limit the solubility of monomers in the reaction mixture, and more recently Smith *et al.* showed that use of nitrile co-solvents in varying proportions was key in giving nanoparticles of COF-5.[13] All previously reported syntheses rely on dried solvents, which require energy, time, and money to produce. It was therefore decided to investigate the synthesis of crystalline COF-5 product using solvents that had not been dried prior to synthesis (Figure 42). Using this as the starting point, a number of reactions were carried out to investigate the sensitivity of COF-5 to synthesis conditions (Table 10). For all reactions the solvent system used was a mixture of acetonitrile/1,4-dioxane/mesitylene; the molar ratio of HHTP:BDA was 1.40 ± 0.3 ($\mu \pm 2\sigma$); and the mean yield was $32.3 \pm 26\%$.

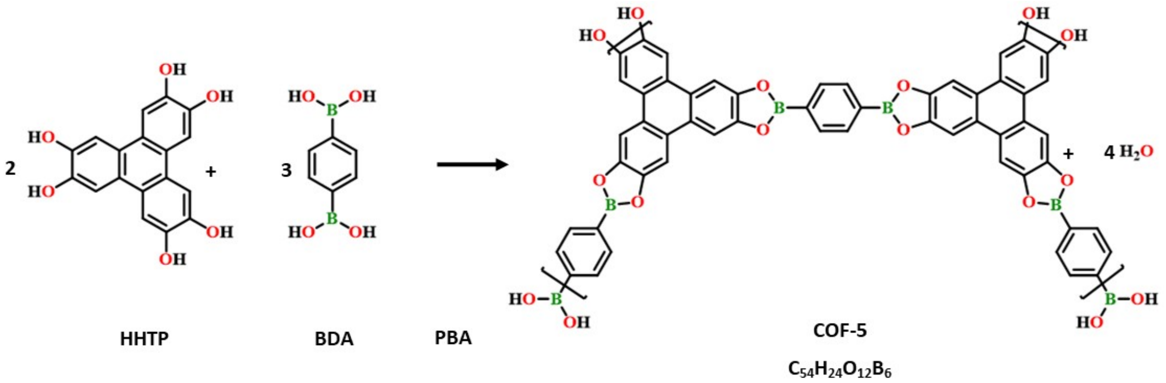

Figure 42: Synthesis scheme for COF-5, illustrating the condensation between hexahydroxytriphenylene (HHTP) and benzenediboronic acid (BDA). Phenyl boronic acid (PBA) can be included as a modulator.

First the effect of time on the reaction system was investigated by heating a stirred reaction mixture 1 hour at 90 °C , and a second mixture for 16 hours at 90 °C . It was found that in both cases, a tan precipitate formed directly in the reaction mixture with no visible differences between the solutions. A higher yield was obtained from the mixture that was heated for a longer time. Further, infrared (IR) spectroscopy and transmission electron microscopy were unable to quantify any meaningful differences between the two products (Figure 43, Figure 44a, b). This suggests that COF-5 formation is rapid, with higher reaction times leading to a greater yield, but that COF-5 forms rapidly as an amorphous polymer. Investigating time versus reaction yield would likely find diminishing returns as the reaction gets closer to full conversion, in line with

No.	HHTP:BDA	Solvent	Temp. / °C	Time / h	Yield / %	Notes
1	1.50:1	15:4:1	90	1	23	-
2	1.13:1	15:4:1	90	16	32	-
3	1.12:1	15:4:1	90	17	23	1 mol% PBA as modulator
4	1.38:1	15:4:1	RT	18	23	-
5	1.55:1	20:4:1	90	17	13	-
6	1.42:1	20:4:1	0	52	0	No solid product
7	1.42:1	20:4:1	90	18	38	Water below 1 %

Table 10: Experimental parameters for COF-5 synthesis, including the molar ratio of HHTP:BDA, temperature, and time. By successively altering the reaction time, temperature, solvent system, and water content a crystalline COF-5 was achieved using reaction number 7. Reactions 1 - 5 gave an amorphous COF-5 polymer. Room temperature (RT) was between 10 - 20 °C.

traditional step-growth polymer kinetics, but this was not investigated further. Next, using a 16 hour reaction time phenyl boronic acid (PBA) was added to the reaction mixture as a modulator. This was not found to significantly affect the yield or morphology of the sample at the concentration used (Figure 44c). PBA was also not detectable in the reaction product via IR spectroscopy, due to the low concentration of PBA in the COF lattice and PBA having overlapping IR vibrations with BDA (Figure 43). PBA was not used in subsequent reactions.

Aiming for a reaction time of 16 hours, the effect of temperature on the reaction system was investigated; this was done by performing the reaction at room temperature (between 10 °C and 20 °C) and comparing to the synthesis at 90 °C. The room temperature reaction formed a precipitate after 16 hours. While all of the other reactions discussed here produced a powder, the room temperature reaction uniquely produced a soft gel that shrank into a brittle monolith on drying. Both the dried gel and the powered COF-5 have the same IR spectrum (Figure 43), and no crystallinity was detected via TEM imaging (Figure 44d). This result suggests that for COF-5 below a threshold temperature an amorphous polymer network forms, and while the monomers react readily at elevated temperatures reducing the reaction temperature leads to a lower rate of reaction. Drawing on the discussion of error-checking in Chapter 1, this implies that at room temperature the rate of error-checking is lower than the rate of COF polymer growth; this results in an amorphous structure. Previous work with COF-5 from Evans *et al.* suggests that boronate ester COFs form by the nucleation-elongation method,[20] unlike imine-COFs that form as an amorphous phase that then crystallises. Therefore, the reaction temperature for COF-5 is

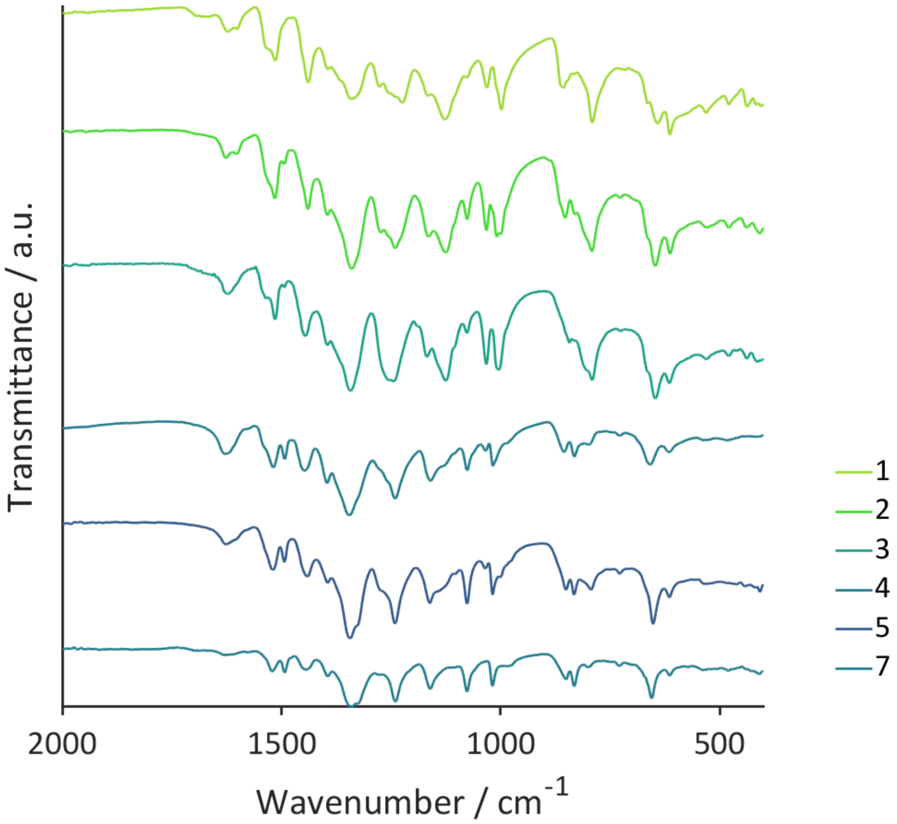

Figure 43: IR spectra for the syntheses in Table 10: (a) 1, (b) 2, (c) 3, (d) 4, (e) 5, and (f) 7. Each spectrum is consistent with the formation of a boronate ester polymer. Differences in intensity of vibrations between spectra can be attributed to the use of attenuated total reflectance (ATR) IR,[19] as mentioned in Chapter 2.

important as there is only one chance to form the COF as a crystalline polymer.

The solvent ratio was adjusted from 15:4:1 to 20:4:1, to see if increasing the amount of nitrile solvent affected the crystallinity. It was not found to make an effect on sample crystallinity although a slight decrease in sample yield was observed (Figure 44e). A bonus reaction was performed at 0 °C which did not yield any solid product, either as precipitate or a colloid; repeating at 0 °C for 52 hours gave the same results. Combined with the temperature results above, this suggests that the activation for the polymerisation reaction lies between 0 -10 °C at atmospheric pressure. This follows on from a previous mechanistic study of COF-5 formation,[12] that found the activation energy was 22- 27 kcal mol^{-1} for the temperature range 60 °C - 70 °C, with second-order rate kinetics. While a kinetic study was not performed here, knowing that the polymerisation reaction will occur at room temperature further demonstrates that COF-5 can be made readily and the activation energy is low. This also agrees with a previous study that was

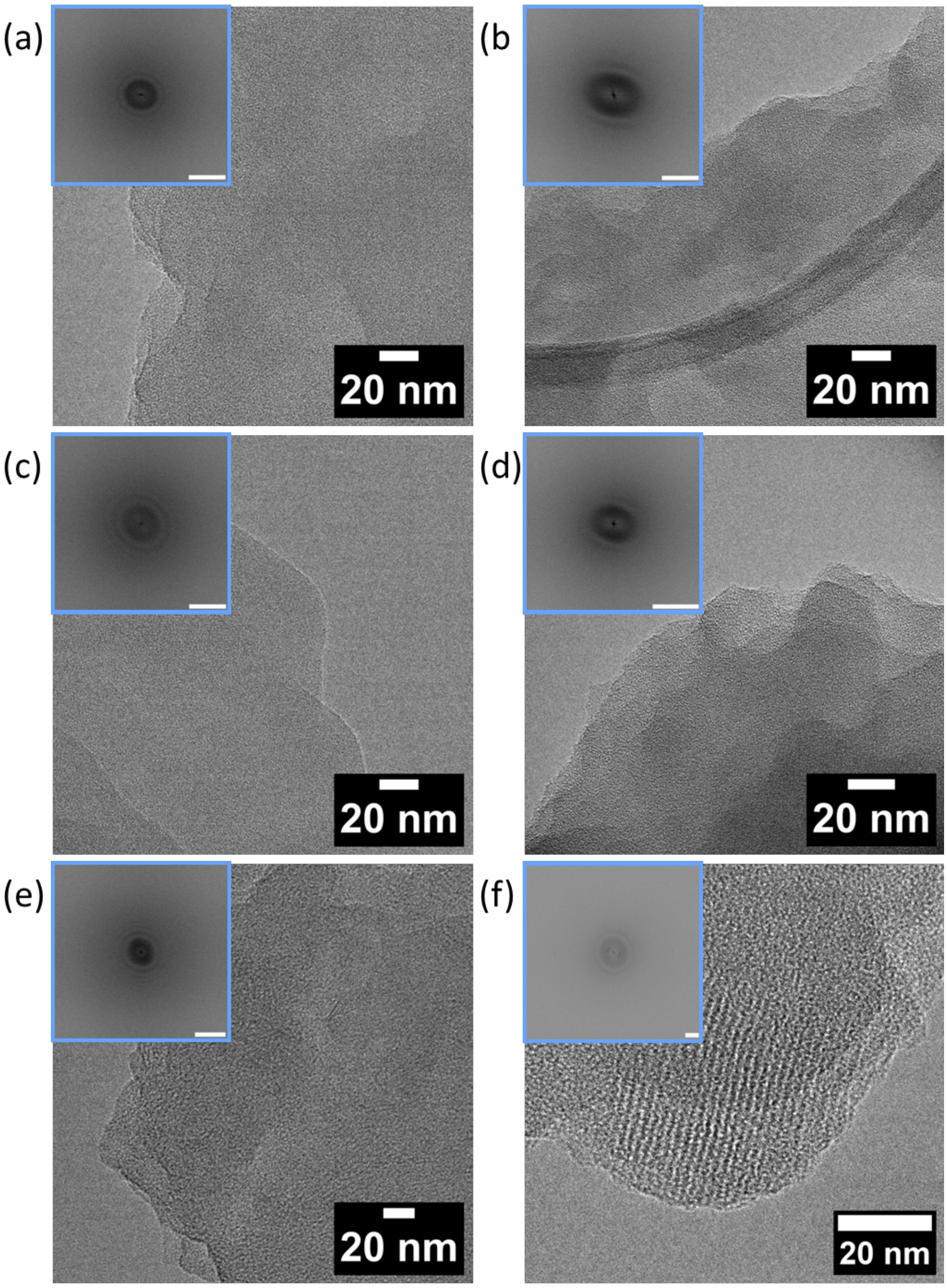

Figure 44: BF-TEM of COF-5 synthesis products, for reaction conditions: (a) 1, (b) 2, (c) 3, (d) 4, (e) 5, (f) 7. It can be seen that (f) is the only sample with visible lattice projections, while the other samples are amorphous. Inserts: Fourier transforms. Scale bar = 2 1/nm.

able to form thin-films of COF-5 at room temperature by drop-casting a monomer mixture onto a glass film followed by exposing the forming film to solvent vapour during film formation.[10]

Crystalline COF-5 was achieved by reducing the amount of water in the reaction mixture to below 1 % (Figure 44f). It has previously been shown that the concentration of water in the reaction mixture can be used to control the size of the COF crystallites.[12] That shows that even with low concentrations and high temperature, a high concentration of water was able to interfere with the process of error-checking and lead to an amorphous COF polymer. Karl-Fischer moisture measurements of the solvent mixture used show that a typical solvent mixture contained 7 - 8 % water by volume. In contrast, a solvent mixture composed of commercially available dried solvents contain 0.8 - 1 % water by volume (10,000 ppm). This synthesis was then used to create COF-5/nanosupport using: graphite, graphitised nanofibres (GNFs), multiwalled carbon nanotubes (MWNTs), single-walled carbon nanotubes (SWNTs).

To summarise, amorphous COF-5 can be synthesised under a range of reaction conditions. The key factor controlling whether COF-5 is synthesised as an amorphous or crystalline powder is the amount of water in the reaction solvent; however, COF-5 does not require absolutely dry solvents for crystalline synthesis. Going forwards in this chapter, the focus is on the products of synthesis conditions number 7.

3.3 Bulk Measurements of Nanocrystalline COF-5

3.3.1 Powder X-ray Diffraction

The powder patterns for the COF-5 and COF-5 hybrids produced show no strong specular diffraction peaks (Figure 45). We know that the diffractometer is working as it gives strong brass peaks when using a brass sample holder insert, non-COF samples give crystal reflections, and it works for everyone else in the School of Chemistry. Thus we must conclude that the sample is not diffracting strongly. This is due to either lack of crystalline material, or small crystallite sizes. This is exacerbated by the small amount of sample that was available for PXRD analysis. In contrast the literature powder pattern[1] contains several reflections below $2\theta = 15°$, and modelling the powder pattern using the literature electronic structure model gives major peaks (I > 1%) at 2θ = 3.43, 5.94, 6.87, 9.10, 12.4, 25.9°; a number of minor peaks are also present in the powder

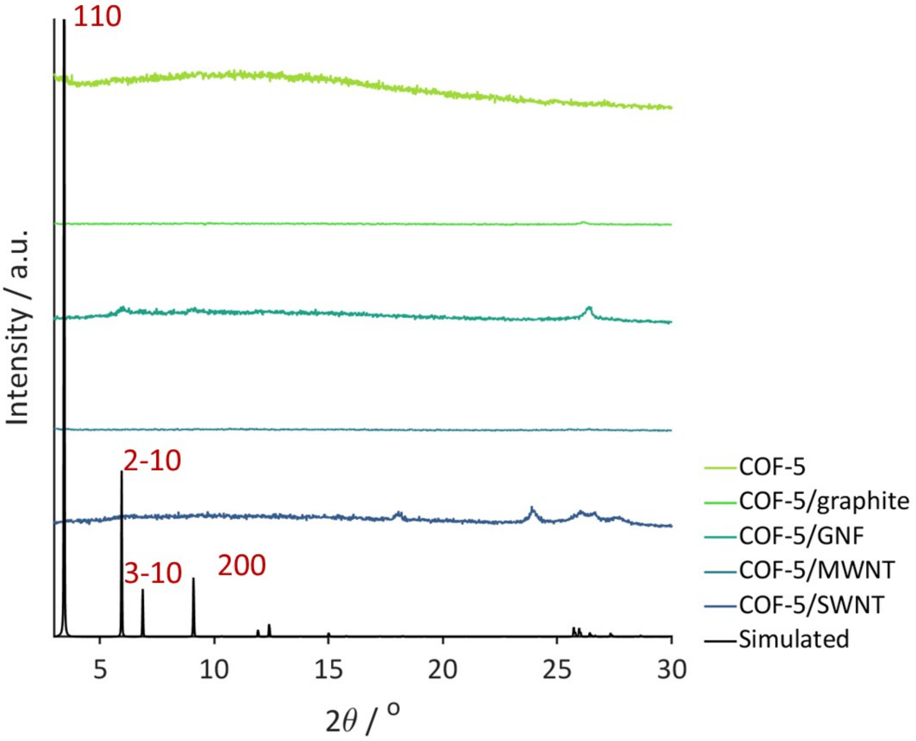

Figure 45: Experimental PXRD patterns for: COF-5, COF-5/graphite, COF-5/GNF, COF-5/MWNT, and COF-5/SWNT. The simulated pattern was made using the literature crystal structure.[1] The Miller indices for the first four reflections of the simulated powder pattern have been indicated in red. The visible diffraction peaks are due to diffraction from the nanocarbon supports.[21,22]

pattern. Smith *et al.*[13] reported a powder pattern with a lower signal-to-noise ratio than Cote *et al.* with only three visible diffraction peaks. Given that this work, Smith *et al.*, and Cote *et al.* all used similar PXRD setups (40 kV, 40 mA, CuKα_1, zero-background holders, no sample grinding) this suggests that smaller COF crystallites leads to a noisier powder pattern. As the crystallites discussed in the TEM section below are the smallest of all of the COF-5 crystallites mentioned in this section, this would account for the poor powder pattern recorded for these materials in spite of evidence for crystallinity from TEM. This also highlights the need for robust local-probe analysis methods such as TEM for these nanoscale crystals.

3.3.2 Infrared Spectroscopy

The chemical bonding of COF-5 was probed by IR spectroscopy (Figure 46). The experimental spectrum agrees well with the literature IR spectrum,[1] with key vibrations corresponding to B-O containing vibrational modes[23] at: 3387, 1342, 1241, 1017, 654 cm^{-1}.

The features of COF-5 and COF-5/nanosupport IR spectra are broadly the same as those of cHBC-BDA-COF discussed in Chapter 2, so the spectra at hand will only be discussed briefly (Figure 47). The spectra contain vibrations arising from boronate ester and boronic acid functional groups,[23] where the latter are unpolymerised monomers that are likely at the edge of the COF polymer. No evidence of boroxine vibrations are seen in the spectra, indicating that COF-1 did not form by self-condensation of benzenediboronic acid during synthesis.[24] IR spectra of COF-5/nanocarbon hybrids often had sloping baselines due to Mié scattering, and often required the spectra to be recorded as potassium bromide pellets rather than attenuated total reflectance spectra.

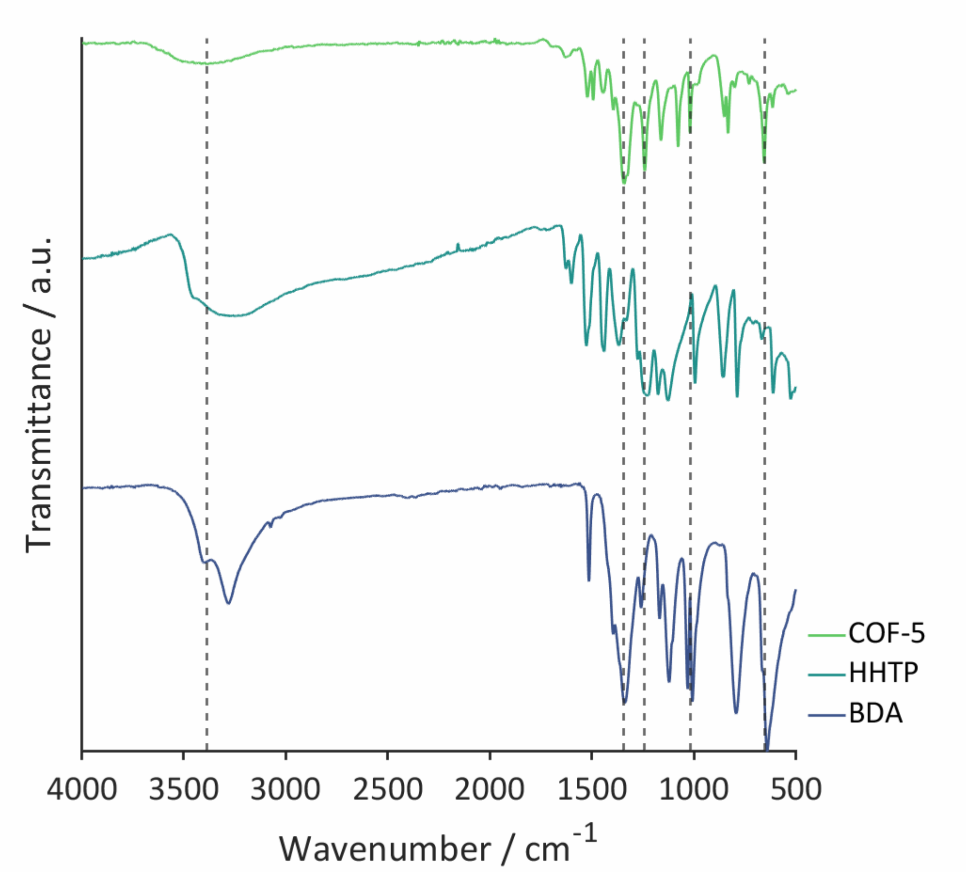

Figure 46: IR spectra of COF-5, HHTP, and BDA. Key COF-5 vibrations corresponding to the boronate ester functionality have been indicated with dotted lines. It can be seen that the three spectra have different vibrations, indicating that polymerisation has taken place within the COF lattice.

The IR spectrum of the amorphous and crystalline COF-5 contains the same boronate stretches without detectable shifts in wavenumber (Figure 43). This implies that that chemical bonding is the same, with the 3D arrangement of the monomers being different; i.e., the differences in mor-

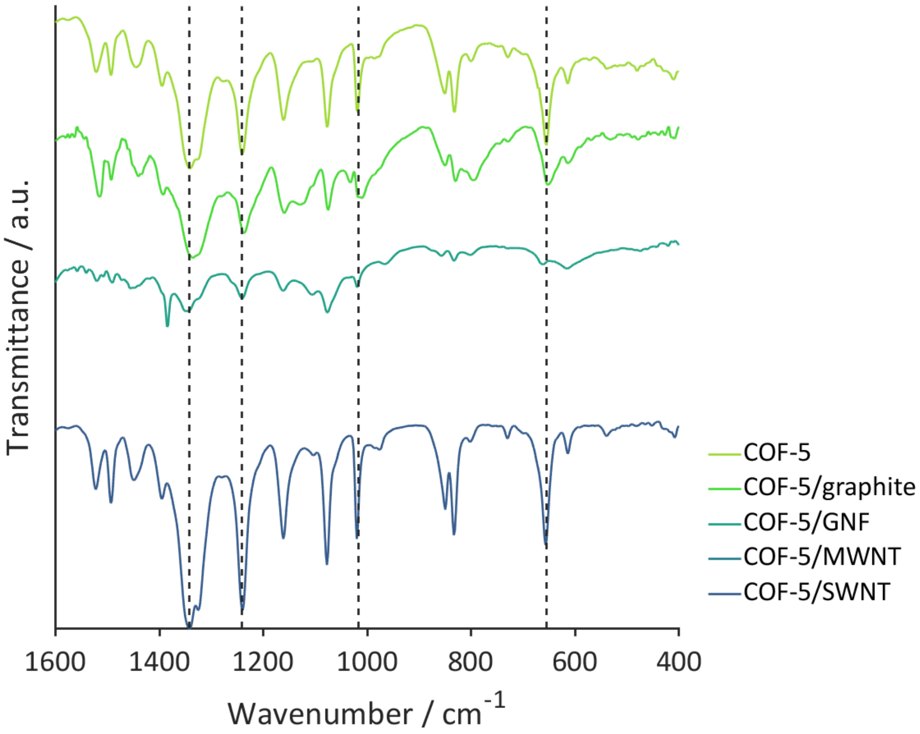

Figure 47: IR spectra of COF-5, COF-5/graphite, COF-5/GNF, COF-5/MWNT, COF-5/SWNT. Key COF-5 vibrations corresponding to the boronate ester functionality have been indicated with dotted lines, which are present across different hybrid materials. These are indicative of polymerisation.

phology and connectivity are not detectable by routine IR. As an amorphous COF polymer is expected to be branched or hyper-branched polymer, it is expected that the amorphous polymer will contain more catechol and boronic acid functionalities, and that these will not be localised to the outside of the polymer. This is theoretically detectable via IR with high energy resolution. Given the broadness of the COF vibrations and the low energy resolution of the available spectrometer, this was not achieved in this work. This also raises the unanswered question of whether crystallinity will affect the chemical properties of the COF, such as surface chemistry. It could be that amorphous COF-5 has more useful surface chemistry for industrial applications than crystalline COF-5 due to the increased amount of unpolymerised functional groups. This remains an open question for future investigation.

3.3.3 MALDI-TOF Mass Spectrometry

Matrix assisted laser desorption-ionisation mass spectrometry (MALDI MS) had no published occurrence of being used on COF-5 at the time of writing. The base peak in the mass spectrum of HHTP is at 324 m/z corresponding to the molecular ion, as well as several peaks at higher m/z. The empirical formulae of the ions in the mass spectrum was found (see Appendix Table 24), and some structures were rationalised (see Appendix Figure 109b). These ions correspond to two or more HHTP fragments adhered together, with no evidence for covalent bonding joining these fragments. The mass spectrum for COF-5 contains different peaks at different intensities to HHTP, indicating a chemical difference between the two samples caused by the polymerisation process (Figure 48). Notably the mass spectrum of COF-5 does not contain a molecular ion at 324 m/z. The base peak of COF-5 at 448 m/z is a fragment of the polymer lattice rather than a single HHTP ion.

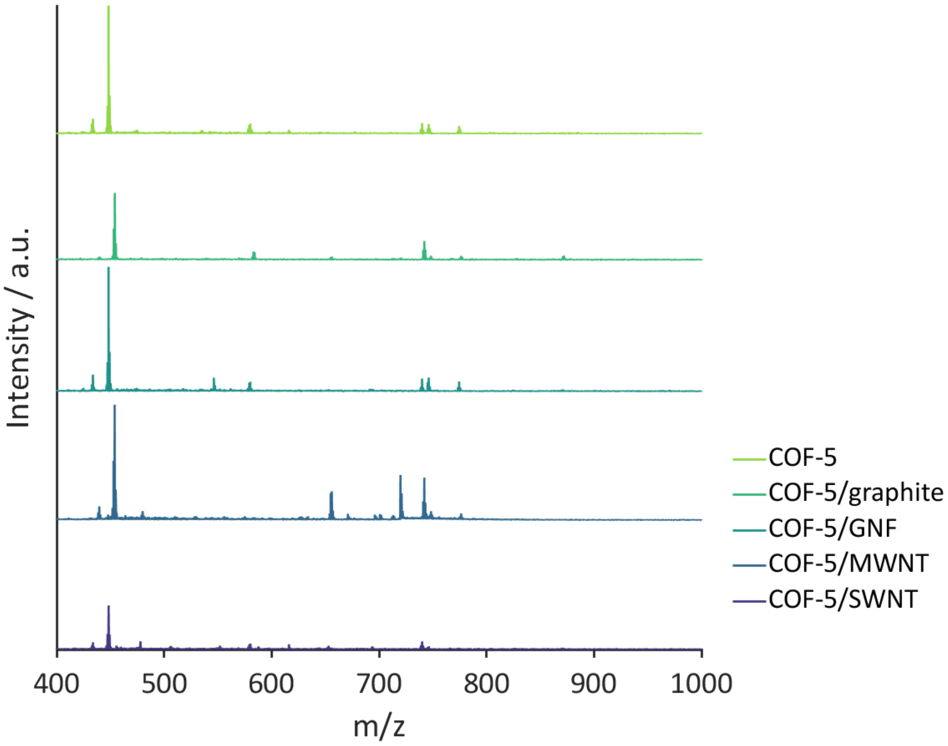

Figure 48: MALDI TOF mass spectra of COF-5, COF-5/graphite, COF-5/GNF, COF-5/MWNT, and COF-5/SWNT. The base peak of the spectra is at 448 m/z, corresponding to a fragment of the COF lattice. Higher m/z peaks can be rationalised as fragments of the 2D COF lattice.

This confirmed that the HHTP and BDA were being joined by boronate ester bonds, and is consistent with the MALDI-TOF of cHBC-BDA-COF in Chapter 2. The consistency between the MALDI of COF-5 and cHBC-BDA-COF may indicate a systematic pattern in MALDI for COFs. The elemental composition of ions was confirmed by comparison to simulated isotope patterns, and it was found that the ratio of ^{11}B:^{10}B gives easily identifiable patterns. The charge on the ions was confirmed by checking the distance between isotope peaks, and it was found that all ions were singly charged. The results for COF-5/nanosupport were consistent with COF-5. It was found that nanocarbon supports affect the spectrum in two ways: at high laser powers, carbonaceous fragments separated by 24 m/z appear at low intensity in the spectrum; at all laser powers, the carbon can act as a matrix, aiding the desorption and ionisation of the COF from the MALDI target plate. As described in the previous chapter, using mechanical mixtures of monomers at different ratios would allow facile identification of the monomer ratio in the COF-5 samples.

3.3.4 Thermogravimetric Analysis

Thermogravimetric analysis (TGA) of COF-5 was undertaken to investigate the thermal properties of crystalline COF-5 (Figure 50). Combustion represents a possible pathway for disposal of a material at the end of it’s useful service life, and considering safe disposal of new materials is important as they are taken forwards to industrial applications as COF-5 may be in the near future. TGA was therefore used as "accelerated lifetime analysis" for end of life disposal of COF-5, and to find the maximum operating temperature of a device containing COF-5.

The primary mass loss in the COF-5 thermogram at 473 °C (Figure 50) was at a slightly lower temperature than has been previously reported for COF-5 (500 °C),[1,25] COF-5 was found to undergo it’s primary mass loss at a higher temperature than HHTP and BDA, consistent with literature TGA.[1] COF-5/nanosupport combusted between 492 - 526 °C (Table 11). The trend of larger nanosupports combusting at a higher temperature seen in Chapter 2 was not well-defined with the COF-5 hybrid materials, likely due to the formation of a range of morphologies within the sample. If the hybrids were to form as a consistent core-shell structure with well defined layer thickness, a better defined combustion temperature trend might be expected. However, it is known from Chapter 2 that COFs often do not form as neat structures.

As discussed in Chapter 2, the thermal degradation pathway of COF-5 is the conversion of the COF into carbon dioxide, water, and boron oxide. The residual mass of boron oxide in the thermograms matches to the theoretical amount of boron oxide that could be formed from the amount of boron in the COF lattice, which can therefore be used to calculate the amount of COF

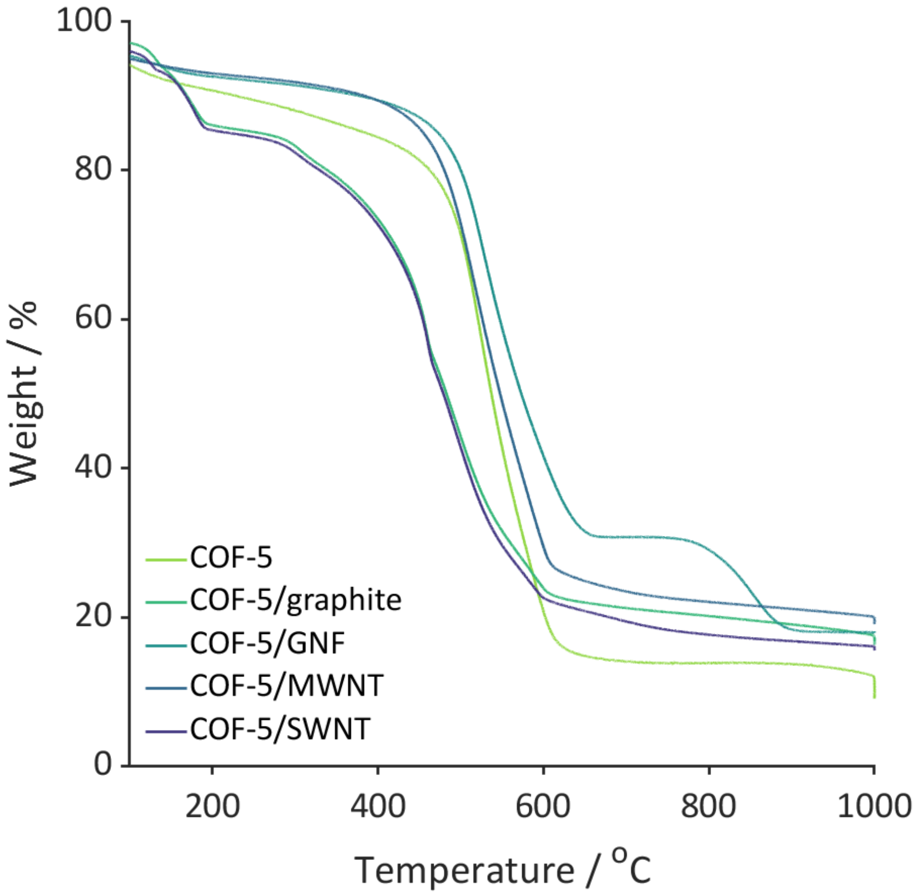

Figure 49: Thermograms for COF-5, and COF-5/graphite, /GNF, /MWNT, and /SWNT. The residual mass in the thermograms is attributed to the formation of boron oxide from the combustion of the COF polymer.

in a COF/nanosupport hybrid sample called the COF loading percentage (Table 11). The oxygen required for this thermal decomposition pathway is available in the compressed air stream of the TGA used, which contains some parts per million of oxygen. COF-5 loading was found to be bewteem 61 - 84 %, comparable to cHBC-BDA-COF loading in Chapter 2, although without a strong trend linking nanosupport diameter and COF-5 loading.

The TGA results suggest that boronate ester COFs can be disposed of safely by incineration. This is safer than disposal by landfill, as there is no risk of leaching of organic compounds from the COFs into soils, and the small amount of solid boron oxide produced can be disposed of.

A potential application for COF-5 was based on the TGA results is using COFs as a carbon source for thermal reduction of metal oxides.[26] As COF-5 combustion to gives carbon dioxide gas, COF-5 could be mixed with metal oxide and used as a carbon source for reduction to el-

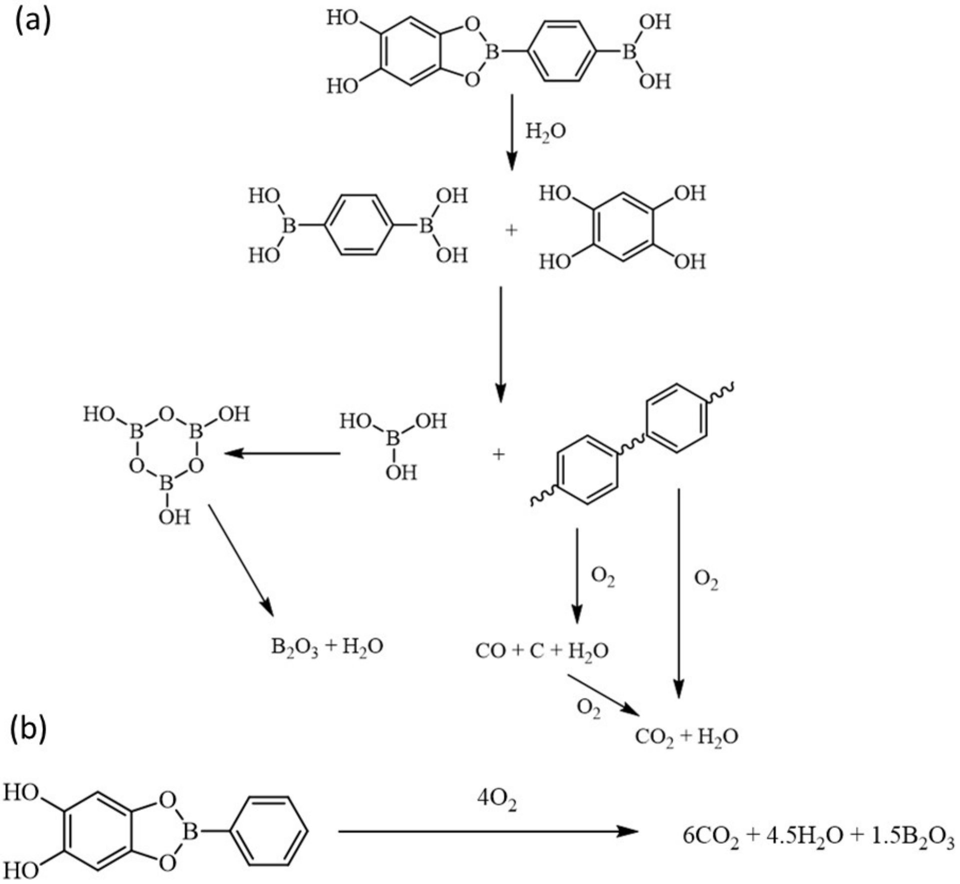

Figure 50: (a) Suggested boronate ester thermal decompostion pathways, showing how a boronate ester functional group could be reduced to carbon dioxide, water, and boron oxide. The joined benzene rings represent an amorphous network of cross-linked aromatic groups. The thermal decomposition of COF-5 likely follows a similar route. (b) Equation for combustion of a boronate ester group, showing the stoichiometry used to calculate COF-5/nanosupport loading.

emental metal. The formation of boron oxide from the combustion process could also act as a flux to reduce the formation of slag during the reduction process. This is envisioned as an end-of-lifetime use for COF-5, a form of recycling that can extract useful work during the disposal of COF-5, rather than a primary use of COF-5.

Material	**COF combustion / °C**	**Support combustion / °C**	**Residual / %**	**COF loading / %**
HHTP	262	-	0	-
BDA	200	-	50	-
COF-5	473	-	0	61
COF-5/graphite	492	581	17.8	75
COF-5/GNF	526	852	18.0	80
COF-5/MWNT	518	581	26.1	84
COF-5/SWNT	494	583	16.2	69

Table 11: Combustion temperature, residual mass and COF loading for COF-5 and COF-5/nanosupports. It can be seen that nanosupports affect the combustion temperature of COF, indicating a change in sample morphology. TGA data for nanosupports can be found in Chapter 2, Table 3.

3.4 Electron Microscopy of Nanocrystalline COF-5

3.4.1 SEM Imaging

The microscale morphology of COF-5 was investigated via SEM (Figure 51). The SEM micrographs reveal that the COF is made up of microscale "foamy" fragments,[27] without any clear crystal morphologies such as plates or needles. These results corroborate the PXRD, as no evidence of crystal shapes like needles or plates was seen. There is little to add other than the SEM imaging is consistent with literature SEM micrographs of COF-5.[1,5]

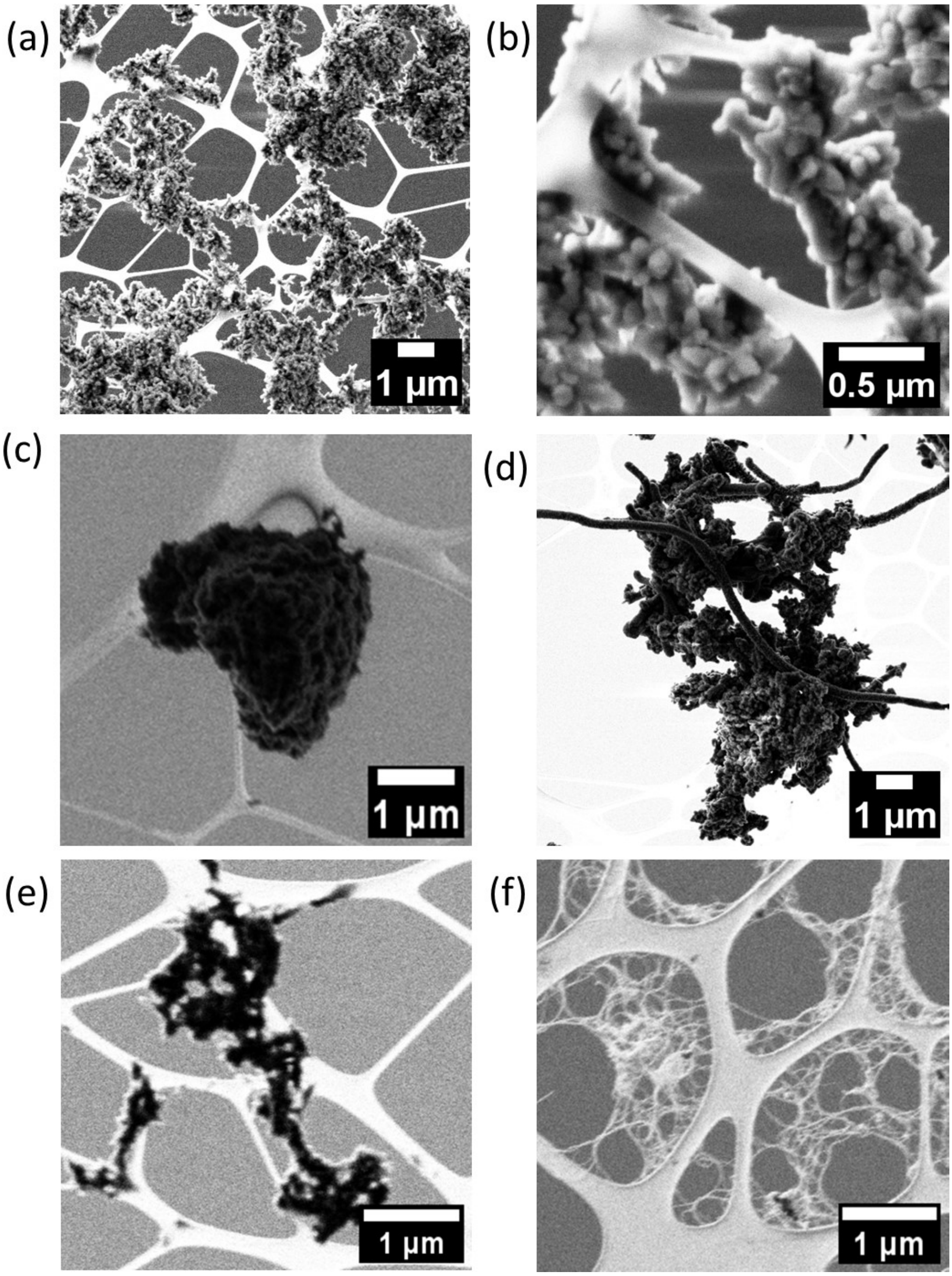

Figure 51: Scanning electron microscope images of COF-5 and COF-5/nanosupport composites. (a) Low- and (b) high-magnification images of COF-5, displaying a foamy morphology. (c) COF-5/graphite, showing how COF-5 forms a foamy layer on the graphite surface. (d) Cluster of COF-5/GNF, illustrating how COF-5 does not form selectively as a thin layer on the GNF surface and the foamy COF morphology. (e) COF-5/MWNT and (f) COF-5/SWNT, which could not be usefully imaged using SEM due to the small size of the COF/nanosupport hybrids.

3.4.2 BF-TEM Imaging

Bright-field TEM (BF-TEM) of COF-5 (Figure 52) was similar to that of cHBC-BDA-COF in Chapter 2. The COF formed a foamy structure from which lattice projections at the edges could be resolved, as these areas are thin enough for coherent electron scattering. The region between the thin edge and thick core can be considered "electron beam translucent", where the material is too thick to give rise to useful phase-contrast images and/or lattice projections overlap to give Moiré fringes. Assuming the opaque regions to be the same composition as the transparent regions, the COF is composed of many small crystallites between 10 - 100 nm. Distributing the measurements of COF-5 lattice projections gave an unimodal distribution with mean of 1.91 ± 0.47 nm (Figure 53a). Splitting the dataset into AC and ZZ data points at 1.97 nm allowed the bimodality *S* to be calculated as 0.62 (Figure 53a). Unlike for cHBC-COF, parallel and perpendicular crystallite sizes could not be usefully measured for COF-5 due to the significant overlap between crystallites.

The lattice projections in COF-5 can be rationalised by considering the overlap of the HHTP nodes in projection. As for the previous chapter, rotating a electronic structure model of COF-5 gives rise to distinct principle armchair (AC), zigzag (ZZ), face-on (FO), and side-on (SO) projections with associated lattice projection values (Figure 52b, c).

BF-TEM of COF-5/GNF revealed AC and ZZ projections with mean distance of 2.31 ± 0.51 nm. As for COF-5, the distribution was unimodal according to coarseness of measurement technique; only one measurement corresponding to the ZZ projection was found, with the remaining being AC projections (Figure 53b). COF lattice projections were only seen to extend away from the surface of the GNF as for cHBC-COF/GNF in Chapter 2. The SAED of COF-5/GNF was only able to detect spotty rings arising from the GNF. Unlike previous work on COF-5/nanotube hybrids,[5] the morphology does not resemble a "homogeneous" core-shell structure and is notably uneven.

For the remaining COF-5/nanosupport hybirds, no lattice projections were seen in TEM. This was expected for COF-5/SWNT and COF-5/graphite, but not for COF-5/MWNT. This may indicate that the reaction conditions need further optimisation for synthesis of crystalline COF-5/nanosupport hybrids for these materials.

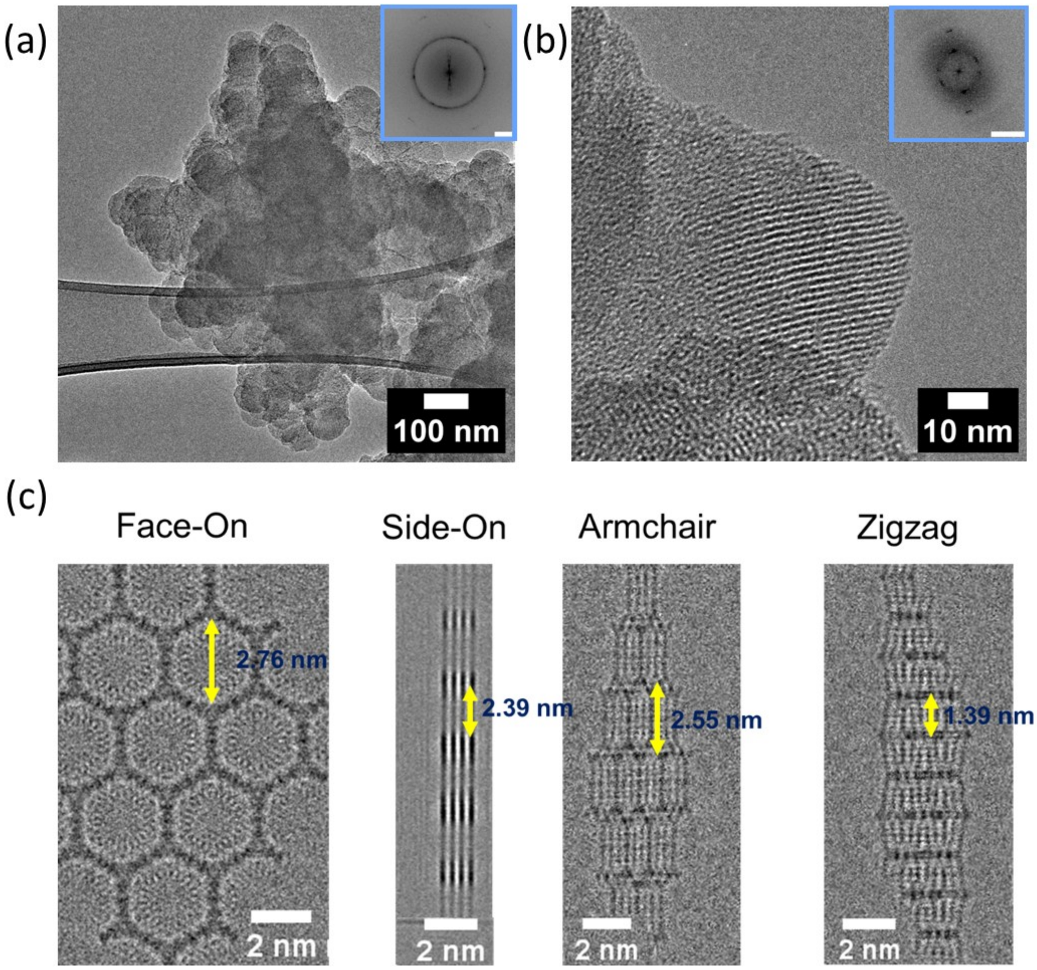

Figure 52: (a) Low-magnification BF-TEM image of COF-5 foam. Insert: Fourier transform, scale bar = 0.2 nm^{-1}. (b) High-magnification BF-TEM image of COF-5 crystallite showing lattice projections with a lattice projections width of 1.9 nm. Insert: Fourier transform, scale bar = 2 nm^{-1}. (c) Image simulations of COF-5 lattice projections. The face-on (FO), side-on (SO), armchair (AC) and zigzag (ZZ) projections are shown along with their characteritic lattice projection distances; respectively 2.76 nm, 2.39 nm, 2.55 nm, and 1.39 nm.

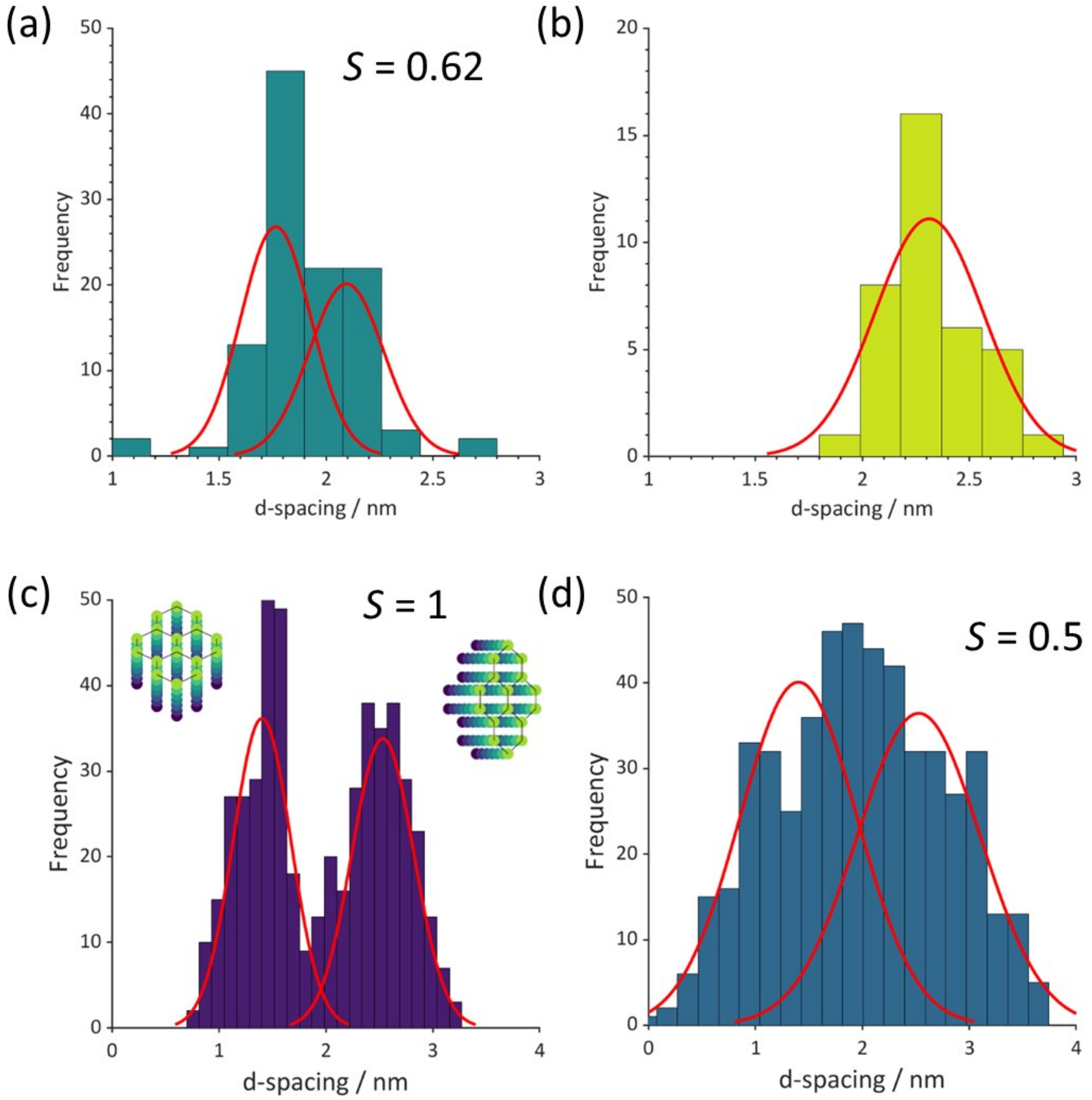

Figure 53: (a) Lattice projection distribution for COF-5, with $S = 0.62$. Distributions indicate the AC and ZZ means. The broad distribution and low number of measurements make detecting two distributions challenging. (b) Unimodal COF-5/GNF lattice projection distribution. Artificial histograms for AC and ZZ using (c) $S = 1$, $\sigma = 0.29$ nm, and (d) $S = 0.5$, $\sigma = 0.58$ nm. For both, $\mu_{AC} = 2.4$ nm, $\mu_{ZZ} = 1.4$ nm, and $\Delta\mu = 1.16$ nm. The red normal curves indicate the AC and ZZ measurements within the datasets. Reducing the bimodal seperation causes the underlying distributions to appear as a single unimodal distribution.

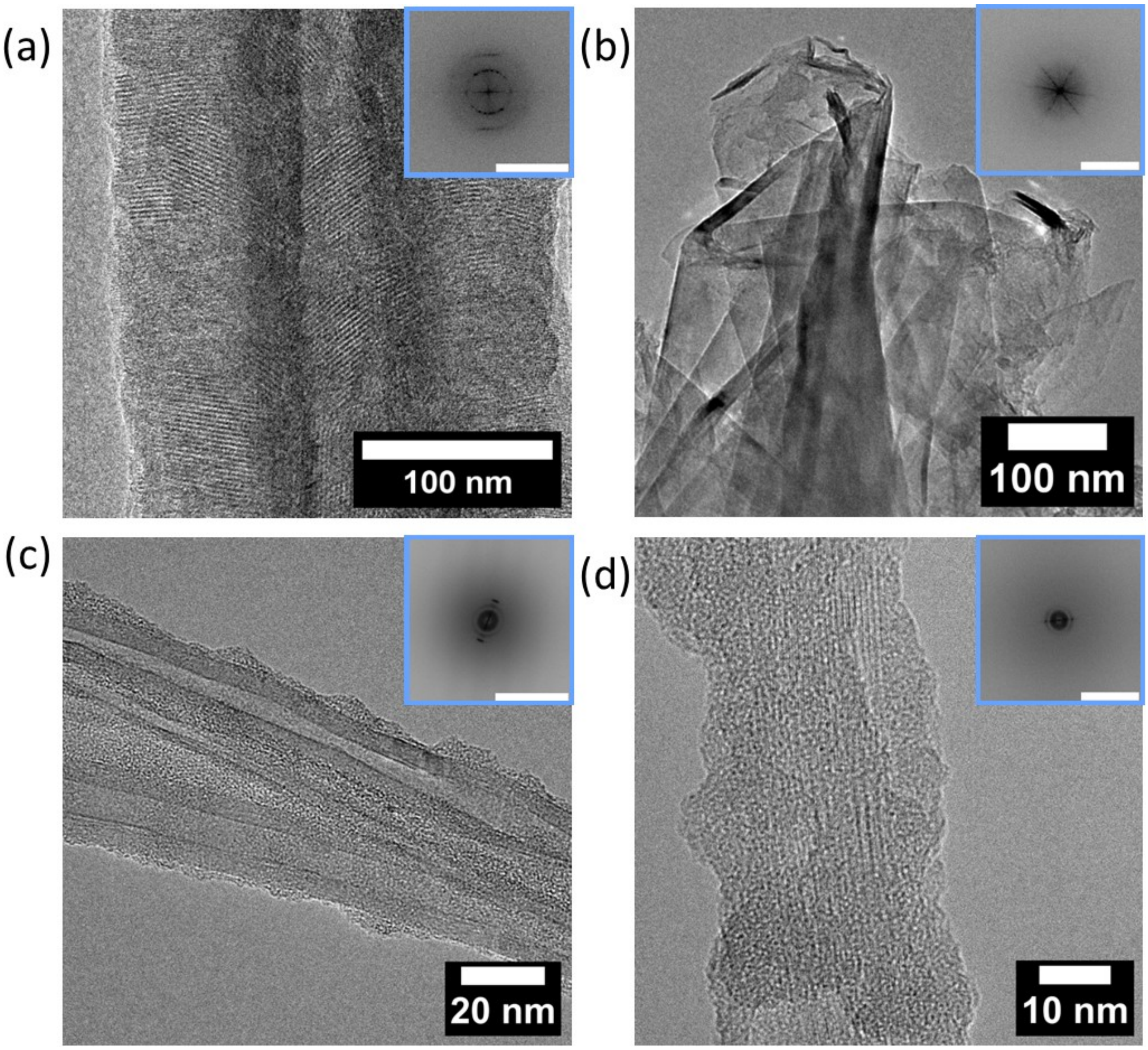

Figure 54: Bright field-TEM images of: (a) COF-5/GNF, with visible lattice projections. Slight variations in COF layer thickness can be seen, and the COF crystallites are not all oriented in the same direction. Insert: FT, scale bar = 1 nm^{-1}. (b) COF-5/graphite. No COF lattice projections can be seen in the image. Insert: FT, scale bar = 0.5 nm^{-1}. (c) COF-5/MWNT. An uneven amorphous layer of COF has formed on the surface of the nanotubes. The layer thickness varies between different tubes. Insert: FT, scale bar = 10 nm^{-1}. (d) Bundle of COF-5/SWNT. The COF has formed on the nanotubes as an uneven amorphous layer, with no lattice projections visible. Insert: FT, scale bar = 10 nm^{-1}.

In the case of COF-5, the AC and ZZ projections occur at 2.55 nm and 1.39 nm respectively. These values were measured from the electronic structure model simulated images. Given the small interval of 1.16 nm between the AC and ZZ projections, and that these projections exist on a continuum, this suggests that the AC and ZZ lattice projections in COF-5 may be indistinguishable in the data set available due to large overlap between the two lattice projection distributions. That is, the unimodal lattice projection distribution may be made up of two overlapping smaller normal distributions. This was tested using computer generated data, comprised of normally distributed data points created using the theoretical mean and a user-defined standard deviation. The theoretical AC and ZZ lattice projections and the experimental standard deviation (0.47 nm) were used to create 500 normally distributed data points, which were then summed together into a single dataset.

As for Chapter 2, histogram binning was chosen to be equally spaced bins. It is worth noting here that different bin sizes can reveal different features of a data set, so there is usually no "best" choice for bin width. The modality of the resulting distribution can be appraised visually and using a bimodal separation index S:

$$S = \frac{\mu_1 - \mu_2}{2(\sigma_1 + \sigma_2)} \tag{13}$$

Where μ are the distribution means and σ are the distribution standard deviations. Setting the value of μ such that $S = 1$ gives a clearly bimodal distribution (Figure 53c). Repeating with larger μ such that $S = 0.5$ gives a unimodal distribution, where the AC and ZZ data points cannot be clearly distinguished from each other (Figure 53d).

Rearranging S slightly:

$$S = \frac{\mu_1 - \mu_2}{2(\sigma_1 + \sigma_2)} = \frac{\Delta\mu}{4\sigma_1} \tag{14}$$

where $\Delta\mu$ is the difference between the means and the standard deviation σ is the same for both projections. It then follow that $S = 1$ when $\Delta\mu = 4\sigma$. From this relationship it becomes clear that to make AC and ZZ distributions more visible in a dataset, either $\Delta\mu$ must be increased by changing the material being studied, or σ should be reduced by using a detector with finer measurement resolution as discussed in the previous paragraph. As a rule of thumb, we can expect a clear bimodal distribution when $S \geq 1$, and a monomodal distribution when $S \leq 0.5$. When $1 \geq S \geq 0.5$ a bimodal distribution may be detectable, but as S becomes closer to 0.5 this becomes more difficult. In this range, the effect of total number of data points in the distribution and the ratio of AC:ZZ data becomes the limiting factor in detecting the presence of two distributions.

For COF-5, $S = 1$ when $\sigma = 0.29$ nm, indicating that a spatial resolution of at most 0.29 nm is required to reliably distinguish between AC and ZZ projections. For the TEM's used in this thesis the pixel size of the camera is less than 0.29 nm above 50,000x magnification, and according to the operators manual the microscope used is capable of 0.25 nm point resolution.[28] We can expect the resolution to be degraded by a combination of the age of the electron source, vibrations in the lab during the imaging session, the quality of the microscope alignment, and the electron flux used for imaging, and the quality/thickness of the sample. In short despite being theoretically possible with the instruments available AC and ZZ distributions were not resolved, implying that a finer measurement resolution is required to find AC and ZZ in COF-5 lattice projection data. This could be achieved using aberration-corrected (AC) TEM, for example.

3.4.3 Selected Area Electron Diffraction

Selected area electron diffraction (SAED) of COF-5 and COF-5/nanosupports revealed no Bragg diffraction spots (Figure 55). As discussed above in the PXRD section, small crystal size leads to weak diffraction compared to literature examples of COF-5 diffraction. Diffraction intensity is proportional to the number of unit cells making up the crystal, so small crystals lead to weaker diffraction spots. As the COF is made up entirely of elements with low atomic form factors, which would lead to weak Bragg diffraction spots. As described in Chapter 1, this could be addressed by growing larger crystals or staining with heavy elements.[7] There is also the unanswered question of the effect of electron beam damage on COF-5 and whether it is destroying the diffraction pattern before it can be recorded - in general for unstable structures it is possible to align the microscope and see a diffraction pattern on the TEM viewing screen, even if the pattern degrades before it can be imaged using the TEM camera, but no pattern was seen.

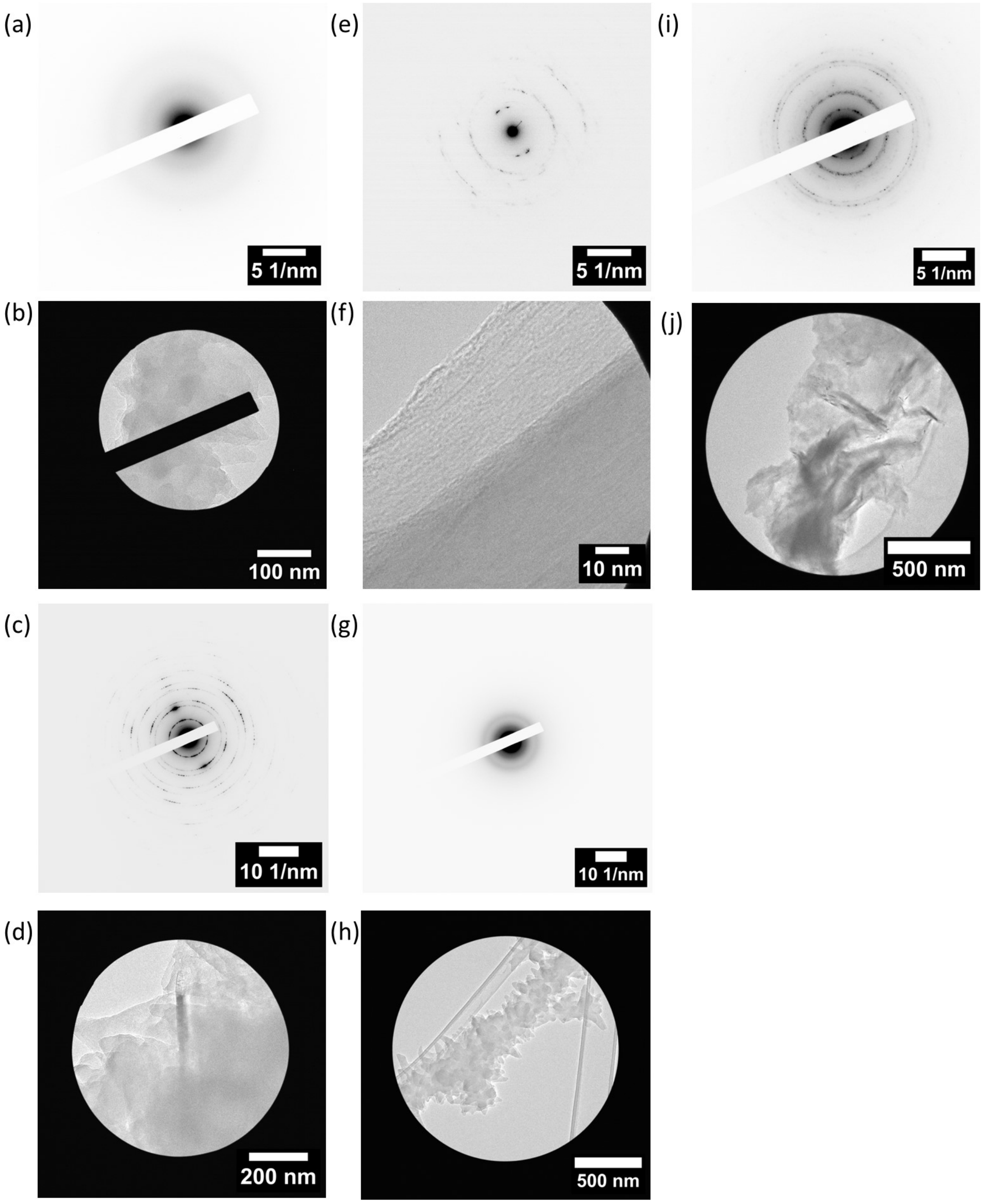

Figure 55: Selected area electron diffraction patterns and corresponding direct-space BF TEM images for: (a, b) COF-5; (c, d) COF-5/graphite; (e, f) COF-5/GNF; (g, h) COF-5/MWNT; (i, j) COF-5/SWNT. The bright spots in the SAED patterns correspond to diffraction from the nanocarbon supports. No diffraction from COF-5 was observed, even when samples had lattice projections visible in BF-TEM imaging.

3.4.4 Electron Energy Loss Spectroscopy

Electron energy loss spectroscopy (EELS) of COF-5 was not well-developed in the literature at the time of writing. Both the low-loss and core-loss spectra of COF-5 were investigated in this work. COF-5 and COF-5/nanosupports contained clear sp^2 carbon K edges(Figure 56a-e). A faint boron K edge was found for COF-5, but background fitting was not able to show a boron K edge for any COF-5/nanosupport samples (Figure 56f-j). The presence of a boron K edge is likely due to the relatively large amount of boron compared to carbon in the COF-5 polymer; for COF-5/nanosupport the concentration of boron is reduced by the presence of nanosupport, which could reduce the intensity of the boron K edge. The elemental formula for the COF-5 repeat unit is $C_{54}H_{24}O_{12}B_6$, with atomic percentages: C = 56%, H = 25%, O = 12%, B = 6 %. A faint oxygen K edge was seen for COF-5, with no edges seen for the COF-5/nanosupport hybrids 56k-o). No other edges were seen in the COF-5 EEL spectrum. As mentioned in the previous chapter, using a more sensitive EELS detector or limiting the collected electrons to the characteristic scattering angle for the boron K edge would be able to show the presence of a boron K edge more easily.

The low-loss EEL spectrum of COF-5 was deconvoluted using the Fourier-log method, then thickness estimates were generated using Kramers-Kronig analysis (Figure 57, 58). For analysis the refractive index of COF-5 was assumed to be 2, consistent with the previous chapter. This gave reasonable thickness estimates; for example the thickness of COF-5/GNF was calculated to be 138 nm, which would correspond to the electron beam passing through the GNF as well as the COF-5 shell. This corresponds to the GNF having 34 nm side walls and 104 nm thick layer of COF-5. The calculated thickness of COF-5 also rationalises well with the observed width of COF-5 crystals in BF-TEM, assuming that the COF does not have anisotropic thickness. This agrees with the foamy morphology observed in BF-TEM and SEM, where the COF foam forms as roughly spherical nodules. The plasmon peaks are broad, implying the materials are semiconductors,[29] and aside from the $\pi - \pi^*$ transition at 9 eV in the spectrum of COF-5/graphite and COF-5/GNF, no interband transitions are seen. A shoulder can be seen in the PSD of COF-5 and COF-5/MWNT that has been removed by deconvolution, highlighting once more the need for better energy resolution to investigate the pre-plasmon region of the low-loss spectrum. The difference in plasmon energies between samples likely represents different morphology for each COF/nanosupport structure.[29]

Sample	t**(KraKro) / nm**	**Plasmon peak / eV**
COF-5	13.8	24 ± 3.0
COF-5/graphite	29.0	25 ± 2.3
COF-5/GNF	138	30 ± 2.6
COF-5/MWNT	29.2	23 ± 3.7
COF-5/SWNT	3.82	22 ± 2.4
pyro(GNF)	79.6	17.75 ± 2.5
pyro(COF-5/GNF)	134	22 ± 5.2
pyro(COF-5)	254	27 ± 5.3
Graphite	14.3	25.4 ± 2.0
GNF	23.4	17.8 ± 2.5
MWNT	3.2	20.3 ± 2.0
SWNT	2.4	22.8 ± 2.0

Table 12: Kramers-Kronig analysis thickness (*t*), plasmon peaks measured from low-loss EEL spectrum for COF-5, COF-5/nanosupports, and pyrolysed COF-5 materials. The position of the plasmon peak is affected by the sample composition, i.e. presence of nanosupports.

As discussed in the previous chapter, the low-loss spectra could not be used for accurate band-gap measurements due to poor energy resolution and effects of spectrum deconvolution. The measured band-gap of COF-5 was 2 ± 3 eV; given the limited energy resolution available, this cannot be meaningfully compared to the literature calculated band-gap of 2.5 eV - 3.3 eV.[2] For COF-5/nanosupport hybrids, conductive nanosupports such as graphite mask the presence of a band gap. In the samples of COF/GNF, COF/MWNT, and COF/SWNT a band gap was detected which is consistent with the band gap of COF-5 (Appendix Table 26).

Overall, EELS of COF-5 has allowed facile elemental analysis and nanoscale spatial resolution band gap measurements. The clear next step for this work is to use an EELS system with better energy resolution to derive optical properties of COF-5/nanosupport hybrids with nanoscale spatial resolution.

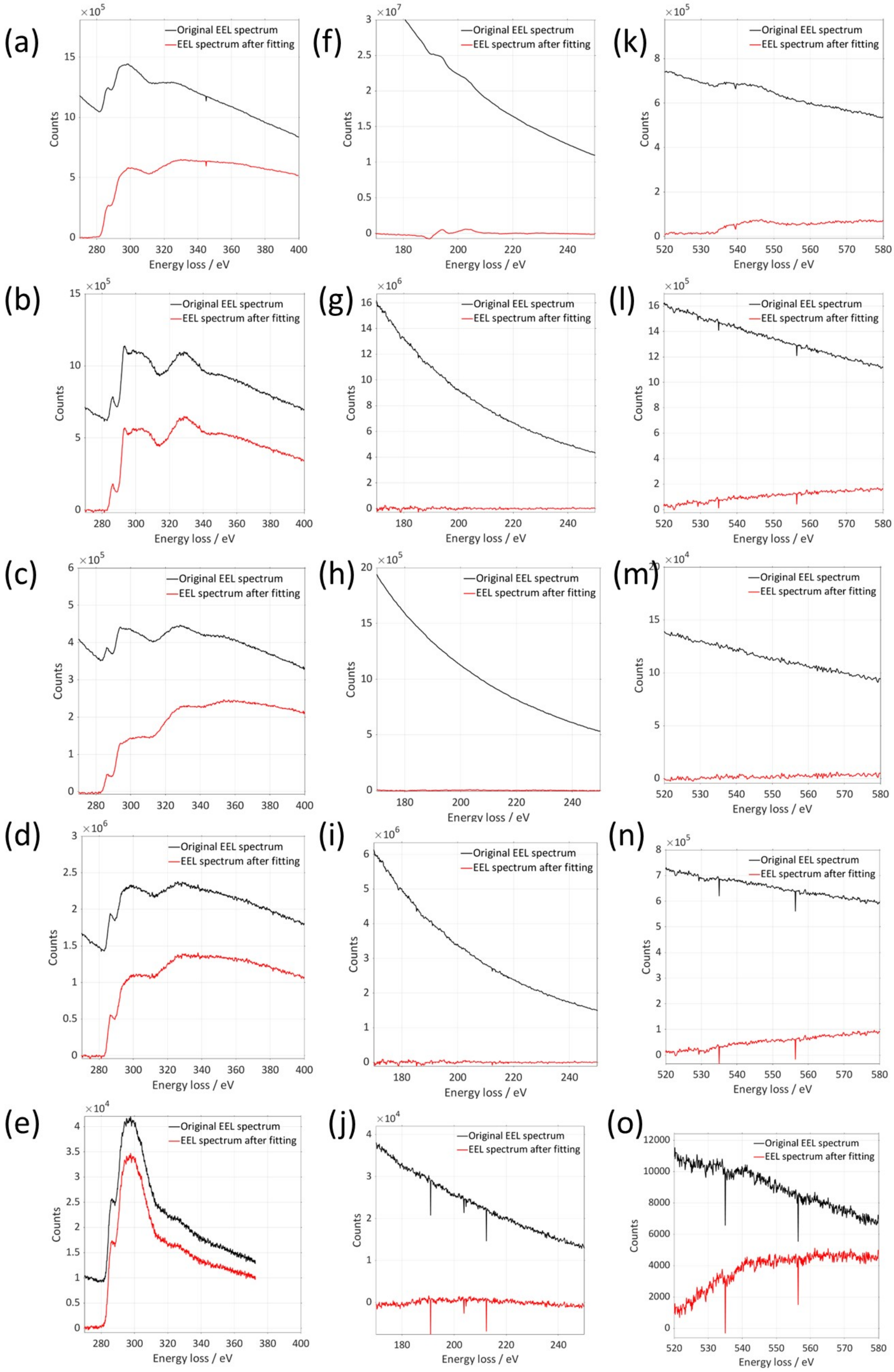

Figure 56: Core loss EEL spectra. Top to bottom: COF-5; COF-5/graphite; COF-5/GNF; COF-5/MWNT; COF-5/SWNT. (a-e) Carbon K edge. (f-j) Boron K edge region. (k-n) Oxygen K edge region. A weak boron K edge was detected for COF-5. Carbon K edges are clearly sp^2 hybridised.

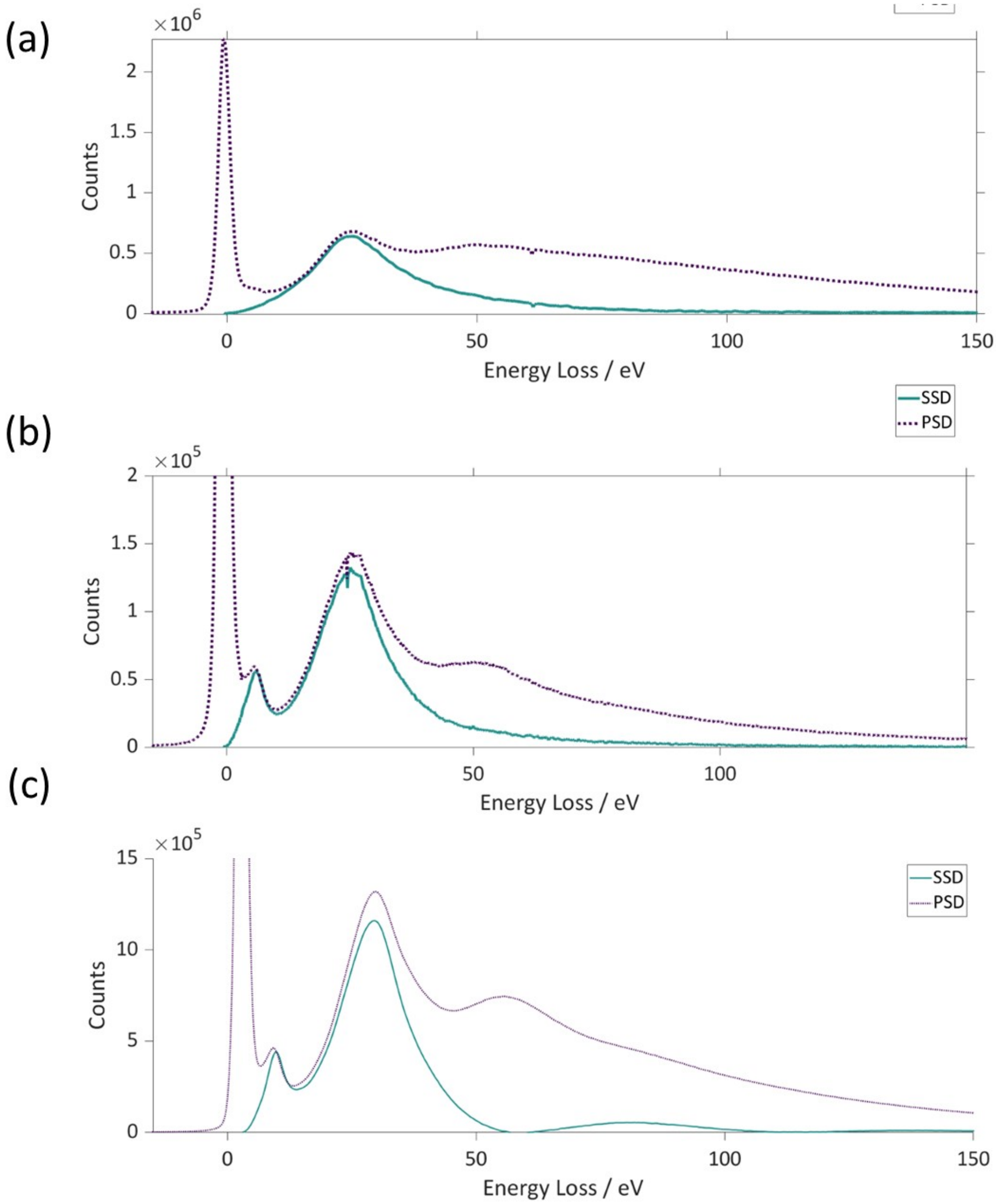

Figure 57: Low-loss EEL spectra for: (a) COF-5; (b) COF-5/graphite, with the peak at 6.2 eV is the $\pi - \pi*$ inter-band transition; (c) COF-5/GNF, showing the effects of plural scattering on the spectrum causing an increase in the plasmon thickness. Plural scattering has little effect on the plasmon energy.

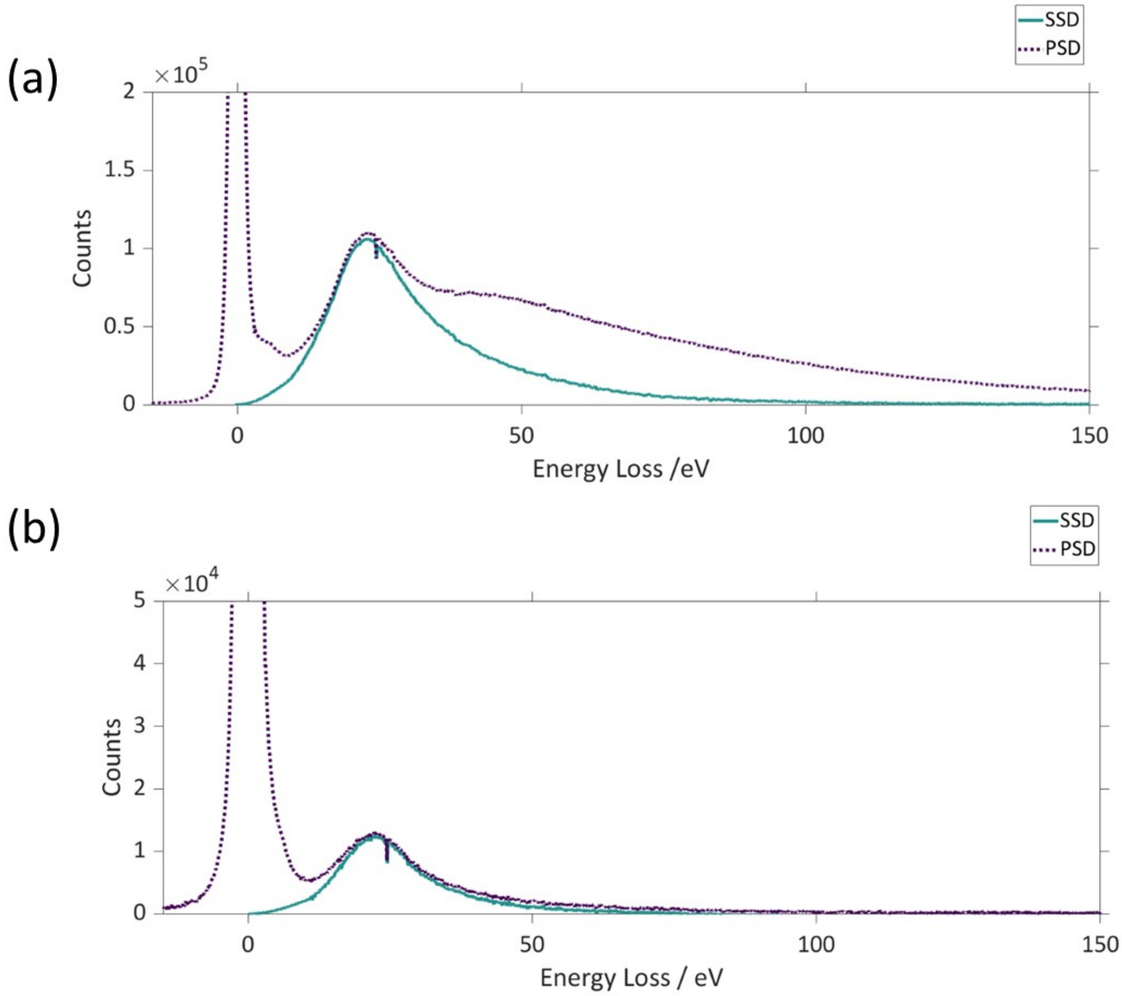

Figure 58: Low-loss EEL spectra of: (a) COF-5/MWNT; (b) COF-5/SWNT. A shoulder can be seen on the COF-5/MWNT zero-loss peak that was removed via deconvolution, highlighting the need for higher energy resolution spectra.

3.4.5 Energy Dispersive X-ray Spectroscopy

Energy dispersive X-ray spectroscopy (EDX) spectra were simulated for an ideal COF-5 over vacuum (Appendix Figure 111b). As for cHBC-BDA-COF in Chapter 2, only carbon and oxygen peaks were seen as the boron peak is low-intensity and overlaps with the carbon peak. It was therefore expected that the boron peak will be difficult to detect in experimental EDX.

All samples contained carbon, due to the carbon support film, COF, and nanocarbon supports in the samples (Figure 59, 60). All samples also contained oxygen, due to oxygen in the COF and oxidation of the support film and nanocarbon supports. Trace elements with abundance less than 1 % were seen in samples, due to common containments: silicon, chlorine, bromine, calcium, sodium, and potassium. Iron, chromium, and copper were also seen, arising from the materials used to make the microscope. Boron was seen in the spectrum of COF-5/MWNT, however for the others boron was not seen due to the overlap between the carbon and boron peaks and the low abundance of boron in the samples compared to carbon.

Overall EDX spectroscopy served to confirm that there were no unexpected elements in the material being examined, all all impurities could be rationalised as coming from expected sources.

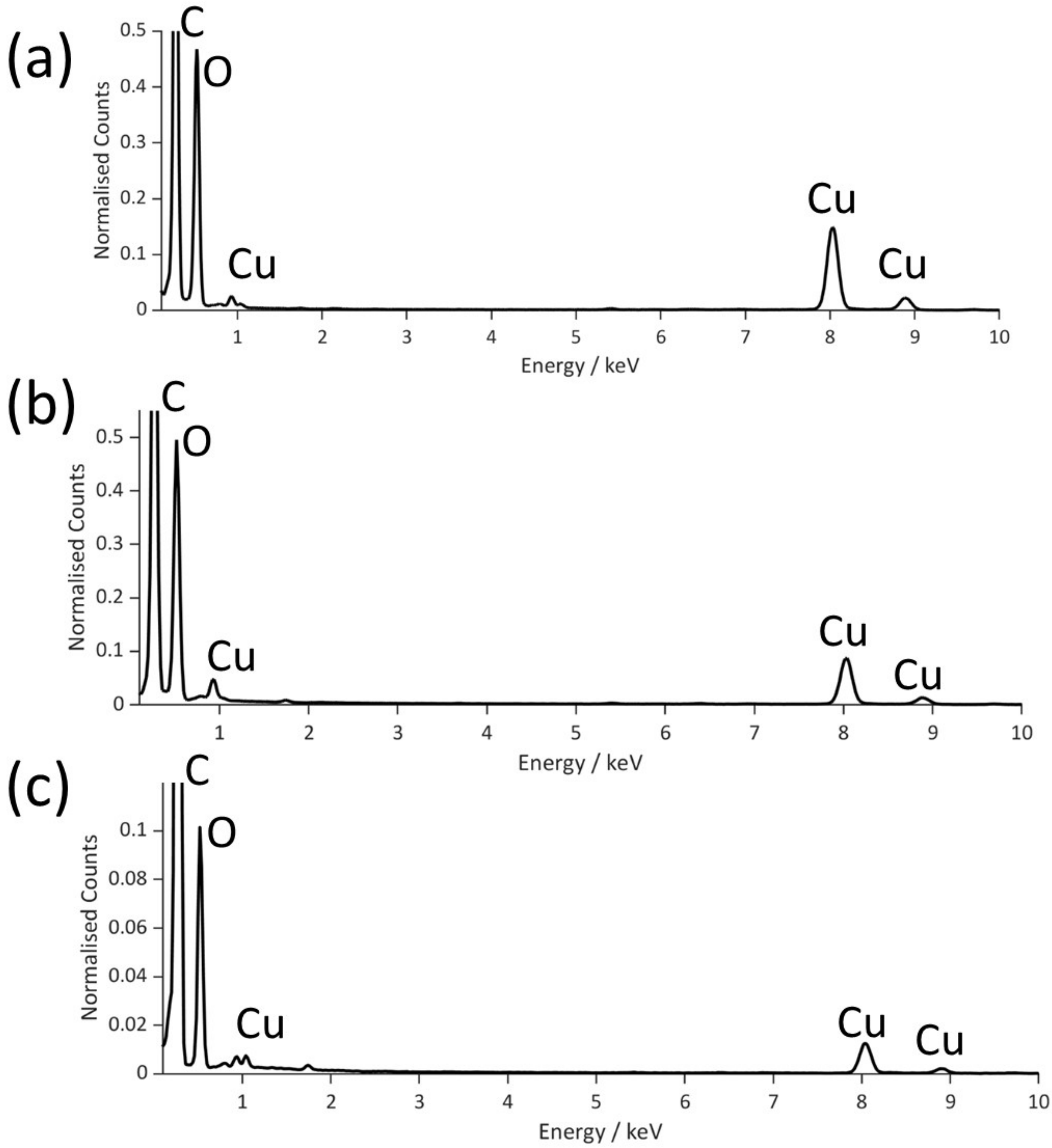

Figure 59: EDX spectra for: (a) COF-5; (b) COF-5/graphite; (c) COF-5/GNF. Carbon and oxygen are from COF-5 and nanosupports, while copper is from the TEM grids used in this work.

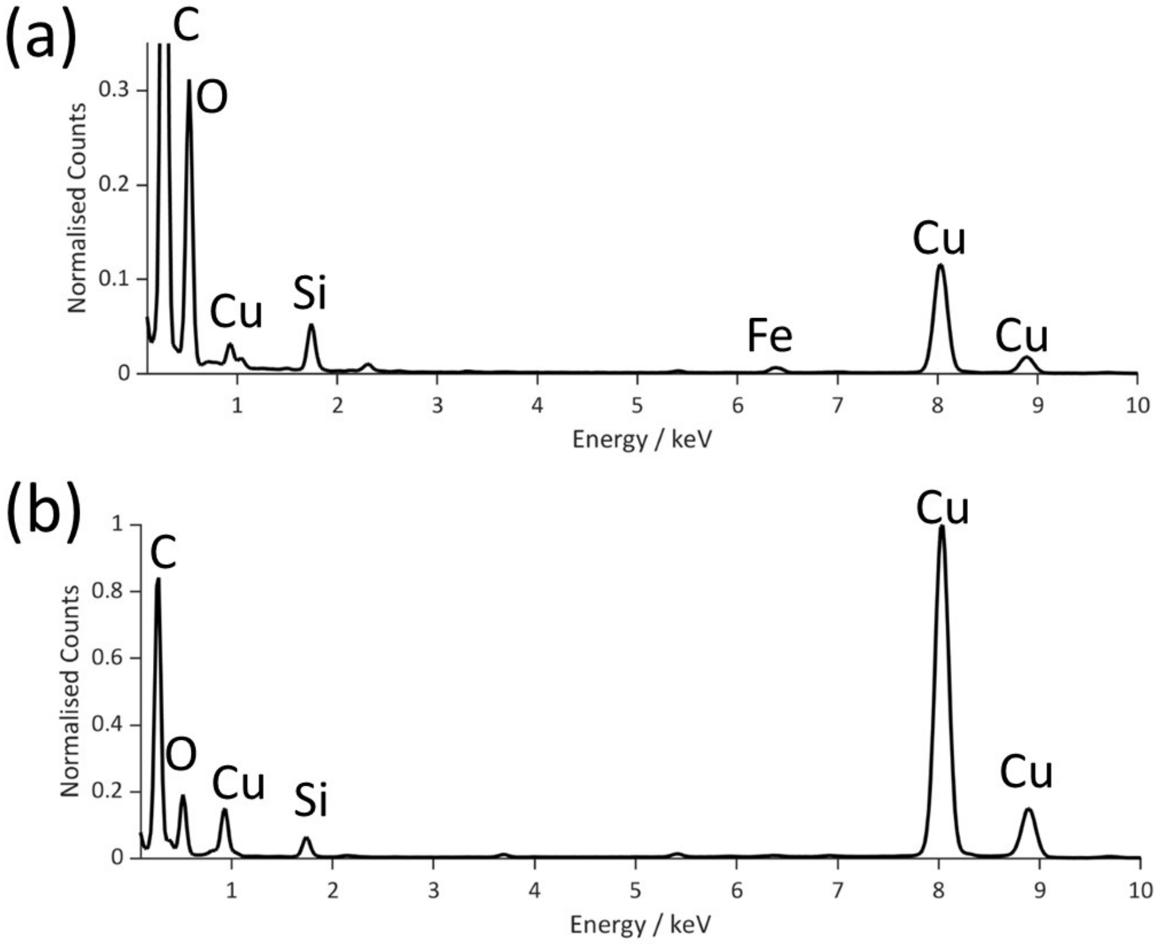

Figure 60: EDX spectra for: (a) COF-5/MWNT; (b) COF-5/SWNT. Carbon and oxygen are from COF-5 and nanosupports, while copper is from the TEM grids used in this work. A weak iron signal is from the materials used to make the TEM column, and silicon is a common contaminant.

3.5 Pyrolysis of COF-5 and COF-5/GNF

3.5.1 Pyrolysis and Bulk Analysis

Having developed understanding for COF-5/nanosupport TEM lattice projections, it was decided to study how these systems change when subjected to high temperature under inert atmosphere. This functions as an extension of the TGA combustion work mentioned earlier in this chapter, with pyrolysis representing another recycling route for COF-5 at the end of it's useful lifetime. COF-5 has previously been pyrolysed to give a boron-doped carbon material,[17] and an X-ray study of structural changes to COF-5 while heated under inert atmosphere has called for application of direct imaging to more fully understand the processes occurring.[25]

The pyrolysis procedure used was to heat the sample to 1000 °C then cool to room temperature, under flow of argon. This prevents any oxidation from occurring during the cooling phase, as by default the TGA uses a stream of compressed air to aid cooling that would cause the pyrolysed sample to combust.

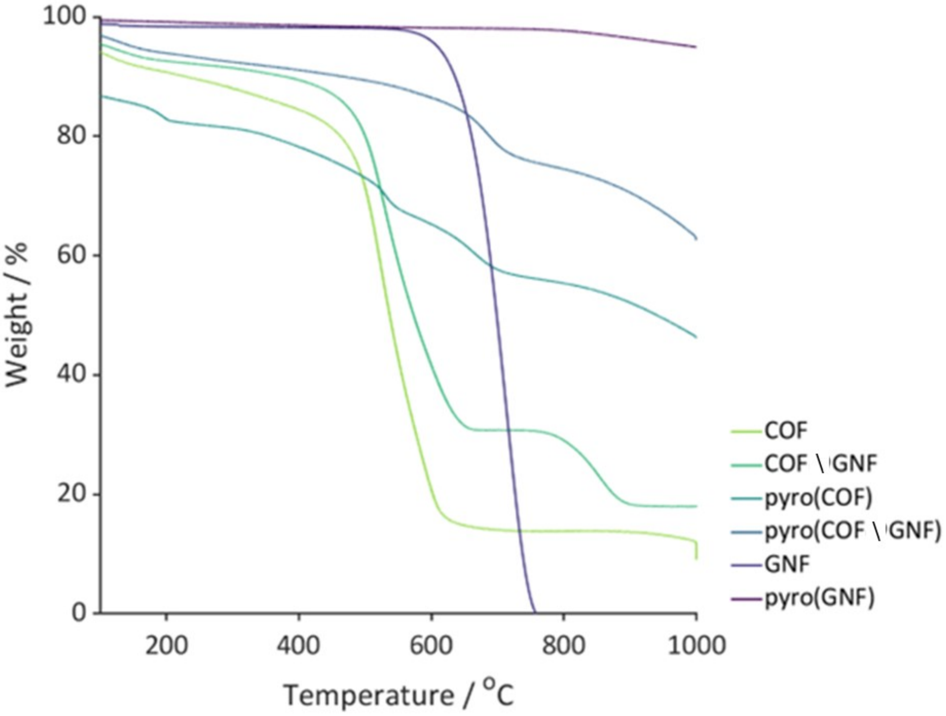

Figure 61: Thermograms for pyrolysis of COF-5, COF-5/GNF, and GNF. Combustion thermograms of COF-5 and COF-5/GNF have been included for comparison. Pyrolysis causes a much smaller mass loss than combustion, less than 5 % in the case of GNFs.

GNFs were pyrolysed as a control (Figure 61). It was found that the total mass loss was 6 % at 1000 °C, which corresponds to loss of adsorbed volatiles and reduction of the oxidised ends of the GNF. It should be noted that the final event in the thermogram is still ongoing at 1000 °C; as the TGA used cannot heat safely above 1000 °C this could not be probed further. The observed thermal processes are probably akin to the industrial process "coking", the transformation of coal to coke by heating coal above 1000 °C under inert atmosphere.[30] Coking can proceed via several catalytic pathways that cause loss of organic materials and volatiles trapped in the coal, and leads to a very pure solid carbon product. Coking an occur in a variety of chemical systems.[31,32] The presence of coking in these samples is, at this stage, conjecture. However BF-TEM images of the pyro(GNF) shows evidence of damage to the GNF side-walls as a result of pyrolysis (Figure 65a), which could be due to reduction of defects and loss of volatiles. The GNF SAED pattern was not affected by pyrolysis. The IR vibrations of pyro(GNF) are very similar to those of GNF

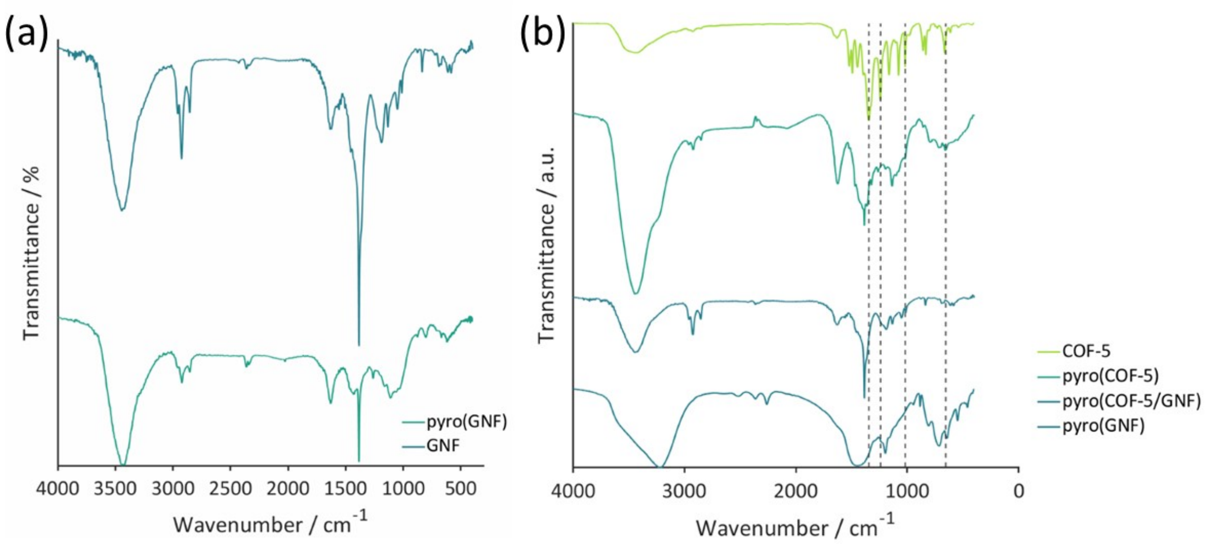

Figure 62: Potassium bromide pellet IR for pyrolysed materials. (a) GNF (top) and pyro(GNF) (bottom). (b) COF-5. pyro(COF-5), pyro(COF-5/GNF), and pyro(GNF). Boronate ester stretches arising from COF-5 have been indicated via dotted lines; these stretches are essentially absent from the pyrolysis spectra. This indicates a significant chemical change as a result of thermal treatment. All spectra have a significant O-H stretch due to water adsorbing into the hygroscopic pellet, as well as C=O stretches from atmospheric carbon dioxide.

(Figure 62a).[33] The pyro(GNF) spectrum shows a decrease in intensity of the C-H stretching modes at 2924 cm^{-1}, and a change in shape of the radial breathing mode at 1383 cm^{-1}. The band at 1186 cm^{-1} that corresponds to the D-band in Raman spectra of GNFs and has been shown to be present in spectra of various nanotubes[34] is largely absent in the pyro(GNF) spectrum, indicating a reduction of defects in the the sample. The is minimal difference in the C=O stretching band at 2362 cm^{-1} arising from carbon dioxide; while CO_2 intercalation has been shown for graphite oxide[35] (and likely occurs for GNFs), and pyrolysis could change the concentration of CO_2 in the GNF, atmospheric CO_2 effectively masks this. The fingerprint region in general has a very different profile. These changes can be rationalised as a reduced amount of amorphous carbon within the sample, fixing of defects within the GNF, and reduction of C-H bonds at the ends of the GNF.

Pyrolysis of COF-5 and COF-5/GNF was achieved using the same conditions as for GNF (Figure 61). As for pyro(GNF), pyro(COF-5) and pyro(COF-5/GNF) have residual mass at 1000 °C corresponding to a reduced carbonaceous material, and there is an ongoing thermal event at 1000 °C that may be a coking process. The IR spectra of the pyrolysed material show attenuation of the B-O stretches characteristic of COFs, and an increase in the vibrations corresponding to graphitic and carbonaceous materials (Figure 62b).

The MALDI mass spectrum of the pyrolysed material gave a weak signal in positive ion mode and no signal in negative ion mode (Figure 63). This is consistent with the mass spectra of carbonaceous materials, which tend to form positive ions (especially if they contain electron-rich aromatic systems). The key finding from the mass spectrum is that neither pyro(COF-5) or pyro(COF-5/GNF) contain ions corresponding to HHTP. This aligns well with the TGA and IR data which suggested that the aromatic COF monomers are converted into an amorphous carbon structure as a result of pyrolysis.

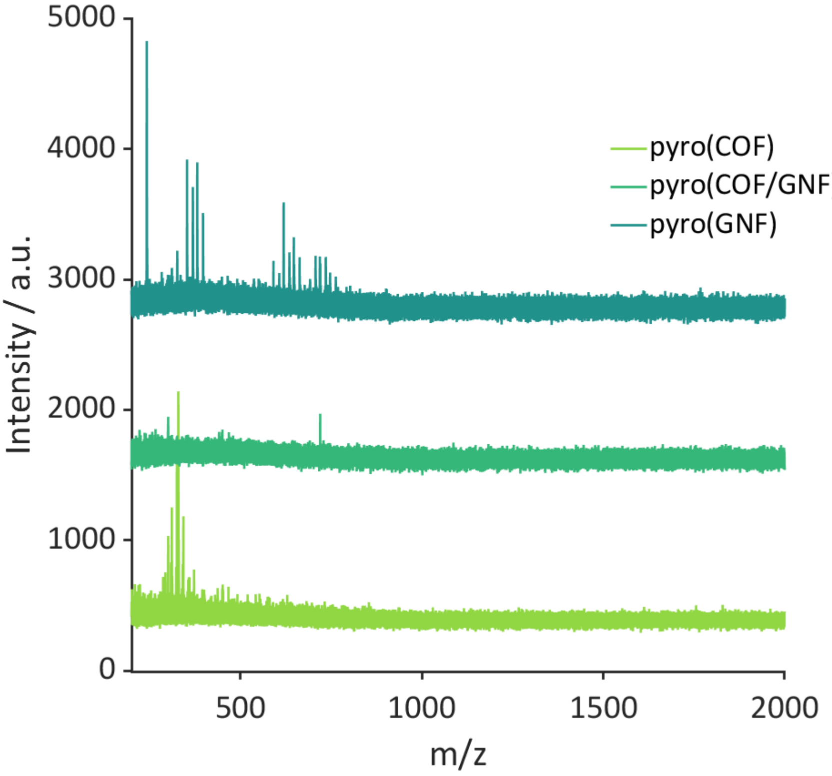

Figure 63: MALDI-TOF MS of pyrolysis products materials, showing a small number of weak peaks resulting from the ionisation of carbonaceous materials. No ions corresponding to COF-5 were seen, suggesting chemical transformation to an amorphous carbonaceous structure.

3.5.2 Electron Imaging and Spectroscopy of Pyrolysed Materials

BF-TEM imaging shows that the material formed at 1000 °C has an amorphous structure (Figure 66). This is consistent with a variable temperature X-ray diffraction study that found that COF-5 becomes amorphous at high temperatures.[25] EDX and EEL spectroscopy was unable to find any evidence of boron, but as discussed in the earlier EELS section this is inconclusive for the actual presence of boron in COF structures. EDX found that pyrolysed material had a lower ratio of oxygen to carbon, corroborating the thermal reduction supposed above (Figure 69). The carbon K edges in the core-loss EEL spectra were still sp^2 hybridised, which no clear boron or oxygen K edges were resolved (Figure 68). Compared to COF-5, pyro(COF-5) has approximately the same energy plasmon peak, but further investigation of the plasmon is limited by the energy resolution available. Pyro(GNF) has a higher energy plasmon than GNFs, but this could be an effect of the GNF diameter rather than the pyrolysis. Pyro(COF-5/GNF) had a lower energy plasmon than COF-5/GNF. SEM imaging was not able to resolve damage to the GNFs, due to the small scale and damage typically being localised to the interior of the GNF (Figure 64a). The SEM images of pyro(COF-5) and pyro(COF-5/GNF) corroborate the findings from BF-TEM (Figure 64b, c).

For further investigation, identical location TEM-pyrolysis-TEM could be undertaken to see the effects of pyrolysis on a local area of the sample; an area could be imaged using a TEM finder grid, followed by pyrolysis of the sample on the grid, which can then be put back into the TEM and the previously viewed area imaged again. Heating above 1000 °C could also be undertaken to investigate whether any further mass loss or structural changes occur in the sample. The materials also could be made on a larger scale (around 0.5 g) so that they could be investigated by CHN and ICP elemental analysis to investigate whether any boron is left in the pyrolysed structure.

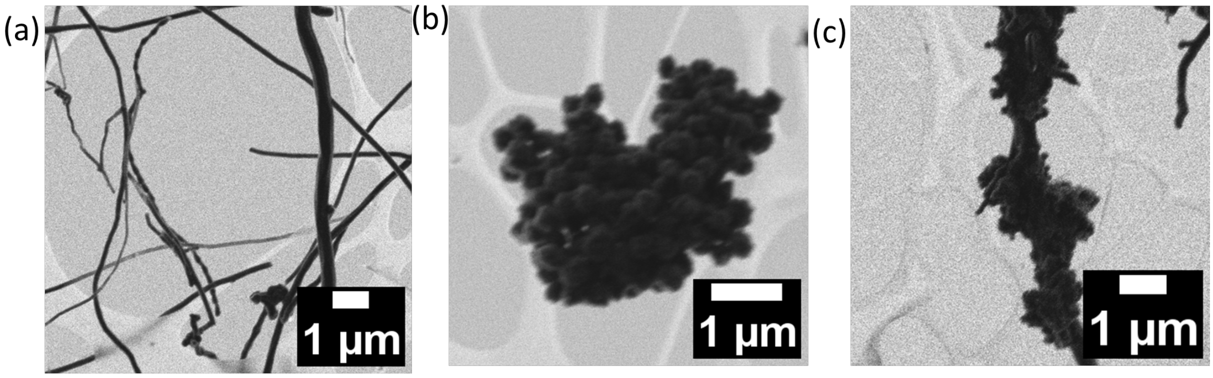

Figure 64: Scanning electron microscopy images of pyrolysis products illustrating the morphology of these materials. (a) Pyro(COF-5). (b) pyro(COF-5/GNF). (c) Pyro(GNF). While the GNF-containing materials appear very similar by SEM, pyro(COF-5) appears to have shrunk compared to the SEM of COF-5. This may indicate pore-collapse during pyrolysis.

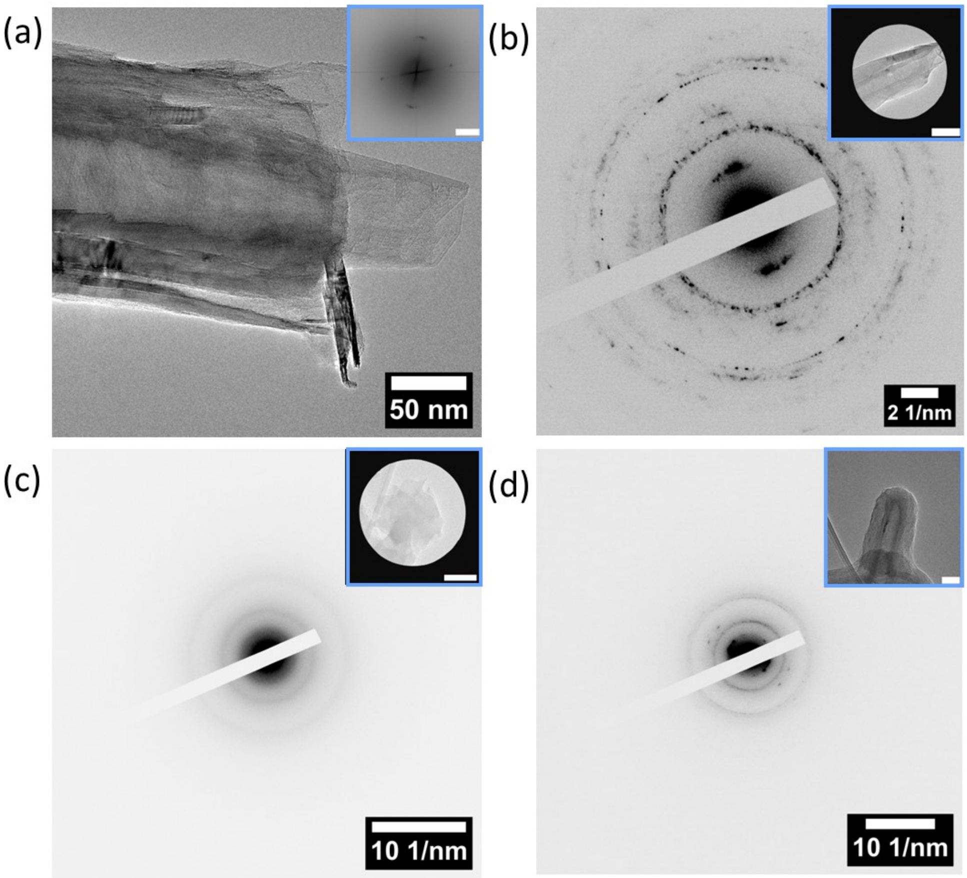

Figure 65: (a) BF-TEM pyro(GNF), illustrating the damage that pyrolysis has on the carbon side-walls. Insert: FT, scale bar = 2 1/nm. (b) SAED of pyro(GNF), with all reflections coming from graphitic carbon. Insert: BF-TEM image of SAED area, scale bar = 100 nm. (c) SAED pattern of pyro(COF-5), showing no specular diffraction. Insert: BF-TEM image of SAED area, scale bar = 100 nm. (d) SAED of pyro(COF-5/GNF), with specular diffraction from the GNF. Insert: BF-TEM image of SAED area, scale bar = 100 nm. These results suggest that the pyrolysis product is an amorphous structure.

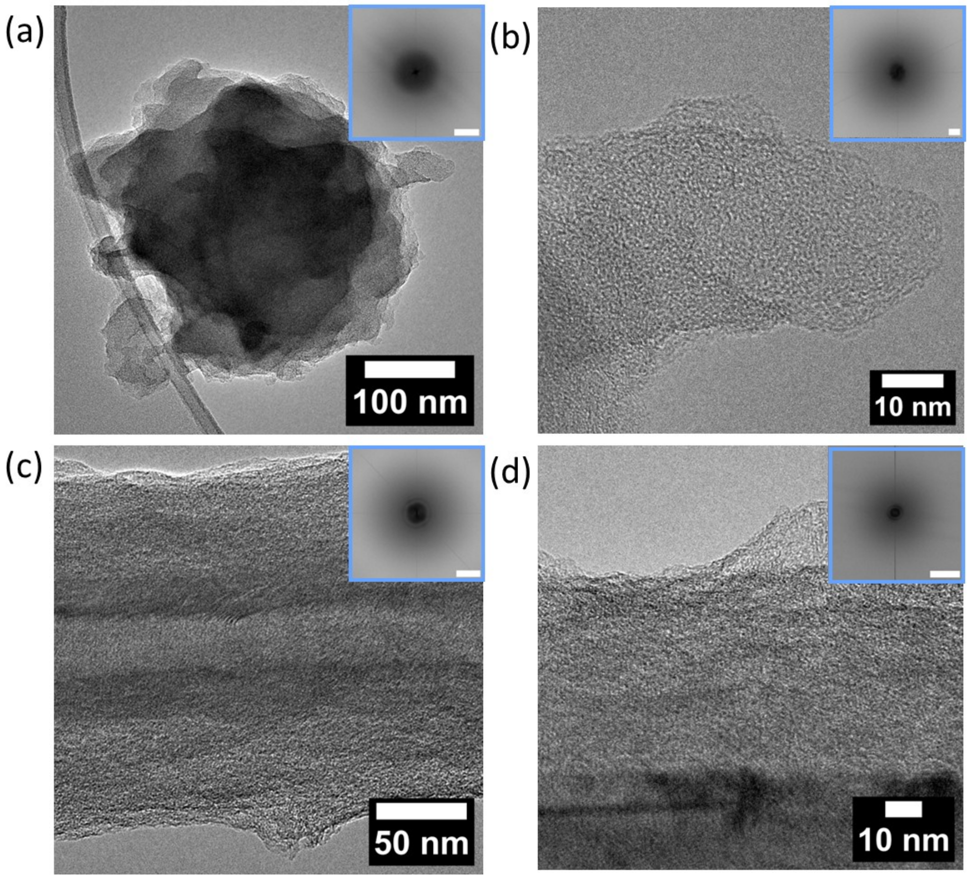

Figure 66: BF-TEM images of: (a) pyro(COF-5), low magnification. No lattice projections or d-spacing can be seen. Insert: FT, scale bar = 10 nm^{-1}. (b) pyro(COF-5), high magnification. The structure is amorphous by BF-TEM, and lacks the distinctive scale shape of the COF-5 crystallites. Insert: FT, scale bar = 1 nm^{-1}. (c) pyro(COF-5/GNF), low magnification. The pyrolysed COF-5 remains as an uneven layer around the nanosupport. Insert: FT, scale bar = 2 nm^{-1}. (d) Pyro(COF-5/GNF), high magnification. No lattice projections can be seen, indicating thermal transformation to a new structure. Insert: FT, scale bar = 2 nm^{-1}.

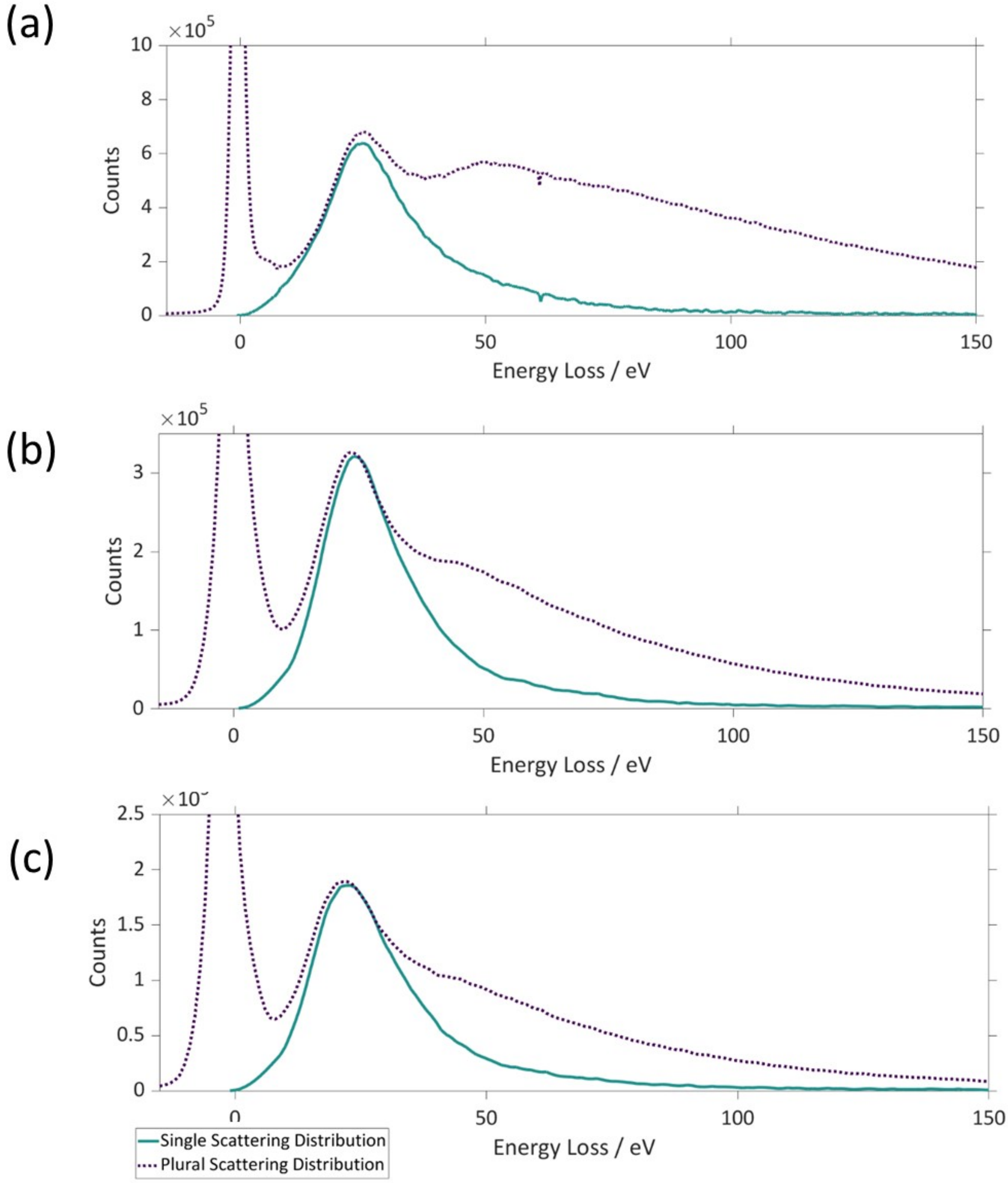

Figure 67: Low-loss EEL spectra of: (a) Pyro(GNF). (b) pyro(COF-5). (c) Pyro(COF-5/GNF). Limitations of deconvolution were discussed earlier and in Chapter 2, and is likely removing information from the pre-plasmon region. A small shoulder can be seen in the plural scattering distribution (PSD) of pyro(COF-5) that is absent in the single-scattering distribution (SSD). The plasmon energy has been affected by pyrolysis, but the low energy-resolution makes this effect difficult to reliably quantify.

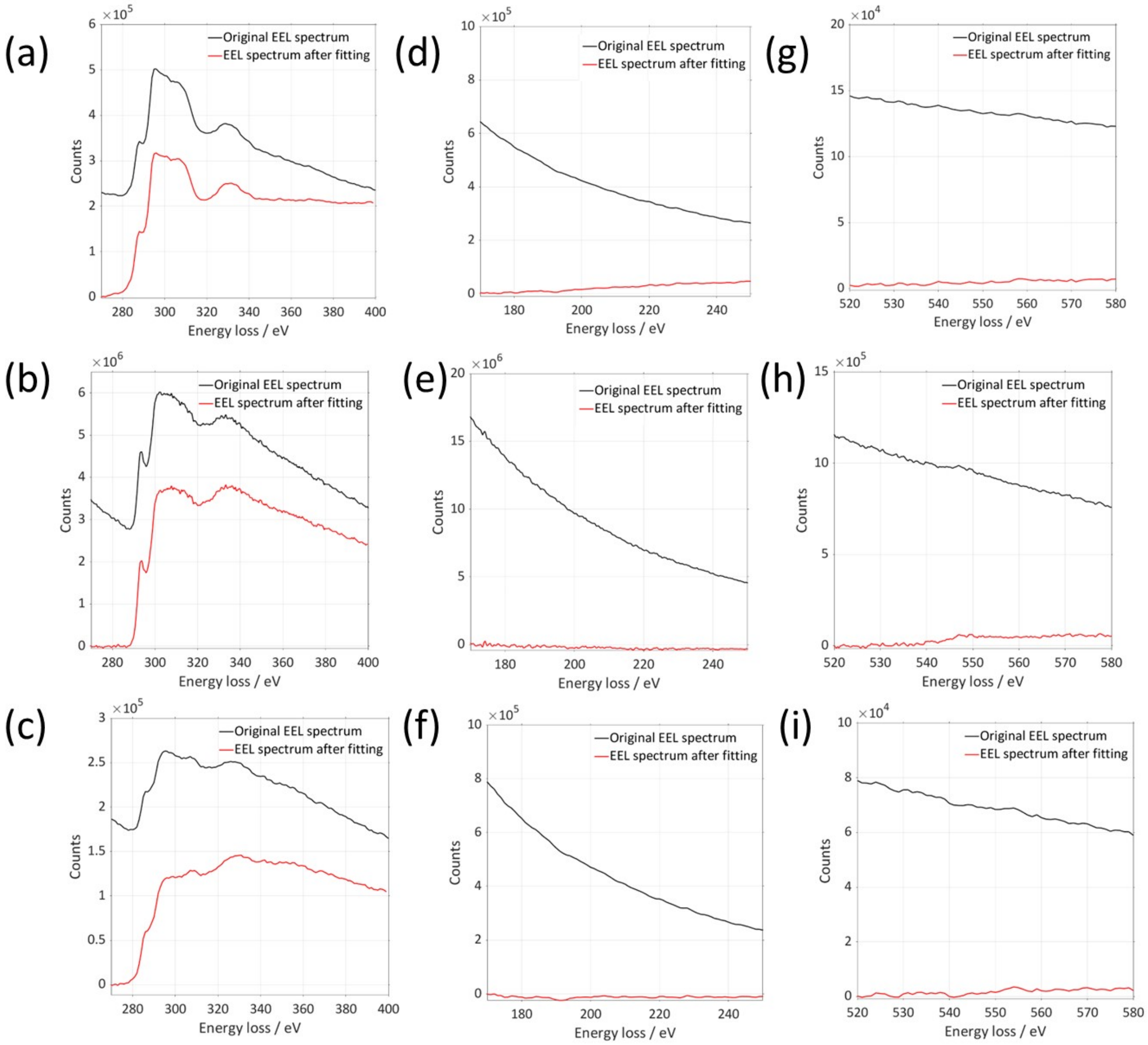

Figure 68: Core-loss EEL spectra of pyrolysis products. Top to bottom: Pyro(GNF), pyro(COF-5), pyro(COF-5/GNF). (a-c) Carbon K edge. (d-f) Boron K edge. (g-i) Oxygen K edge. The carbon K edges are sp^2 hybridised, indicating that the pyrolysis products may contain aromatic carbon. Lack of boron K edges does not mean there is no boron in the structure of these material due to the detection issues discussed earlier in this thesis.

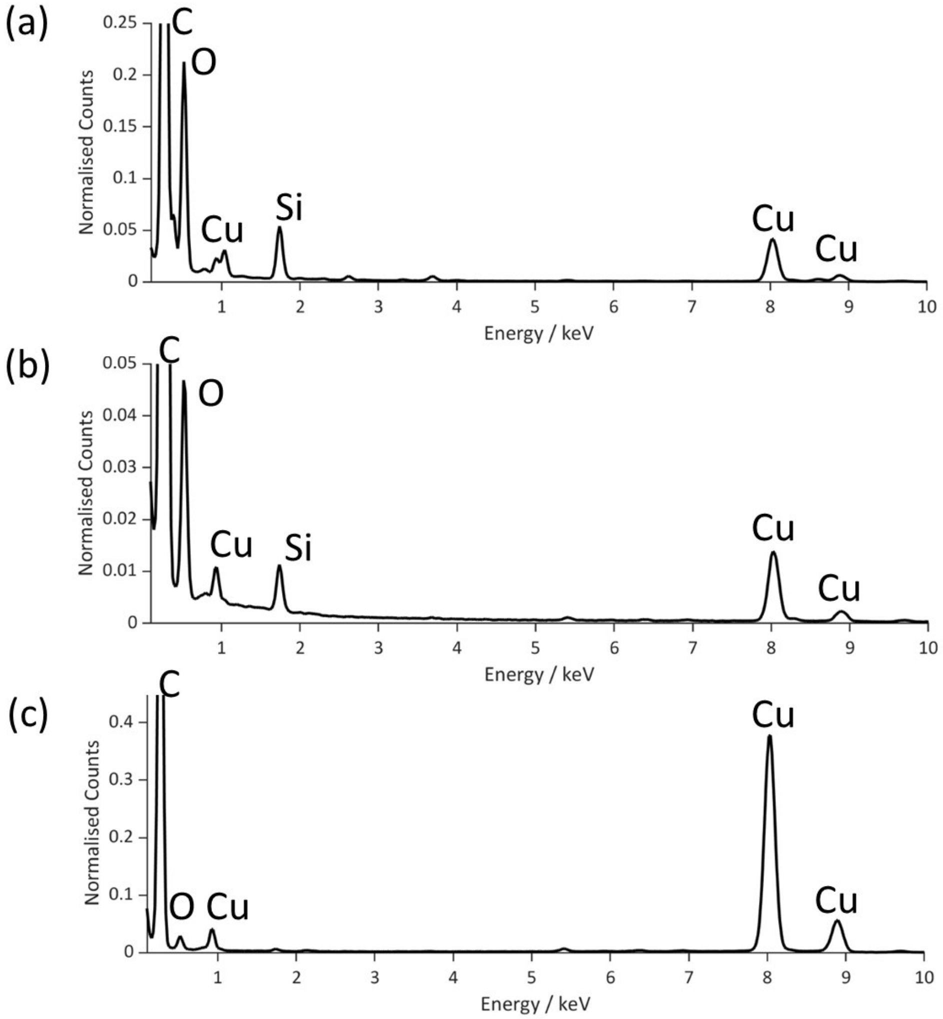

Figure 69: EDX spectra of pyrolysis products. (a) pyro(COF-5). (b) pyro(COF-5/GNF). (c) pyro(GNF). The carbon and oxygen signals are due to the sample, while copper and silicon are common contaminants in EDX as discussed earlier in this thesis.

3.6 Summary

COF-5 was synthesised via a modified literature procedure[13] to give COF-5 as nanocrystalline foamy COF. Amorphous COF-5 was found to form readily under a range of reaction conditions with concentration of water in the solvent system being the most important factor in amorphous COF formation, consistent with previous studies on COF-5 formation.[12] This is likely due to water and low temperatures preventing error-checking from forming a crystalline polymer. COF-5 was then successfully hybridised with GNFs, and acrystalline COF-5/nanosupport was achieved using graphite, MWNTs, and SWNTs. The IR spectrum of amorphous and crystalline COF-5 were found to be essentially identical, with evidence of boronate ester formation through the appearance of characteristic vibrations in the spectrum.[23] MALDI mass spectrometry was able to provide evidence of COF-5 polymerisation, and the application of standard samples to quantify ion ratios was suggested. TGA was used to find the loading of COF-5 on the nanosupports used, and found that the size of nanosupports affected the thermal stability of COF-5. PXRD and SAED were unable to show any specular diffraction peaks arising from COF-5, rationalised as being due to the small size of the COF-5 crystallites. SEM imaging was consistent with previous studies of COF-5.[1]

BF-TEM imaging of COF-5 and COF-5/GNF revealed nanoscale crystallites. A lattice projection distribution was not able to show underlying AC and ZZ distributions, with computer-generated data being used to show that this is an effect of the TEM spatial resolution and low number of measurements made. BF-TEM showed that nanosupports led to thin layers of COF-5 at the surface of the nanosupport, but the presence of COF-5 not associated with nanosupport showed no strong driving force for selectively forming COF-5 at the nanosupport surface. Increasing the nanosupport surface area correlated with thinner layers of COF-5 on the nanosupport, and thick materials such as COF/graphite were largely electron-beam opaque. Effective TEM analysis was therefore limited to the thin edges of these hybrid materials.

The first in-depth EELS analysis of COF-5 was conducted, establishing the profile of the and energy of the plasmon peak and using the core-loss EELS for elemental analysis, supported by EDX spectra. Thickness measurements from EELS rationalised well with the observed size in BF-TEM. Finally, COF-5 and COF-5/GNF were pyrolysed at 1000 °C to investigate possible disposal of COF-5 and COF-5 hybrids at the end of their useful work life. This was found to produce an amorphous carbon material by TEM imaging and spectroscopy.

Overall the application of MALDI, TGA, and TEM to COFs has been developed beyond the current state-of-the-art. Combined with Chapter 2, this work shows that COFs can be fruitfully studied with a combined nanoscale/bulk methodology involving TEM, TGA, and MS. In particular, BF-TEM imaging reveals morphology information that is hidden if only bulk-scale characterisation is used.

3.7 Future Work

There are many profitable lines of inquiry that could be pursued:

- Optical band gap measurements of COF-5 and COF-5/nanosupports, in order to compare to high-resolution EELS band gap measurements. This will reveal if nanosupports are having an effect on the optical properties of COF-5.
- Higher spatial resolution TEM imaging, with a focus on tomography to investigate the changes in COF-5 lattice projection distance and lattice projection length during a rotation.
- Pyrolysis at temperatures higher than 1000 °C to find out if there are any thermal processes such as graphitisation that could be applied to COF-5.
- Development of COF-5/nanosupport synthesis to produce crystalline COF-5 on the surface of MWNTs, SWNT, and silica nano-particles.

3.8 Experimental

General

All work was carried out by the author unless otherwise indicated. Synthesis was carried out using standard laboratory practice with Pyrex glassware with reagents bought from Merck, Alfa-Aesar, Fischer Scientific or Acros Organics and used without further purification unless explicitly stated.

IR spectra were recorded on solids using a Bruker Alpha FTIR Spectrometer using a Bruker Platinum ATR attachment over the range 4000-600 cm^{-1}, or as a potassium bromide pellet with less than 1 mg of sample and 150 mg of potassium bromide.

Thermogravimetric analysis (TGA) was performed with a TA Q500 Thermogravimetric Analyser. Measurements were performed using platinum pans and were run in air. The parameters for all experiments were ramp 10 °C per minute from 20-1000 °C, then isothermal for 10 mins at 1000 °C. Air flow was 60 mL min^{-1}. Pyrolysis was carried out by heating dry powder samples in a platinum TGA pan at 10 °C per min to 1000 °C under flow of argon gas, then cooling under flow of argon gas to 100 °C. The sample was then removed from the TGA and air cooled to room temperature and recovered.

Coulometric Karl-Fischer titration was performed using a Mitsuibishi CA-100 moisture meter. The anode solution was AQUAMICRON AKX, and the cathode solution AQUAMICRON CXU. Calibration was performed by University of Nottingham technicians using NIST traceable water standards.

MALDI-ToF MS measurements were recorded using a Bruker ultraFlexIII (Bruker Daltonik, Bremen, Germany). Samples were dispersed in acetone or chloroform without a matrix unless otherwise indicated then drop-cast on a stainless steel target plate (type MTP384; Bruker Daltonik, Bremen, Germany). The sample was ionised using a pulsed solid-state UV laser (355 nm, 500 μJ, 66.7 Hz shot frequency). The instrument was operated in reflectron mode. Data was acquired using the on-board flexControl software (v3, B185;Bruker Daltonik, Bremen, Germany) and processed using Bruker's flexAnalysis software (v3, B96;Bruker Daltonik, Bremen, Germany).

Powder X-ray diffraction measurements were made by the author or W. Cull with a PANalytical Xpert Pro using Cu(Kα_1) radiation (λ=1.5432 Å) from $2° - 40°$ 2θ on a zero-background silicon holder or a brass sample holder in Bragg-Brentano geometry.

Transmission electron microscopy (TEM) was performed using either a JEOL 2100PLUS transmission electron microscope with an accelerating voltage of 200 kV or a JEOL 2100F transmission electron microscope with an accelerating voltage of 200 kV, located at the University of Nottingham Nanoscale and Microscale Research Centre. COF and COF@GNF samples were prepared via bringing a copper TEM grid coated with "lacey" carbon film (Agar Scientific UK) by dispersing the dry sample in HPLC grade IPA and drop-casting on the TEM grid. Analysis was performed using Gatan Microscopy Suite 3 and ImageJ FIJI software.[36,37] Fourier-transforms of real-valued images are presented as the magnitude of the original complex-valued Fourier-transform. Energy-dispersive X-ray spectroscopy (EDX), electron energy loss spectroscopy (EELS) and selected-area electron diffraction (SAED) measurements were taken using the JEOL 2100PLUS transmission electron microscope. EELS background fitting was performed using the literature software.[38] EELS Fourier-log convolution and Kramers-Kronig analysis was performed using literature software.[39] EDX simulation was performed using NIST-DTSA-II Power Tools for Microanalysis "simulation alien", using the Monte Carlo model of a bulk homogeneous material. Simulations were performed using 200 kV accelerating voltage, 60 nAs probe dose, and 0 ° incident angle.[40]

Scanning electron microscopy (SEM) and scanning transmission electron microscopy (STEM) were aquired using a Zeiss Crossbeam 550 FIB-SEM at an accelerating voltage of 30 kV at a working distance of 4.0 mm on a lacy carbon coated TEM grid. Analysis was performed using SmartTiff (v03.00.03) and ImageJ FIJI software.[36,37]

Computer-generated Histograms

Computer generated histograms were made using the MATLAB *normrnd* command. An array of x data points were generated using a user defined AC mean and standard deviation. x more data points where then generated using a user defined ZZ mean and the same standard deviation. These two sets of data points where then concatenated to give a single array of y data points from which a histogram was generated using the *histfit* command. The resulting histogram was fitted to a normal distribution. For presentation purposes, the *histogram* command was used to plot a histogram of array y.

Statistical Analysis

The sample standard deviation σ was calculated using the usual equation:[41,42]

$$\sigma(x) = \sqrt{\frac{\Sigma(x-\mu)^2}{N-1}} \tag{15}$$

where μ is the mean and N is the number of measurements. The bimodal separation index S was calculated via:[43]

$$S = \frac{\mu_1 - \mu_2}{2(\sigma_1 + \sigma_2)} \tag{16}$$

where μ is the mean and σ is the standard deviation. This index assumes that the data is comprised of two normal distributions.

Nanosupport Preparation

P2 SNWT and PD30 MWNTs were processed according to the methods developed by K. Fung.[44]

PR19 graphitised nanofibres were used without further purification. IR (KBr) νmax cm^{-1}: 3449br, 2959s, 2924s, 2852s, 2362w, 1633br, 1383s, 1190br, 1132w, 1052w, 1011w, 835w, 689w, 584w.

PD30 multi-walled carbon nanotubes were (10 mg, 0.83 mmol) were heated at 530 °C for 2 minutes, then cooled to room temperature and washed with nitric acid (1 M, 10 mL), washed with aqueous sodium hydroxide (1 M, 10 mL), then washed with deionised water (10 mL) to give a black powder and a pale yellow filtrate. The black powder product was dried under reduced pressure overnight then used without further purification (7.6 mg, 0.63 mmol, 76 %). IR (KBr) νmax cm^{-1}: 3544, 3472, 3414, 2957, 2920, 2850, 2353, 1637, 1617, 1385, 1260, 1099, 802.4, 623.9, 474.1.

P2 single-walled carbon nanotubes (50 mg, 4.2 mmol) were refluxed in nitric acid (3 M, 50 mL) for 2 hours. The nanotubes were filtered off and washed with deionised water (50 mL). The resulting black powder was dried under reduced pressure overnight, then used without further purification (45.6 mg, 3.8 mmol, 90 %). IR (KBr) νmax cm^{-1}: 3437br, 2920s, 2852s, 1629br, 1578vs, 1385vs, 1132br, 607br.

Graphite was treated according to the literature procedure.[45] Black graphite powder (85.5 mg, 7.1 mmol) was emulsified with 4:1 deionised water/hexane (30 mL) by vigorous shaking then poured into a mixture of glass beads (21 g, diameter = 2 mm) and deionised water (75 mL). The solution was decanted from the beads, then then beads were washed 5 times with hexane (30 mL). The resulting metallic silver coloured beads were washed with acetone (30 mL) which was then decanted from the beads. The grey solid graphite product collected via filtration and dried under reduced pressure overnight. The metallic grey product was used without further purification (19.6 mg, 1.6 mmol, 23 %). IR (KBr) νmax cm^{-1}: 2351, 1432, 1093, 870.1.

COF-5 synthesis

COF-5 was prepared according to a modified literature procedure. HHTP (29 mg, 0.089 mmol) and benzene-1,4-diboronic acid (23.1 mg, 0.14 mmol) were mixed with 20:4:1 acetonitrile/1,4-dioxane/mesitylene (10 mL) and immersed in an ultrasonic bath for 15 mins. The black solution was then syringe filtered (PTFE, 2 μm) into a flame-dried 50 mL reaction vessel and diluted to 30 mL with the remaining solvent mixture. The reaction vessel was sealed and heated to 90 °C for 16 hours. The resulting light tan precipitate was collected via filtration, washed with THF (10 mL), then acetone (10 mL), then hexane (10 mL). The product was dried under reduced pressure overnight (31.2 mg, 0.035 mmol, 39 %). IR (KBr)$\nu_{\max}$ / cm^{-1}: 3387 (OH), 1633, 1522, 1493, 1446, 1395 (CO_2B), 1342 (BC), 1327, 1278, 1241 (CO), 1161, 1077 (BO), 1017, 849.1, 831.1, 800.2, 728.5, 654.6 (BO), 613.6 (CO_2B), 539.6 (OH), 480.2, 408.3. MS (MALDI-ToF) m/z 774.5 (6.5), 746.3 (8.1), 740.0 (8.7), 677.4 (2.3), 616.1 (3.7), 597.5 (2.5), 580.3 (8.4), 542.8 (2.6), 535.6 (3.4), 474.7 (3.7), 488.3 (100), 433.7 (12), 424.8 (2.7).

COF-5/nanosupport was made by including the dry nanosupport into the reaction vessel.

COF-5/graphite: HHTP (33.2 mg, 0.099 mmol), BDA (20.3 mg, 0.12 mmol), graphite (6 mg, 0.5 mmol), 30 mL solvent mixture. Product was a dry black power (25.5 mg, 0.028 mmol, 27 %). IR (KBr)$\nu_{\max}$ / cm^{-1}: 3389, 3283, 1514, 1491, 1440, 1393, 1335, 1237, 1159, 1128, 1075, 1032, 1009, 849.5, 831.1, 794.1, 656.5, 613.5, 529.4, 478.1, 408.3. MS (MALDI-ToF) m/z 878.4 (7.2 %), 872.1 (11), 828.1 (7.9), 776.4 (11), 796.1 (7.7) 748.3 (11), 742.1 (32), 720.0 (8.2), 713.1 (7.7), 646.1 (9.6), 583.1 (17), 539.2 (8.1), 511.1 (7.9), 498.1 (8.1), 479.1 (8.5), 469.1 (8.1), 454.1 (100), 439.9 (9.9), 421.9 (8.0).

COF-5/GNF: HHTP (29.8 mg, 0.092 mmol), BDA (23.4 mg, 0.14 mmol), PR19 GNF (5.9

mg, 0.49 mmol), 30 mL 20:4:1 acetonitrile/1,4-dioxane/mesitylene. Product was a dry black power (31.2 mg, 0.034 mmol, 37 %). IR (KBr)ν_{max} / cm^{-1}: 3325, 1522, 1491, 1450, 1393, 1342, 1321, 1237, 1159, 1077, 1019, 972, 847.4, 831.1, 726.4, 654.7, 611.5. MS (MALDI-ToF) m/z 774.5 (0.88 %), 746.2 (1.2), 740.0 (1.1), 693.6 (0.29), 580.3 (0.84), 488.3 (100), 433.7 (1.4), 424.7 (0.35).

COF-5/MWNT: HHTP (32.1 mg, 0.099 mmol), BDA (23.4 mg, 0.14 mmol), PD30 MWNT (6.0 mg, 0.5 mmol), 30 mL 20:4:1 acetonitrile/1,4-dioxane/mesitylene. Product was a dry black power (41 mg, 0.044, 44 %). IR (KBr)ν_{max} / cm^{-1}: 3490, 1629, 1522, 1493, 1448, 1395, 1344, 1325, 1239, 1161, 1106, 1077, 1019, 974.7, 849.5, 833.1, 800.3, 730.3, 656.6, 613.5, 539.7, 408.3. MS (MALDI-ToF) m/z 776.4 (6.7), 748.3 (8.8), 742.1 (38), 720.0 (40), 713.1 (5.3), 700.9 (6.3), 671.0 (6.5), 656.0 (26), 627.0 (4.2), 574.9 (4.4), 556.0 (4.3), 529.0 (4.5), 510.0 (4.3), 480.0 (8.8), 453.9 (100), 439.7 (13).

COF-5/SWNT: HHTP (31.0 mg, 0.096 mmol), BDA (22.5 mg, 0.14 mmol), P2 SWNT (6.0 mg, 0.5 mmol), 30 mL 20:4:1 acetonitrile/1,4-dioxane/mesitylene. Product was a dry black power (46.1 mg, 0.049 mmol, 52 %). IR (KBr)ν_{max} / cm^{-1}: 3445, 1522, 1493, 1448, 1395, 1342, 1325, 1239, 1161, 1077, 1019, 974.7, 849.5, 833.1, 802.2, 728.5, 656.6, 613.5. MS (MALDI-ToF) m/z 870.0 (6.7), 748.3 (8.8), 740.1 (20), 693.6 (8.8), 653.2 (10), 616.2 (13), 587.7 (8.7), 580.3 (15), 506.4 (9.6), 478.0 (20), 448.3 (100), 433.8 (18).

Pyrolysis

Pyro(COF-5): Dry COF-5 powder (4.12 mg, 0.004 mmol) was heated to 1000 °C under flow of argon gas, then cooled to room temperature and collected. Product was a black powder (1.98 mg, 48 %). IR (KBr)ν_{max} / cm^{-1}: 3441, 2963, 2918, 2074, 1627, 1467, 1385, 1360, 1321, 1260, 1194, 1134, 1095, 1079, 1017, 857.8, 796.3, 714.2, 658.8. MS (MALDI-ToF) m/z 372.3 (36 %), 343.0 (55), 329.1 (100), 325.1 (77), 311.2 (58), 301.2 (48), 293.1 (35), 287.1 (34).

Pyro(GNF): Dry PR19 GNF powder (2.74, 0.23 mmol) was heated to 1000 °C under flow of argon gas, then cooled to room temperature and collected. Product was a black powder (2.56 mg, 93 %). IR (KBr)ν_{max} / cm^{-1}: 3441, 2957, 2924, 2854, 2427, 2362, 1623, 1383, 1186, 1133, 1048, 1013, 837.3, 689.6, 611.6, 584.9. MS (MALDI-ToF) m/z 763.0 (62 %), 747.3 (63), 735.3

(65), 719.2 (66), 707.1 (66), 663.2 (66), 647.3 (69), 635.1 (67), 619.3 (75), 607.2 (64), 591.2 (65), 397.1 (65), 381.2 (81), 369 (77), 353 (81), 326.2 (66), 242.2 (100).

Pyro(COF-5/GNF): Dry COF-5/GNF powder (2.34 mg, 0.002 mmol) was heated to 1000 °C under flow of argon gas, then cooled to room temperature and collected. Product was a black powder (1.40 mg, 60 %). IR (KBr)ν_{max} / cm^{-1}: 3220, 2516, 2364, 2259, 1440, 1196, 944.0, 884.5, 804.5, 708.0, 642.3, 547.9, 459.7. MS (MALDI-ToF) m/z 719.9 (100 %), 301.2 (99).

References

(1) A. P. Cótê, A. I. Benin, N. W. Ockwig, M. O'Keeffe, A. J. Matzger and O. M. Yaghi, *Science*, 2005, **310**, 6.

(2) X. Liu, J. Tan, A. Wang, X. Zhang and M. Zhao, *Phys. Chem. Chem. Phys.*, 2014, **16**, 23286–23291.

(3) N. L. Campbell, R. Clowes, L. K. Ritchie and A. I. Cooper, *Chemistry of Materials*, 2009, **21**, 204–206.

(4) J. W. Colson, A. R. Woll, A. Mukherjee, M. P. Levendorf, E. L. Spitler, V. B. Shields, M. G. Spencer, J. Park and W. R. Dichtel, *Science*, 2011, **332**, 228–231.

(5) J. Yoo, S. Lee, S. Hirata, C. Kim, C. K. Lee, T. Shiraki, N. Nakashima and J. K. Shim, *Chemistry Letters*, 2015, **44**, 560–562.

(6) J. Wang, J. Li, M. Gao and X. Zhang, *Nanoscale*, 2017, **9**, 10750–10756.

(7) M. Calik, T. Sick, M. Dogru, M. Döblinger, S. Datz, H. Budde, A. Hartschuh, F. Auras and T. Bein, *Journal of the American Chemical Society*, 2016, **138**, 1234–1239.

(8) S. T. Yang, J. Kim, H. Y. Cho, S. Kim and W. S. Ahn, *RSC Advances*, 2012, **2**, 10179–10181.

(9) A. M. Evans, L. R. Parent, N. C. Flanders, R. P. Bisbey, E. Vitaku, M. S. Kirschner, R. D. Schaller, L. X. Chen, N. C. Gianneschi and W. R. Dichtel, *Science*, 2018, **361**, 6.

(10) D. D. Medina, J. M. Rotter, Y. Hu, M. Dogru, V. Werner, F. Auras, J. T. Markiewicz, P. Knochel and T. Bein, *Journal of the American Chemical Society*, 2015, **137**, 1016–1019.

(11) J. Yoo, S.-J. Cho, G. Y. Jung, S. H. Kim, K.-H. Choi, J.-H. Kim, C. K. Lee, S. K. Kwak and S.-Y. Lee, *Nano Letters*, 2016, **16**, 3292–3300.

(12) B. J. Smith and W. R. Dichtel, *Journal of the American Chemical Society*, 2014, **136**, 8783–8789.

(13) B. J. Smith, L. R. Parent, A. C. Overholts, P. A. Beaucage, R. P. Bisbey, A. D. Chavez, N. Hwang, C. Park, A. M. Evans, N. C. Gianneschi and W. R. Dichtel, *ACS Central Science*, 2017, **3**, 58–65.

(14) B. J. Smith, N. Hwang, A. D. Chavez, J. L. Novotney and W. R. Dichtel, 2015, **51**, 7532–7535.

(15) R. P. Bisbey, C. R. DeBlase, B. J. Smith and W. R. Dichtel, *Journal of the American Chemical Society*, 2016, **138**, 11433–11436.

(16) T. Bao, P. Tang, D. Kong, Z. Mao and Z. Chen, *Journal of Chromatography A*, 2016, **1445**, 140–148.

(17) Y.-B. Huang, P. Pachfule, J.-K. Sun and Q. Xu, *Journal of Materials Chemistry A*, 2016, **4**, 4273–4279.

(18) C. T. Stoppiello, H. Isla, M. Martínez-Abadía, M. W. Fay, C. D. J. Parmenter, M. J. Roe, B. Lerma-Berlanga, C. Martí-Gastaldo, A. Mateo-Alonso and A. N. Khlobystov, *Nanoscale*, 2019, **11**, 2848–2854.

(19) B. C. Smith, *Fundamentals of Fourier Transform Infrared Spectroscopy*, CRC Press, 1st edn., 2011.

(20) A. M. Evans, I. Castano, A. Brumberg, L. R. Parent, A. R. Corcos, R. L. Li, N. C. Flanders, D. J. Gosztola, N. C. Gianneschi, R. D. Schaller and W. R. Dichtel, *Journal of the American Chemical Society*, 2019, **141**, 19728–19735.

(21) M. M. Ngoma, M. Mathaba and K. Moothi, *Scientific Reports*, 2021, **11**, 23805.

(22) S.-C. Lim, J. Lee, H. H. Kwak, J. W. Heo, M. S. Chae, D. Ahn, Y. H. Jang, H. Lee and S.-T. Hong, *Inorganic Chemistry*, 2017, **56**, 7668–7678.

(23) M. K. Smith and B. H. Northrop, *Chemistry of Materials*, 2014, **26**, 3781–3795.

(24) E. L. Spitler, M. R. Giovino, S. L. White and W. R. Dichtel, *Chemical Science*, 2011, **2**, 1588–1593.

(25) A. M. Evans, M. R. Ryder, W. Ji, M. J. Strauss, A. R. Corcos, E. Vitaku, N. C. Flanders, R. P. Bisbey and W. R. Dichtel, *Faraday Discussions*, 2021, **225**, 226–240.

(26) J. Plewa and J. Skrzypek, *Chemical Engineering Science*, 1989, **44**, 2817–2824.

(27) H. S. Sasmal, A. K. Mahato, P. Majumder and R. Banerjee, *Journal of the American Chemical Society*, 2022, **144**, 17.

(28) *JEM-2100Plus Electron Microscope Instructions*, JEOL ltd., 2015.

(29) R. Brydson, *Electron Energy-Loss Spectroscopy*, Taylor and Francis, Oxford, 2001.

(30) J. R. Rostrup-Nielsen, *Catalysis Today*, 1997, **37**, 225–232.

(31) R. Franz, E. A. Uslamin and E. A. Pidko, *Mendeleev Communications*, 2021, **31**, 584–592.

(32) F. M. Bkangmo Kontchouo, Z. Gao, X. Xianglin, Y. Wang, Y. Sun, S. Zhang and X. Hu, *Journal of Environmental Chemical Engineering*, 2021, **9**, 106383.

(33) N. Agasti, M. A. Astle, G. A. Rance, J. Alves Fernandes, J. Dupont and A. N. Khlobystov, *Nano Letters*, 2020, **20**, 1161–1171.

(34) J.-L. Bantignies, J.-L. Sauvajol, A. Rahmani and E. Flahaut, *Physical Review B*, 2006, **74**, 195425.

(35) S. Eigler, C. Dotzer, A. Hirsch, M. Enzelberger and P. Müller, *Chemistry of Materials*, 2012, **24**, 1276–1282.

(36) J. Schindelin, I. Arganda-Carreras, E. Frise, V. Kaynig, M. Longair, T. Pietzsch, S. Preibisch, C. Rueden, S. Saalfeld, B. Schmid, J.-Y. Tinevez, D. J. White, V. Hartenstein, K. Eliceiri, P. Tomancak and A. Cardona, *Nature Methods*, 2012, **9**, 676–682.

(37) J. Schindelin, C. T. Rueden, M. C. Hiner and K. W. Eliceiri, *Molecular Reproduction and Development*, 2015, **82**, 518–529.

(38) K. L. Fung, M. W. Fay, S. M. Collins, D. M. Kepaptsoglou, S. T. Skowron, Q. M. Ramasse and A. N. Khlobystov, *Ultramicroscopy*, 2020, **217**, 113052–113052.

(39) R. F. Egerton, *Electron Energy-Loss Spectroscopy in the Electron Microscope*, Springer New York, New York, 3rd edn.

(40) *NIST DTSA-II*, NIST, `https://www.nist.gov/services-resources/software/nist-dtsa-ii` (visited on 02/27/2023).

(41) M. Bonamente, *Statistics and Analysis of Scientific Data*, Springer New York, New York, NY, 2017.

(42) L. Wasserman, *All of Statistics: A Concise Course in Statistical Inference*, Springer New York, New York, NY, 2004.

(43) C. Zhang, B. E. Mapes and B. J. Soden, *Quarterly Journal of the Royal Meteorological Society*, 2003, **129**, 2847–2866.

(44) K. L. Y. Fung, Ph.D. Thesis, University of Nottingham, Nottingham, 2021.

(45) M. Lotya, Y. Hernandez, P. J. King, R. J. Smith, V. Nicolosi, L. S. Karlsson, F. M. Blighe, S. De, Z. Wang, I. T. McGovern, G. S. Duesberg and J. N. Coleman, *Journal of the American Chemical Society*, 2009, **131**, 3611–3620.

4 Graph Theory Modelling of Covalent Organic Frameworks

4.1 Introduction

4.1.1 Chemical Graph Theory

In Chapters 2 and 3 it was shown that the lattice projections of cHBC-BDA-COF and COF-5 are systematic and related to their lattice topology. It is therefore useful to attempt to put TEM imaging of COFs on a robust theoretical framework to more fully understand the experimental TEM presented thus far, with a particular focus on hexagonal 2D COFs. In particular this chapter seeks to answer why these materials have systematic TEM projections, and if these projections can be predicted prior to performing experimental TEM. A suitable large-scale modelling technique that could produce structures similar to those seen in experimental TEM would allow deeper understanding of the processes that form these structures. To do this, the author presents graph theory.

Graph theory is a branch of mathematics concerned with modelling pairwise relationships using networks, the titular graph, constructed of nodes linked by edges. Much of the information for this section is drawn from *Introduction to Graph Theory* by West.[1] Nodes and edges are the basic building blocks of graphs (Figure 70a). Edges associated with a scalar are said to be weighted, where the weight is often represented as the length or thickness of the edge (Figure 70b). Where the edges have an associated direction, the graph is said to be a directed graph (Figure 70c). The number of edges connected to a node is the degree or valence of that node. If an edge starts and ends at the same node, it is called a loop. Complete graphs have every unique pair of edges connected by a node (Figure 70d). A pseudograph or multigraph is a graph that allows multiple edges between pairs of nodes (Figure 70e); graphs are otherwise called simple. Planar graphs have edges that only intersect at their endpoints, which allows them to be embedded into a plane. Planar graphs contain faces, which are regions bounded by edges. The relation between faces, edges, and nodes is given by Euler's formula:

$$n - e + f = 2 \tag{17}$$

Where n is the number of nodes, e is the number of edges, and f is the number of faces. Each graph will have one unique face called the "infinite" or "outside" face, which is made up of the area outside the graph (Figure 70f).

Graphs are often analysed via walks, which is a sequence of edges connecting nodes. Open walks start and end on different nodes, and are otherwise closed (Figure 70g). Walks are generally most useful when they are restricted such that each edge in a walk is unique, or when all edges and nodes in the walk are unique. Walks can be used to find the shortest route from one node to another, indicating to what degree those nodes are separated, or can be used to find all nodes within a specific walk distance. For example, a walk could be used to find all nodes separated by 4 edges from a given starting node.

As well as diagrammatic representation, graphs can be expressed via an adjacency matrix (Figure 71). This is a square matrix of *m* columns and *m* rows where *m* is the number of nodes in the graph. Each element then represents whether an edge exists between two nodes. For example, element (1, 3) would represent the relationship between nodes 1 and 3. It is common to then set this element to 1 to indicate an edge, and 0 to indicate no edge. Adjacency matrices are often symmetric about the diagonal elements, e.g. element (3, 1) = (element 1, 3). As a results graphs lend themselves to computations via matrix mathematics, and are closely linked to combinatorics and topology.

The utility of graph theory to chemists was perhaps first noted by Sylvester, who recognised that skeletal formulae are graphs representing chemical structure,[2] allowing the mathematical methods of graph theory to mesh into existing chemical structure theories that were being developed by Kekulé. This was the beginning of chemical graph theory. A key point is that the way a graph is drawn does not necessarily imply any physical information such as distance between nodes. As long as the connectivity of nodes is preserved, any spatial arrangement of nodes is allowed (Figure 72). To use graphs to model physical structures such as those seen in previous chapters, extra information like chemical bond lengths or bond angles must be imposed on the graph.

Chemical graph theory has been applied to a wide range of problems with encouraging results. Pogliani identified that unweighted graphs or multigraphs without information identifying

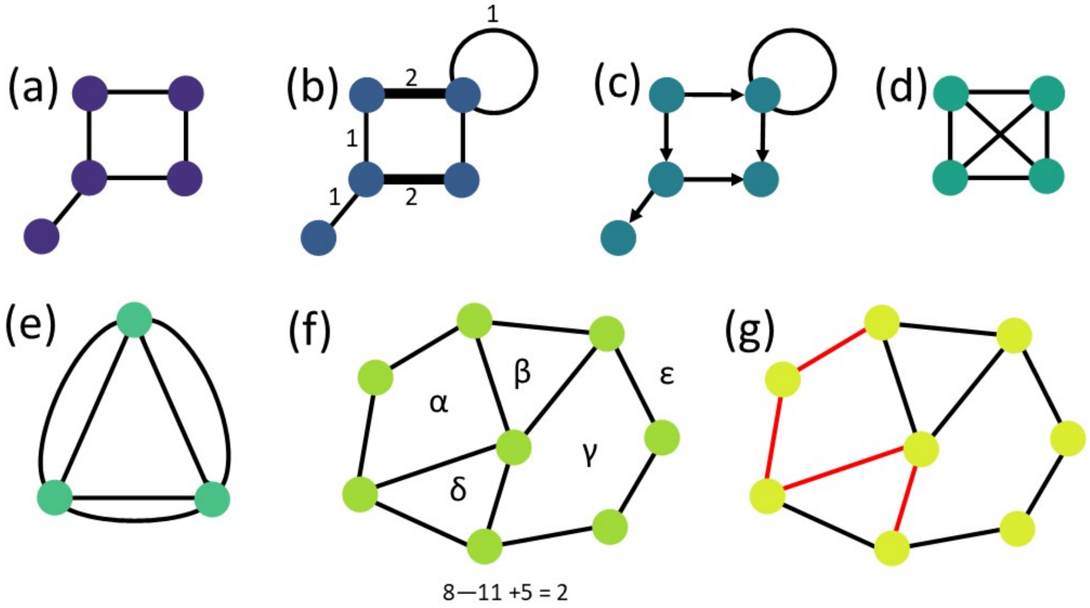

Figure 70: (a) An undirected planar graph. Nodes are represented as purple circles, and edges as black lines. (b) An undirected weighted planar graph, where the scalars represent edge weight (also shown by edge thickness). A loop is present. (c) A directed planar graph. The edges have been replaced with arrows that indicate their direction. (d) A complete graph, each unique pair of nodes is connected by edges. (e) A complete multigraph. Each pair of nodes is connected by two edges. (f) Graph illustrating Euler's formula. The graph has 8 nodes, 11 edges, and 5 faces. The sum below the graph confirms Euler's formula. Faces are indicated by Greek letters, where ϵ indicates the infinite face. (g) Graph illustrating an open walk containing 4 edges (red edges).

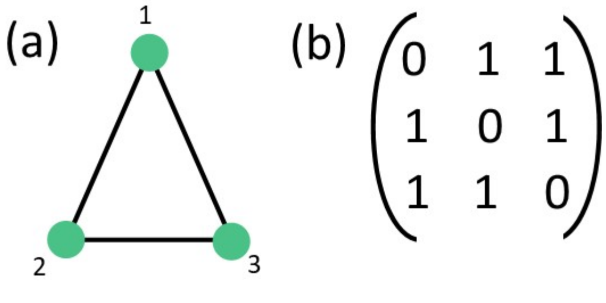

Figure 71: (a) An undirected graph with three nodes. Each node has been labelled with a number. (b) The corresponding adjacency matrix describing the graph. Each element indicates whether there is an edge between node. For example, nodes 1 and 3 are connected so element (3,1) is set to 1. As this is a symmetric matrix element (3, 1) = (1 ,3). The diagonal elements are set to 0 as no nodes have loops.

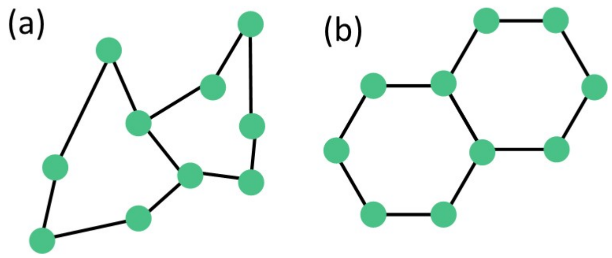

Figure 72: Two representations of the same graph, where (a) has random node placement and variable edge length and (b) places nodes in a hexagonal arrangement with consistent edge length. Both graphs could be represented by the same adjacency matrix. By limiting where nodes are allowed to be placed, (b) gives a more accurate representation of a physical chemical structure. If the nodes are assumed to be carbon atoms, this graph becomes the skeletal formula for decalin.

the element associated with each node can apply to more than one chemical structure, with the given example being the graphs of butane and dichloroethane.[3] They then developed complete graphs to contain information about core electron structure to aid in distinguishing chemical graphs that have similar atomic connectivity, with a major advantage being the ability to express the core electron structure as a matrix. Chemical graphs have also been used to investigate crystalline structures. Husain *et al.* were able to develop topological descriptions for a number of crystal structures, which was particularly useful in aiding visualisation of structures.[4] Proteins have been modelled as graphs extensively.[5,6] Yan *et al.* used graphs due to their low computational cost, and were able to use graphs to model all possible conformations of a protein structure and find clusters in side-chain conformation. They attribute the effectiveness of this approach to the ease of solving graph-theoretical problems compared to problems in other modelling methods.[7]

For modelling large networks graphs are often paired with Monte-Carlo methods, which uses repeated random sampling to investigate a system. Monte-Carlo methods may also be called stochastic modelling. Lin *et al.* investigated the topology of polymer gel networks formed from four-valent nodes using a Monte-Carlo approach. They found that their results matched well to experimental NMR data of polymer networks and were able to calculate at what point a system would form a gel.[8] Gunduz *et al.* investigated the mechanical strength of polymers, which allowed them to investigate large networks with good agreement to experimental data.[9] Kryven *et al.* used Monte-Carlo methods to simulate formation of a molecular network from multifunctional precursors, and were able to investigate linseed oil polymerisation to show that the initial composition of the oil can drastically change the graph topology, which has application in studying drying of oil paints. In particular, they found that dilute oil led to more cyclisation in the network and therefore a mechanically weaker polymer.[10]

Forming large networks via graph theoretical modelling is a "shortcut" that works by looking at generalised systems and focussing on topology and geometry, at the cost of removing chemical information from the model. Graph theoretical modelling therefore represents a much more coarse-grained modelling technique than many typically applied in chemistry (i.e. density functional theory),[11] with far fewer degrees of freedom. This type of modelling is more similar to that seen in biological sciences for protein simulation.[12] Simulations also typically reply on matrix calculations rather than calculus, and graph theoretical models are more generalisable as they reduce systems to their essential topology.

4.1.2 Aims and Objectives

At the time of writing, graph theoretical modelling of crystalline covalent organic frameworks (COFs) was not found in the literature. COFs are suitable for this type of modelling as the monomer connectivity can be easily represented using graphs. It has been identified in the literature that the extended structure of COFs is difficult to represent visually due to the large number of atoms that exist in COF monomers,[13] and graphs could allow a visually straightforward way to express this information.

In this chapter two graph modelling techniques will be developed; a *structural* model for representing the TEM projections of COFs, and a *stochastic* model for investigating how COFs form in solution. The structural model will reduce COFs to their essential connectivities and be used to understand the lattice projections of COFs in TEM The stochastic model will be used to investigate the formation of large COF structures to attempt to recreate the TEM projections seen in previous chapters. Both models will elucidate the experimental TEM discussions in previous chapters. To achieve this, the following sub-goals are defined:

- The relationship between parallel projections of specific common COF geometries, relative to a fixed an optical axis, will be investigated using graphical models of COF lattice fragments.

- A continuous map of COF rotations relative to a fixed optical axis will be defined and used to rationalise the frequency of TEM projections in experimental data.
- The effect of randomness on polymer size will be investigated via a 1-dimensional model.
- The effect of randomness on polymer morphology and crystallinity will be investigated via 2D and 3D models of a randomly constructed network of 2D hexagonal sheets.

4.2 2D Parallel Projection Graph Theory Structure Models

4.2.1 Deriving Graph Models from COF Lattices

It is important to understand the different direct-space projections that arise from COF lattices in TEM. The first step is to take a real structure and reduce it to a graph. Using cHBC-BDA-COF as an example we can identify that the COF is formed of C3 symmetric cata-hexabenzocoronene (cHBC) monomers joined by C2 symmetric benzenediboronic acid (BDA) monomers, with the fundamental topology being a hexagonal 2D sheet. Individual sheets are AA stacked to form a 3D structure. Nodes will be used to represent the monomers making up the 2D lattice; this could be done either via representing cHBC as 3-covalent nodes and BDA as 2-covalent nodes, or by discarding BDA from the graph model to give a network of 3-covalent nodes. It was decided here to use a network of 3-covalent nodes for simplification of stochastic modelling described later in this chapter, and for TEM contrast-forming reasons that will be discussed presently. Having defined the role of nodes in the graph model, edges are used to indicate connectivity of monomers. For the example of cHBC-BDA-COF, an edge shows how two cHBC monomers are joined in the hexagonal COF lattice and implies the existence of a BDA monomer. However, the BDA monomers does not physically exist in the model.

Turning to modelling TEM contrast, we know that the monomers present in a 2D COF lattice will provide amplitude contrast in a TEM image. Therefore, the nodes in the graph model represent both the location of a monomer and a contrast-forming region of the lattice. For the example of cHBC-BDA-COF, this justifies discarding the BDA monomers from the graph model as they contribute little to the TEM projections formed by the COF lattice as judged by image simulation. To summarise this process before moving on; nodes in the graph represent monomers in a real COF structure, which are the regions that will provide amplitude contrast in a TEM image. Edges represent monomer connectivity.

4.2.2 Modelling TEM Contrast via Graph Models

The main difference from TEM image formation is the use of a binary transmission model: no transmission occurs at nodes, and complete transmission occurs everywhere else. The nodes act like infinitely dense structures that absorb all incoming radiation with a well defined radius - this sharply defines whether radiation is transmitted or not. It would be possible to use partly transparent nodes to model electron beam transmission, but this was not pursued here. Of importance to note is that no scattering of the electron beam is modelled so no phase-contrast effects are taken into account. Modelling phase contrast is possible using existing software packages such as QSTEM.[14] This is not possible with a graph theoretical method as the nodes do not correspond to specific atoms and the edges are not representative of bond lengths, so there is not enough information present in the model to work out how an electron beam would scatter from the sample. However the process of rendering these structures on a 2D viewing screen such as computer monitor or printed page does approximate the results of TEM image formation, as it reduces a 3D structure to a 2D projection. This approach lets the wide parameter space of COFs (e.g. morphology or chemical functionality) be reduced to the topology of the theoretical lattice. This is a useful simplification that enables general trends to be considered without having to model multiple specific chemical systems. The size of the nodes in the visualisation software could be altered to simulate the size of structures, and the effect of optical resolution. For example, larger nodes would model reduced optical resolution; the nodes thus visualise the core of an Airy disc.

4.2.3 Establishing Graph Lattice Projections

The graph theoretical models were then used to define principal projections (Figure 73). Principal projections correspond to particular zone-axis patterns in direct space. Zone-axis patterns are "high-symmetry" orientations of a crystal such that the incident beam is normal to a Bragg plane *hkl*, and more generally are any orientation of a crystal normal to the incident beam. Principal projections are thus zone-axes defined using the real-space crystal to give a generalisable set of zone-axes that allow easy discussion of the structure in 3D real space. Indeed the following discussion will be seen to be an abstraction of crystallographic principles away from real crystals to theoretical graph models, in order to provide a framework to consider TEM projections of real crystals later in this thesis.

A graph theoretical model of an AA stacked 2D hexagonal sheet of *P6mm* symmetry was made (Figure 74a). This was achieved by superimposing 4 sheets of *P6mm* symmetry with the same x- and y-coordinates, but different z-coordinates for each sheet. AA stacked 2D hexagonal sheets are a common COF topology.[15] The constructed stack was then rotated to simulate different orientations with regards to an optical axis normal to the viewing screen. Rotating the model to an arbitrary angle give a lattice projection formed by the overlap of the nodes in the graph. These lattice projections are typically composed of a series of parallel lines where the distance between adjacent lines is the *lattice projection width*, and the length of the lines is the *lattice projection length*.

Four principal projections based on the geometry of the 2D COF lattice were defined: face-on (FO), side-on (SO), armchair (AC), and zigzag (ZZ). The SO projection is a 90° rotation of the FO projections, and the AC and ZZ projections are arrived at by rotating the FO projection 45° towards the armchair or zigzag edges respectively. FO corresponds to looking down the COF pore channels, i.e. the 2D sheet is normal to the optical axis. AC and ZZ edges were chosen as hexagonal sheets have distinct armchair and zigzag edges. These represent ideal lattice projections that can be used to discuss lattice projections arising from intermediate rotations of a COF lattice more easily.

This analysis was then carried out for four more common AA stacked 2D COF sheet topologies: Kagome, trigonal, square, and rhombic (Figure 74b - e). For each, four principal projections were defined as for AA hexagonal sheets. For the square and rhombic lattices, AC and ZZ edges are not present so the principal projections are defined using the edge and corner of the sheets, to give edge-on (EO) and corner-on (CO) projections. These different lattice topologies

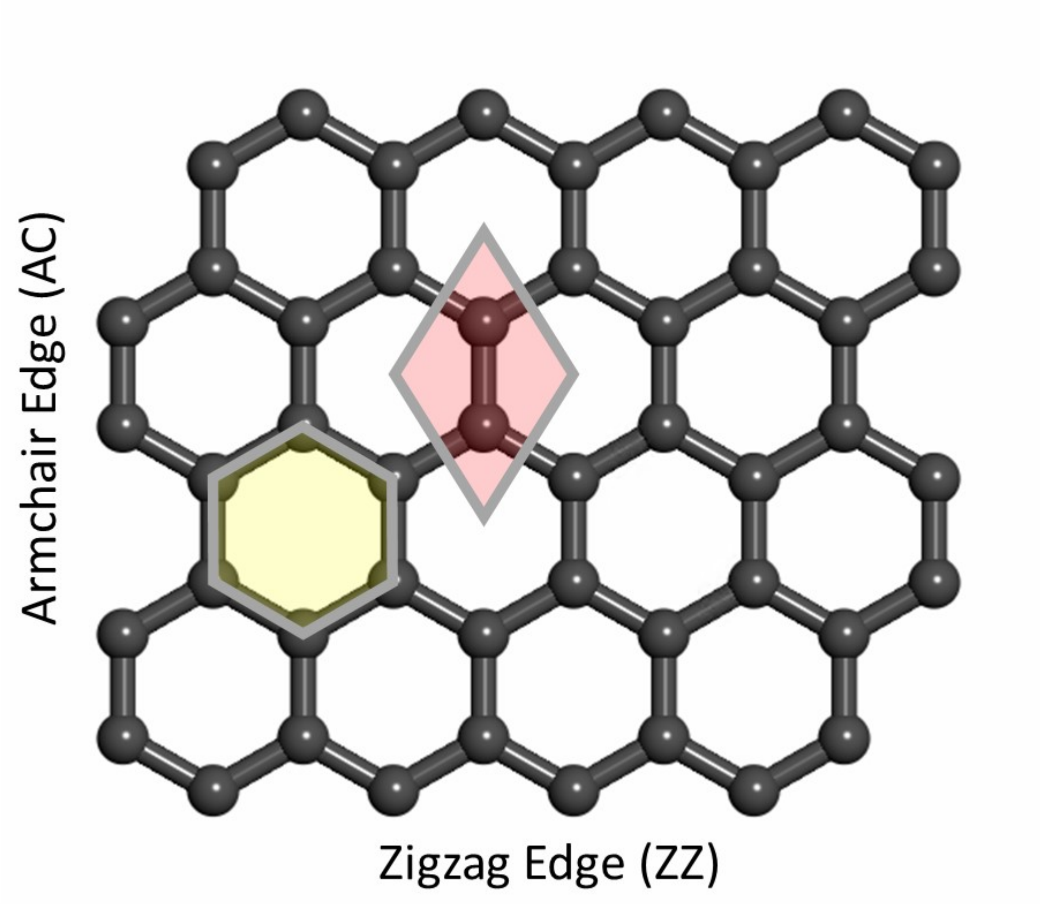

Figure 73: Sheet of graphene illustrating the armchair (AC) and zigzag (ZZ) edges present in hexagonal 2D sheets. The red diamond indicates unit cell of graphene. The yellow hexagon indicates the structural feature used to define projections. A hexagonal projection is the most obvious zone-axis in bright-field TEM imaging, hence it is defined as the face-on (FO) projection. The other projections are then defined based on the structural features of the lattice, such as the AC and ZZ edges.

are grouped into two categories due to the symmetry of their 2D lattices. Each corresponds to a 2D Bravais lattice: hexagonal, trigonal, and kagome all correspond to *p6mm* wallpaper groups; square is *p4mm* and rhombic is an affine transformation of this into *pmm*. Hence, each group has the same underlying symmetry and so gives rise to projections with the same connectivity. The physical origin of this in 3D space is a rotation, which can also be thought of in 2D space as a non-rigid transformation of the projection (anisotropic scaling). For example, rotating the FO projection of a square lattice gives rise to a lower symmetry rectangular projection by shortening the two opposite sides of the square projection. Continuing this rotating leads to a series of parallel lines which are the lowest symmetry orientation of the system. Overall, the projection goes from *P4mm* to *pgg* to *pmm* (Figure 75).

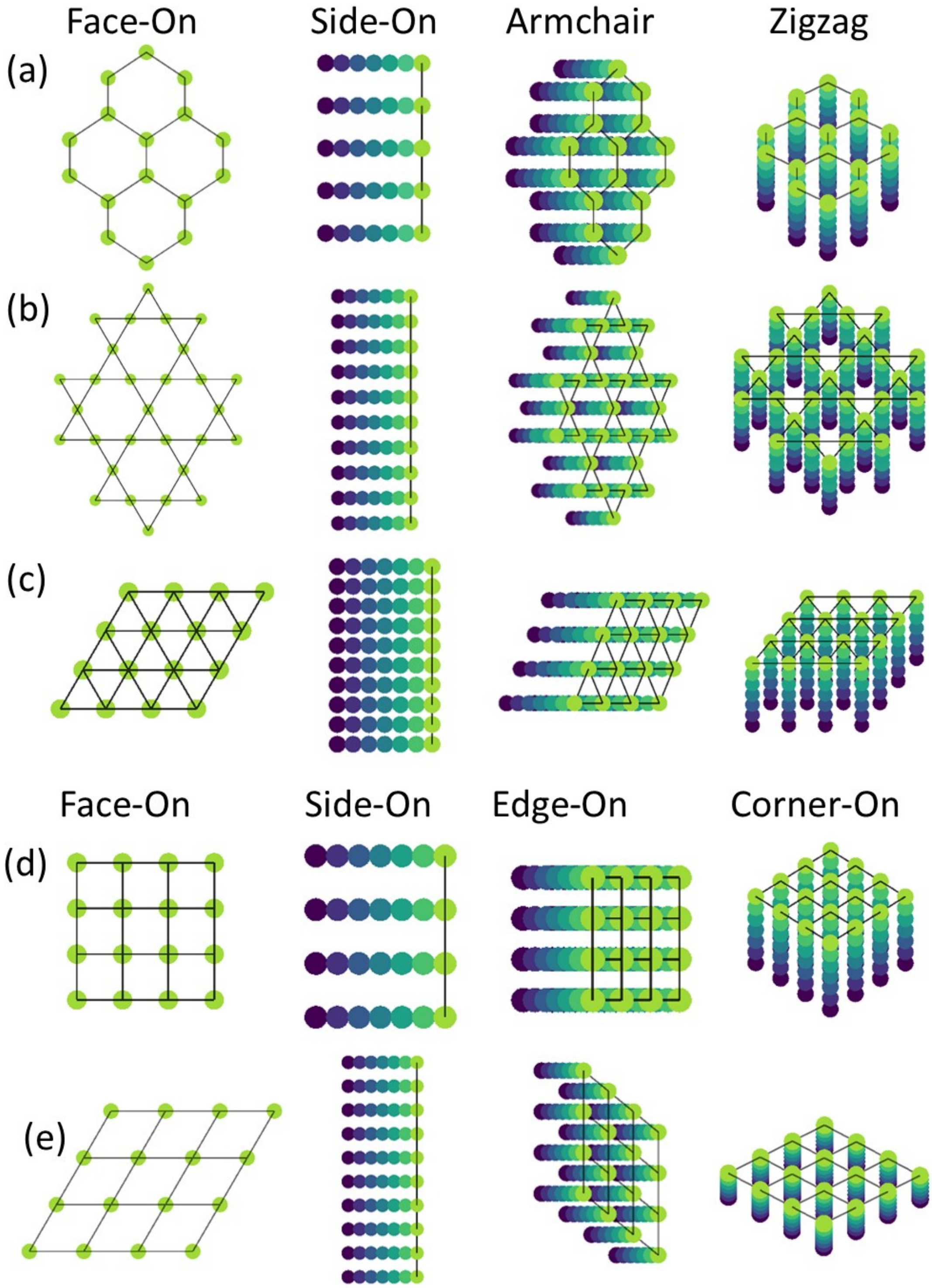

Figure 74: Principal projections for (a) hexagonal, (b) kagome, (c) trigonal, (d) square, and (e) rhombic (diamond) AA stacked sheets. Side-on (SO) projections are a 90° rotation of the face-on (FO) projections, and the remaining projections are 45° rotations of the FO projection towards the armchair/zigzag edges or edge/corner of the 2D sheet respectively. Each principal projection has a unique lattice projection caused by overlap of nodes in projection. Each layer has been colour-coded to illustrate how several layers overlap to form a projection. The nodes represent regions of contrast-forming density, while the edges represent connectivity and have been included for illustrative purposes.

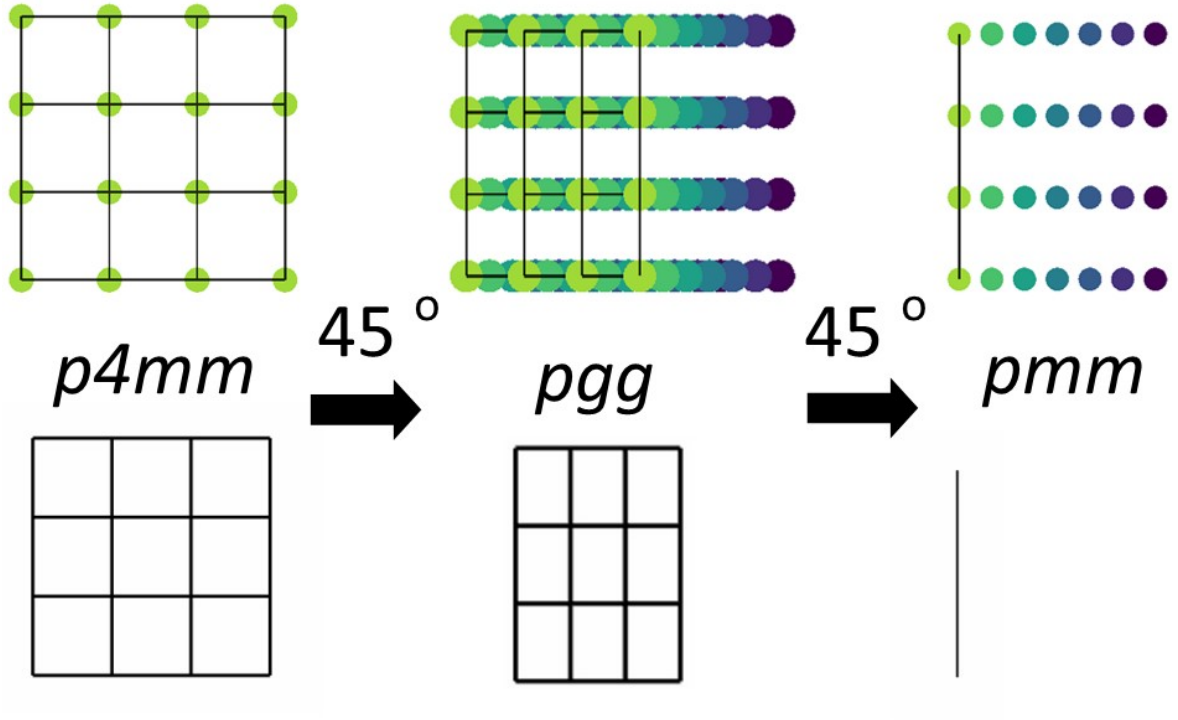

Figure 75: Example showing how the projection changes during the rotation of a square lattice. The lattice starts in a face-on projection, moves through the edge-on projection, and ends in the side-on projections. The 2D wallpaper group of the black lattice has been indicated.

4.2.4 Comparing Graph Models to Real Structures

Comparing the DFT structural model of cHBC-BDA-COF[16] to the graph theoretical model for AA-hexagonal sheets shows that the graph model captures the essential details of the COF structure (Figure 76). In the DFT model the cata-hexabenzocoronene (cHBC) monomers have greater nuclear density than the benzenediboronic acid (BDA) monomers so contribute more contrast in the image simulations. The overlap of the cHBC nodes in projection compared to the relatively low-contrast BDA monomers then leads to patterns of light and dark lines in the image simulation (lattice projections). Discussed above, the graph model uses nodes to represent cHBC monomers - cHBC monomers contribute more to forming lattice projections than BDA monomers. BDA monomers have not been modelled in the graph. The edges in the graph indicate the connectivity of the 2D COF sheets.

Rotating the graph and DFT models the gives rise to distinct lattice projections based on how the cHBC nodes overlap, which is derived ultimately from the geometry of the lattice. The measured spacings in the DFT model and the image simulation agree well with each other;

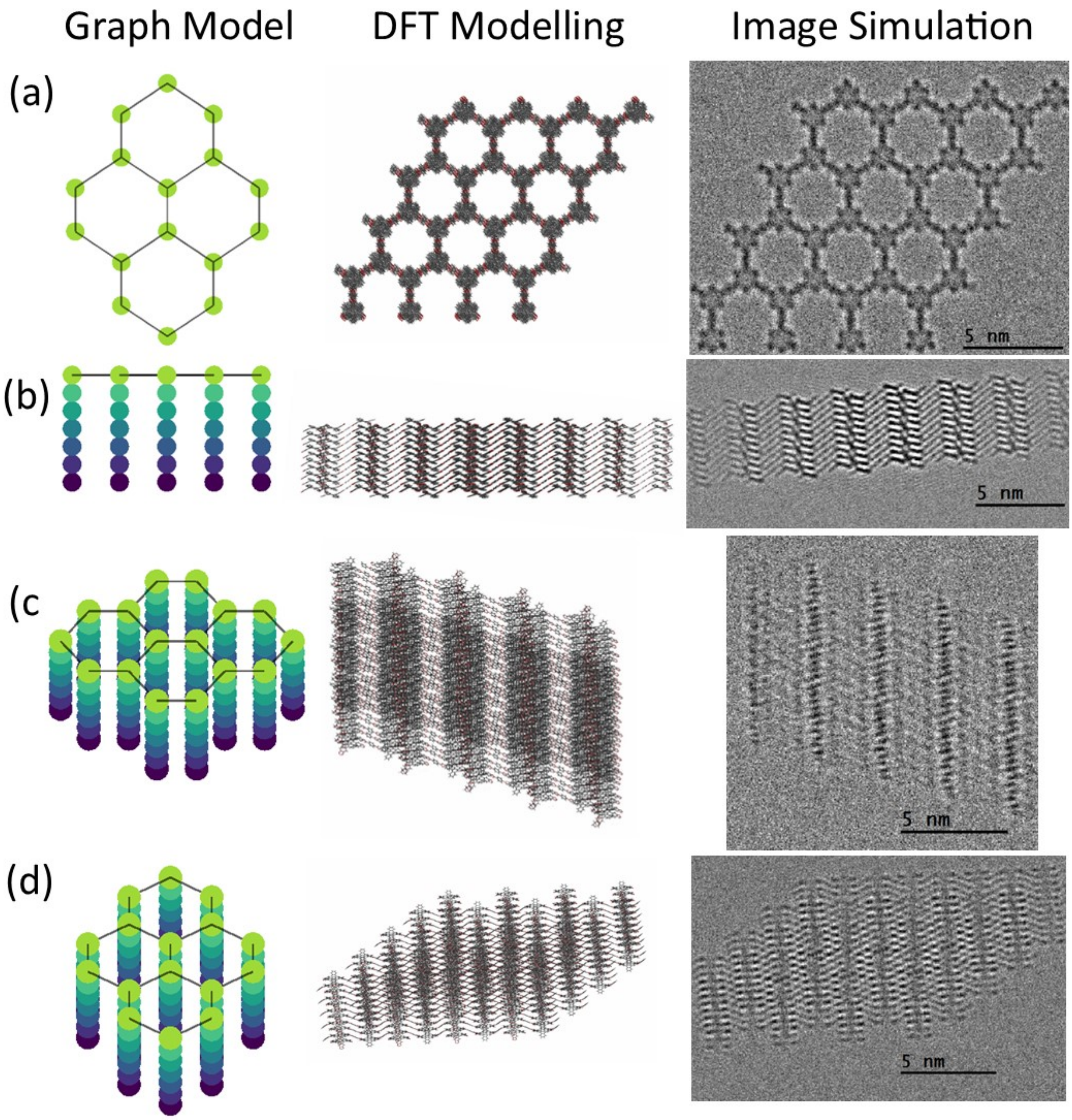

Figure 76: Comparison of graph theoretical model, DFT structural model,[16] and QSTEM image simulation for cHBC-BDA-COF, for the (a) face-on, (b) side-on, (c) armchair, and (d) zigzag principal projections. It can seen that each projection has systematic patterns of bright and dark contrast arising from the structure of the COF lattice.

the graph model does not give absolute spacings as the edge length is not representative of the distance between cHBC monomers in the COF. However, the graph model accurately predicts the relative lattice projection patterns for each projection with the exception of the AC projection. The graph model predicts that the AC projection should occur as two closely spaced fringes with a larger separation between sets of two (Figure 76c), while the DFT model and image simulation show a single broad fringe. This is due to the cHBC monomers being large such that the two closely spaced fringes overlap and give the appearance of one large fringe. This could be corrected in the graph model by increasing the size of the nodes to better represent these specific monomers, but for this work the current results were suitable. Therefore the theoretical projections of COF lattices can be seen to come primarily from the geometry of the COF lattice, while the experimental projections will be a combination of the geometry and the chemical makeup of the COF.

These models are only accurate for thin samples. Image simulation of cHBC-BDA-COF shows that increased thickness in projection leads to regions of the sample appearing amorphous (Figure 77). This aligns with the experimental TEM in previous chapters, which could only resolve lattice projections at the edge of larger COF structures. Past a particular thickness threshold that depends on the sample, and outside of specific orientations such as the FO projection, the sample will appear amorphous by BF-TEM imaging.

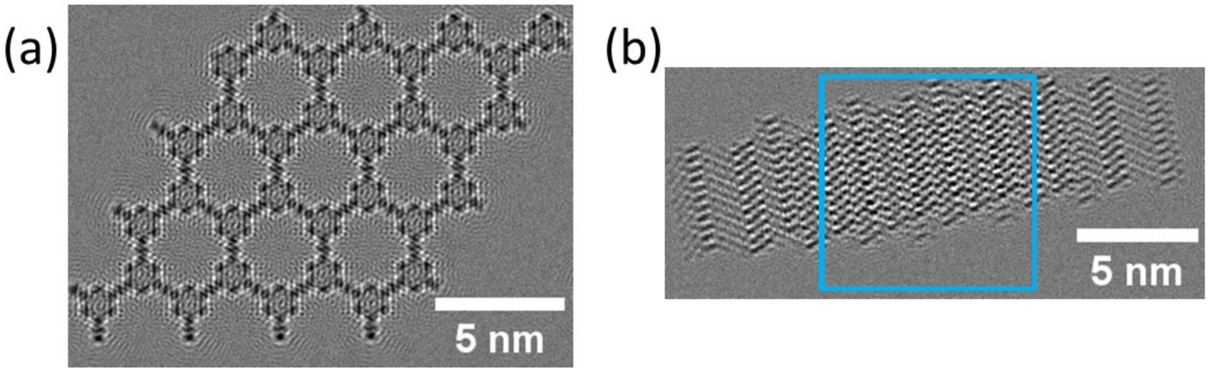

Figure 77: Image simulation cHBC-COF in (a) FO projection (θ, ϕ) = (0, 0) and (b) rotated to an arbitary angle (θ, ϕ) = (80, 20). The model contains 20 stacked COF sheets. It can be seen in (b) that the central region of the model (blue box) does not contain easily identifiable lattice projections due to thickness effects; lattice projections can still be identified at the thin edges of the model.

4.2.5 Creating Stereographic Maps of Lattice Projections

A stereographic projection (stereogram) was used to map the absolute rotational relationship between lattice projections (Figure 78a). A stereogram of a unit sphere was used as it is a useful tool for visualising spheres on a 2D plane, and preserves the precise angular relationship between points while distorting distance between points. It also allows reference to each projection via spherical polar coordinates using the polar (θ) and azimuthal (ϕ) angles (Figure 78b). This was achieved in a similar way to stereograms used for crystallographic studies;[17] briefly, an imaginary sphere is constructed around the model such that the optical axis is passes through the poles of the sphere - these points are marked as the FO projection. The sphere and model are rotated as one object while the optical axis remains stationary. As each principal projection is aligned with the optical axis, it is marked onto the surface of the sphere. This is repeated for all the principal projections to give a spherical map that accurately contains all of the angular relationships between different principal projections.

To account for all of the minor projections that arise from infinitesimal rotations of the model away from the principal projections, boundaries between each principal projection were defined corresponding to the locus of points equidistant between projections (coloured areas in Figure 78c). The projections in each area are then considered to be a rotation of the principal projection that area corresponds to. In essence this is a development of the rotation tableau method that is used for high resolution TEM (HRTEM) of small crystals or single molecules, where HRTEM images are simulated for several discrete rotations of a model - these corresponds to the principal projections discussed here. An example of a rotational tableau for polyoxometallates by Jordan *et al.* demonstrates clearly how the rotation of a sample relative to the optical axis leads to different projections, which they achieved using multislice HRTEM simulation for $[P_2W_{18}O_{62}]^{6-}$.[18] The main advantage of the 3D map is it is a continuous representation of rotations instead of discrete, and for large structures like COF lattices a tableau may have to be very large to convey the appropriate level of structural detail.

Using the equidistant approximation is required as it further simplifies the system by assuming that no principal projection is "stronger" than another and thus covers more surface area of the 3D map. This approximation should be born in mind when analysing practical results as it

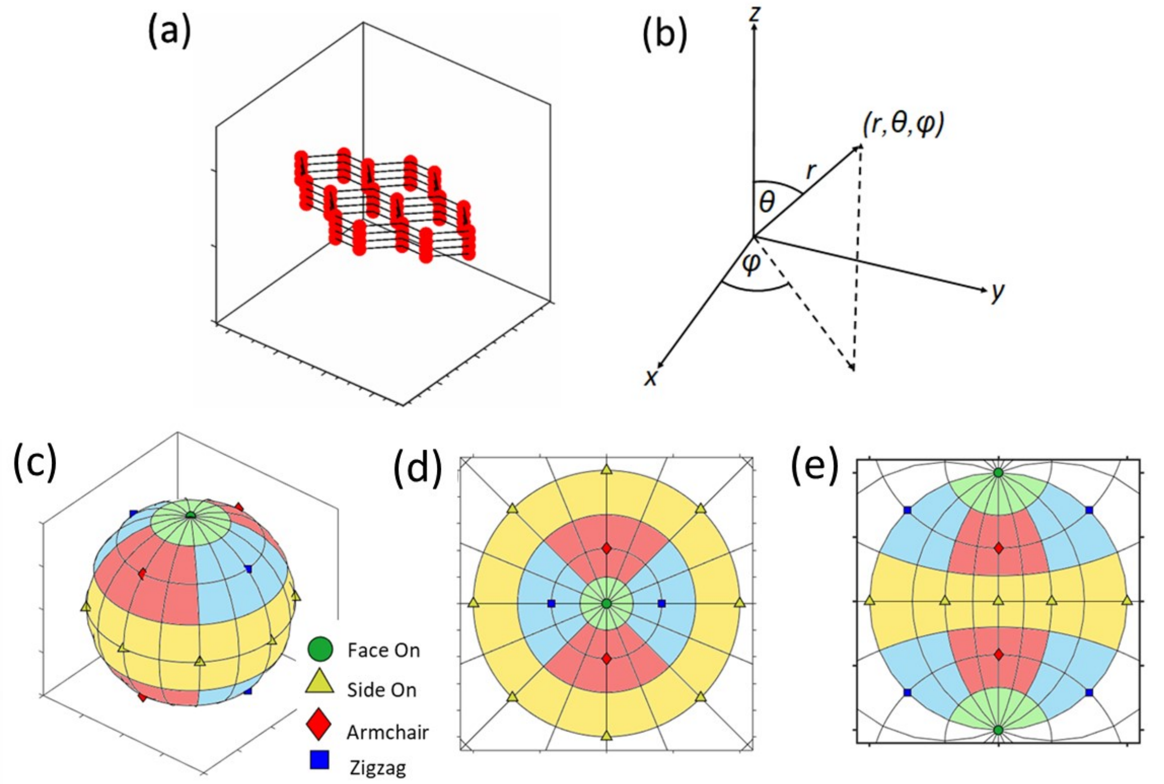

Figure 78: (a) Example AA stacked hexagonal sheet. (b) Diagram illustrating the azimuthal (ϕ) and polar (θ) angles in a spherical polar coordinate system. For a unit sphere centered at the origin, any point on the surface can be uniquely defined using (r, θ, ϕ) and, for $0 : \phi : 2\pi$ and $0 : \theta : \pi$. For example, the poles of the sphere are (1,0,0) and (1,π,0). (c) Spherical map of rotational relationship between hexagonal face-on (green), side-on (yellow), armchair (red), and zigzag (blue) projections. (d) Hemispherical polar stereographic projection of spherical map. (e) Hemispherical equatorial stereographic projection of spherical map. The shaded areas indicate the areas closest to each principal projection. The stereographic projections preserve the angular relationship between projections but distort the size of the shaded areas.

may not hold true in all situations. Polar and azimuthal (equatorial) hemispherical stereograms were then constructed from the 3D map using a stereographic projection (Figure 78d, e). The resulting stereograms are intuitive to read and can be constructed from any arbitrary projection point on the surface of the sphere.

4.2.6 Projection Probabilities

Taking the equidistant assumption, it then follows that the ratio of the area of each region on the 3D map to the total area of the map represents a probability of that projection being randomly picked if all possible orientations of the sphere to the optical axis are equally likely. In an experimental context this would correspond to no preferential alignment of the sample on the TEM grid. Using the equation for surface area of a spherical cap and taking the radius of the sphere to be 1 the surface area of each region can be calculated:

$$A = 2\pi r^2(1 - cos\theta) \tag{18}$$

$$A_{FO} = 4\pi r^2(1 - cos\theta_x) \tag{19}$$

$$A_{SO} = 4\pi r^2 - 4\pi r^2(1 - cos\theta_y) \tag{20}$$

$$A_{AC+ZZ} = 4\pi r^2 - A_{FO} - A_{SO} = 4\pi r^2[(1 - cos\theta_y) - (1 - cos\theta_x)] \tag{21}$$

$$A_{AC} = A_{ZZ} = 2\pi r^2[(1 - cos\theta_y) - (1 - cos\theta_x)] \tag{22}$$

Where A is the surface area of a spherical cap, θ_x is the polar angle at which the FO projection area ends (= $22.5°$) and θ_y is the polar angle at which the SO projection area starts (= $67.5°$). A_{FO}, A_{SO}, and A_{AC}, A_{ZZ} are the respective areas of the FO, SO, AC, and ZZ projections. The surface areas and probabilities are summarised in Table 13. Statistically significant deviation from the ratio of these probabilities would imply that the sample contains preferential alignment with regards to the optical axis of the TEM. Statistical significance can be defined by the experimentalist, such as falling outside of a 2σ confidence interval. This is relevant to experimental TEM findings where projections did not occur equally frequently,[16] discussed in detail in Chapters 2 and 3.

Projection	**Surface Area / units^2**	**Probability**
Face On	0.48	0.04
Side On	4.8	0.38
Armchair	3.6	0.29
Zigzag	3.6	0.29
Total	4π	1

Table 13: Probabilities of each principal projection of a hexagonal lattice based on sphere surface area for a unit sphere. The probability is the ratio of the surface area of the projection and the total surface area of the sphere.

To demonstrate this, computer generated data was made using three probability regimes: those in Table 13, for these probabilities tweaked so AC $\neq$ ZZ, and using the assumption that all

Projection	**P_1**	**Draws**	**P_2**	**Draws**	**P_3**	**Draws**
FO	0.25	249923 ± 433	0.04	3993 ± 218	0.04	4011 ± 133
SO	0.25	25076 ± 641	0.38	38055 ± 713	0.38	38049 ± 755
AC	0.25	24924 ± 657	0.29	28992 ± 778	0.19	19018 ± 375
ZZ	0.25	25008 ± 684	0.29	28961 ± 263	0.39	38921 ± 832
FO	0.25	2.2 ± 4	0.04	0.6 ± 4	0.04	0.4 ± 2.7
SO	0.25	2.2 ± 6.5	0.38	3.8 ± 12	0.38	4.2 ± 6
AC	0.25	3 ± 8	0.29	2.8 ± 8	0.19	2.2 ± 8
ZZ	0.25	2.6 ± 7	0.29	2.8 ± 10	0.39	3.2 ± 5

Table 14: Mean and 5σ standard deviations for different probabilities (P) of projections, for 10^4 draws and 10 draws. Each set of conditions was repeated 5 times to give allow calculation of a standard deviation. P_1 uses the equidistant assumption; P_2 is for the calculated probabilities in Table 13; and P_3 uses modified P_2 to illustrate when AC does not equal ZZ. For a large sample size, changing the probability has a clear impact on the draws, while for a small sample size the effect is less pronounced. This demonstrates the idea that small datasets from TEM may be unrepresentative.

projections occur equally frequently. For a given dataset, if the observed occurrences reject the equidistant assumption to an arbitrary threshold for statistical significance, this would show that preferential alignment is occurring in the dataset. The data was generated by randomly drawing a number between 0 and 1, then assigning it to FO, SO, AC, or ZZ based on the probability boundaries to simulate the effect of randomly orientating a crystallite on a surface. This was carried out for 10^4 draws and 10 draws, each being repeated 5 times. The results show that changing the probability of each projection occurring can be seen with a large number of draws while the effect is less pronounced for a small number of draws (Table 14). Looking to future experimental work, this approach could be used to establish how many observations would be required to conclusively show evidence of preferential alignment - this could be used to set a benchmark for number of experimental observations that need to be taken.

4.2.7 Stereographic Maps of Other Topologies

Stereographic maps were also made for a square lattice (Figure 79), which has a different projection map to hexagonal lattices. For other common lattice topologies (AA stacked kagome, trigonal, and rhombic)[15] explicit stereographic maps were not made as the majority of the experimental work later in this thesis is concerned with AA stacked hexagonal lattices. This said, it is expected that kagome and trigonal would have the same stereogram as hexagonal lattices, and rhombic would have the same as square lattices. This is due to the rotational symmetry of the 2D sheets and the underlying geometry; a rhombic lattice is an affine transformation of a square lattice; trigonal and kagome lattices both have AC and ZZ edges. Therefore the 3D projection maps produced are generalisable across all real materials that have the same topology and geometry; further graph contrast methodology could be extended to any crystalline condensed matter made of stacked 2D sheets, such as graphite or molybdenum sulphide.

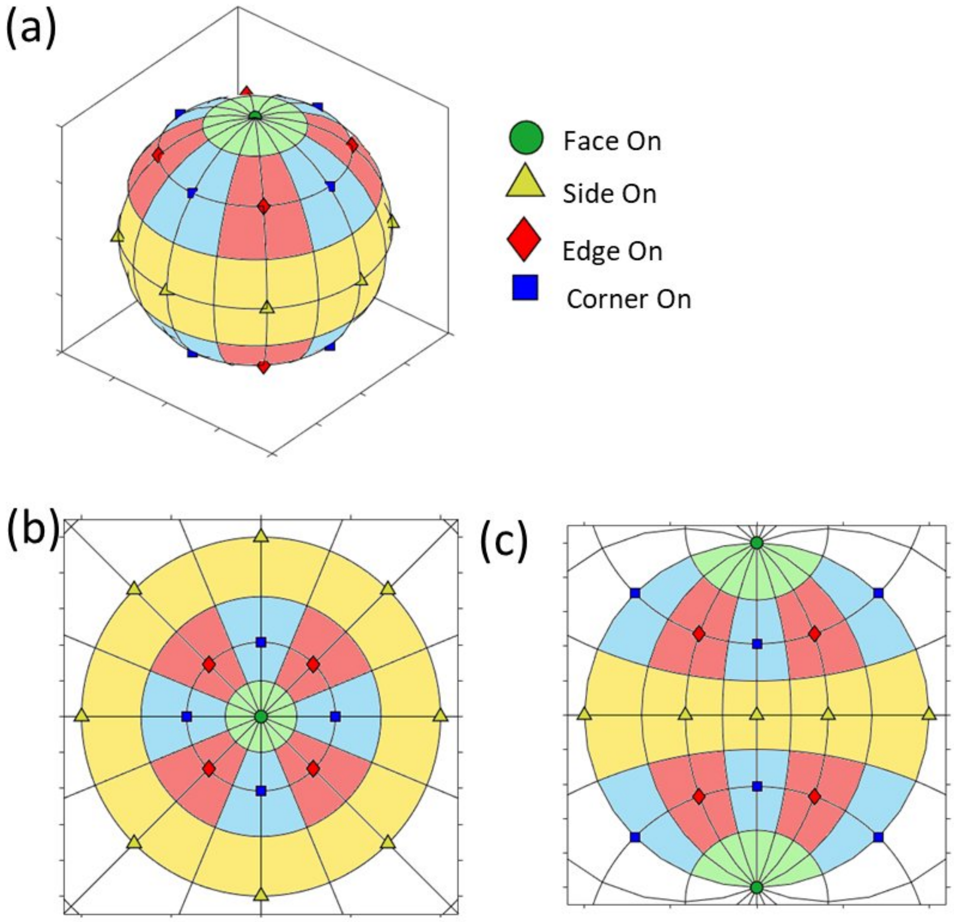

Figure 79: (a) Spherical map of rotational relationship between face-on (green), side-on (yellow), edge-on (red), and corner-on (blue) projections for an AA stacked square topology lattice. (b) Hemispherical polar stereographic projection of spherical map. (c) Hemispherical equatorial stereographic projection of spherical map. The shaded areas indicate the areas closest to each principle projection. The stereographic projections preserve the angular relationship between projections but distort the size of the shaded areas.

4.2.8 Prediction of Lattice Projections

The graph theoretical models also allow prediction of the of lattice projection width and lattice projection length at particular (r, θ, ϕ) (Figure 80). The lattice projection length varies as a function of the polar angle:

$$L(\theta) = L_1|cos(\theta)| + L_2|cos(\theta)| \tag{23}$$

Where $L(\theta)$ is the lattice projection length orthogonal to the rotation axis at angle θ, L_1 is the maximum true height of the sample and L_2 is the minimum true height of the sample (Figure 80a-c). This gives a function that varies continuously between a maximum and minimum value.

It was expected that the lattice projection width varies as a function of the azimuthal angle via a similar function:

$$d(\phi) = d_{AC}|cos(\phi)| + d_{ZZ}|cos(\phi)| \tag{24}$$

Where $d(\phi)$ is the lattice projection width at angle ϕ, d_{AC} is the lattice projection width of the AC projection and d_{ZZ} is the lattice projection width of the ZZ projection (Figure 80d-f).

The projections form a pattern that repeats every 30°, which corresponds to 360/12, and indicates the projection is changing between one dominated by the AC edge to one dominated by the ZZ edge (Figure 81). However, modelling this rotation series reveals that not all intermediate angles contain visible lattice projections (Figure 82). This represents a very idealised case, and repeating these measurements for a model of COF-5 showed a pattern that matched more closely to the above equation (Figure 83). As the monomers in real COFs are not spheres, the projections do not correspond perfectly to the theoretical projections in Figure 82. As mentioned earlier rotating real COF structures may also cause them their thickness relative to the beam direction to increase, obscuring the lattice projections (Figure 77).

For a thin sample projections can then be measured experimentally and used to work out the relative rotation of the COF structure with regards to the optical axis, as the visible projection is a function of the rotation of the structure in 3D space.

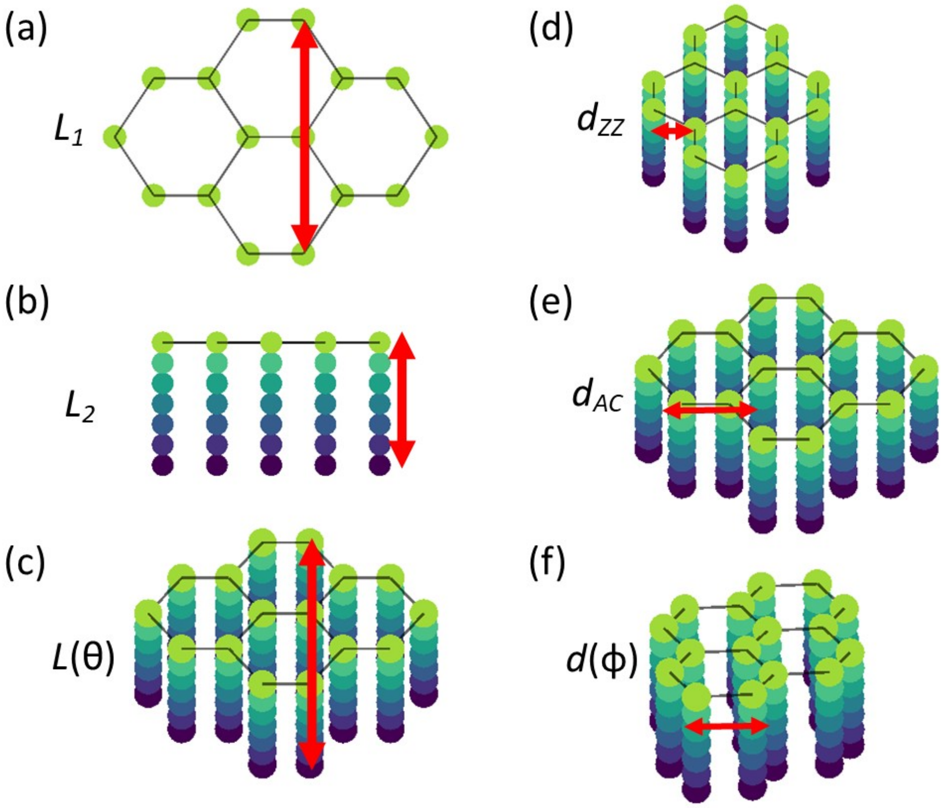

Figure 80: Diagrams illustrating (a-c) lattice projection length $L(\theta)$ and (d-f) lattice projection width $d(\phi)$ on graph theoretical models of AA-stacked hexagonal sheets. The red arrows represent the corresponding quantity being illustrated.

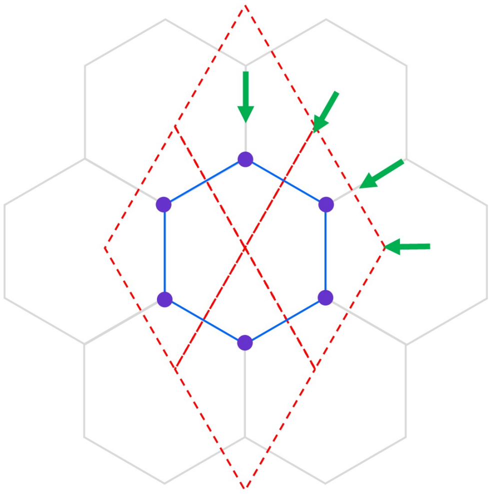

Figure 81: Illustration of how hexagonal patterns repeat during a rotation. The green arrows indicate the viewing direction at different points during a rotation series, with the purple circles indicating nodes on the hexagonal graph (blue lines). The small red dashed diamonds indicate the unit cell of a hexagonal sheet (4 pictured in total). It can be seen that the viewpoint arrows alternate between ZZ and AC during a 90° rotation.

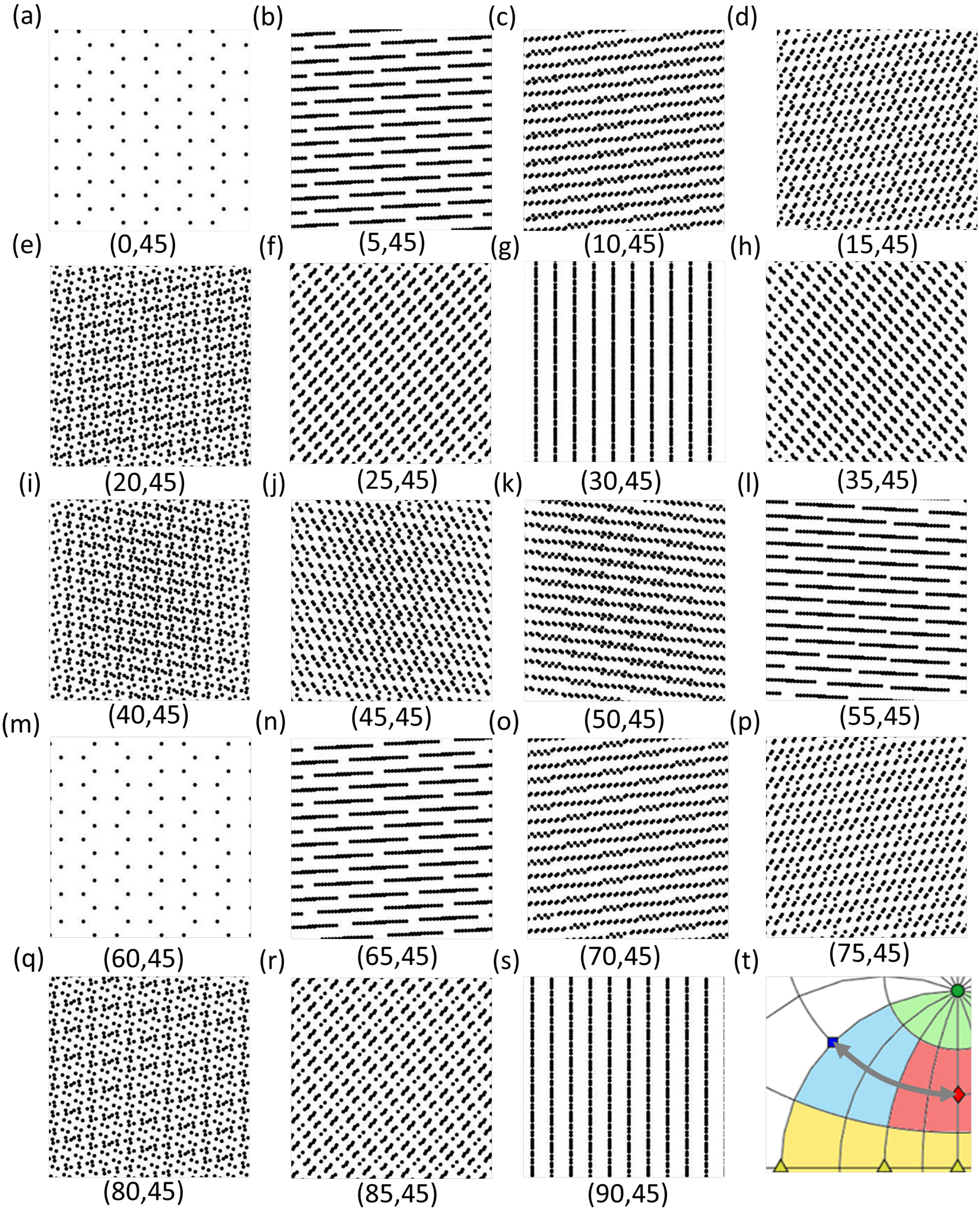

Figure 82: (a-s) Rotational tableau for AA stacked hexagonal sheets made of point nodes, with the rotation indicated in spherical polar coordinates below each image. Images (a) and (s) represent the armchair and zigzag projections. The tableau is periodic over 60°. (t) Azimuthal stereographic projection indicating the full rotational range.

4.2.9 Recovering COF Orientation From Lattice Projections

Using the relationship between projection and orientation in space above it is theoretically possible to measure the lattice projection length during a tilt series of a COF crystallite, then compute the approximate rotation of the COF crystallite relative to an optical axis in real space. This was not achieved reliably for experimental COF-5 data. An experimental data set would consist of lattice projection width (d) and lattice projections length (L) as a function of the TEM stage tilt angle (ρ). The challenge is that given $d(\rho)$ and $L(\rho)$, how can one recover the azimuthal and polar angles, ϕ and θ (Figure 84)?

To recover the azimuthal angle from the observed lattice projection distance the above equations can be applied, taking advantage of the fact that they resemble equations for simple harmonic motion[19] to express them in terms of alternative variables:

$$d(\rho) = kcos(\phi + \alpha) \tag{25}$$

$$k = \sqrt{d_{AC}^2 + d_{ZZ}^2} \tag{26}$$

$$\alpha = tan^{-1}(d_{AC}/d_{ZZ}) \tag{27}$$

$$\phi = cos^{-1}(d(\rho)/k) - \alpha \tag{28}$$

Where k is the maxima of oscillation and α is the initial phase. The sign of α and the application of sine or cosine depends on the quadrant of the function. As d_{AC} and d_{ZZ} are known from the electronic structure model of COF-5, calculation of the azimuthal angle is straightforward. An equivalent function exists for the polar angle:

$$L(\rho) = \kappa cos(\theta + \beta) \tag{29}$$

$$\kappa = \sqrt{L_1^2 + L_2^2} \tag{30}$$

$$\beta = tan^{-1}(L_1/L_2) \tag{31}$$

$$\theta = cos^{-1}(L(\rho)/\kappa) - \beta \tag{32}$$

Where κ is equivalent to k and β is equivalent to α. Calculating the polar angle is challenging as the real space maximum length (L_1) and minimum length (L_2) of a crystallite under experimental conditions are unknown. The function used passes through inflection points when $L(\theta) = L_1$ and $L(\theta) = L_2$; if an experimental data set passes through one of these points, it will be easily recognisable. If the data does not pass through an inflection point then iterative fitting over the range $\theta = 0°$ to $90°$ can be attempted, the assumption being that the best fit will be the true polar angle range. Fits that do not make physical sense, e.g. around the inflection point of the function, can be rejected.

Fitted Data Points	**RMSE**	L_1 **/ nm**	L_2 **/ nm**	**Computed Angle Range** / °	**Real Angle Range** / °
35	0.13	11.9	4.01	0 - 170	0 - 170
18	0.16	11.8	4.06	30 - 110	25 - 105
9	0.14	12.1	4.10	0 - 40	85 - 125
5	1.45	10.4	7.15	10 - 30	110 - 130

Table 15: Number of fitted data points, reduced mean square error (RMSE), L_1 and L_2 for fits of data generated with Equation X. As expected, fewer data points increases the RMSE and reduces the accuracy of L_1 and L_2. The true values were $L_1 = 12$ nm and $L_2 = 4$ nm.

This approach was tested with computer-generated data, by using the equation for $L(\rho)$ to generate data points at $5°$ intervals over a $180°$ range. A random sample of a sequential sequence of $L(\rho)$ data points was taken from the generated data, then the stage tilt angle ρ was set as $0°$ for the first measurement in the sample. This gave a data set analogous to experimental tomography data, where the projected line length is known as a function of the microscope stage tilt. The language of tomography, the lattice projections could be considered an in-built fiducial marker that gives information on the 3D orientation of the COF.

$L(\rho)$ and ρ were fitted to the equation for $L(\rho)$; then the values of ρ were increased by $5°$ and another fit performed. In essence each possible set of polar angles the data could correspond to are being fitted against. This gave a series of goodness of fit values and value of L_1 and L_2 for each angle range (Table 15). This approach was found to perform well for large data samples and those that occur near inflection points, however for small data samples this approach would generally give a range of angles over which the data could be fitted.

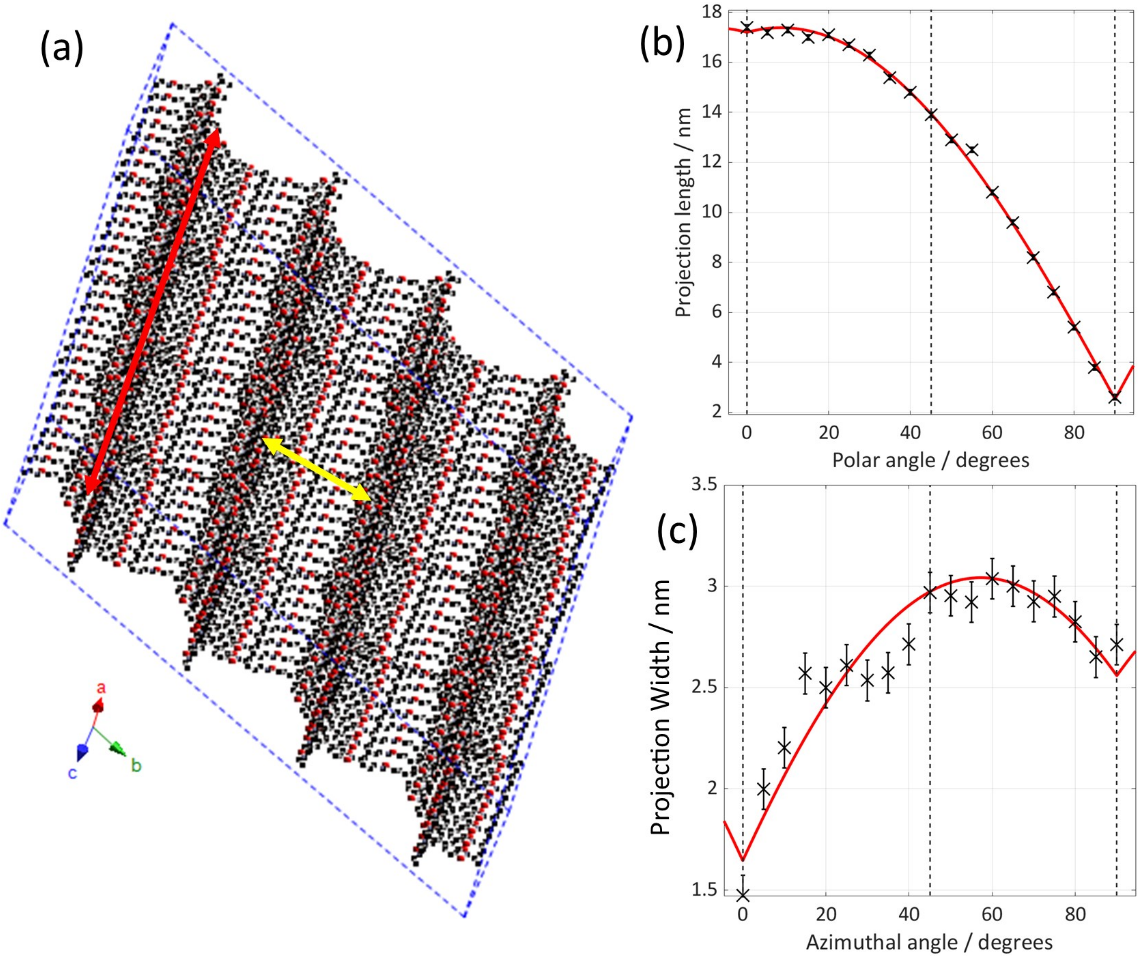

Figure 83: (a) DFT structure model of COF-5 where red and yellow arrows indicate the lattice projection distance and lattice projection length. (b) Lattice projection length versus polar angle for azimuthal angle = 0°, and (c) lattice projection width versus azimuthal angle for polar angle = 45°. The error bars represent the 2σ standard deviation.

An ideal experimental dataset would be of high spatial resolution and high tilt resolution, giving finely sampled data for the fitting. As has been noted in the TEM tomography literature, the accurate measurement of microscope stage tilt is essential for reconstructing 3D information from 2D TEM images.[20] The biggest drawback is that it has not yet been experimentally proven that the lattice projection distance and lattice projection length will follow the functions suggested in this thesis, but once a suitable dataset has been acquired the equations and fitting could be modified to find the "real" function. It is also worth mentioning that the imaging focus will likely affect the lattice projections, which is another topic that could be investigated.

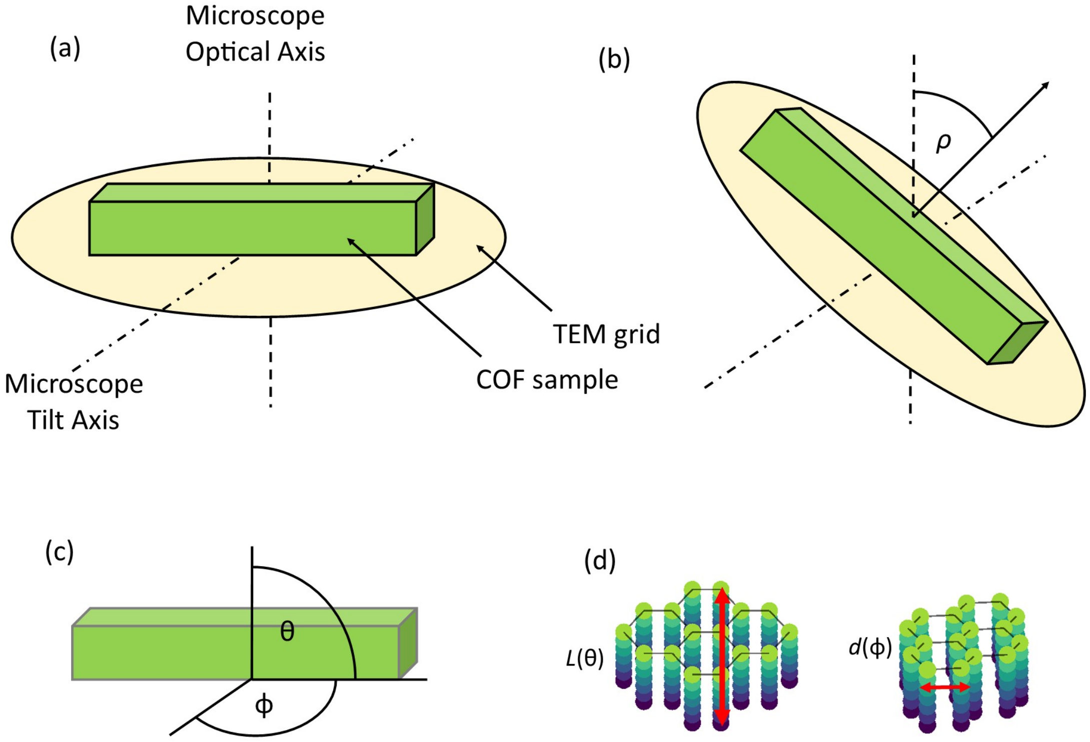

Figure 84: (a, b) Illustration of the stage tilt angle (ρ), which is controlled by the microscope operator. (c) Illustration of the azimuthal and polar angles, ϕ and θ, which are relative to the COF crystallite. (d) Graph theoretical models indicating the lattice projection length $L(\theta)$ and lattice projection width $d(\phi)$.

4.3 Graph Theory Stochastic Modelling of Polymer Morphology

4.3.1 Conceptualising a Stochastic Graph Model

A model was then developed to investigate the COF formation process, and to help provide visual intuition for how COF polymers grow using a stochastic graph model. As with the structural models above, this is generalisable to all structures of the same topology which form via similar kinetics. In practice, this approach was also successful in giving MChem project students a very visual introduction to COF growth processes, first as a thought experiment and then as the series of models presented here.

Here briefly is the thought experiment underlying the polymer growth models below. Imagine a growing 2D COF polymer in solution, with an arbitrarily dilute solution and arbitrarily quick monomers addition so that at any time only one new monomer can be added to the COF sheet. The 2D sheet is aligned with the x-y plane, and the face-on projection is normal to the z-axis. Monomers can approach the growing polymer from any direction, so over time the polymer should tend to growth equally in all directions. However as monomers can adsorb to the polymer to form a new layer, or add covalently to an existing layer, if either bonding process is more favourable than the other, then the polymer will start to exhibit preferential growth in either the x-y plane or the z-axis. In essence we can imagine the COF growth processes as being probabilistic.

From *Principles of Polymer Chemistry* chapter seven,[21] step-growth polymers grow via a series of discrete addition steps which typically causes a slow initial growth in molecular weight. Monomers also disappear quickly from such reaction mixtures, and the majority of growth comes from oligomers combining to form longer chain polymers. To account for this, it is often assumed that the reactivity of the functional groups remains the same whether they are part of oligiomers or monomers, such that step growth polymerisation can be treated like the reactions of small molecules. Many step-growth polymerisation reactions are equilibrium reactions, such as polyesterification. Thus, the reaction conditions must be tuned so that the equilibrium constant shifts towards the products. COFs are essentially step-growth polymers, but their precise growth mechanisms have not yet been thoroughly investigated. Further, COFs containing monomers of different chemical functionality may have different growth kinetics. Therefore it is useful to investigate COF polymer growth using a simplified model of step-growth polymerisation.

4.3.2 1D Polymer Size Model

Stochastic graph generation was selected as the process by which models would be made. The ultimate goal of this modelling technique was to generate structures similar to those which can be observed in the experimental TEM literature (see literature review, Chapter 1). This further allows testing for the presence of projections in a graph whose structure is not rigorously designed by the researcher, helping bridge the gap from theory to experimental TEM. For example the structure used to generate the tableau in Figure 82 is a perfect crystal, which is not representative of the wide range of COF morphologies seen in the literature. The modelling process uses a simplified reaction scheme in order to create a structure similar to that which can be observed in the experimental TEM literature. The first step was creating a simple proof-of-concept model to test how probability of addition and loss of monomers from a polymer affects the size of the polymer. This was done by modelling the size of the polymer, but not the connectivity of the monomers. Two variables were defined - monomers (*mon*) and polymer (*pol*). At the start of the simulation,

$$mon = x \tag{33}$$

$$pol = 0 \tag{34}$$

where x is an arbitrary integer that represents the total number of monomers in the system. At each simulation step, one of two random draws were allowed:

$$\mathsf{P}(\mathsf{loss}) = (mon = mon + 1, pol = pol - 1) \tag{35}$$

$$\mathsf{P}(\mathsf{add}) = (mon = mon - 1, pol = pol + 1) \tag{36}$$

with the probabilities P(loss) and P(add) defined as

$$\mathsf{P}(\mathsf{add}) = y \tag{37}$$

$$\text{P(loss)} = 100 - y \tag{38}$$

Where y is an arbitrary number $100 \geq y \geq 0$. These rules can be summarised as the polymer either grows by one unit or becomes smaller by one unit at each simulation step. This matches the assumption that step-growth occurs as a series of discrete steps. The main drawback to this simulation method is that the simulation steps are time-independent, so cannot be used to interrogate reaction kinetics and cannot generate absolute rate constants. However, the ratio of P(add)/P(loss) is in effect a relative rate constant, or an equilibrium constant K_{eq} (Table 16).

This method models the growth of a single polymer, and does not model multiple polymers competing for a limited pool of monomers. Polymer growth also only occurs via monomers, and the role of oligiomers is not considered. However this approach allows a conceptually straightforward way to investigate the effect of probability on polymer size.

P(add)	**P(loss)**	**K_{eq}**	**P(add)**	**P(loss)**	**K_{eq}**
0	100	0	55	45	1.2
5	95	0.05	60	40	1.5
10	90	0.11	65	35	1.86
15	85	0.18	70	30	2.3
20	80	0.25	75	25	3
25	75	0.33	80	20	4
30	70	0.43	85	15	5.7
35	65	0.54	90	10	9
40	60	0.67	95	5	19
45	55	0.82	100	0	N/A
50	50	1	-	-	-

Table 16: Probability of monomer addition (P(add)), probability of monomer loss (P(loss)), and corresponding equilibrium constants (K_{eq}) used in the 1D polymer size model. K_{eq} is calculated as the ratio of P(add):P(loss); when $K_{eq} > 1$ the model polymer is more likely to gain monomers than loose them.

Simulations were performed for a range of equilibrium constants (Table 16). Each simulation contained 200 monomers and was run for 10×10^5 simulation steps, which allowed for equilibration of the mean polymer size (Figure 85a). Increasing the number of monomers delays the point at which equilibrium is reached (see Appendix Figure 107).

From the equilibrated data the mean polymer size and standard deviation were computed (Table 17). The trivial results are that for K_{eq} = 1/0 the polymer grows to the maximum size and is stable there for the whole simulation, and for K_{eq} = 0, the polymer does not increase in size.

P(add)	$\mu \pm 3\sigma$	**P(add)**	$\mu \pm 3\sigma$	**P(add)**	$\mu \pm 3\sigma$
0	0.0 ± 0.0	35	100.1 ± 5.5	70	198.9 ± 0.1
5	99.3 ± 4.4	40	100.2 ± 4.9	75	199.1 ± 0.1
10	101.0 ± 4.0	45	100.3 ± 5.7	80	199.2 ± 0.1
15	101.5 ± 4.8	50	99.7 ± 4.9	85	199.3 ± 0.1
20	99.9 ± 5.6	55	195.3 ± 0.5	90	199.4 ± 0.1
25	100.3 ± 5.1	60	197.7 ± 0.2	95	199.5 ± 0.1
30	100.4 ± 4.8	65	198.5 ± 0.2	100	200.0 ± 0.0

Table 17: Mean and 99.7 % confidence intervals for 1D polymer simulation, taken over 1000 repeats over the simulation step range 4×10^5 to 10×10^5. For P(add) > 50, the mean polymer size rapidly reaches the maximum value, with a narrow standard deviation indicating a low size distribution. For P(add) < 50, the mean plateaus at 100 with a large standard deviation indicating that at each point there are a range of polymers sizes extant between repeats.

This confirmed the simulation was operating as expected.

Examining the mean polymer size for different equilibrium constants (Figure 85a), it can be seen that two polymer formation regimes are present. When $K_{eq} > 1$, monomer addition dominates over monomer loss and the polymer rapidly grows to the maximum possible size and is then stable for the rest of the simulation - this corresponds to a growth stage and an equilibrium stage. As K_{eq} approaches 1, the equilibrium phase gets smaller as the polymer takes more simulation steps to reach it's maximum size. During the equilibrium phase, the mean size remains in the range 200 - 195, but the standard deviation of the mean increases indicating a wider range of polymer sizes between repeats at each simulation step. The distribution of polymer sizes was examined for P(add) = 65 at two points: during the growth phase it is normal distribution, while during the equilibrium phase it skewed towards the maximum value (Figure 85b, c).

When $K_{eq} < 1$ the growth phase is extended due to the loss of monomers from the growing polymer. The polymer size distribution for P(add) = 45 during the equilibrium phase shows clear skew towards the smaller polymer sizes (Figure 85d). This means that more steps are needed to reach the equilibrium phase. During the equilibrium phase, the mean polymer size is in the range 99 - 101 with a very large standard deviation. This is due to all possible polymer sizes being present across the repeat simulations, seen in the size distribution for P(add) = 45 (Figure 85e).

From these results it can be seen that when $K_{eq} > 1$, the polymer will tend to grow larger,

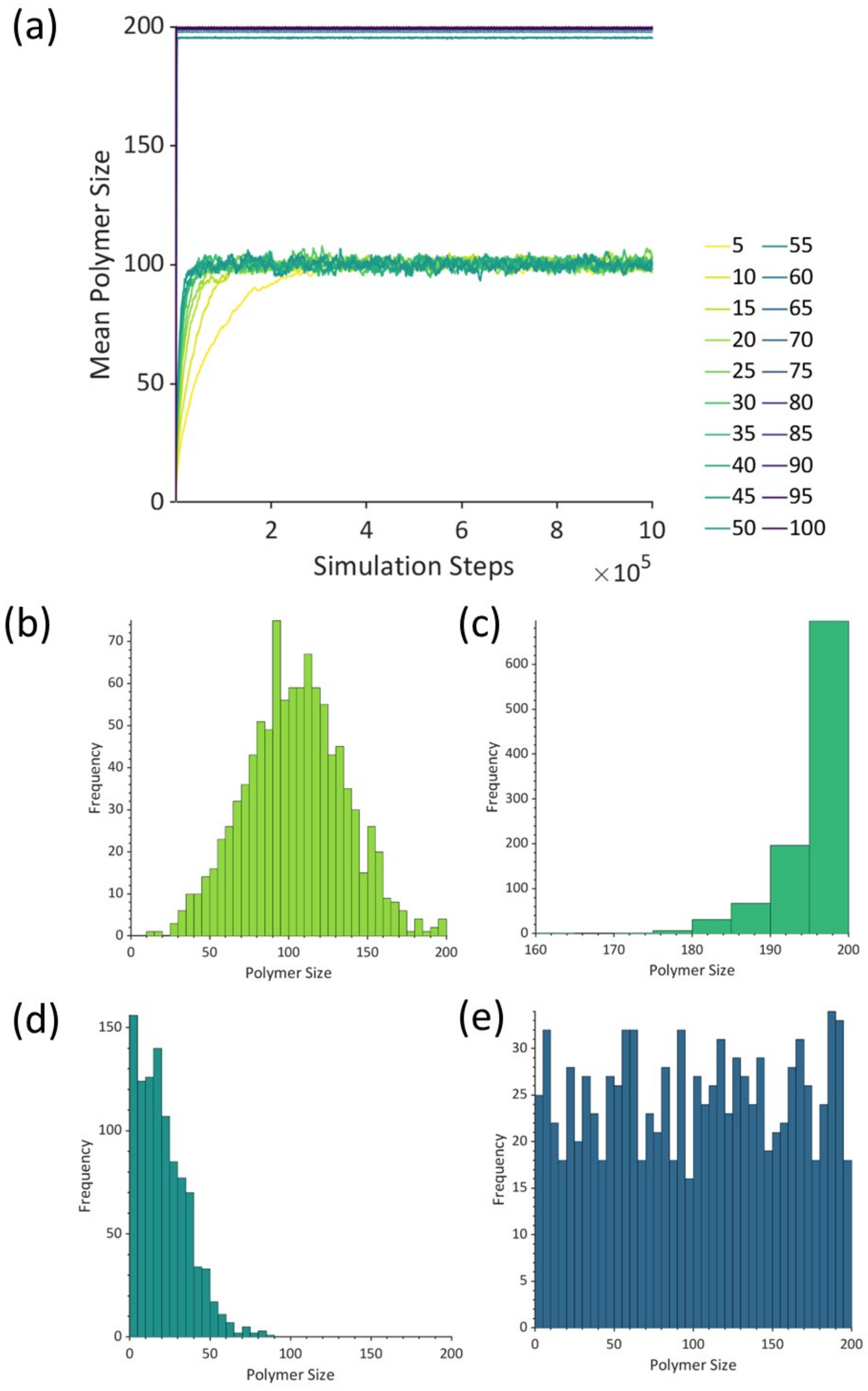

Figure 85: (a) Plot of model growth, showing two distinct growth regimes for P(add) > 0.5 and P(add) < 0.5. Distribution of polymer sizes for P(add) = 0.65 at (a) 1×10^3 steps and (b) 5×10^5. The distribution goes from a skewed normal distribution centered around a polymer size of 110 to a distribution were the majority of polymers are at the maximum possible size. Distribution of polymer sizes for P(add) = 0.45 at (d) 1×10^3 steps and (e) 5×10^5 steps. The first distribution shows that while some polymer growth occurs, the majority of polymers have a small size with none larger than 100 units. At equilibrium, all possible polymer sizes are represented with a low frequency for any given polymer size.

and as K_{eq} increases above 1 there will be a narrower distribution of polymer sizes at any point of the simulation. This result rationalises well with current understanding of reaction equilibria, and confirms that the simplified growth models used here approximate step-growth polymer formation processes.

4.3.3 2D Polymer Connectivity Model

The next step was to build a model where the node connectivity was recorded, but the spatial relationship between the nodes was not defined. This model builds a network of nodes which can be used to track how many bonds each node has, and the distribution of number of bonds relative to the covalency of the nodes. This model was operated using P(add) = 1, i.e. $K_{eq} » 1$. This meant that nodes were only added to the graph, and were never removed. Nodes were added randomly to the polymer network by forming a new edge with any unsaturated node. This was tested for nodes of covalency 2-6 for 5,000 steps, with each covalency regime being repeated 1,000 times.

It was found that as the covalency increases, the distribution of bonds per node widens (Figure 86). This means that the number of saturated nodes in the polymer decreases, and that the polymer network can accept a new node at many locations. In contrast 2-covalent nodes simulating a linear polymer are made up almost entirely of saturated nodes, with only two unsaturated nodes from which the polymer chain can grow. In practical terms, this means that a growing COF polymer will be able to grow indefinitely as long as monomers are available. The reason for this trend is that as more monomers are added to the polymer the number of new bonding sites increases faster than they are used up, e.g. a 3-covalent node uses up one bonding site, but adds two more. In reality is may not be the case due to ring-closing, where a monomer forms bonds to multiple sites in the polymer lattice. For 3-covalent monomers, this causes the formation of 6-membered rings in the polymer network.

A simple solution to allow ring closing was implemented by checking for nodes within an arbitrary number of steps from the added node, and allowing a bond to form between these nodes if they are close enough (Figure 87) which creates rings of monomers within the polymer structure. The arbitrary number used was 6, in order to stimulate the formation of 6-membered rings.

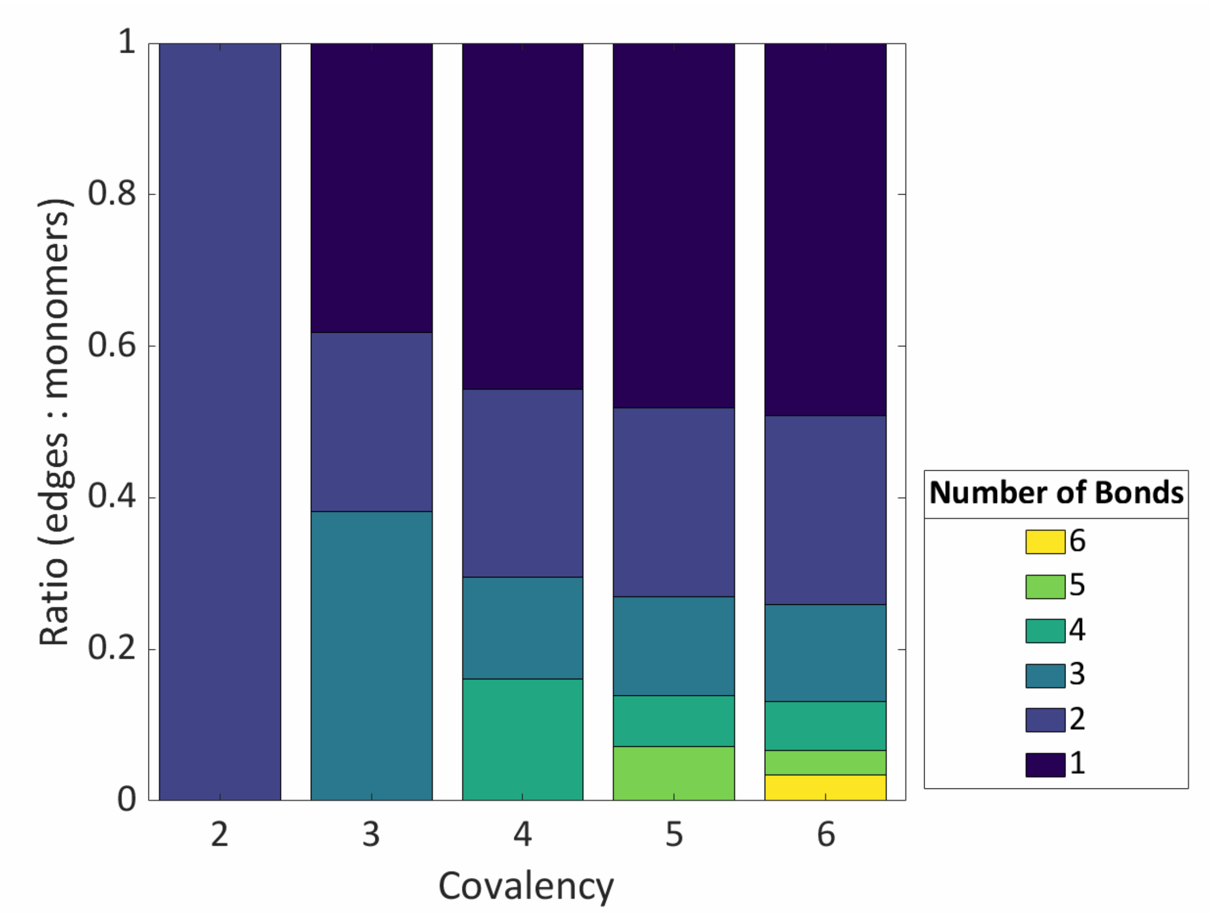

Figure 86: Number of nodes with 1, 2, 3, 4, 5, or 6 bonds for simulations with different covalency, normalised by the number of monomers in the simulation. As covalency increases there tend to be more unsaturated nodes, due to the increase in the number of vacant binding sites for each new node that is added to the structure. For any covalency above 2, a growing polymer will have many available sites for addition of monomers.

This increases the amount of saturated nodes in the graph, and creates a densely interconnected network of nodes.

This simulation essentially models an amorphous polymer network of varying connectivity, and gives insights into how a polymer network forms. It can be surmised that if there is no mechanism to encourage ring closing behaviour, the network will tend to form as a hyper-branched polymer, but where there is a driving force for ring closing rings will form readily. These graphs also show that at any point these polymer networks will have many unsaturated nodes available to which new nodes can add, the number of which is reduced if the graph undergoes ring-closing behaviour. From this it can be inferred that for a real polymer system, cross-linking will occur readily if there is enough energy available and that as more monomers are added to the polymer there will be more sites available for the polymer to grow from, leading to runaway growth.

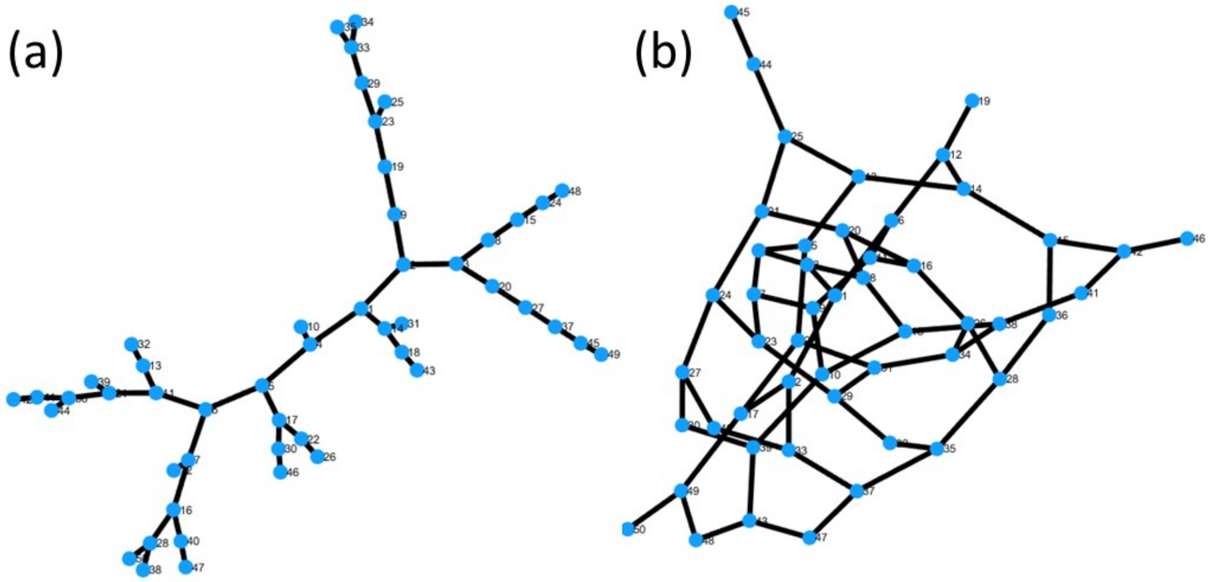

Figure 87: Illustration of 2D connectivity models for covalency of 3 with (a) no ring closing and (b) ring closing allowed. When ring closing is allowed, the graph is much more interconnected. When no ring closing is allowed, the graph forms many separate branches. The absolute spatial position of the nodes in these models are not defined, only the node connectivity. Each node is labelled by a unique number.

4.3.4 2D Polymer Structure Model

Building on the insights of the above work, a model was designed to simulate random growth of a polymer crystal. The resulting COF simulation script (COFSim) uses a randomly built 2D graph to represent a hexagonal polymer sheet where all nodes are in the x-y plane (Figure 88a-c).

The model operates in the $K_{eq} \gg 1$ probability regime, and the simulation ends once the polymer reaches the maximum possible size, i.e. only the growth phase is simulated, and the equilibrium phase is not modelled. At each simulation step, a new node is added to the graph by randomly joining to an existing node. The covalency and connectivity of nodes was predefined so each node could only have 3 edges, edges were separated around nodes by 120° and were of fixed length, and nodes could not occupy the same position in space. Ring closing was controlled by a probability factor P(RC). This builds on the previous model by adding absolute coordinates for nodes, rather than tracking only the nodes connectivity. Each simulation contained 5,000 monomers and was repeated 1,000 times. Simulations were run for ring closing probabilities 0 : 0.1 : 1. It was found the simulation time scaled approximately to the square of the number of monomers in the simulation.

This resulted in 2D hexagonal sheets (Figure 88a-c). As the ring closing probability decreases from 1, the number of unsaturated nodes in the structure increases. For ring closing probability of 0, this results in a 2D hyper-branched polymer as was seen in the previous section. The polymer shape at the end of the simulation for each ring closing probability was quantified by dividing the simulation area in to quadrants centred on the origin and counting how many nodes were in each quadrant, then taking the mean across 1,000 repeats (Figure 88d). It was found that for each probability regime, there was no meaningful variation in the number of nodes per quadrant. This shows that there is no preferential growth direction for the 2D sheet on average, and ring closing does not affect the growth direction. As ring closing does not affect graph shape, it can be concluded that the graphs in all cases are growing from unsaturated nodes concentrated at the outside of the sample. In a real polymer, the IR signal would expect to change depending on the saturation of the polymer. If the polymer contains mostly 1- or 2-bonded nodes, then a IR stretches for monomers would be proportionally stronger due to the unpolymerised functionalities on the nodes. If the polymer contains mostly 3-covalent nodes, then the IR will contain proportionally stronger polymer stretches.

The mean number of bonds in the structure was then calculated for each probability regime (normalised to the number of monomers in the graph), which showed that as ring closing probability increases the mean number of bonds in the 2D sheet increases linearly between a minimum

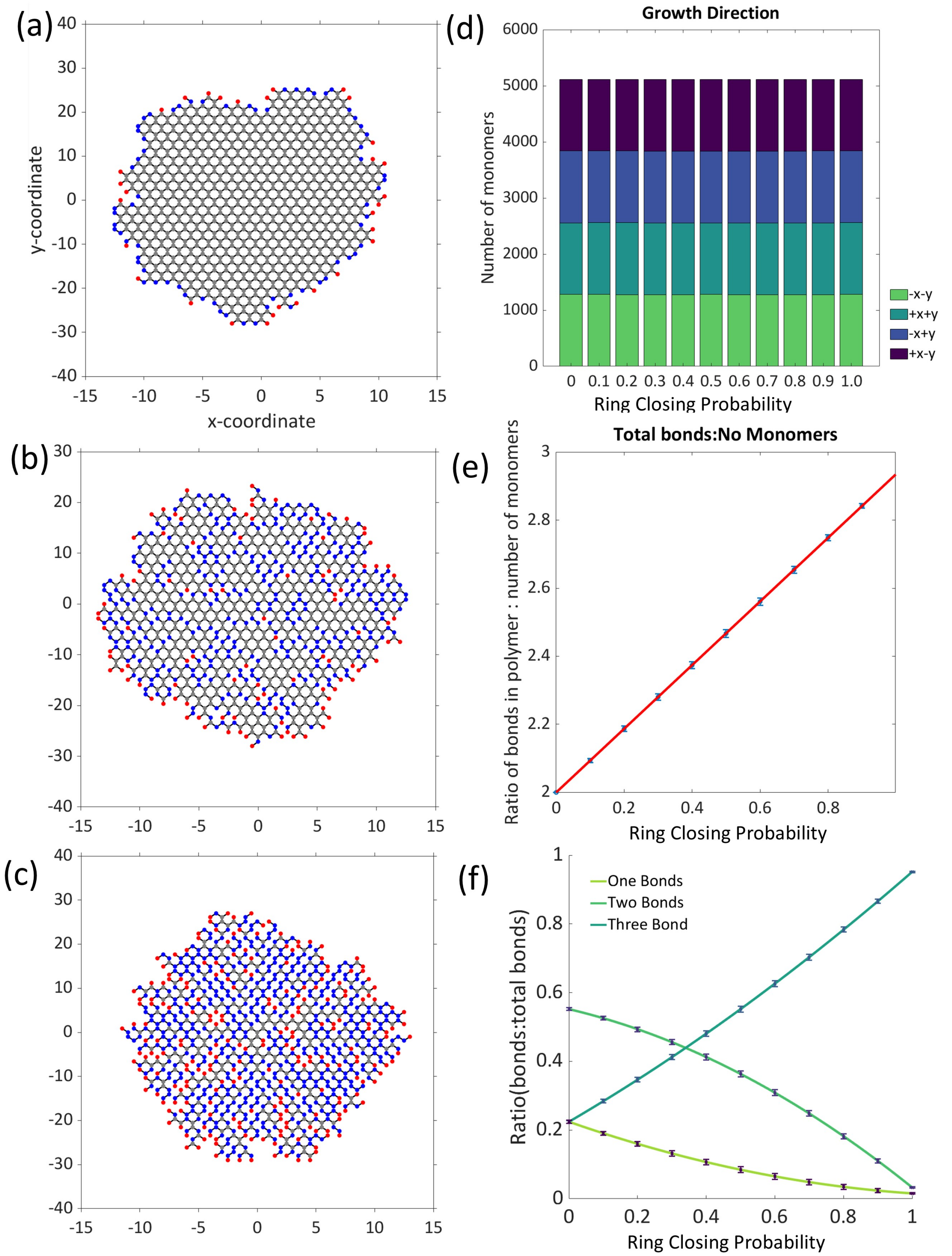

Figure 88: Example graphs for (a) 100% ring closing probability, (b) 50% ring closing probability, and (c) 0% ring closing probability. Each graph has 1000 3-covalent monomers. Grey monomers are saturated, blue monomers have 2 bonds, and red monomers have 1 bond. (c) Average number of monomers in 4 quadrants for different probability regimes, showing no preferential growth direction; (d) average ratio of total number of bonds to number of monomers in model, showing a linear increase as ring closing probability increases; (f) ratio of monomers with 3, 2, and 1 bonds to the total number of monomers in the model. Ring closing reduces available bonding sites for new monomers.

and maximum for P(RC) = 0 and P(RC) = 1 (Figure 88e). The number of nodes with 1, 2 and 3 bonds was then quantified, which shows that as P(RC) increases the number of saturated nodes increases while the number of 1- and 2-covalent nodes decreases (Figure 88)f). As expected, the number of nodes with 1- and 2-edges decreases while the number of nodes with 3-edges increases. This reflects that the total number of bonds in the polymer increases. The main results of these tests are that absence of bonds within the bulk of the polymer does not affect the growth of the polymer as the polymer grows from the the ring of unsaturated nodes on the outside of the polymer.

4.3.5 Structural Features of 2D Sheets

As the simulated 2D sheets are of *P6mm* symmetry, they contain the associated structure features that derive from this: armchair edges, zigzag edges, and Klein edges. The sheets also contained fjord, bay, and deep bay structures that are found in polyaromatic hydrocarbons[22] and hexagonal sheets. These features would be expected in any planar 2D sheets, such as graphene, molybdenum sulphide, or thin layer COFs. Abadia *et al.* observed via experimental TEM the existence of AC and ZZ edges in hexagonal 2D COFs,[23] however as most TEM of COF does not focus on acquiring HRTEM images of the edge of COF sheets it is unknown whether COFs can form Klein edges or other features of hexagonal 2D sheets. Klein edges in atomic hexagonal sheets such as graphene are known to be unstable and spontaneously rearrange, and their existence and reordering has been observed by experimental TEM.[24,25] However, for COFs it is possible a "Klein edge" would be indefinitely stable as the edge would be formed of relatively rigid COF monomers rather than relatively flexible single atom bonds (Figure 89a,b). To answer this question, the ideal tools would be experimental imaging and electronic structure modelling of a specific target COF structure.

The simulations in this thesis did not capture defects such as reconstructed zigzag edges or Stone-Wales defects;[26] it is currently unknown if these exist in COFs. The model is currently constrained to placing nodes in a hexagonal lattice, so Stone-Wales defects cannot form, and there is no mechanism for edge breaking and reforming to allow a defect to occur by itself. It can also be rationalised as the model representing rigid multi-atom COF monomers instead of

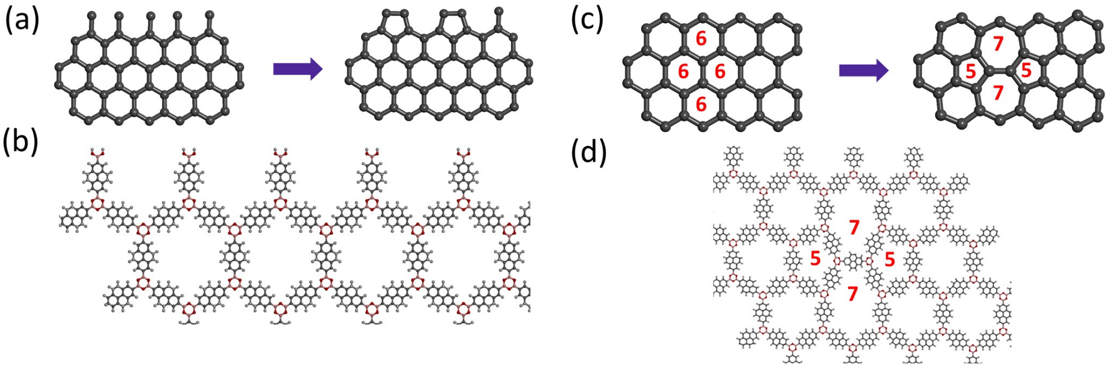

Figure 89: (a) Klein edge reconstruction in a sheet of graphene. This rearrangement is possible due to the short distance between atoms and the low energy barrier to reconstruction. (b) "Klein edge" in Py-COF. Here, the distance between monomers is much further, and bending the pyrene units to the correct angle would cause overlap with other parts of the lattice. (c) Stone-Wales rearrangement in a sheet of graphene. (d) Theoretical "Stone-Wales" defect in Py-COF.

single carbon atoms, which would be less likely to undergo rearrangements due to the much higher energy barrier compared to a Stone-Wales defect in an atomic lattice such as graphene. Of interest is the lack of vacancies in the simulated 2D sheets. Vacancies appear rarely in the bulk sheet, and typically the ragged edges of the 2D sheet are filled in as the simulation progresses. In contrast, the edges of the graph are not uniform, showing that while growth is uniform on average, at specific instances the growing edge is disorganised. This existence of particular defect types and rearrangement processes is likely linked to the types of monomer making up the COF lattice. This highlights another area where electronic structure modelling would be a good candidate for investigating the presence of these features in a specific target structure. Investigation via experimental TEM imaging will likely be challenging as it would require the synthesis of very thin COF sheets.

It is worth mentioning briefly that when using a graph model, each of the above sheet features is associated with a specific pattern of node covalency (Figure 90). For example, an AC edge will have node covalency in the pattern [...2-2-3-3-2-2-3-3...] while a ZZ edge will be [...2-3-2-3...]. In theory this could be used to create automated recognition of these features in generated graphs, but was not developed further here beyond colour coding node covalency. This could be an ideal target for developing graph modelling of COF sheets further, as it would allow fast analysis of the structure of very large sheets.

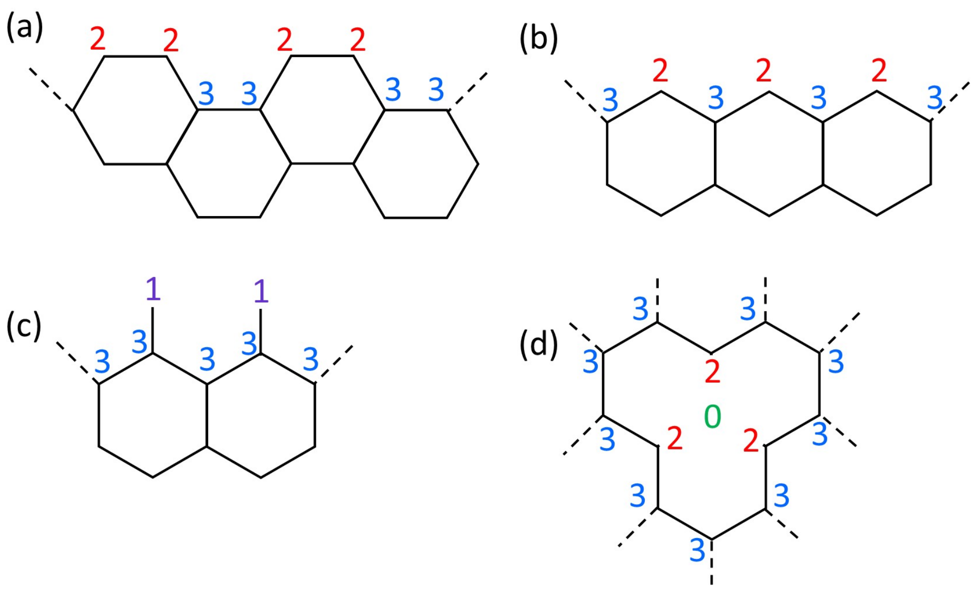

Figure 90: Node covalency patterns for (a) armchair edge, (b) zigzag edge, (c) Klein edge, (d) point vacancy.

4.3.6 3D Polymer Structure Model

To make stochastic 3D graph models an extra term was included in the 2D model to allow new nodes to be added to the graph by adsorbing on top of or below an existing node, which was controlled with a probability factor P(ads). In an experimental context, this could represent strength of $\pi - \pi$ interactions or changing reaction temperature. This gives a 3D graph composed of several 2D layers (Figure 91). When P(ads) = 0, the modelled structure is a 2D sheet equivalent to the 2D polymer structure model, and when P(ads) = 100 the structure is a 2D stack of nodes with no covalent bonding. There is an implicit probability of covalent bonding P(cov), where P(cov) = 1 - P(ads). The probability ratio P(ads)/P(cov) is again a relative rate constant that describes how likely adsorption is relative to covalent bonding. The effect of varying P(ads) on the number of layers and the mean number of nodes per layer was measured (Table 18), which shows that as the probability of adsorption increases the models tend to have more layers that contain fewer nodes. Higher P(ads) have a wider 3σ standard deviation for number of layers, but a lower 3σ standard deviation for nodes per layer. The growth direction for the 3D models was quantified by using octants and counting the number of nodes in each octant at the end of simulation, which showed no preferential growth direction, however qualitatively and from the mean number of layers it can be seen that higher adsorption probability leads to longer needlelike morphology which is not detected by the octant method. This is because the octants and the centre of the graph are aligned with the axes origin.

P(ads)	Mean number of layers	Mean monomers per layer
0	1	1000
10	11.6 ± 4.2	117.6 ± 48.0
20	11.7 ± 4.3	87.0 ± 31.4
30	14.2 ± 4.7	71.1 ± 23.7
40	17.0 ± 5.9	59.7 ± 20.6
50	20.0 ± 6.5	50.6 ± 16.3
60	23.6 ± 8.5	43.0 ± 15.3
70	23.4 ± 10.9	35.8 ± 13.0
80	36.2 ± 17.0	28.3 ± 12.4
90	56.0 ± 35.0	18.6 ± 11.1
100	1000	1

Table 18: Mean and 99.7 % confidence intervals for 3D polymer simulation number of layers and nodes per layer. As the probability of adsorption increases, simulated structures tend to have more layers and each layer tends to contain fewer nodes.

Max change in coordinate	$\lvert\Delta\bar{x}\rvert$	$\lvert\Delta\bar{y}\rvert$	$\lvert\Delta\bar{z}\rvert$
±0	0	0	0
±0.1	0.00026	0.00037	0.0008
±0.25	0.0049	0.0029	0.0044
±0.5	0.0075	0.0015	0.0116
±0.75	0.0178	0.0022	0.0119
±1	0.0226	0.0056	0.0242

Table 19: Magnitude of mean change in coordinates for adding noise to 3D stochastic model. As the maximum possible change in position increases, the mean change also increases. All numbers in arbitrary units.

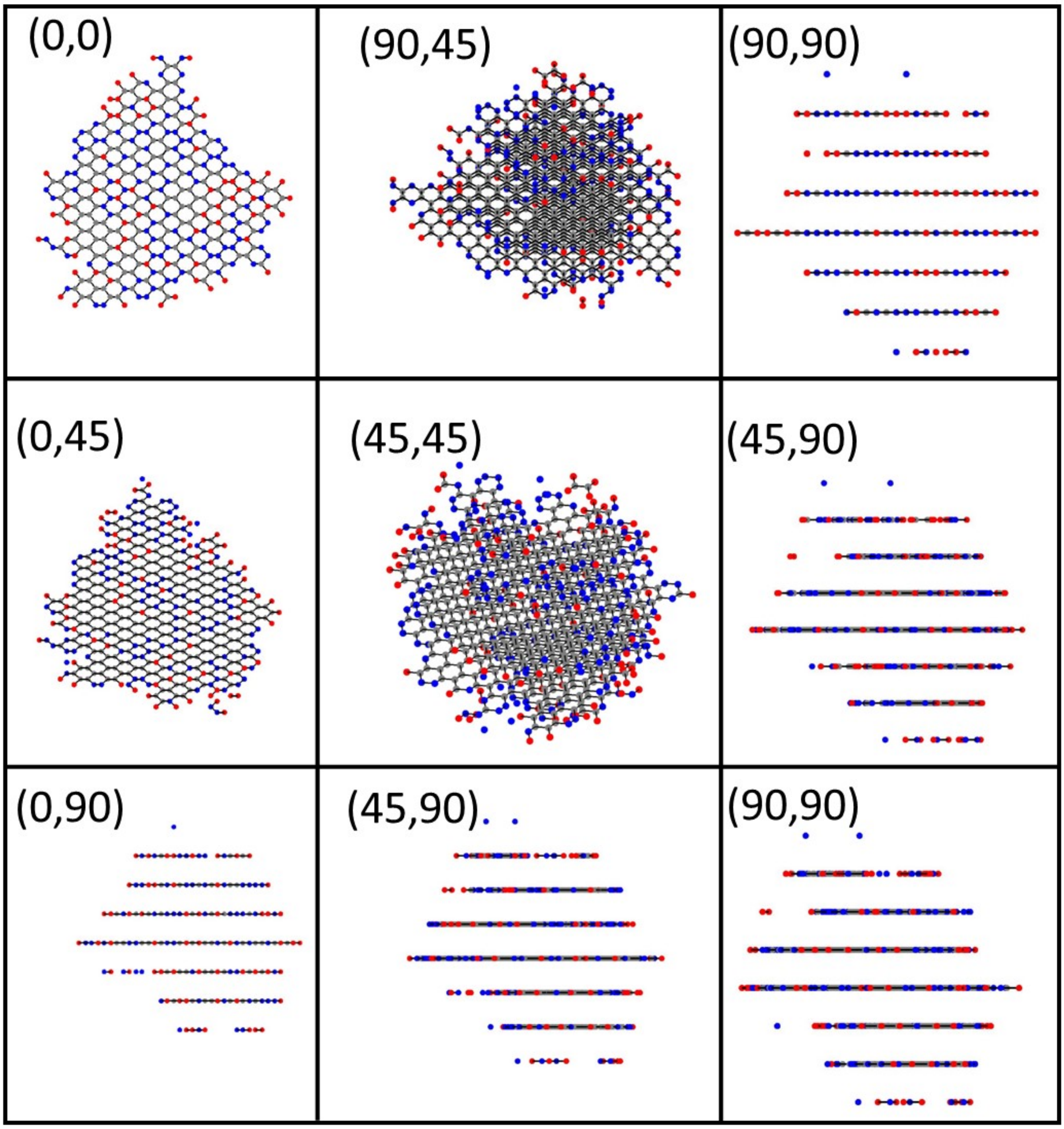

Figure 91: Rotational tableau of model COF structure with rotation relative to the FO projection indicated. The numbers in brackets indicate the azimuthal and polar angles relative to the FO projection at (0, 0). The images illustrate how the visible projection changes as a function of rotation.

4.3.7 Multiple Nucleation Sites

To investigate the effect of crystals competing for a limited pool of monomers the simulation was modified to have four nucleation points from which the graphs could grow, separated such that the final structures did not overlap in 3D space by placing one in each quadrant of the x-y plane (Figure 92). Rotating the modelled structures so that they overlap in projection showed that they still give rise to the expected 2D projections. The end goal of this would be to simulate structures comparable to those seen by Castano *et al*. They observed grain boundaries in thin COFs using Fourier filtered HRTEM images.[27] Grain boundary simulation could then be extended from 2D sheets to 3D COF structures, and effects such as electron beam damage and the effect of modelling conditions on grain formation could be modelled.

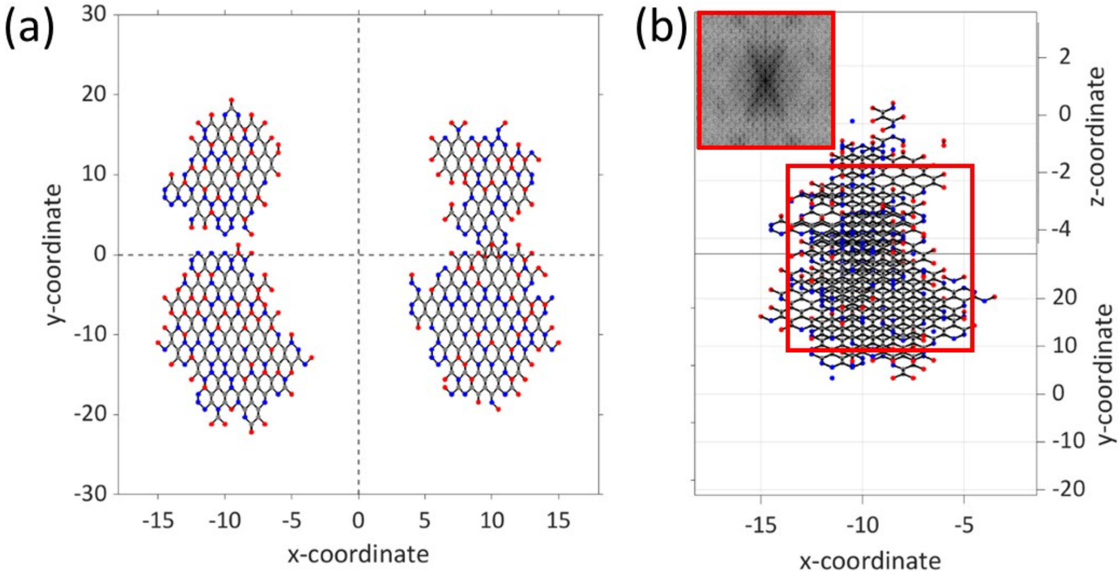

Figure 92: (a) Example of competitive crystal growth with 1500 monomers and 4 nucleation sites. The two crystals on the right have grown towards each other and now overlap. The dotted lines indicate the x- and y-axes. (b) Zigzag projection of left hand crystals, showing the presence of a zigzag projection occurring from two crystals that overlap in projection space but not in real space. Insert: Fourier transform of region in red box showing spots indicating a ZZ projection. This FT is the magnitude of the calculate complex-valued FT.

4.3.8 Quantifying Reductions in Crystallinity

Next, the effect of acrystallinity on the direct-space projections was investigated. Crystallinity is defined here as a structure that repeats periodically in 3D space. Two crystal aberrations were considered: removal of nodes, to model a crystal that contains vacancies, and noise in node positions. Noise was added to the node positions by altering the (x, y, z) coordinates of each node by a random value x such that x is less than or equal to 100 % one edge length in the graph. This redistributed the nodes randomly in a sphere around their crystal lattice position, but retains their connectivity in to other nodes (Table 19). Comparing this approach to experimental amorphous materials, this technique does not accurately simulate the formation of an amorphous structure unless the structure forms as a crystal then spontaneously become amorphous. The reverse of this process is known for some imine-linked COFs, which form as an amorphous structure and then crystallise. However, randomising nodes positions this way approximates well the effect of electron beam damage causing disorder in a lattice. It was found that the crystallinity of the observed projection could be quantified using Fourier transforms (FTs). For the FO projection of a graph with 1000 nodes, random noise was added for the range 0:5:100% of a graph edge length (Figure 93a-c). A Fourier transform was then taken of each projection (Figure 93d-f). A line profile was established for the resulting FT series, from which the number of bright spots along the line profile (Figure 93g) and the intensity of the first two spots was measured over the full FT series (Figure 93h). The spot intensity was normalised to the intensity of the center spot. It can be seen that the number of spots along the line profile decreases rapidly as noise increases, indicating a less ordered FO projection. The brightness of the monitored spots also decreases over the course of the series, indicating there are fewer periodic features contributing to the spot in the FT. The edges were removed from the graph, as otherwise they would contribute to the FT, which during development led to spots that never faded due to periodic edges present in all images. If the edges represented structural elements rather than connectivity it would be appropriate to include them in the FT. These results indicate that judging crystallinity of a sample by eye may be inaccurate, as the FT is able to detect periodic features even when the graph "looks amorphous".

These results also demonstrate that some subjectivity is required in order to quantify loss of crystallinity in a sample; if crystallinity in this graph is judged by loss of half the spots in the FT then the graph is amorphous at 10% noise, but if the graph is amorphous when the 2nd bright spot becomes invisible then it is amorphous at 40% noise. In essence this method is measuring the disorder in a crystal, with the practitioner left to decide the acceptable limit for damage in a sample and at which point the sample is "amorphous". For example Egerton has commented on the existence of several ways to define the "characteristic dose" of a sample.[28] The "end-point dose" is the fluence at which a signal is no longer measurable, such as when a diffraction spot vanishes. This gives a total fluence budget for the TEM operator to perform a measurement before the signal is no longer detectable. Characteristic dose can be defined as fluence needed to reduce the signal intensity by a factor of 1/e; assuming that the loss of signal intensity is an exponential decay, this means that the following equations can be used to find the rate of sample decay:

$$I = I_0 \exp(-\tau F) \tag{39}$$

$$\ln(I/I_0) = -\tau F \tag{40}$$

Where I is the intensity of a signal (e.g. a diffraction spot), I_0 is the initial signal intensity, F is the fluence, and τ is the rate of damage. When $I/I_0 = 1/e$, it follows that:

$$\ln(1/e) = -1 = -\tau F_c \tag{41}$$

$$F_c = \tau^{-1} \tag{42}$$

Where F_c is the critical fluence. The advantage of this method is gives a characteristic rate of decay for a sample that is independent of the instrument on which the measurement is performed. Egerton clarifies that each metric of characteristic dose is approximate, as the exact dose may depend on factors such as sample thickness.[28]

These results map on well to the experimental TEM literature. As explained by Egerton, electron beam damage can be monitored using the diffraction pattern of a sample. As the regular arrangement of atoms in a crystal is disrupted Bragg spots or rings fade, first affecting the outermost spots that correspond to smaller spacings and are more sensitive to atomic displacement.[28] This has been seen in experimental TEM, where Fung *et al.* (coincidentally my Masters research) monitored the degradation of organic crystals under the electron beam via selected area electron diffraction and FTs of direct-space images.[29,30] They quantified loss of crystallinity by monitoring the brightest pair of spots in the diffraction pattern over time; also used in my Masters research was monitoring direct-space HRTEM of organic crystals and using the FT to identify when the the periodic features were gone, i.e. the bright spots were no longer detectable against the background noise. This was used to give a minimum critical electron fluence that these materials were stable at. Therefore this graph theoretical technique can be used to estimate roughly at which point a real structure is no longer representative of the original structure. It should be born in mind that a FT of an image is not equivalent to an experimentally recorded diffraction pattern; a diffraction pattern is a slice through the 3D reciprocal lattice of the structure while a FT is a mathematical operation performed on a 2D real-valued image. A diffraction pattern may not be fully symmetric around the centre beam due to sample tilt changing whether some reflections fall on the Ewald sphere, but spots in a FT will always come in pairs due to the process of the Fourier transform. With this limitation in mind, this graph theoretical approach is an adequate approximation of atomic displacement due to beam damage that can be monitored via FTs.

To more thoroughly model beam damage effects, an initial investigation into node removal was begun. This serves to model loss of atoms via direct knock-on damage and surface sputtering. This was achieved by removing all of the even numbered nodes in the simulated graphs (Figure 94). The graphs were then rotated to confirm that they still contained the expected projections, although these became less visible as more nodes were removed. This could be quantified using the same FT methodology as for introducing noise into the structure if one were inclined to do so. A more robust method to randomly remove nodes from the structure could also be developed.

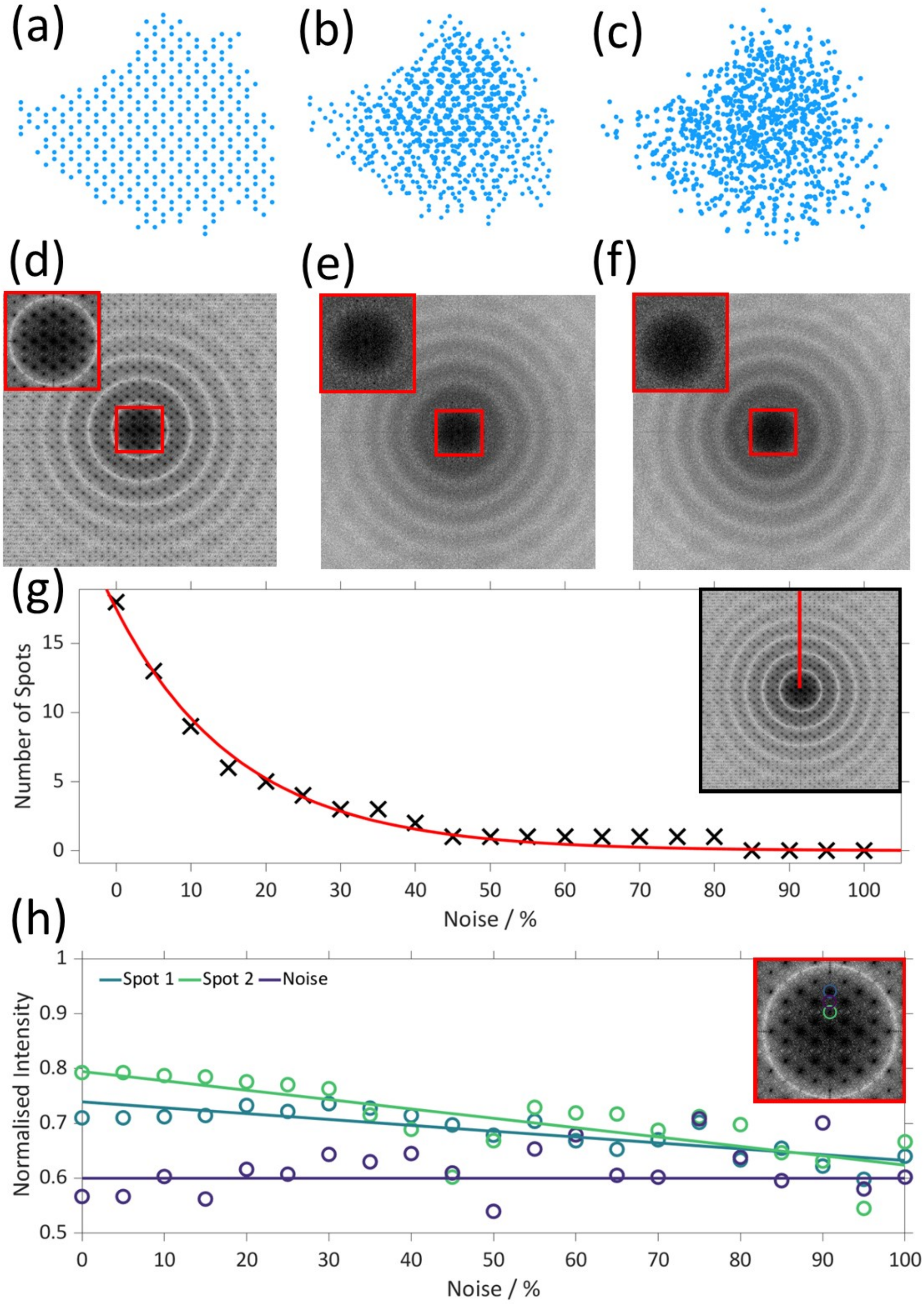

Figure 93: (a-c) Stochastic graphs with added 0%, 25%, and 100% positional noise. (d-f) Corresponding Fourier transforms (FTs). Insert: enlarged central region of FT. (g) Plot of number of spots along line profile of FT for each value of added noise, showing that number of spots decreased rapidly from 0 - 40% noise, then remained steady. The centre spot was not included in the count. Insert: 0% noise FT with red line indicating position of line profile. (h) Plot of normalised spot intensity versus noise for the 1st spot (green), second spot (blue), and the region of noise between them (purple). The 1st spot has a slight decrease in intensity over the series, while the second spot is approximately at the intensity of the noise by 40% added noise. Insert: enlarged 0% noise FT showing the areas spot intensity was measured. FTs here represent the magnitude of the calculated complex-valued FT.

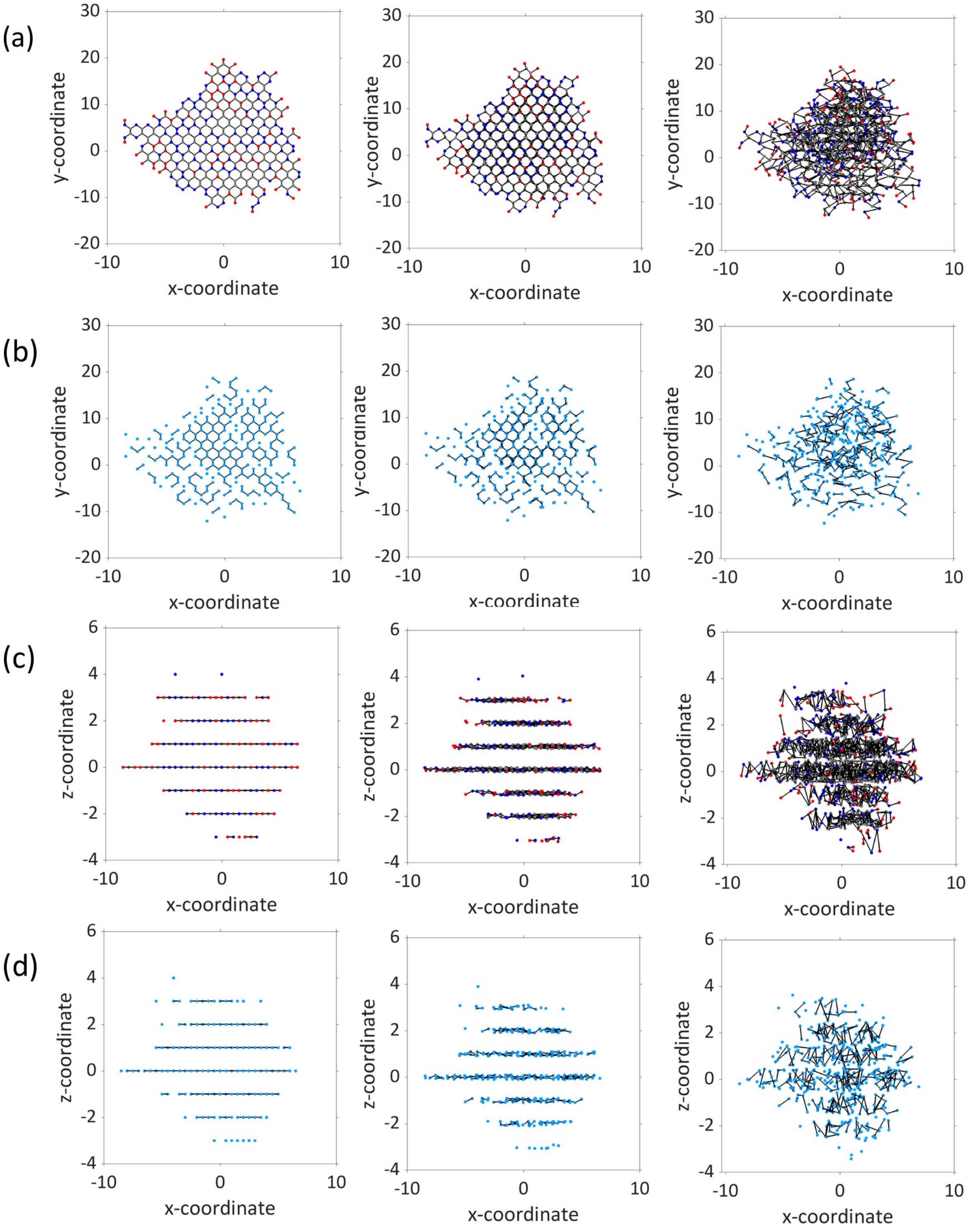

Figure 94: Illustration of the effect of disorder on lattice projections. Column 1 contains graphs with no added noise, column 2 has 10% noise, and column 3 has 50% noise. (a) Face-on (FO), no deletions. (b) FO, all even nodes deleted. (c) Side-on (SO), no deletions. (d) SO, all even nodes deleted. Principle lattice projections can be seen even when noise is added to the structures or when nodes are removed, highlighting that large amount of damage to the structure will be required to completely remove these projections.

4.4 Summary

This chapter has developed graph theoretical modelling of TEM images of COFs, which underpins the experimental work throughout the rest of this thesis. Graph theoretical structural models were explained, and used to model the crystal structure of several common COF geometries. For the example of cHBC-BDA-COF, the graph theoretical model was compared to image simulations and DFT structural models to show that TEM images of COFs will contain projections arising from the orientation of the COF crystallite relative to the optical axis in the microscope, the projections being defined based on symmetry of the real space structure and being analogous to zone axes. This was shown to be valid for TEM imaging of thin samples via image simulation. The approach described in this text is commensurate with crystallography, and an abstraction of it to general cases. Stereographic projections were then used to create maps showing the rotational relationship between these projections. It was then shown that this can be used to calculate the probability of a projection occurring from the surface area of the maps, which can be compared to experimental data to see if there is a statistically meaningful preferred orientation of the sample relative to the optical axis. Finally, equations were derived to predict the rotational orientation of a crystallite based on the projections measured in direct-space TEM images.

A hexagonal AA-stacked lattice was then selected as the target for a stochastically generated graph theoretical model of a COF crystallite. The underlying graph growth behaviour was found using a simple polymer size model, which was used as the base for a simple connectivity model investigating how the covalency of nodes affects the connectivity of a graph. This allowed formation of 2D and 3D crystalline graphs, and the graph growth direction was analysed. Investigating the properties of the graphs found that they contained structural features such as Klein edges that are known to occur in real (non-COF) structures. Finally, the effect of noise on the face-on projection of a stochastic graph was investigated using Fourier transforms, which established that noise led to a decrease in crystallinity. This represents a quantitative way to establish how much disorder in a crystal structure represents the conversion from a crystal to an amorphous structure, via monitoring the number and intensity of bright spots in Fourier space. This was linked to experimental work, and works to simulate the effect of electron beam damage on a crystal structure.

Overall, this chapter has demonstrated the utility of graph theoretical models simulating crystalline COF structures, and has lain the groundwork for stochastic simulations of COF structures using COFsim.

4.5 Future Work

Stochastic graph modelling of crystalline COFs was started relatively late in this body of research and is essentially absent in the literature. This chapter has also focussed largely on the theory behind COFsim, and has attempted to justify it as a useful technique. Therefore plenty of work is left to be done developing the theory and software to have a stronger link to experimental TEM, and to develop the predictive abilities of COFsim. A few useful directions are outlined below:

- Extend structural modelling to AB stacked sheets of common lattice topologies.
- Develop equilibrium modelling of COFsim structures, by simulating breaking/reforming of edges and dynamic loss and addition of nodes.
- Develop stochastic models beyond hexagonal AA-stacked 2D sheets to a range of other common COF geometries, such as Kagome or square lattices and true 3D COFs.
- Continue to investigate the effect of defects on the crystallinity of a stochastic graphs, by using Fourier transforms to quantify the crystallinity.
- Generate real chemical structures from graphs by replacing nodes with elements or monomers. then pursue TEM image simulation and simulated diffraction patterns of these structures. For example graphite can be made by replacing each node with a carbon atom and changing the edge length to be the C-C bond distance, or COF-1 could be made by replacing each node with benzenediboronic acid. This would also allow simulation of imperfect crystals and large structures.
- Implement modelling of amorphous COF growth by allowing nodes to be placed away from equilibrium crystal lattice positions during graph formation.
- Fine tune node size in graph models to better represent specific monomers, and better simulate the effect of optical resolution and magnification.

- Develop simulation of electron beam damage by modelling bond breaking and sputtering as well as atomic displacement.
- The simulation process can be improved to more accurately model the process of step growth polymerisation, for example the inclusion of oligiomers as well as monomers.
- Simulate multiple crystals competing for the a limited number of monomers to see if mechanisms such as Ostwald ripening could occur for these types of crystal, and compare to relevant experimental literature.[31]
- Use a seed for random number generation to allow the same graph to be created twice.

4.6 Computational Details

General

All modelling was done by the author unless otherwise indicated. Models were made using MATLAB (9.11.0.1837725 (R2021b) Update 2) with the following add-ons: Curve Fitting Toolbox (v3.6, MathWorks), Image Processing Toolbox (v11.4, MathWorks), Statistics and Machine Learning Toolbox (v12.2, MathWorks), and perceptually uniform colormaps (v1.3.2, Ander Biguri). Information on the MATLAB language and software can be found on the MathWorks website[32] or contained within MATLAB installation via the *doc* command. Scripts were written in MATLAB and can be found in the electronic supporting information or by request to the author. Fourier transforms (FTs) were performed using an FFT algorithm in FIJI. Biova Discovery Studio Visualiser (v20.1.0.19295), CrystalMaker (v 2.0.7), and VESTA (v 3.4.8)[33] were used to visualise literature electronic structure models with models for figures being made using Discovery Studio Visualiser. QSTEM was used for TEM image simulation.[14,34]

Iterative Fitting of Tilt Data

Fitting was performed using the MATLAB *fittype* command with the equation $L(\rho) = L_1|cos(\theta)| + L_2|cos(\theta)|$. The tilt angle data was set such that $\theta = 0 : 5^\circ : E$, where E is the number of data points in the array. This data was fitted to the equation via the *fit* command, then each angle data point was increased by 5° and the process repeated. This gave values of L_1, L_2, and goodness-of-fit for each fitting.

1D Polymer Size Model

This simulation is performed by the script MC_ 1D_ polymer_ size_ model.m. The user can define the number of monomers in the simulation as *noMTotal* > 0, and the total number of times to repeat the simulation as *totalSim* > 0. The variable *s* is used to track the size of the polymer, and *noM* is used to track the number of monomers in the simulation. The probability for addition Pad is defined by the user as a value between zero and one. The probability for loss is computed as $1 - Plo$. Running the script creates a table in the MATLAB Workspace called Results which contains the size of the polymer at each simulation step for each repeat. Statistics such as mean or median polymer size can then be computed using the relevant MATLAB commands, or the *writetable* command can be used to save the table Results in a format that can be read by other data processing software.

During a simulation step, a random number *x* is generated using the *rand* command. *x* is compared to the probability thresholds defined by the user, then either *s* will be increased by 1 and *noM* decreased by 1, or vice versa. The script allows for a third option, whereby no change occurs, by setting *Pad* and *Plo* such that there is an interval bewteen them, e.g. *Pad* = 0.1 and *Plo* = 0.1. The simulation repeats this step for the length of the for loop defined by the user. If *totalSim* > 1, the simulation will then repeat from the beginning until the entire simulation has been run *totalSim* number of times.

2D & 3D Polymer Structure Models

This simulation is performed by the script MC_ 3D_ polymer_ simulation_ v7.m. The user can define the following variables as "1" for on or "0" for off: *RingForming*, which controls whether nodes attempt ring closing; *workingGraph*, which creates a MATLAB figure at each simulation step for visualisation of the growth process for debugging; *plotting*, which creates a MATLAB figure at the end of the simulation for visualisation of the create graph; *colourCoding*, which colours the nodes in the MATLAB figure based on the number of edges each node has; *Sta-*

tisticalAnalysis, which quantified the graph growth direction using octants; *FullClosure*, which forces all possible ring closing steps to occur during graph formation; *NoiseOn*, which will add positional noise to each node at the end of the simulation.

randLowerLimit controls the amount of positional noise added to each node as a value between 0 and 1. *AdsorptionProbability* controls the probability of node forming a new 2D sheet by defining a value between 1 and 0, where 0 forms a 2D sheet and 1 forms a stack of nodes. *RingProbability* controls the ring closing behaviour of the graph as a value between 1 and 0, where 1 is always ring forming and 0 is never ring forming. *noMonomers* is defined as an integer greater than 0, and controls how many nodes will be in the final graph. The bond length factors (*xFactor, yFactor, and zFactor*) are set to 1 as standard and can be used to scale the bond length in the graph. *widthFactor* can be set as a positive integer to give each node a physical size, and is set to 0 as default. Extra nucleation points for simulating competing crystal growth are added by defining the coordinates of one or more nodes in the following manner:

```
CoOrdMat(1,1:3) = [10,10,0]; CoOrdMat(2,8) = 1;
```

For each nucleation pointed added, the value of *min* must be increased by 1 on lines 68, 132, and 141. By default, the first node is placed at (0, 0 ,0) and *min* = 2.

Running the script will create several items in the MATLAB workspace. *CovBonMat* is a n-by-n connectivity matrix for the graph, where *n* = *noMonomers*. *CoOrdMat* is an n-by-8 array which stores the coordinates of the nodes, where row *x* corresponds to node *x*, and whether there are any adjacent nodes. *CoOrdLUT* is an array storing the coordinates for each position adjacent to a given node. *AvailNodesLUT* is an array containing the identity of each node that can accept a new edge at the current simulation step, generated by the master list *NodesLUT*. By default, the script displays the number of each simulation step in the MATLAB console as it is completed.

Once complete, the MATLAB workspace will contain *CoOrdMat* and *CovBonMat*, which can be used to plot the created graph using the *graph* and *plot* commands:

```
CovBonGraph=graph(CovBonMat);
CovBonGraph_plot=plot(CovBonGraph,'XData',CoOrdMat(:,1),'YData',
```

```
CoOrdMat(:,2),'ZData',CoOrdMat(:,3));
```

A table *Results* will be created, which contains: the total number of nodes, the covalency of the nodes, the total possible number of edges that could be in the graph, the total number of edges in the graph, and the ratio of edges to nodes. If *StatisticalAnalysis* = 1, then the number of edges in each octant will also be included.

During a simulation step, the total number of edges to each node is calculated as *rowSum*. This is used to remove saturated nodes from *NodesLUT*. The new node is then chosen to add via adsorption or covalent bonding to an existing node by comparing a random number to *AdsorptionProbability*, then a node that can accept a new bond is chosen randomly from *AvailNodesLUT*. If this is the first simulation step, the 3D coordinates of the new node are then generated and stored in *CoOrdMat*. Otherwise the bonding position of the new node is randomly chosen from those available on the selected node, and the coordinates of the new node generated and stored. A check of the new coordinates in *CovBonMat* against the values in *CoOrdLUT* is performed to find any adjacent nodes in the x-y planes and the z-direction, which are marked in *CovBonMat*. If *RingForming* is on and an adjacent node is available, then an adjacent node is randomly selected and a new edge created if a random number exceeds a threshold defined by *RingProbability*. *CovBonMat* and *CoOrdMat* are updated, then *min* is increased by 1 and the next simulation step begins. The simulation ends when *min* = *noMonomers* + 1.

References

(1) D. West, *Introduction to Graph Theory*, Prentice Hall, Illinois, 2nd edn., 2001.

(2) J. J. Sylvester, *Nature*, 1878, **17**, 284.

(3) L. Pogliani, *Journal of Mathematical Chemistry*, 2008, **43**, 1233–1255.

(4) S. Husain, F. A. Abolaban, A. Ahmad, M. Ahsan Asim and Y. Ahmad, *Computer Systems Science and Engineering*, 2022, **40**, 835–850.

(5) A. N. Jha, G. Ananthasuresh and S. Vishveshwara, *Journal of Theoretical Biology*, 2007, **248**, 81–90.

(6) S. Patra and S. Vishveshwara, *Biophysical Chemistry*, 2000, **84**, 13–25.

(7) Y. Yan, S. Zhang and F.-X. Wu, *Proteome Science*, 2011, **9**, S17.

(8) T.-S. Lin, R. Wang, J. A. Johnson and B. D. Olsen, *Macromolecules*, 2018, **51**, 1224–1231.

(9) G. Gündüz, M. Dernaika, G. Dikencik, M. Fares and L. Aras, *Molecular Simulation*, 2008, **34**, 541–558.

(10) I. Kryven, J. Duivenvoorden, J. Hermans and P. D. Iedema, *Macromolecular Theory and Simulations*, 2016, **25**, 449–465.

(11) W. Koch and M. C. Holthausen, *A Chemist's Guide to Density Functional Theory*, Wiley, 1st edn., 2001.

(12) S. Kmiecik, D. Gront, M. Kolinski, L. Wieteska, A. E. Dawid and A. Kolinski, *Chemical Reviews*, 2016, **116**, 7898–7936.

(13) C. Gropp, S. Canossa, S. Wuttke, F. Gándara, Q. Li, L. Gagliardi and O. M. Yaghi, *ACS Central Science*, 2020, **6**, 1255–1273.

(14) *QSTEM: Quantitative TEM/STEM Simulations*, QSTEM: Quantitative TEM/STEM Simulations, `https://www.physik.hu-berlin.de/en/sem/software/software_qstem` (visited on 02/23/2023).

(15) M. O'Keeffe, M. A. Peskov, S. J. Ramsden and O. M. Yaghi, *Accounts of Chemical Research*, 2008, **41**, 1782–1789.

(16) B. L. Weare, R. W. Lodge, N. Zyk, A. Weilhard, C. L. Housley, K. Strutyński, M. Melle-Franco, A. Mateo-Alonso and A. N. Khlobystov, *Nanoscale*, 2021, **13**, 6834–6845.

(17) D. B. Williams and C. B. Carter, *Transmission electron microscopy: a textbook for materials science*, Springer, New York, 2nd ed, 2008.

(18) J. W. Jordan, K. L. Y. Fung, S. T. Skowron, C. S. Allen, J. Biskupek, G. N. Newton, U. Kaiser and A. N. Khlobystov, *Chemical Science*, 2021, **12**, 7377–7387.

(19) G. R. Fowles and G. L. Cassiday, *Analytical mechanics*, Thomson Brooks/Cole, Belmont, CA, 7th ed, 2005.

(20) M. Hayashida, M. Malac, M. Bergen, R. F. Egerton and P. Li, *Review of Scientific Instruments*, 2014, **85**, 083704.

(21) A. Ravve, *Principles of Polymer Chemistry*, Springer New York, New York, NY, 2012.

(22) R. K. E. Gover, Ph.D. Thesis, University of Nottingham, 2016.

(23) M. Martínez-Abadía, C. T. Stoppiello, K. Strutynski, B. Lerma-Berlanga, C. Martí-Gastaldo, A. Saeki, M. Melle-Franco, A. N. Khlobystov and A. Mateo-Alonso, *Journal of the American Chemical Society*, 2019, **141**, 14403–14410.

(24) J. S. Kim, J. H. Warner, A. W. Robertson and A. I. Kirkland, *ACS Nano*, 2015, **9**, 8916–8922.

(25) K. He, A. W. Robertson, S. Lee, E. Yoon, G.-D. Lee and J. H. Warner, *ACS Nano*, 2014, **8**, 12272–12279.

(26) K. Mustonen, A. Markevich, M. Tripathi, H. Inani, E.-X. Ding, A. Hussain, C. Mangler, E. I. Kauppinen, J. Kotakoski and T. Susi, *Advanced Functional Materials*, 2019, **29**, 1901327.

(27) I. Castano, A. M. Evans, R. d. Reis, V. P. Dravid, N. C. Gianneschi and W. R. Dichtel, *Chemistry of Materials*, 2021, **33**, 1341–1352.

(28) R. Egerton, *Micron*, 2019, **119**, 72–87.

(29) K. L. Fung, B. L. Weare, M. W. Fay, S. P. Argent and A. N. Khlobystov, *Micron*, 2023, **165**, 103395.

(30) K. L. Y. Fung, Ph.D. Thesis, University of Nottingham, Nottingham, 2021.

(31) B. J. Smith, L. R. Parent, A. C. Overholts, P. A. Beaucage, R. P. Bisbey, A. D. Chavez, N. Hwang, C. Park, A. M. Evans, N. C. Gianneschi and W. R. Dichtel, *ACS Central Science*, 2017, **3**, 58–65.

(32) *MathWorks Help Center*, MathWorks, 2023, `https://uk.mathworks.com/help/index.html?s_tid=CRUX_lftnav` (visited on 07/02/2023).

(33) K. Momma and F. Izumi, *J. Appl. Crystallogr., 44, 1272-1276 (2011).*, 2011, **44**, 1271–1276.

(34) C. Koch, Ph.D. Thesis, Arizona State University, Arizona, 2002.

5 Electron Beam Dynamics of Covalent Organic Polymers

5.1 Aims and Objectives

The unifying concept of this thesis is that electron beams (e-beams) interact with COF samples, from which useful information can be gained. Up until this point the focus has been on transmission electron microscopy (TEM) imaging and spectroscopy, but in this chapter the effect of e-beam damage on organic polymers will be analysed. Common e-beam damage pathways were discussed in Chapter 1, with the main takeaway being that covalent organic frameworks (COFs) are likely susceptible to beam damage but further work is required to establish exactly how beam sensitive they are. Studying the e-beam sensitivity of COFs will allow careful design of TEM experiments, so that imaging and spectroscopy can be completed before the sample structure degrades and becomes unrepresentative of the compound. Further, studying e-beam sensitivity is the first step towards using electron irradiation to drive chemical reactions in the TEM. Known variously as chemTEM[1] and SMART TEM,[2] the practice of using a TEM e-beam as combined energy source and imaging tool has allowed further understanding of e-beam damage mechanisms in polyaromatic heterocycles (PAHs),[3] deriving activation energy for thermally driven reactions,[4] the effects of confinement on small molecule stability,[5] and direct observation of a variety of chemical processes stimulated by the e-beam.[6] These studies are often phrased as a form of chemical kinetics, with efforts to extract rate constants for e-beam induced reactions, although they can include elements of chemical thermodynamics with the e-beam as the energy source. Therefore, chemical changes as a result of e-beam irradiation can be grouped under the umbrella term *e-beam dynamics* in order to capture that changes occur to a system as a result of energy transfer over time but without limiting oneself to chemical kinetics or chemical thermodynamics.

Beyond the TEM, e-beams have a major industrial application in cross-linking organic polymers.[7,8] Briefly, this works on the premise that e-beam irradiation forms radicals on polymer chains that undergo cross-linking reactions with adjacent chains.[9,10] The result of this is a desirable change in the properties of the polymer, such as increasing wear resistance or other mechanical properties.[11] This process is sometimes described as curing the polymer,[12] and e-beam curing of polymers has been identified as being faster and more flexible than traditional thermal curing methods.[9] The accelerating voltage used for e-beam curing varies, with voltages as high as 1 MeV reported.[11] Electron irradiation has seen useful application via electron-beam lithography. Lithography typically takes place at a lower accelerating voltage than TEM, around 30 - 60 kV, with a larger current.[13] Self-assembled monolayers (SAM) of aromatic molecules are used as resists that are cross-linked by the e-beam to give carbon nanomembranes with properties such as conductivity and thickness that depends on the molecules making up the original SAM.[13–19] e-Beam irradiation has even been used to form crystalline COFs.[20]

Given the industrial significance of e-beam irradiation of organic polymers this chapter will study crystalline COFs under the e-beam at 200 kV. Specifically:

- Both direct-space and reciprocal-space approaches to studying loss of crystallinity will be trialled in order to establish the point at which samples become amorphous under the e-beam.
- Via reference to crystal structures and literature values for e-beam stability, possible damage pathways for COFs will be suggested.
- This analysis will be applied to two COFs, cHBC-BDA-COF and Py-COF; then extended to a crystalline 1D polymer, Bet-P-1.

5.2 Recap of Electron Beam Damage Pathways

The main e-beam damage pathways were discussed in Chapter 1, but will briefly be recapped here. As described by Egerton the accelerating voltage, sample thickness, and sample makeup determines what damage mechanisms will be prevalent in a sample.[21] At 200 kV direct knock-on damage will be able to eject both hydrogen and carbon from the sample;[1] given that the samples imaged in this chapter are not monolayer COFs, we can expect direct knock-on damage to be the least important damage mechanism due to its low rate. We can expect radical formation via radiolysis to be an important damage pathway, as organic molecules are known to be susceptible to radiolytic bond scission, leading to cross-linking within the sample.[22] Electrostatic charging is also expected to occur due to loss of secondary electrons via ionisation, with the associated outcomes of sample drift or mechanical rupture of the sample.[22] Of course heating is expected to play a role in e-beam damage of COFs, but as expounded by Egerton the temperature increased caused by inelastic scattering of the e-beam may be so low as to be negligible.[22]

With these damage pathways in mind the outcome expected is that during irradiation of COFs visible crystal planes will fade, and any specular diffraction spots will fade as a function of the cumulative electron fluence. This can be used to find the characteristic dose needed to cause a sample to become amorphous. The definition used here is the "end-point dose" mentioned in the last chapter, which is the fluence at which point a signal can no longer be detected.[22] Other physical indications of damage that may occur are sample drift and sample thinning. For consistency with the flux/fluence terminology used throughout this thesis, *characteristic dose* will be referred to as *critical fluence*.

5.3 cHBC-BDA-COF

cHBC-BDA-COF was discussed at length in Chapter 2, where it was mentioned that this material did not have a crystalline selected area electron diffraction (SAED) pattern (Figure 95). An attempt was made to quantify the e-beam stability of this COF using direct space TEM imaging (Figure 96).

Imaging was performed at 200 kV accelerating voltage, and at constant electron flux. This allowed calculation of the cumulative fluence for each frame, and the total fluence at the end of the image series. The average flux varied between samples due to slight differences in microscope set-up (e.g. field-of-view, brightness), but the total fluence for each of the three areas imaged is comparable (Table 20).

During irradiation the COF was found to drift away from the field of view, implying that it is charging under the e-beam, and imaging was ceased when the COF was no longer in the field of view. Translation while under the e-beam was common for COFs throughout this thesis and typically occurred at high electron flux or, as was the case here, from extended exposure to the e-beam. This further implies a build up of charge within the sample, which we can assume to be positive charge.[22] As discussed in the mass spectrometry results in Chapter 3, cHBC-BDA-COF also tended to form positive ions under ultra-violet and visible light irradiation.

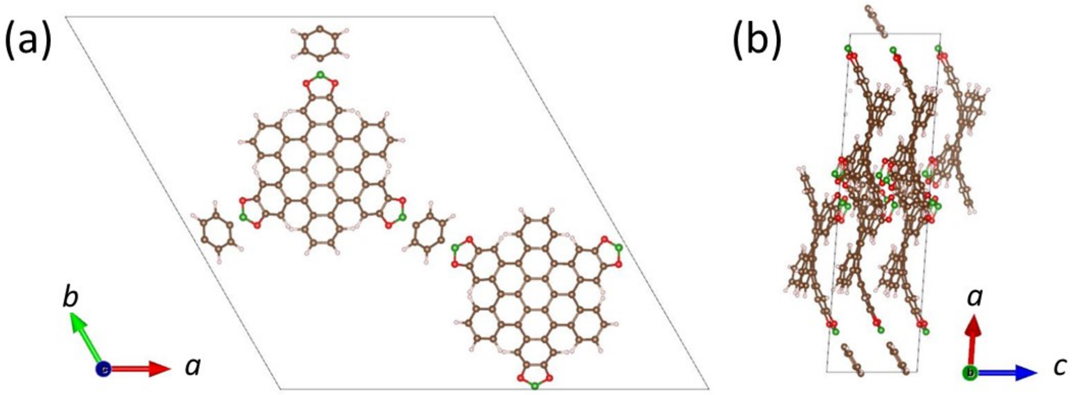

Figure 95: Models of the unit cell of cHBC-BDA-COF, looking down (a) the *c*-axis (only one layer of COF shown for clarity), and (b) looking down the *b*-axis. It can be seen that the different layers of the COF are in close contact.

Series	Total Time / s	Total Fluence / e$^-$ nm^{-2}	Average Flux / e$^-$ nm^{-2} s^{-1}
1	408	2.09 x 10^6	5113 ± 54
2	686	1.54 x 10^7	22454 ± 221
3	313	1.53 x 10^7	48770 ± 198

Table 20: Table of total time, total fluence, and mean electron flux for each image series of cHBC-BDA-COF.

Over the imaging time it was found that the visible d-spacing of the material did not noticeably change, with electron fluence as high as 1.54 x 10^7 e$^-$ nm^{-2}. The Fourier transform (FT) of the images also does not show conclusive evidence of beam damage, as spots can be seen in the FT at the start and end of the image series. This can be rationalised by considering that the COF lattice is relatively rigid and the COF monomers are held in place by covalent bonds, which limits their ability to shift within the crystal. Further, the d-spacings arising from armchair (AC) and zigzag (ZZ) projections will require substantial dislocation from equilibrium crystal positions before they become unrecognisable; this was shown in Chapter 2 using 3D graph theoretical models by adding noise to the nodes positions, which found that d-spacing was visible even when nodes were far from equilibrium positions.

The change in appearance between the images at the start and end of the direct-space image series can be rationalised as translations of the sample due to charging, change in focus over the image series as a result of translation, and possibly as a result of build up of amorphous carbon at the site of imaging. Therefore for cHBC-BDA-COF, no conclusive critical fluence could be established.

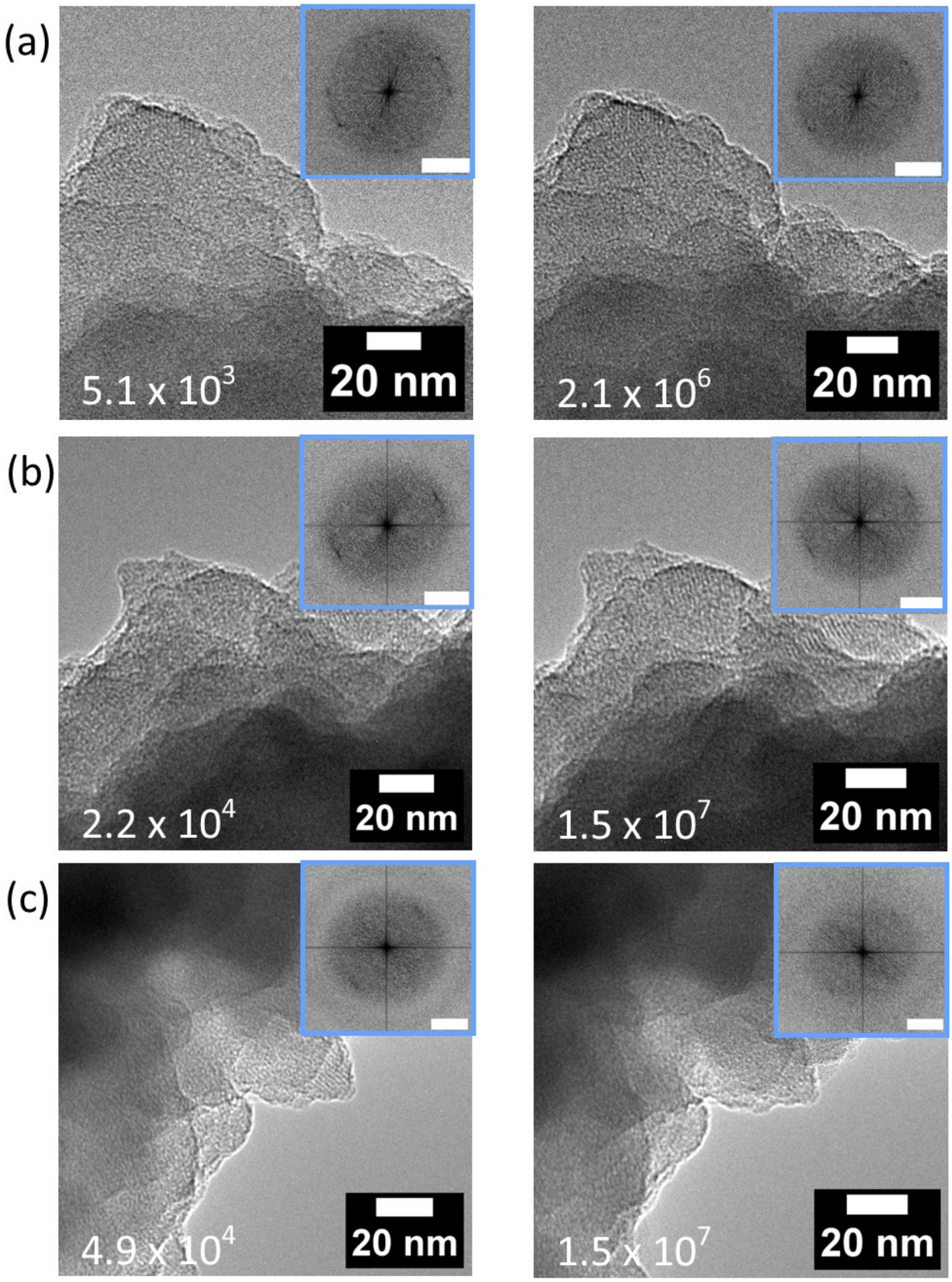

Figure 96: Start and end of e-beam stability series for cHBC-BDA-COF. (a) Series 1, (b) series 2, (c) series 3. Changes over the course of the image series can be attributed to sample drift; no clear loss of crystallinity was observed. Cumulative fluence is indicated in e^{-} nm^{-2} on each image. Inserts: Fourier transform of image, scale bar = 0.5 nm^{-1}.

5.4 Pyrene-COF

Late in the day for this PhD research new cameras were installed on the TEMs used in this thesis, which facilitated faster data acquisition for e-beam dynamics studies and imaging at a lower electron flux. This allowed more effective studies of e-beam damage processes in reciprocal space, which was applied going forwards.

Pyrene-COF (Py-COF) was synthesised via the literature procedure as micron-sized crystals with a good SAED pattern,[23] and used as a test system for e-beam dynamics studies of COFs (Figure 97). Py-COF has been studied extensively in the literature; Py-COF has been used to study COF nucleation processes,[24] has been investigated for its ability to generate a photocurrent and other optical properties,[23,25] has been synthesised as a thin film[26,27] and as nanocrystals[23]. Py-COF was selected for this work as unlike COF-5 and cHBC-BDA-COF, its good SAED pattern allows application of the methodology used for studying the degradation of polyaromatic heterocycles under the e-beam.[3,22]

Py-COF is a 2D AA stacked hexagonal COF made of the self-condensation of pyrene-2,7-diboronic acid monomers joined by boroxine functional groups. Infrared spectroscopy (IR) of Py-COF found characteristic boroxine and boronic acid vibrations as expected for a boroxine polymer terminated by unpolymerised boronic acid groups (1379, 1315, 1237, 796, 718, 599 cm^{-1}). MALDI-ToF found ions at a m/z corresponding to two pyrene fragments joined by a boroxine functional group, suggesting that the lattice tends to fragment at the boroxine functionality (see Apendix Figure 109c) and Appendix Table 25). PXRD of Py-COF shows it contains several low-intensity peaks (17, 19, 23, and 27 °), which do not match to the literature PXRD for the modelled structure of Py-COF.[23] As with the other COFs in this thesis the peaks in the powder pattern of Py-COF are low-intensity, so Pawley fitting or other methods could not be applied to further investigate this powder pattern. The energy dispersive X-ray (EDX) spectrum of Py-COF shows a clear oxygen peak and the usual contaminants (Figure 99a). The low-loss electron energy loss spectrum (EELS) has a plasmon at 23 eV, and the core-loss EELS contains clear boron, carbon, and oxygen K edges (Figure 99b-d).

Py-COF was imaged at 200 kV in diffraction mode, allowing the changes in crystallinity of the sample to be followed by monitoring the changes in brightness of diffraction spots. It was

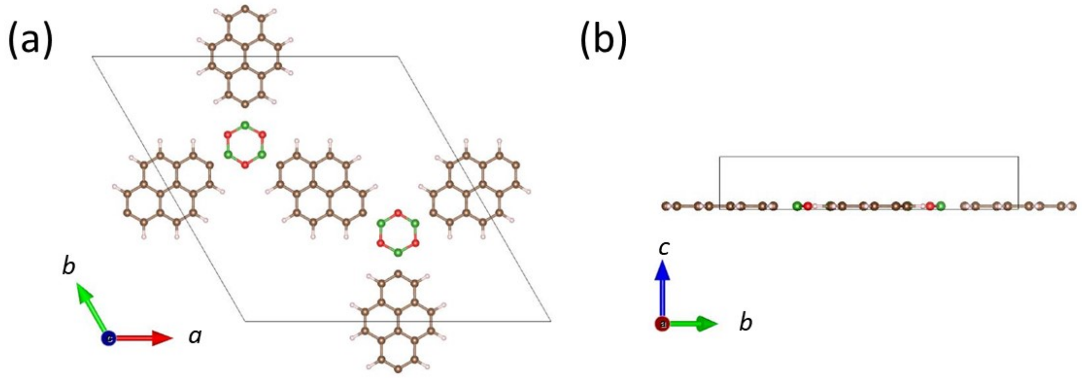

Figure 97: Models of the unit cell of Py-COF, looking down (a) the c-axis and (b) the b-axis. The pyrene subunits are joined by boroxine rings, and the stacked sheets are in close contact.

Series	**Total Time / s**	**Total Fluence / e$^-$ nm^{-2}**	**Average Flux / e$^-$ nm^{-2} s^{-1}**
1	392	3.60 x 10^4	178 ± 28
2	344	3.80 x 10^4	223 ± 0.5
3	177	3.04 x 10^4	171 ± 2.2

Table 21: Time, total fluence, and average flux for each image series of Py-COF.

found experimentally that the diffractions patterns tended to change via spot fading, implying that if Py-COF was drifting under the e-beam the movements were relatively small. Less drift was seen compared to cHBC-BDA-COF due to the lower electron flux used for Py-COF, and due to the imaging of larger COF structures which would have meant charge would not be concentrated in a small area. Charging has also been noted to often not occur below a certain threshold flux in inorganic oxides,[28] so a similar effect may be occuring here.

Three areas of Py-COF was examined, at similar electron flux and with comparable total dose (Table 21). Py-COF was found to be unstable under the e-beam, with electron fluence of 3.04 - 3.6 x 10^4 e$^-$ nm^{-2} enough to cause all bright spots to fade from the SAED pattern. This was achieved with a low electron flux of 171 - 223 e$^-$ nm^{-2} s^{-1}, which allowed precise determination of the end point of the sample degradation. No physical changes in sample morphology, such as shrinking or cracking, were noticed. Taking the mean of the total fluence of each series as the critical fluence of Py-COF gives a value of $(3.48 \pm 0.79) \times 10^4$ e$^-$ nm^{-2} required to render Py-COF acrystalline ($\mu \pm 2\sigma$).

The degradation of Py-COF was followed by monitoring the intensity of two SAED diffraction spots; the closest spot to the centre of the diffraction pattern indicates the point at which the sample is no longer crystalline, while following a second diffraction spot illustrates the rapid loss of order that occurs during irradiation. It was found that while the closest diffraction spots had the longest lifespan, often all of the other diffraction spots vanished from the diffraction pattern within a few tens of seconds. This indicates a rapid loss of long-range order within the sample, followed by a gradual loss of short-range order. This is rationalised as small displacements of monomers from equilibrium positions in the COF unit cell, followed by progressively larger disruptions to crystalline order that culminate in the loss of organised 2D hexagonal sheets. Overall, Py-COF has allowed an interesting first look into the instability of crystalline COFs under e-beam irradiation.

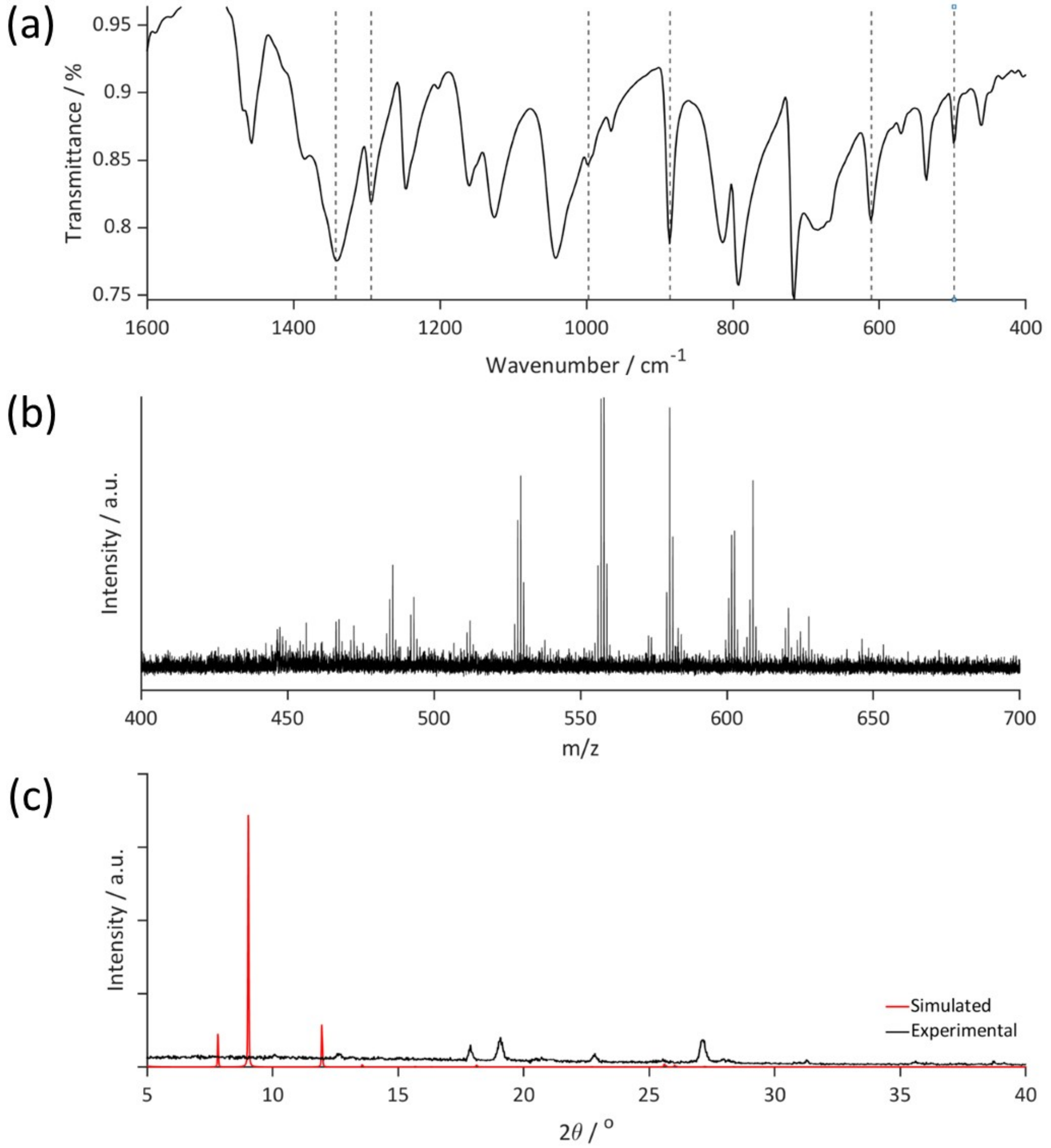

Figure 98: (a) FTIR spectrum with boroxine vibrations marked with dotted lines. These are indicative of polymerisation. (b) MALDI MS of Py-COF, showing several ions corresponding to fragments of the extended 2D lattice. (c) Simulated PXRD (red) and experimental PXRD (black). The experimental powder pattern does not match well to the simulated reflections, likely due to small crystal sizes.

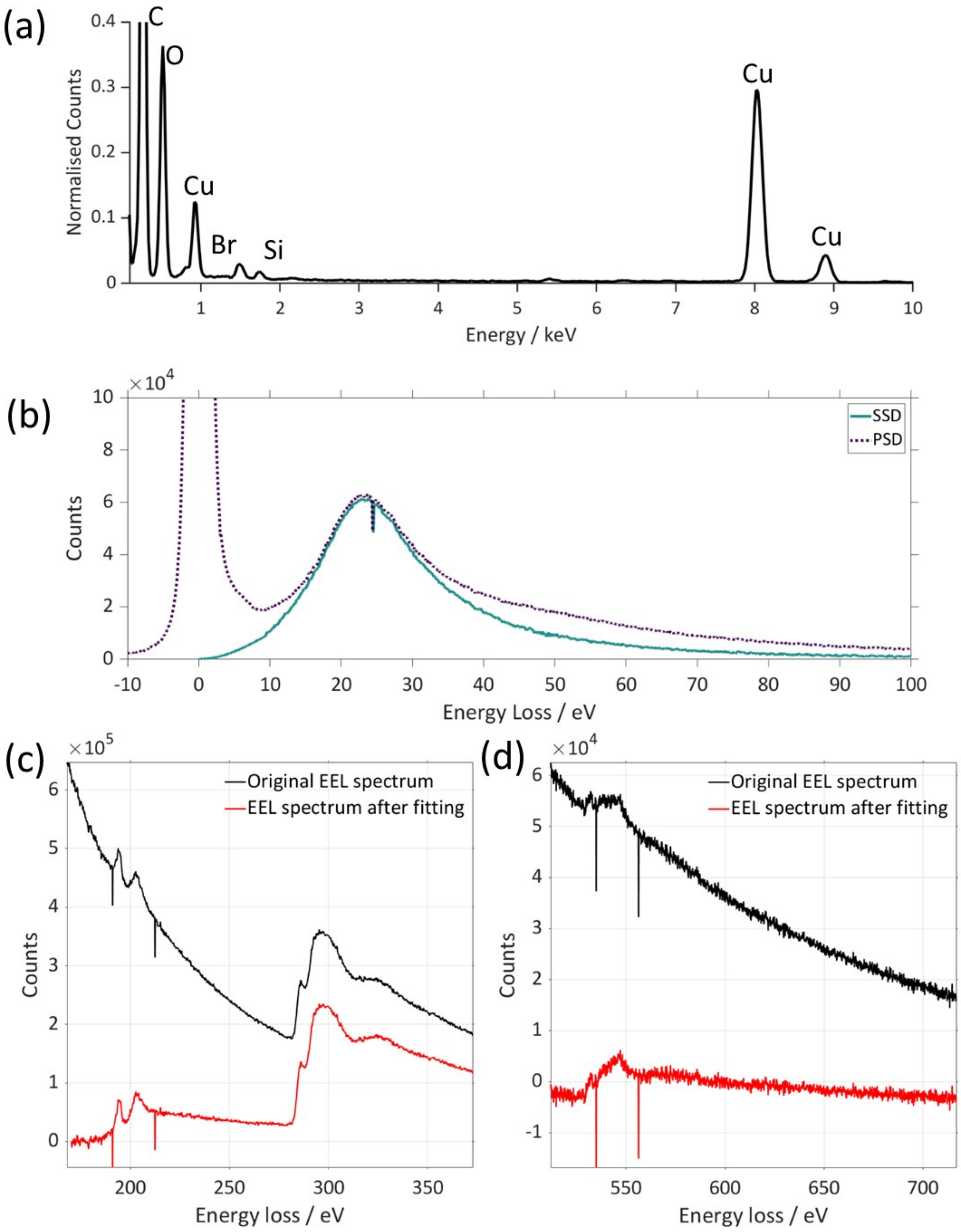

Figure 99: (a) EDX spectrum of Py-COF, showing a clear oxygen peak from the boroxine functional group, as well as copper from the TEM grid common containments bromine and silicon. (b) Low-loss EEL spectrum of Py-COF, showing a small difference between the single-scattering distribution (SSD) and plural scattering distribution (PSD). A small shoulder is visible in the zero-loss peak of the PSD, likely the $\pi - \pi^*$ inter-band transition. (c) Boron, carbon, and (d) oxygen K edges for Py-COF.

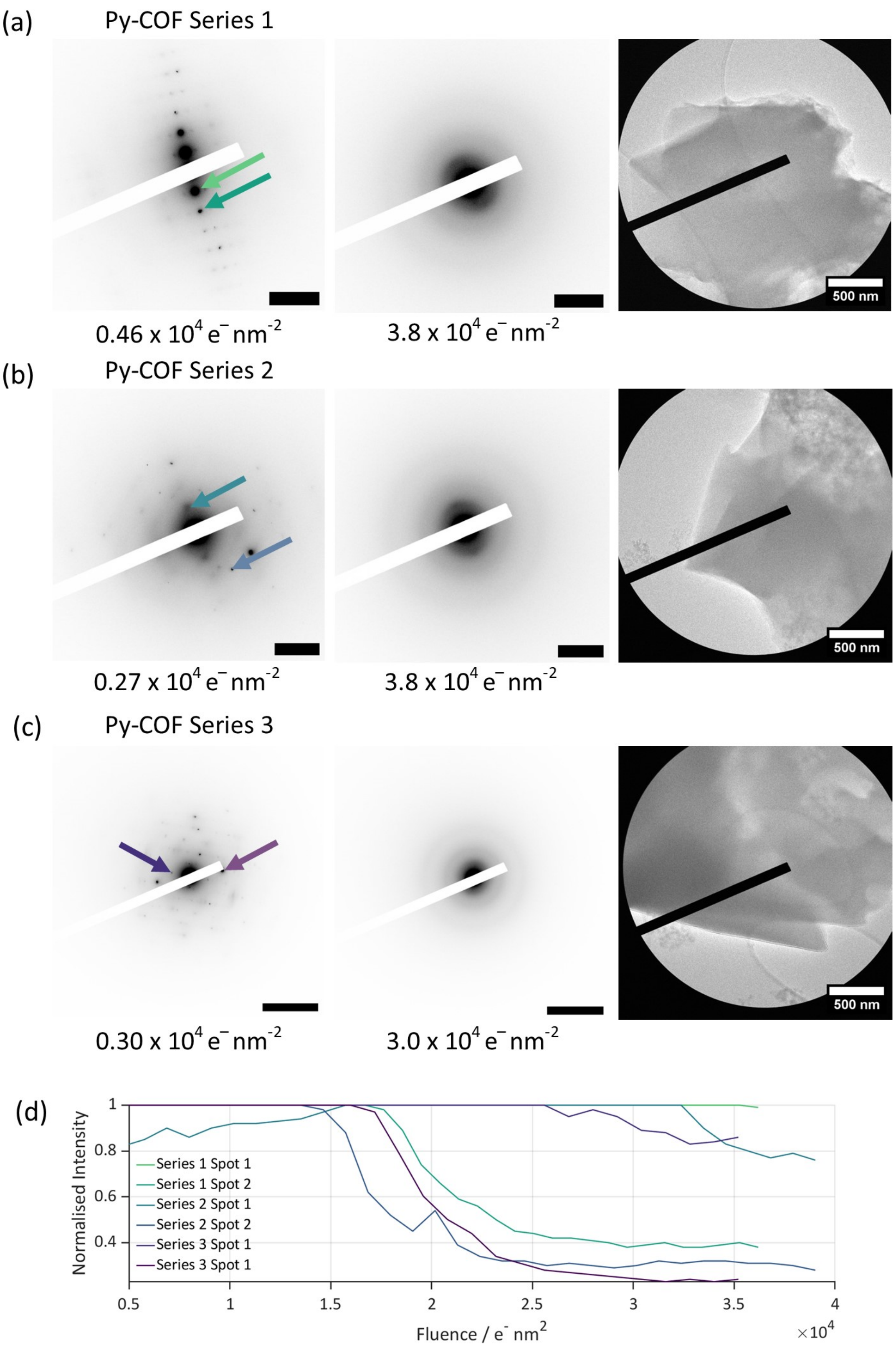

Figure 100: Image series for Py-COF: (a) Series 1, (b) series 2, (c) series 3. Cumulative fluence is indicated in e$^-$ nm^{-2} below each image. SAED scale bars are 5 1/nm. (d) Plot of spot intensity as a functional of cumulative fluence for two spots from each diffraction pattern (colour coded). Series 2 spot 2 first increases in intensity due to crystal movement, under the beam, then reduces as a result of beam damage. The spot 1 plots appear to be at 1 due to small variations in intensity that are hidden by the scale of the plot.

5.5 Bet-P-1

Bet-P-1 was synthesised by collaborators at the University of the Basque Country, with the author providing electron microscopy.[29] Bet-P-1 has been dubbed a "1D polymer", in contrast to the 2D and 3D nomenclature used for COFs, and is essentially a step-growth polymer formed via successive condensation reactions with the key feature being it is formed as microscale crystals (Figure 101). The monomers are joined by imine functional groups in long chains, which then pack into crystals. Bet-P1 has a crystal structure solved by MicroED, has been established to be a direct gap semiconductor, and has interesting charge carrier mobility.[29] Of relevance to this work is that Bet-P-1 represents an organic crystal with similar structural features to COFs (e.g. made of organic monomers that are similar to polyaromatic heterocycles) that can be used to study the e-beam stability of COFs and organic polymers more generally. Bet-P-1 has been characterised by techniques such as PXRD and IR spectroscopy (Figure 102). The EDX spectrum of Bet-P-1 has clear oxygen and nitrogen peaks arising from the polymer, while the low-loss EELS spectrum has a plasmon at 26 eV (Figure 103).

As for Py-COF the e-beam stability of Bet-P-1 was studied in reciprocal space at 200 kV (Figure 104). While diffraction spots mostly faded over time, Bet-P-1 exhibited a noticeable instance of the diffraction pattern changing during irradiation during series 2 (Figure 104b) . This is either due to Bet-P-1 requiring greater total fluence than Py-COF, so there was more time for translation under the beam to occur, or Bet-P-1 is more susceptible to charging than Py-COF. Four areas of Bet-P-1 were examined, with similar electron flux and comparable total fluence (Table 22).

It was found from SEM that Bet-P-1 forms as needles, which allows the thickness of the sample in the direction of the optical axis to be estimated as on the order of 500 nm (Appendix Figure 110). The material was found to be surprisingly robust in terms of fluence needed to cause all diffraction spots to fade, with over thirty minutes of continuous irradiation at a flux of 729 ± 1.2 e^{-} nm^{-2} s^{-1} required in one case. This result is an exception, as the other regions images were lost most diffraction spots after between $(4.5 - 4.7) \times 10^5$ e^{-} nm^{-2}. As discussed by Egerton, the critical fluence may depend on sample thickness.[22] These values are a power of ten larger than those needed to cause the diffraction pattern of Py-COF to fade, and in all cases there was some diffuse diffraction present in the pattern at the end of imaging. In series 1 the two diffraction spots closest to the direct beam never vanished entirely, and had roughly 80% of their original intensity at the end of imaging (Figure 105a). Plotting the intensity of the diffraction spots as a function of cumulative fluence for the other series it can be seen that while a decrease in intensity is observed as fluence increases, as many spots were close to the direct beam the intensity remains relatively high even at the end of the series (Figure 105b-d). This means that while it is relatively easy to appraise visually when a diffraction spot has faded, the numerical value for intensity does not necessarily show this point as well as would be hoped.

Calculating the critical fluence for Bet-P-1 gave $(7.31 \pm 9.23) \times 10^5$ e$^-$ nm^{-2} $(\mu \pm 2\sigma)$. The large standard deviation is a result of the unusually stable result in series one. Overall, Bet-P-1 has proven to be more robust than Py-COF, and much more robust than expected from previous studies of PAHs.

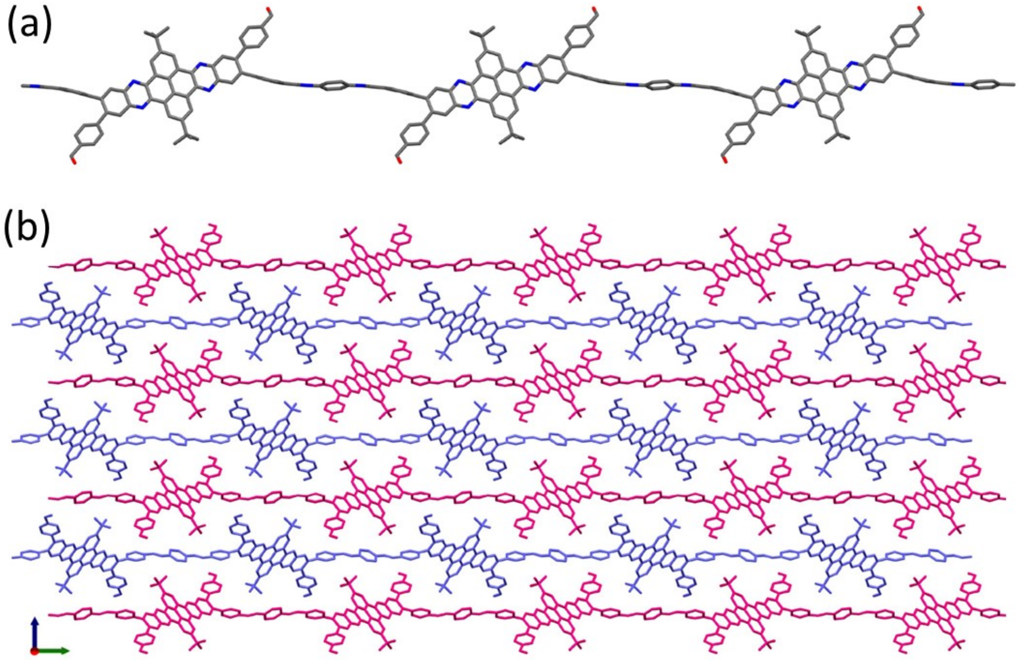

Figure 101: (a) Model of the 1D polymer chains that constitute BET-P-1. (b) Model of the crystal structure of BET-P-1, looking down the *c*-axis. It can be seen that each monomer has several neighbours to allow beam-induced cross-linking to occur. Adapted with permission from ref. [29]. Copyright 2022 American Chemical Society.

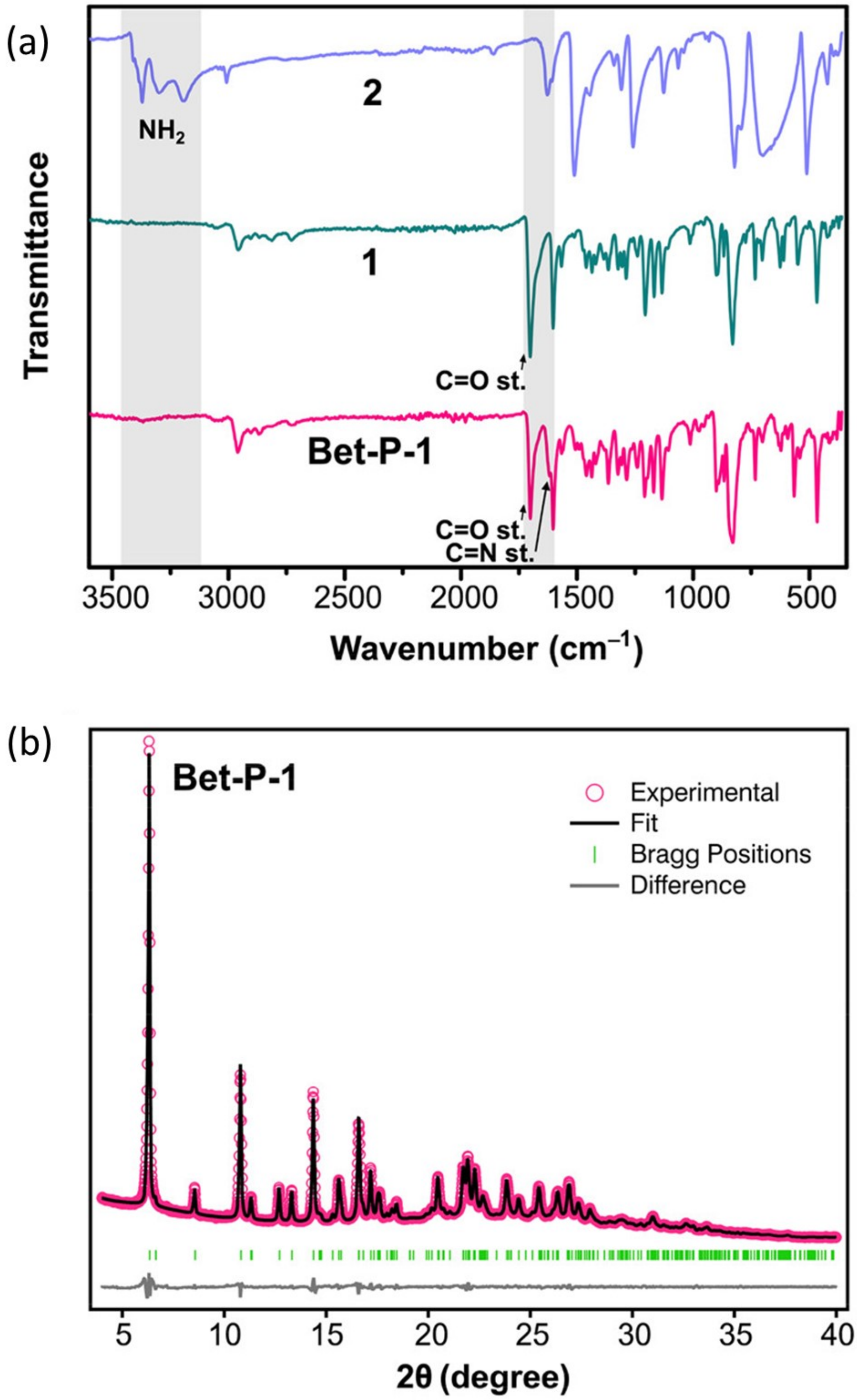

Figure 102: For Bet-P-:1 (a) IR spectrum of the polymer and its monomers showing imine stretches indicating polymerisation; (b) PXRD of Bet-P-1 with indicated Pawley fitting. The close fit indicates the polymer has the calculated crystal structure. Reused with permission from ref. [29]. Copyright 2022 American Chemical Society.

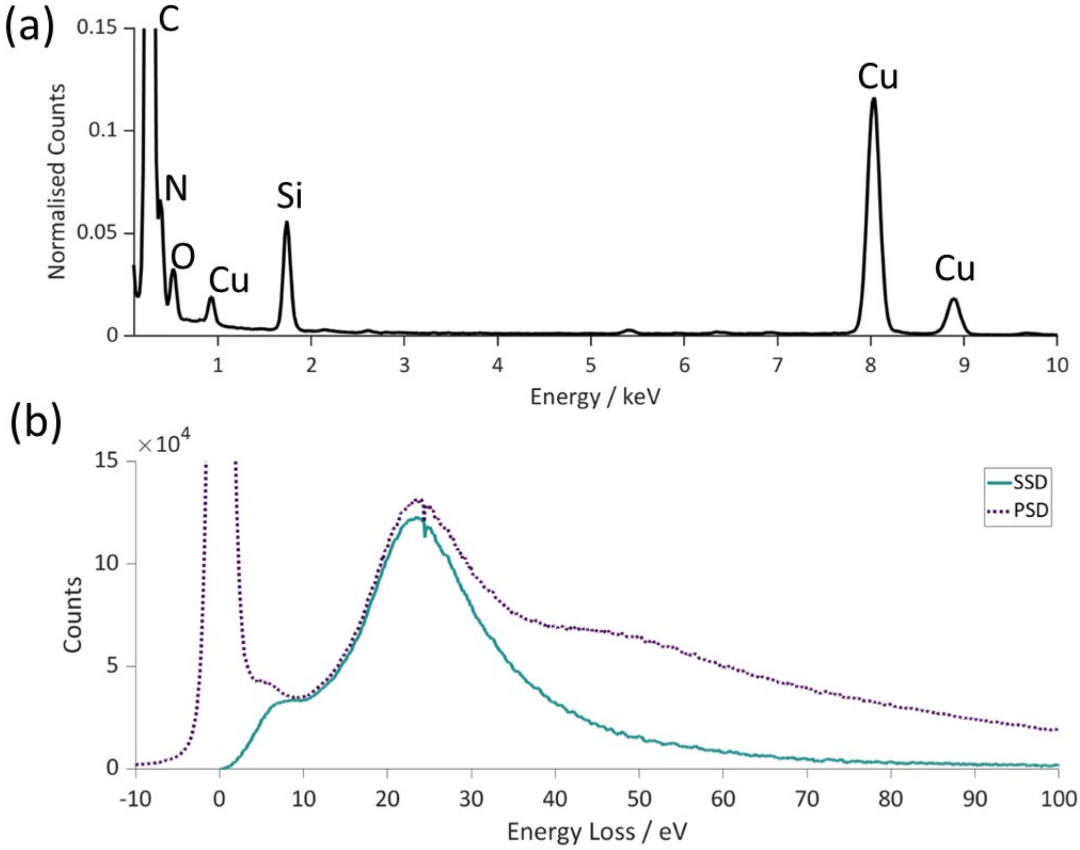

Figure 103: (a) EDX spectrum of Bet-P-1 with clear nitrogen and oxygen peaks from the polymer, with other peaks being common lab contaminants. (b) Low-loss EEL spectrum of Bet-P-1. There is a clear $\pi - \pi^*$ transition at 7 eV in the single scattering distribution (SSD). The plural scattering distribution (PSD) is noticeably higher intensity than the SSD due to sample thickness.

Series	Total Time / s	Total Fluence / e$^-$ nm^{-2}	Average Flux / e$^-$ nm^{-2} s^{-1}
1	1951	1.42×10^6	729 ± 1.2
2	951	5.67×10^5	596 ± 15
3	541	4.88×10^5	448 ± 259
4	619	4.50×10^5	727 ± 16

Table 22: Time, total fluence, and average flux for each image series of Bet-P-1.

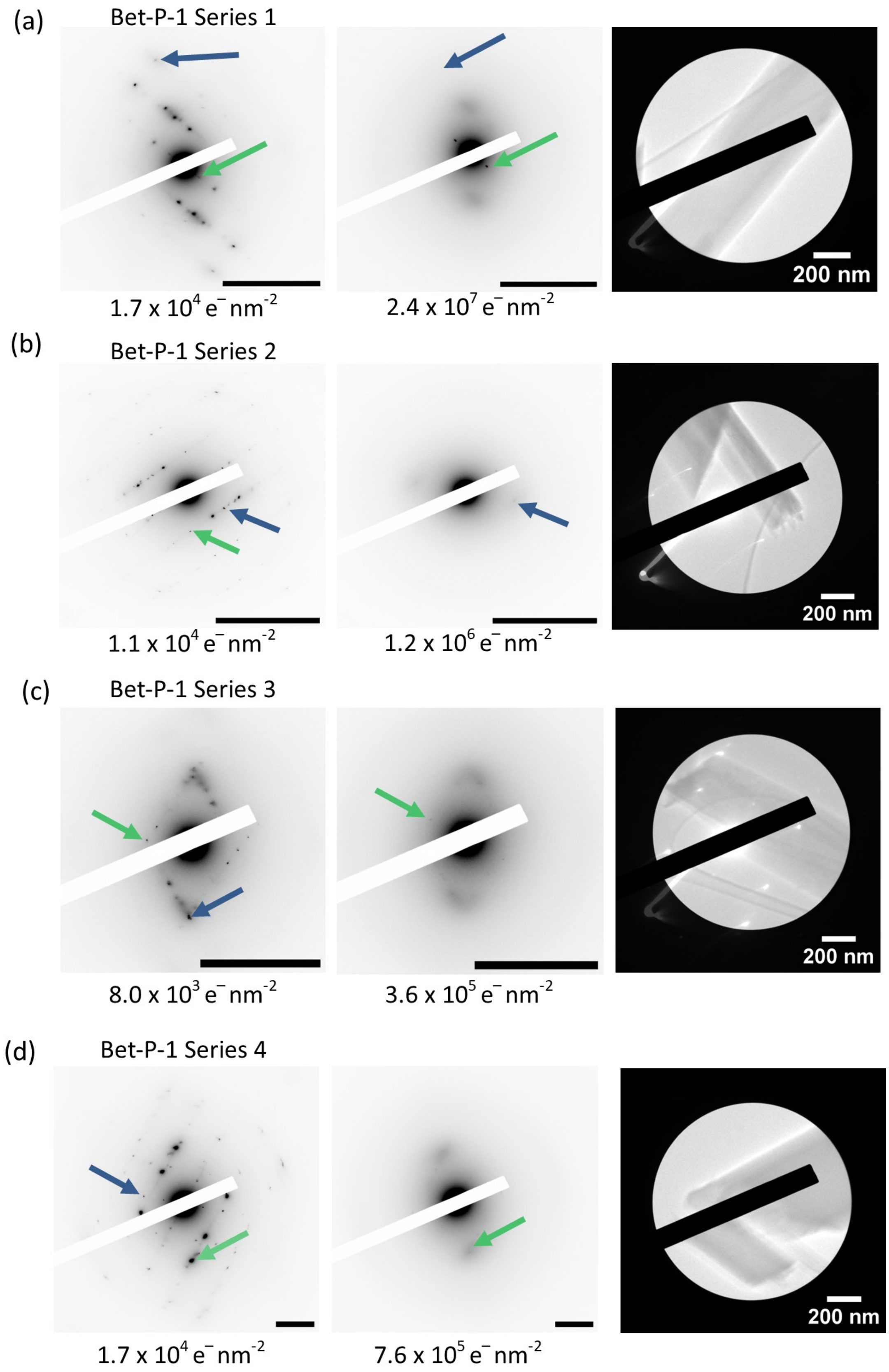

Figure 104: Image series for Bet-P-1: (a) series 1, (b) series 2, (c) series 3, (d) series 4. Cumulative fluence is indicated in e$^-$ nm^{-2} below each image. Tracked diffraction spots are indicated with coloured arrows, and were found to becomes less intense as a function of cumulative fluence. SAED scale bars are 5 1/nm.

(a) Bet-P-1 Series 1

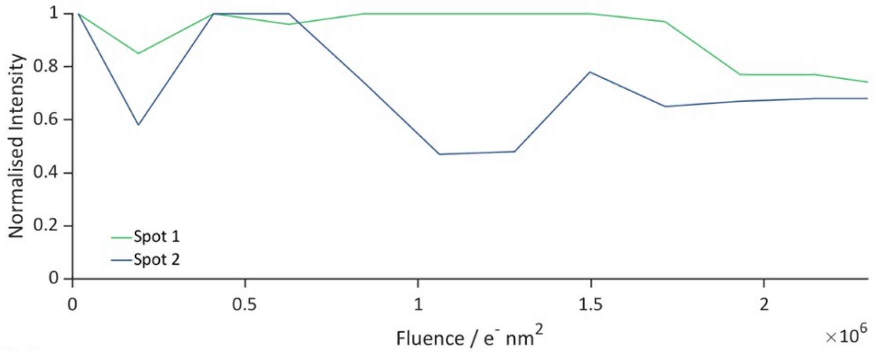

(b) Bet-P-1 Series 2

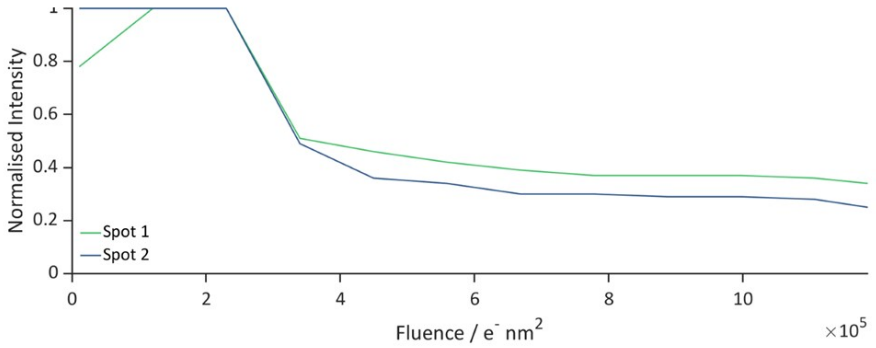

(c) Bet-P-1 Series 3

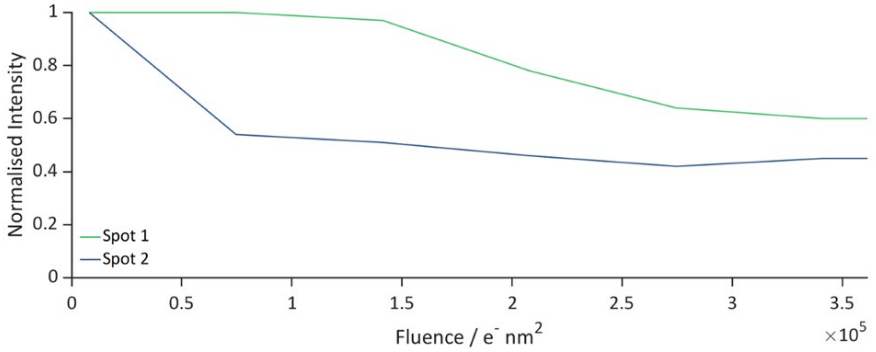

(d) Bet-P-1 Series 4

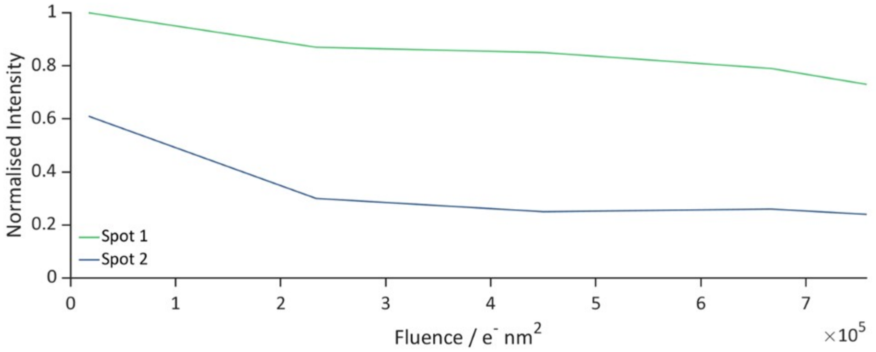

Figure 105: Plots of diffraction spot intensity as a function of cumulative fluence for Bet-P-1 image series. (1) Series 1, (b) series 2, (c) series 3, (d) series 4. The intensity tends to decrease as a function of fluence, indicting beam damage is occurring in the sample.

5.6 Hypothetical Beam Damage Pathways

Drawing from the structures of these materials, the e-beam damage pathways in COFs and 1D polymers can be inferred (Figure 106). The rigid 2D lattice of Py-COF and c-HBC COF will likely hinder reactions between radicals and ions formed by radiolysis, as the monomers are held far apart with covalent bonds hindering their movement. This means that reactions between adjacent monomers in the x-y plane of the COF sheet are unlikely. The distance between COF sheets in the z-direction varies between COFs, but is 0.348 nm for Py-COF or appropriately double the length of a C-C bond. It is reasonable that if both sheets distort towards each other then cross-linking reactions could occur between them, although depending on the angle between the two monomers then there could be substantial bond strain in any new bonds formed. Drawing on a literature example of monovacancies in graphene, which can be caused by e-beams ejecting a single carbon atom from a graphene sheet, carbon atoms surrounding a monovancy that are separated by 0.209 nm are able to form a new bond to form a 5-membered ring.[30,31]

Looking at e-beam damage in few-layered graphene at 200 kV, Wang *et al.* show that these structures underwent shrinking and the loss of their diffraction pattern by SAED which they explain via loss of carbon atoms via sputtering as the main damage pathway.[32] There does not seem to be evidence for cross-linking driven by radical formation in graphene. However a study of radiation induced grafting in carbon nanofibres did suggest that the formation of radicals as a result of beam damage was a major contributing factor.[33] These results reinforce the assumption that for the thick COFs in this work, radical formation based damage pathways are the most important.

The likely point of lattice breakdown is the functional group between monomers, i.e. boronate ester or boroxine functional group. Radiolysis breaking or weakening these points in the COF lattice would allow much greater freedom of movement for the monomers in the 2D COF lattice. This could feasibly allow rotations of these monomers to make cross-linking reactions more favourable. Looking at the MALDI-TOF of boronate ester COFs in Chapters 3 and 4, it was found that the COFs tended to fragment first at the boronate ester functional group. Assuming the e-beam damage mechanisms are similar to thermal damage pathways discussed in Chapters 3 and 4, then e-beam damage could form boron oxide and an amorphous carbon lattice

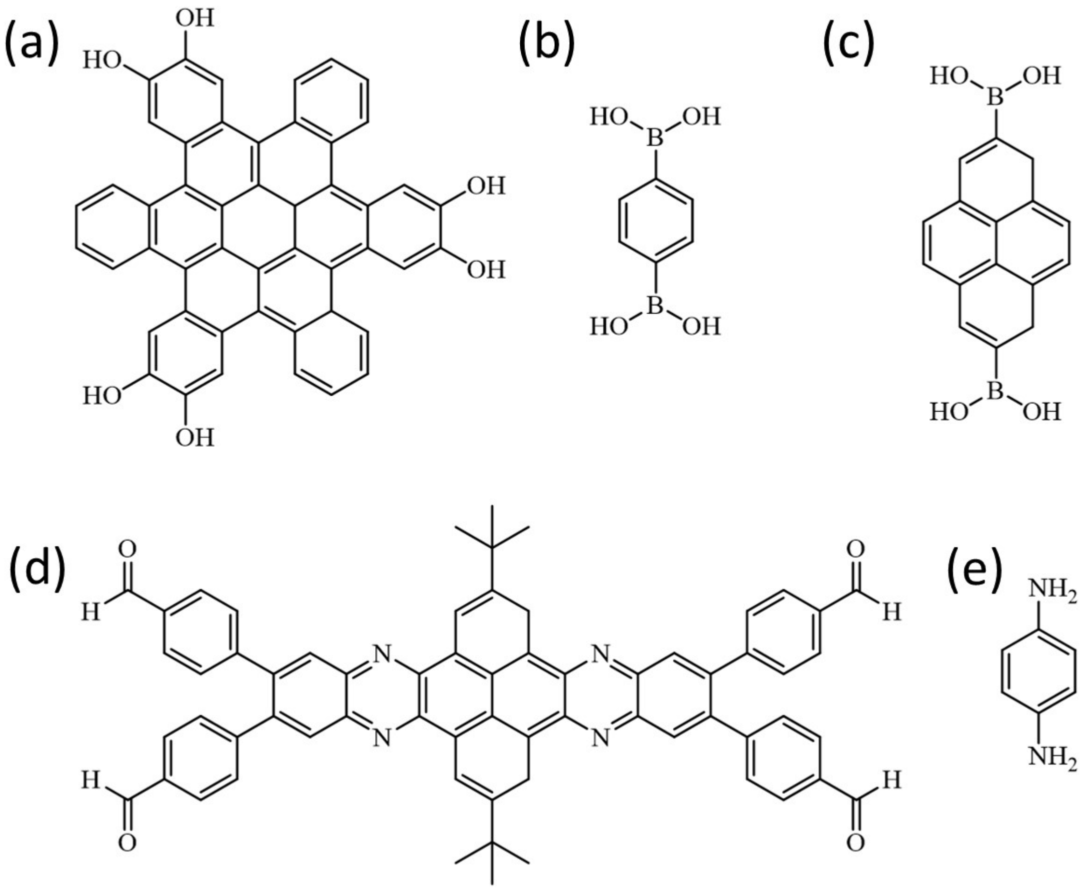

Figure 106: Monomers used to make the polymers in this chapter. (a) Catahexabenzocoronene. (b) Benzenediboronic acid. (c) Pyrenediboronic acid. (d) Dibenzotetraazahexacene. (e) Diaminobenzene.

as the end product.

In terms of ionisation COFs are typically rich in aromatic functional groups, and we know from EDX and EELS in previous chapters that COFs do are readily ionised by the e-beam. Therefore one would expect a build-up of positive charge in the COF polymer, with thicker samples acquiring a larger charge. Depending on whether the COF is conjugated, and the size of the aromatic systems in the COF, this could cause the lattice to be damaged by mechanical forces from Coulomb explosion.[22]

Direct knock-on damage is likely to contribute to the formation of radicals in the COFs via C-H bond scission.[1] These will be localised to the aromatic rich monomers, and could contribute to cross-linking between the monomers in the COF lattice. However, direct knock-on damage will be far slower than other damage pathways unless these pathways are suppressed. Thermogravimetric analysis in Chapters 3 and 4 showed that COFs tend to need to be heated to several hundred degrees to undergo combustion or pyrolysis, and as mentioned earlier e-beam heating may be as low as a 2 K increase. Further a study of e-beam deposition of gaseous trimethyl borate on a silicon surface found that increasing the temperature did not cause an increased rate of B-O bond scisson.[34] Overall, current evidence suggests that thermal-led damage pathways are not of vital importance to COF e-beam stability.

Looking at previous work undertaken on PAHs,[3] it was found that hexazatrinapthylene (HATN) and coronene required a critical fluence on the order of 1.5×10^4 and 1.31×10^4 $^{-}$ nm^{-2} respectively to become amorphous, as judged by the SAED pattern.[3] It was also found that perchlorocoronene (PCC) and perchlorocopper phthalocyanine retained crystallinity up to a critical fluence of 4.0×10^4 $^{-}$ nm^{-2}, with the exact critical fluence not established due to exceptional beam stability of these materials. Comparing to this work it can be seen that Py-COF had a similar e-beam stability to copper phthalocyanines, while Bet-P-1 was able to withstand a power of ten times more fluence.

Of these molecules, it has been shown that PCC encapsulated in single-walled carbon nanotubes undergoes a cross-linking reaction with neighbouring PCC molecule, via elimation of a chlorine dimer forming an aryne and subsequent Diels-Alder cycloaddition.[35] While speculative, this could indicate a cross-linking pathway in COF: first e-beam bond scission leads to the formation of an aryne via elimation of a hydrogen dimer, which could undergo a Diels-Alder cycloaddition with nearby aromatic systems.

5.7 Summary

This chapter has been an exploratory look at e-beam damage in COFs and similar organic polymers. cHBC-BDA-COF was investigated via direct-space methodology, which was unable to determine a critical fluence for the amorphisation of this structure. In contrast for Py-COF and Bet-P-1 indirect-space methodology was able to provide critical fluences of $(3.48 \pm 0.79) \times 10^4$ and $(7.31 \pm 9.23) \times 10^5$ e^{-} nm^{-2} respectively. In these samples the diffraction patterns tended to fade over time indicating the sample was not drifting under the e-beam. A discussion of possible beam damage pathways found that radical formation via bond scission was the most likely pathway for degradation of the materials in this chapter, in light of their relative thickness. This was theorised to lead to cross-linking reactions within the polymer lattice, which could happen for example via Diels-Alder cycloaddition as seen in a literature example of PCC.[35] Comparing to literature examples of PAHs, the Py-COF and Bet-P-1 were found to be more stable than hexazatrinapthylene and coronene, but less stable than halogenated analogues. Overall it has been seen that for these material a microscope operator has only a few minutes of irradiation time to collect meaningful data, after which point the sample will no longer be representative of the crystalline polymer. This knowledge will be invaluable for studying these materials under the e-beam, and the successful application of indirect-space damage investigation methodology will allow wider uptake of e-beam damage investigations by the COF community.

5.8 Future Work

As this chapter was only able to scratch the surface of COF e-beam stability, there is plenty of further investigation that could be undertaken:

- The precise e-beam damage pathways in COFs should be investigated via electronic structure modelling and experimental work, for example MALDI mass spectrometry has been shown to cause similar damage to e-beam damage.[35,36]
- The role of COF morphology, topology, and functionality on e-beam stability should be investigated by making a variety of COFs with different monomers and functional groups; these COFs should also be made in a variety of morphologies with particular reference to sample thickness to uncover how these factors affect sample stability under irradiation.
- Once damage pathways are well understood selective chemical modification to COFs via e-beam irradiation can be pursued, or COFs can be intentionally designed to be more e-beam stable.
- The methodology used here for e-beam damage investigations should be applied broadly to other COFs and organic polymers.

5.9 Experimental

General

All work was carried out by the author unless otherwise indicated. Synthesis was carried out using standard laboratory practice with Pyrex glassware with reagents bought from Merck, Alfa-Aesar, Fischer Scientific or Acros Organics and used without further purification unless explicitly stated. All synthesis and characterisation of Bet-P-1 aside from SEM and TEM was carried out by collaborators at the University of the Basque Country.

IR spectra were recorded on solids using a Bruker Alpha FTIR Spectrometer using a Bruker Platinum ATR attachment over the range 4000-400 cm^{-1}.

Thermogravimetric analysis (TGA) was performed with a TA Q500 Thermogravimetric Analyser. Measurements were performed using platinum pans and were run in air. The parameters for all experiments were ramp 10 °C from 20-1000 °C, then isothermal for 10 mins at 1000 °C. Air flow was 60 mL min^{-1}.

Coulometric Karl-Fischer titration was performed using a Mitsuibishi CA-100 moisture meter. The anode solution was AQUAMICRON AKX, and the cathode solution AQUAMICRON CXU. Calibration was performed by University of Nottingham technicians using NIST traceable water standards.

MALDI-ToF MS measurements were recorded using a Bruker ultraFlexIII (Bruker Daltonik, Bremen, Germany). Samples were dispersed in acetone or chloroform without a matrix unless otherwise indicated then drop-cast on a stainless steel target plate (type MTP384; Bruker Daltonik, Bremen, Germany). The sample was ionised using a pulsed solid-state UV laser (355 nm, 500 μJ, 66.7 Hz shot frequency). The instrument was operated in reflectron mode. Data was acquired using the on-board flexControl software (v3, B185;Bruker Daltonik, Bremen, Germany) and processed using Bruker's flexAnalysis software (v3, B96;Bruker Daltonik, Bremen, Germany).

Powder X-ray diffraction measurements were made with a PANalytical Xpert Pro using Cu(Kα_1) radiation (λ=1.5432 Å) from $2^\circ - 40^\circ$ 2θ on a zero-background silicon holder or a brass sample holder in Bragg-Brentano geometry.

Transmission electron microscopy (TEM) was performed using a JEOL 2100Plus transmission electron microscope with an accelerating voltage of 200 kV, located at the University of Nottingham Nanoscale and Microscale Research Centre. Samples were prepared by dispersing the dry sample in HPLC grade IPA and drop-casting on to a copper TEM grid coated with "lacey" carbon film (Agar Scientific UK). Analysis was performed using Gatan Microscopy Suite 3 and ImageJ FIJI software.[37,38] Fourier-transforms of real-valued images are presented as the magnitude of the original complex-valued Fourier-transform. Energy-dispersive X-ray spectroscopy (EDX), electron energy loss spectroscopy (EELS) and selected-area electron diffraction (SAED) measurements were taken using the JEOL 2100PLUS transmission electron microscope. EELS background fitting was performed using the literature software.[39] EELS Fourier-log convolution and Kramers-Kronig analysis was performed using literature software.[40]

Scanning electron microscopy (SEM) was acquired using a Zeiss Crossbeam 550 FIB-SEM at an accelerating voltage of 30 kV at a working distance of 4.0 mm on a lacy carbon coated TEM grid. Analysis was performed using SmartTiff (v03.00.03) and ImageJ FIJI software.[37,38]

Direct Space e-Beam Stability Measurements

A Gatan Model 994 UltraScan 1000XP CCD camera was used. The TEM was aligned for BF-TEM imaging and set to the lowest flux that gave good image contrast, then using the live view of the camera a suitable region of the sample was found. Images were taken manually as fast as possible until the end of the image sequence. Mean flux was calculated by averaging the intensity over a region of vacuum for each frame in the series and converting the pixel intensity in counts into electrons per area. This average flux was then used to calculate the cumulative fluence for each frame and the total fluence for the entire series.

Reciprocal Space e-Beam Stability Measurements

A Gatan Model 1095 OneView CMOS camera was used. The microscope was aligned for BF-TEM imaging and SAED. The camera was set to in-situ capture mode, with a 10s lookback buffer and 0.5s frame rate (2 fps). Using the camera live view, at constant flux a crystal was found then the TEM switched to diffraction mode and the capture started. The lookback buffer ensured that the entire time the crystal was under irradiation is included in the image series. Capture was continued until all diffraction spots had faded and 10s had passed, or until the diffraction pattern was stable for several minutes. At the end of the series an area of vacuum was found in imaging mode and recorded for several seconds, which was later used to calculate the average electron flux during the series. The raw data was binned by a factor of 1/20 prior to analysis.

cHBC-BDA-COF

cHBC-BDA-COF was made according to the procedure described in Chapter 3.

Py-COF Synthesis

Deprotection of Pyrene-2,7-diboronic acid

Pyrene-2,7-diboronic acid, pinacol ester (150 mg, 0.377 mmol) was added to degassed dichloromethane. Boron tribromide (0.6 mL, 1 mol dm^{-3}, 0.6 mmol) was added to the solution and immediately became yellow. This was left to stir at room temperature for 18 hours. The dichloromethane was evaporated off under a flow of inert atmosphere, then methanol (10 mL) was added slowly to quench excess boron tribromide. The methanol was removed under flow of inert gas and the solid product dried. The final product was isolated as a grey powder (94.6 mg, 0.326 mmol, 86.5 %). IR (ATR) νmax cm^{-1}: 3327.73 (OH), 2952.74 (C-H), 1603.28 (C=C), 1379.49 (B-O), 1333.41 (B-C) ^{1}H NMR (400 MHz, (C_2D_3N): δ 8.66 (s, 4H), 7.95 (s, 4H) MALDI-ToF-MS (m/z): calculated for $C_{16}H_8(B(OH)_2)_2$: 289.89; observed: 289.5 [M]+.

Synthesis of Pyrene-COF

Py-COF was made according to the literature procedure.[23] Briefly, pyrene-2,7-diboronic acid (9.4 mg, 0.03 mmol) was dissolved in dry acetonitrile/mesitylene (10 ml, 7:3) then heated at 100 ° for three days. The precipatate was filtered, washed with excess acetone, and dried to give Py-COF as a yellow solid (3.5 mg, 0.004 mmol, 15 %). IR (KBr)ν_{max} / cm^{-1}: 3258, 3039, 1789, 1762, 1602, 1456, 1387, 1342, 1294, 1245, 1159, 1126, 1040, 997.5, 966.5, 886.5, 814.7, 792.1, 716.1, 683.4, 611.5, 570.5, 535.6, 498.7, 461.7. MS (MALDI-ToF) m/z 627.9 (25), 621.0 (28), 608.9 (73), 602.6 (54), 580.5 (97), 573.2 (18), 558.0 (100), 529.6 (73), 512.3 (24), 493.1 (32), 486.0 (43), 472.7 (22), 467.6 (24), 456.4 (23).

Bet-P-1 Synthesis

Bet-P-1 was made and characterised by collaborators at the University of the Basque Country.[29] Briefly: Dibenzotetraazahexacene (6 mg, 6.4 μmol) and benzene-1,2-diamine (1.39 mg, 12.8 μmol) were sonicated in 0.5 mL of n-butanol in a pre-scored 2 mL ampoule. Then, acetic acid 6M (0.05 mL) was added to the mixture. The suspension was degassed by using three freeze-pump-thaw cycles. The ampoule was sealed off using flame and heated at 125 °C for 5 d. The yellow precipitate was collected by filtration and washed five times with anhydrous tetrahydrofuran, chloroform, and acetone. The powder was dried at 85 °C under vacuum for 12 h affording 6.81 mg of Bet-P-1 as a yellow powder (90 % yield).

References

(1) S. T. Skowron, T. W. Chamberlain, J. Biskupek, U. Kaiser, E. Besley and A. N. Khlobystov, *Accounts of Chemical Research*, 2017, **50**, 1797–1807.

(2) E. Nakamura, *Accounts of Chemical Research*, 2017, **50**, 1281–1292.

(3) K. L. Fung, B. L. Weare, M. W. Fay, S. P. Argent and A. N. Khlobystov, *Micron*, 2023, **165**, 103395.

(4) K. L. Y. Fung, S. T. Skowron, C. S. Allen and A. N. Khlobystov, *Chemical Communications*, 2021, **57**, 10628–10631.

(5) S. T. Skowron, S. L. Roberts, A. N. Khlobystov and E. Besley, *Micron*, 2019, **120**, 96–103.

(6) J. Biskupek, S. T. Skowron, C. T. Stoppiello, G. A. Rance, S. Alom, K. L. Y. Fung, R. J. Whitby, M. H. Levitt, Q. M. Ramasse, U. Kaiser, E. Besley and A. N. Khlobystov, *ACS Nano*, 2020, **14**, 11178–11189.

(7) T. Zaharescu and G. Varca, *Radiation Physics and Chemistry*, 2022, **194**, 110043.

(8) M. Maitz, *Biosurface and Biotribology*, 2015, **1**, 161–176.

(9) D. Abliz, Y. Duan, L. Steuernagel, L. Xie, D. Li and G. Ziegmann, *Polymers and Polymer Composites*, 2013, **21**, 341–348.

(10) A. Singh, *Nuclear Instruments and Methods in Physics Research Section B: Beam Interactions with Materials and Atoms*, 2001, **185**, 50–54.

(11) M. Slouf, H. Synkova, J. Baldrian, A. Marek, J. Kovarova, P. Schmidt, H. Dorschner, M. Stephan and U. Gohs, *Journal of Biomedical Materials Research Part B: Applied Biomaterials*, 2008, **85B**, 240–251.

(12) J. Raghavan and M. R. Baillie, *Polymer Composites*, 2000, **21**, 619–629.

(13) P. Angelova, H. Vieker, N.-E. Weber, D. Matei, O. Reimer, I. Meier, S. Kurasch, J. Biskupek, D. Lorbach, K. Wunderlich, L. Chen, A. Terfort, M. Klapper, K. Müllen, U. Kaiser, A. Gölzhäuser and A. Turchanin, *ACS Nano*, 2013, **7**, 6489–6497.

(14) W. Geyer, V. Stadler, W. Eck, M. Zharnikov, A. Gölzhäuser and M. Grunze, *Appl. Phys. Lett*, 1999, **75**, 2401–2403.

(15) T. Weimann, W. Geyer, P. Hinze, V. Stadler, W. Eck and A. Gölzhäuser, *Microelectron. Eng.*, 2001, **57-58**, 903–907.

(16) T. Felgenhauer, C. Yan, W. Geyer, H.-T. Rong and A. Gölzhäuser, *Appl. Phys. Lett.*, 2001, **79**, 3323–3325.

(17) A. Küller, M. A. El-Desawy, V. Stadler, W. Geyer, W. Eck and A. Gölzhäuser, *J. Vac. Sci. Technol. B*, 2004, **22**, 1114–1117.

(18) W. Eck, V. Stadler, W. Geyer, M. Zharnikov, A. Gölzhäuser and M. Grunze, *Adv. Mater.*, 2000, **12**, 805–808.

(19) A. Turchanin, D. Käfer, M. El-Desawy, C. Wöll, G. Witte and A. Gölzhäuser, *Langmuir*, 2009, **25**, 7342–7352.

(20) M. Zhang, J. Chen, S. Zhang, X. Zhou, L. He, M. V. Sheridan, M. Yuan, M. Zhang, L. Chen, X. Dai, F. Ma, J. Wang, J. Hu, G. Wu, X. Kong, R. Zhou, T. E. Albrecht-Schmitt, Z. Chai and S. Wang, *Journal of the American Chemical Society*, 2020, **142**, 9169–9174.

(21) R. Egerton, *Microscopy Research and Technique*, 2012, **75**, 1550–1556.

(22) R. Egerton, *Micron*, 2019, **119**, 72–87.

(23) A. M. Evans, I. Castano, A. Brumberg, L. R. Parent, A. R. Corcos, R. L. Li, N. C. Flanders, D. J. Gosztola, N. C. Gianneschi, R. D. Schaller and W. R. Dichtel, *Journal of the American Chemical Society*, 2019, **141**, 19728–19735.

(24) G. Zhan, Z.-F. Cai, K. Strutyński, L. Yu, N. Herrmann, M. Martínez-Abadía, M. Melle-Franco, A. Mateo-Alonso and S. D. Feyter, *Nature*, 2022, **603**, 835–840.

(25) S. Wan, J. Guo, J. Kim, H. Ihee and D. Jiang, *Angewandte Chemie International Edition*, 2009, **48**, 5439–5442.

(26) Y. Li, Q. Chen, T. Xu, Z. Xie, J. Liu, X. Yu, S. Ma, T. Qin and L. Chen, *Journal of the American Chemical Society*, 2019, **141**, 13822–13828.

(27) N. Bilbao, C. Martín, G. Zhan, M. Martínez-Abadía, A. Sanz-Matías, A. Mateo-Alonso, J. N. Harvey, M. Van der Auweraer, K. S. Mali and S. De Feyter, *ACS Nano*, 2020, **14**, 2354–2365.

(28) R. Egerton, *Ultramicroscopy*, 2013, **127**, 100–108.

(29) E. De Bolós, M. Martínez-Abadía, F. Hernández-Culebras, A. Haymaker, K. Swain, K. Strutyński, B. L. Weare, J. Castells-Gil, N. M. Padial, C. Martí-Gastaldo, A. N. Khlobystov, A. Saeki, M. Melle-Franco, B. L. Nannenga and A. Mateo-Alonso, *Journal of the American Chemical Society*, 2022, **144**, 15443–15450.

(30) L. Rodrigo, P. Pou and R. Pérez, *Carbon*, 2016, **103**, 200–208.

(31) A. W. Robertson, B. Montanari, K. He, C. S. Allen, Y. A. Wu, N. M. Harrison, A. I. Kirkland and J. H. Warner, *ACS Nano*, 2013, **7**, 4495–4502.

(32) Y. Wang, Y. Feng, F. Mo, G. Qian, Y. Chen, D. Yu, Y. Wang and X. Zhang, *Applied Physics Letters*, 2014, **105**, 023102.

(33) M. Evora, J. Araujo, E. Ferreira, B. Strohmeier, L. Silva and C. Achete, *Applied Surface Science*, 2015, **335**, 78–84.

(34) A. A. Martin and P. J. Depond, *Beilstein Journal of Nanotechnology*, 2018, **9**, 1282–1287.

(35) K. L. Fung, S. T. Skowron, R. Hayter, S. E. Mason, B. L. Weare, N. A. Besley, Q. M. Ramasse, C. S. Allen and A. N. Khlobystov, *Physical Chemistry Chemical Physics*, 103395.

(36) R. K. E. Gover, Ph.D. Thesis, University of Nottingham, 2016.

(37) J. Schindelin, I. Arganda-Carreras, E. Frise, V. Kaynig, M. Longair, T. Pietzsch, S. Preibisch, C. Rueden, S. Saalfeld, B. Schmid, J.-Y. Tinevez, D. J. White, V. Hartenstein, K. Eliceiri, P. Tomancak and A. Cardona, *Nature Methods*, 2012, **9**, 676–682.

(38) J. Schindelin, C. T. Rueden, M. C. Hiner and K. W. Eliceiri, *Molecular Reproduction and Development*, 2015, **82**, 518–529.

(39) K. L. Fung, M. W. Fay, S. M. Collins, D. M. Kepaptsoglou, S. T. Skowron, Q. M. Ramasse and A. N. Khlobystov, *Ultramicroscopy*, 2020, **217**, 113052–113052.

(40) R. F. Egerton, *Electron Energy-Loss Spectroscopy in the Electron Microscope*, Springer New York, New York, 3rd edn.

6 Conclusion

This thesis has developed the application of transmission electron microscopy (TEM) of covalent organic frameworks (COFs) beyond the current state-of-the-art. As survey of the literature made clear that advanced bright-field (BF) imaging and TEM spectroscopy were under-represented, it was decided to focus on these elements of TEM applied to COFs. To achieve this several systems of COF and COF/nanosupport were made as test systems for TEM techniques. The COFs cHBC-BDA-COF and COF-5 were made as powders, and were hybridised with with graphite, graphitised nanofibres (GNFs), multi-walled carbon nanotubes (MWNTs), single-walled carbon nanotubes (SWNTs), and silica nanoparticles. It was found that use of dilute reaction systems, nitrile co-solvents, modulators, and the exclusion of water was necessary to form crystals of COFs; this can be linked to these conditions promoting reaction reversibility and slowing the rate of COF growth, giving more time for error-checking to form a crystalline structure.

COFs and COF/nanosupport hybrids were analysed via bulk spectroscopic and crystallographic methods. Powder X-ray diffraction (PXRD) was unable to find evidence of crystallinity in these systems, but infrared spectroscopy (IR) was able to find evidence of COF formation via the appearance of polymer functional group vibrations. Thermogravimetric analysis (TGA) was used to find the decomposition temperature of COFs, and as a method to quantify COF loading on a nanosupport. TGA was also used to prepare pyrolysed materials from COF-5 and COF-5/GNF. Matrix-assisted laser desorption-ionisation mass spectrometry (MALDI MS) was applied to COFs for the first time; it was found MALDI was able to find ions corresponding to fragments of the COF lattice, and that similar spectra were given by mechanical mixtures of polymers. This suggested that standard samples of monomer mixtures could be used to help identify the ratio of monomers in an unknown structure, allowing more accurate identification of the COF structure.

Bright-field TEM (BF-TEM) imaging was found to be a powerful tool for understanding COF morphology. Where bulk spectroscopic methods found small differences between samples, BF-TEM was able to show that these were due to the different nanoscale morphologies. In particular nanosupports lead to the formation of thin layers of COF at their surface, but the presence of COF not associated with nanosupport in these samples confirms no strong driving force to selectively form hybrids. Therefore, BF-TEM imaging of reaction products gives information about how the reaction took place. The biggest utility of BF-TEM was revealing crystallinity were none was thought to be present. Throughout, it was seen that samples with no indexable PXRD reflections were in fact composed of nanocrystals; these crystals gave no detectable diffraction by PXRD or SAED. Tilt-series were used to show how the crystal projections change as a function of angle, and to show the variable thickness of COF/nanosupport. As COF applications drive towards COF/nanosupport hybrids and thin-layer COFs, and in light of the known difficulty of analysing the crystal structures of small materials via diffraction, the ability of TEM imaging to accurately ascertain the crystallinity and morphology of nanoscale materials will be critical.

TEM spectroscopy in the form of electron energy loss spectroscopy (EELS) and energy dispersive X-ray spectroscopy (EDX) were applied to cHBC-BDA-COF and COF-5. EDX was used for qualitative elemental analysis, and confirmed that the samples did not contain any unexpected elements. TEM-EELS was used to find core-loss edges of carbon and oxygen for COF samples, but was unable to give a boron K edge for most cases. This was rationalised as being due to the low concentration of boron in the samples and the limits of the detectors used. Low-loss EELS was used to quantify sample thickness using Kramers-Kronig analysis, and to establish the plasmon energy and peak profile. EELS thickness measurements were found to match well to BF-TEM measurements, and will be useful for samples where tilt-series cannot be used to rigorously establish sample thickness. Poor energy resolution and effects of deconvolution hindered the investigation of band-gaps. Aberration-corrected scanning transmission electron microscopy (AC-STEM) EELS was applied to cHBC-BDA-COF/GNF, which found a boron K edge - this was used to create a STEM-EELS map showing the boron was localised to the outside edge of the GNF. The low-loss spectrum was used for vibrational EELS (VEELS), which found a difference in the vibrations present at the edge of the hybrid and the centre. These findings confirmed that the sample consisted of a layer of COF surrounding GNF support. Overall EELS and EDX were found to be useful techniques for elemental characterisation of COFs with nanoscale resolution.

A coarse-grained graph theoretical model was developed to put the TEM lattice projections of COFs on a firm theoretical basis prior to delving into experimental TEM imaging, which found that the projections of COFs can be derived from their topology. Hexagonal 2D COFs were found to have face-on (FO), side-on (SO), armchair (AC), and zigzag (ZZ) lattice projections; this matched to the experimental TEM of cHBC-BDA-COF and COF-5. BF-TEM imaging found that the lattice projections of experimental systems did not occur equally frequently, which was rationalised as an effect of sample thickness. A stochastic 3D graph model was also created to simulate the structure of real COF crystallites, which was used to try and quantify at which point a sample could be said to have switched from amorphous to crystalline. It was found that there is no clear cut-off point and some judgement from the experimental practitioner is required to decide when a sample is no longer crystalline.

An exploratory look was made into the electron beam sensitivity of COFs using cHBC-BDA-COF, pyrene-COF (Py-COF), and a non-COF polymer Bet-P-1. cHBC-BDA-COF was examined using direct-space methodology which was unable to find a threshold fluence past which the sample was amorphous. Py-COF and Bet-P-1 were examined using reciprocal-space methodology, which was used to find the threshold fluence for these materials. The possible electron beam (e-beam) damage pathways for these materials were then discussed, which found that the mostly likely damage pathway for these materials was radical formation leading to cross-linking.

Overall, this thesis has looked at a range of bulk and TEM techniques that can be used to characterise COFs and COF hybrids and found that a holistic methodology involving novel modelling, TEM, and bulk measurements is a powerful way to uncover information about the structure of these materials.

7 Appendices

Here is a series of things that do not fit into the main text, for better or for worse.

7.1 Thesis Poems

The following verses are attempts to distill the essence of this thesis into as small a package as possible. As a haiku:

Covalent framework
in electron microscope,
analysis blooms.

More lighthearted is the limerick:

There once was a young'un from Norwich,
Whom's science was awfully niche,
Covalent frameworks he made,
In the TEM were they laid,
And the resulting publications bewitch.

Most arduous the sonnet:

During autumn some years ago the start
Of work began. To make framework 'valent,
And learn a scientists' method by heart,
were the goals set: into that mired path went.
With coffee for fuel monomer turned
To polymer, into a microscope
Firm plac'd. Under e-beam sample's soon burned.
Is the task without a lonesome hope?
A published article or two guide on,
Aid given by those who alongside work

Pushes task to reach an end as time is gone.

And so my final words in this affair:

The hardest part of this whole time

Was finding couplets that would rhyme.

7.2 Additional 1D Stochastic Polymer Modelling

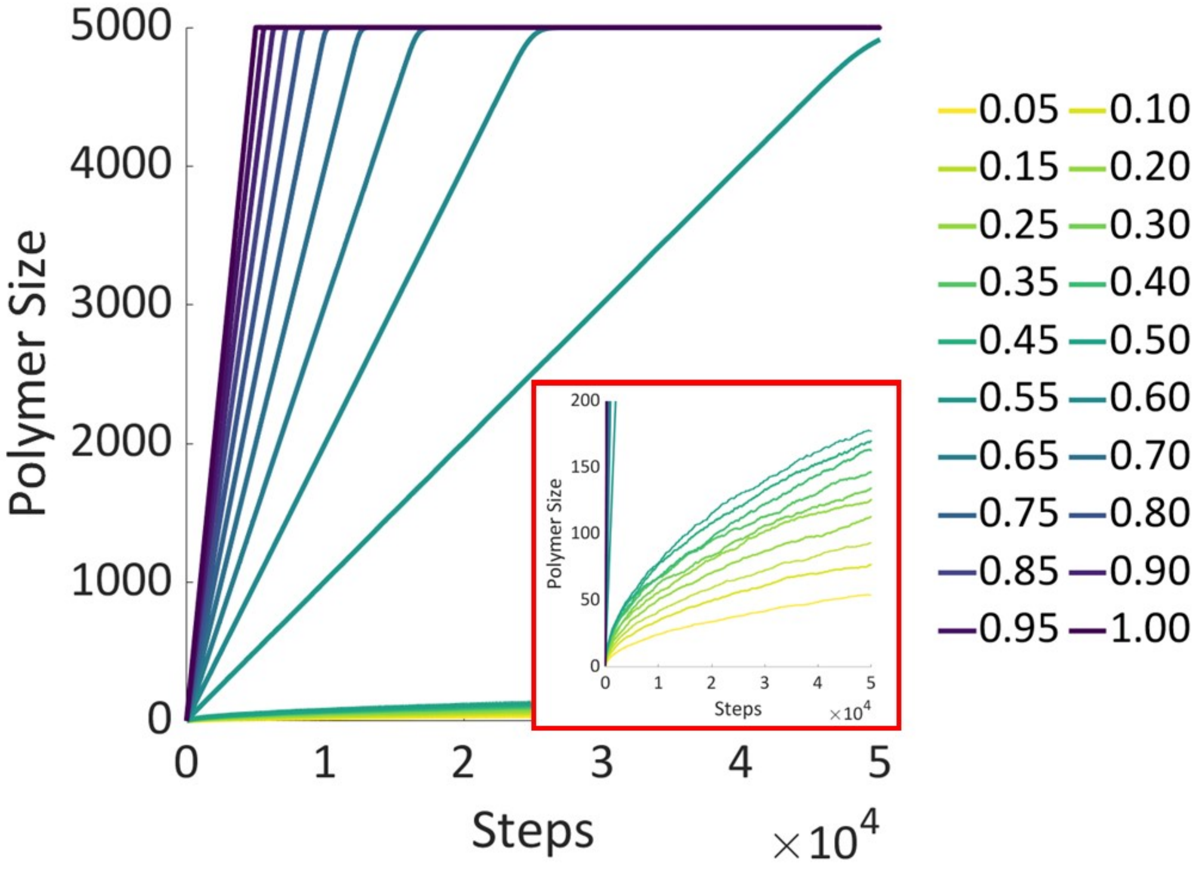

Figure 107: Graph of 1D polymer size model growth using 5000 monomers. The equilibrium phase for P(add) < 0.5 requires more steps than could be simulated, crashing the authors computer. Insert: magnified for P(add) < 0.5. The key indicates P(add) as a decimal.

7.3 MALDI Mass Spectrometry

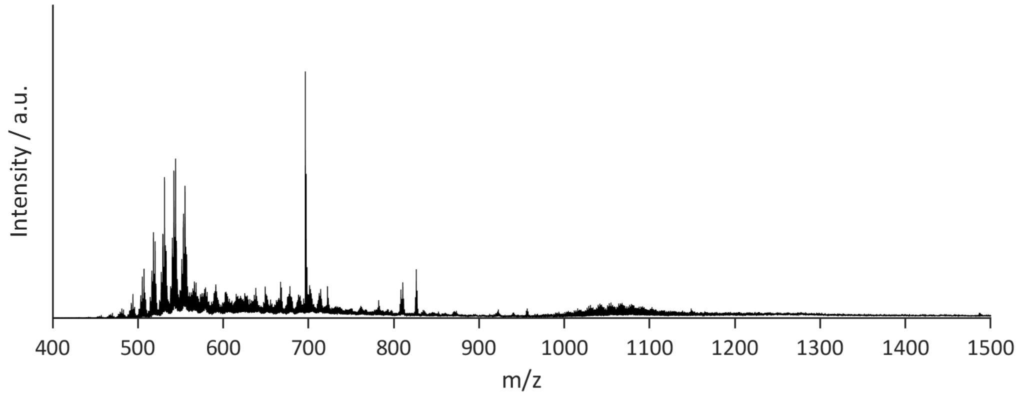

Figure 108: MALDI MS of a dry mechanical mixture of cHBC and BDA, containing many of the same ions as the mass spectrum of cHBC-BDA-COF. This indicates that the laser may induce polymerisation.

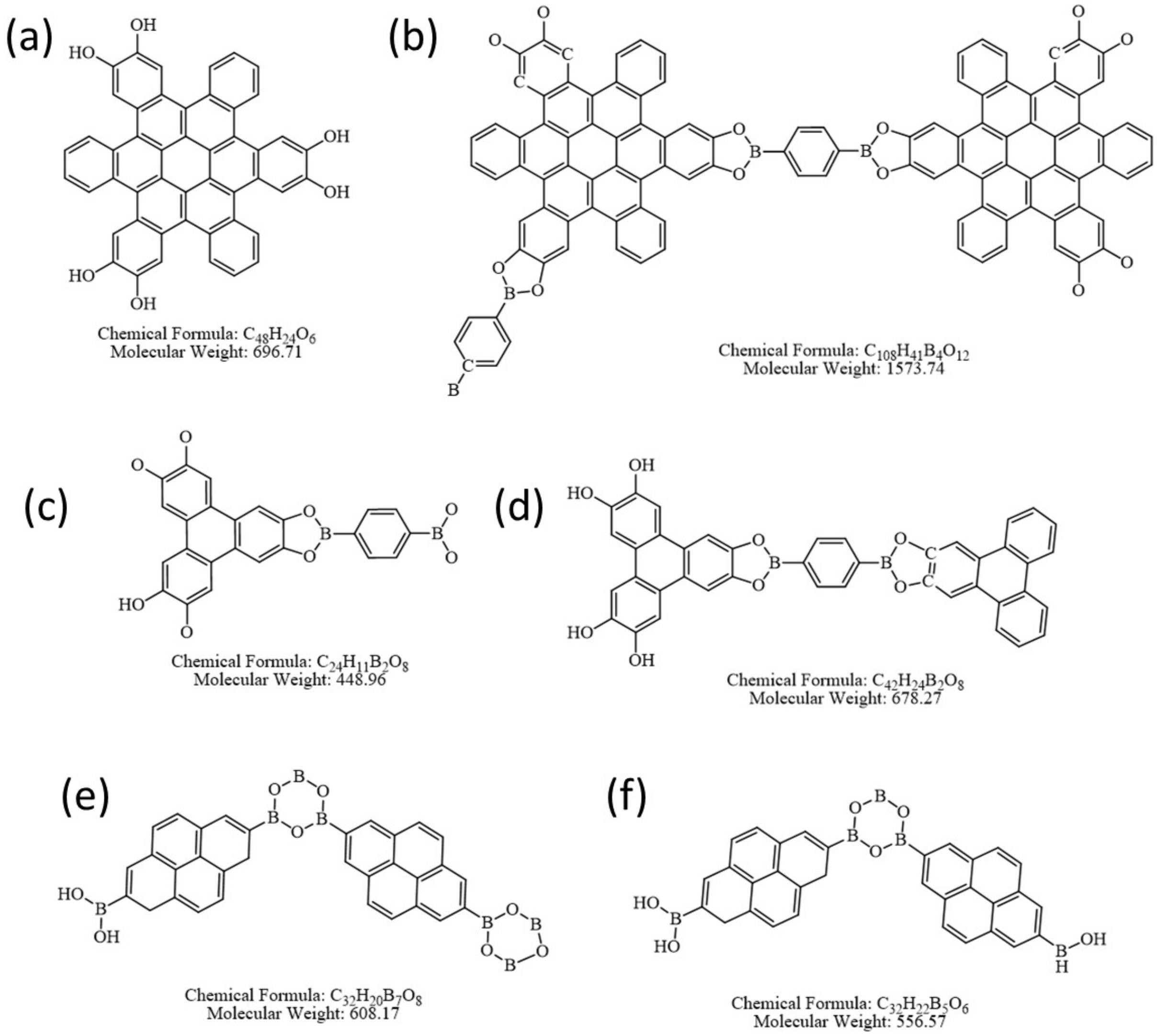

Figure 109: Select suggested MALDI MS ion fragments for: (a, b) cHBC-BDA-COF; (c, d) COF-5; (e, f) Py-COF. (a, c, e) Are the respective base peaks, while (b, d, f) are illustrative examples of higher mass ions, and how they tend to fragment at the boronate ester or boroxine functional groups. Structures are a rationalisation of the empirical ion formulae found from the mass spectrum. All ions have a +1 charge, omitted for clarity.

m/z	Assignment
1487	$C_{102}H_{37}B_3O_{12}^+$
1149	$C_{81}H_{26}B_2O_8^+$
1121	$C_{81}H_{30}B_2O_6^+$
1092	$C_{76}H_{29}B_2O_8^+$
882	$C_{59}H_{24}B_2O_8^+$
864	$C_{60}H_{26}B_2O_6^+$
850	$C_{59}H_{24}B_2O_6^+$
826	$C_{55}H_{21}B_3O_7^+$
810	$C_{54}H_{22}B_4O_6^+$
798	$C_{54}H_{21}B_3O_6^+$
782	$C_{54}H_{22}B_3O_5^+$
775	$C_{54}H_{24}B_2O_5^+$
734	$C_{52}H_{19}BO_5^+$
722	$C_{48}H_{18}B_3O_6^+$
712	$C_{48}H_{18}B_2O_6^+$
710	$C_{48}H_{16}B_2O_6^+$
696	$C_{48}H_{24}O_6^+$
694	$C_{48}H_{22}O_6^+$
678	$C_{48}H_{22}O_5^+$
667	$C_{49}H_{20}BO_3^+$
655	$C_{48}H_{15}O_4^+$
649	$C_{46}H_{22}BO_4^+$
638	$C_{46}H_{22}O_4^+$

Table 23: Empirical formulae for MALDI-MS ions of cHBC-BDA-COF. All ions have a +1 charge.

m/z	Assignment
774.5	$C_{43}H_{23}B_4O_{12}^+$
746.2	$C_{42}H_{26}B_2O_{12}^+$
740.0	$C_{42}H_{21}B_2O_{12}^+$
677.4	$C_{42}H_{24}B_2O_8^+$
616.1	$C_{42}H_{19}B_3O_{10}^+$
597.5	$C_{36}H_{14}B_2O_8^+$
580.2	$C_{36}H_{15}B_2O_7^+$
542.8	$C_{32}H_{17}B_2O_7^+$
535.6	$C_{31}H_{13}B_2O_8^+$
474.7	$C_{26}H_{13}B_2O_8^+$
448.3	$C_{24}H_{11}B_2O_8^+$
433.7	$C_{24}H_{12}B_2O_7^+$
424.8	$C_{24}H_{18}B_2O_6^+$

Table 24: Empirical formulae for MALDI-MS ions of COF-5. All ions have a +1 charge.

m/z	**Assignment**
627.9	$C_{32}H_{18}B_9O_8^+$
621.0	$C_{32}H_{21}B_8O_8^+$
608.9	$C_{32}H_{20}B_7O_8^+$
602.6	$C_{38}H_{23}B_4O_5^+$
580.5	$C_{32}H_{21}B_6O_7^+$
573.2	$C_{32}H_{23}B_5O_7^+$
558.0	$C_{32}H_{22}B_5O_6^+$
529.6	$C_{32}H_{22}B_4O_5^+$
512.3	$C_{32}H_{21}B_4O_4^+$
493.1	$C_{32}H_{18}B_4O_3^+$
485.9	$C_{32}H_{20}B_3O_3^+$
472.7	$C_{32}H_{18}B_2O_4^+$
467.6	$C_{32}H_{20}B_3O_2^+$
456.4	$C_{32}H_{18}B_2O_2^+$

Table 25: Empirical formulae for MALDI-MS ions of Py-COF. All ions have a +1 charge.

7.4 COF-5 EELS Band Gap Measurements

Sample	**Band gap / eV**
COF-5	2 ± 3.0
COF-5/graphite	0 ± 2.7
COF-5/GNF	3 ± 2.6
COF-5/MWNT	1.4 ± 2.7
COF-5/SWNT	1.5 ± 2.4
pyro(GNF)	0 ± 2.5
pyro(COF-5/GNF)	0 ± 5.2
pyro(COF-5)	1 ± 5.3

Table 26: Band gaps measured from low-loss EEL spectra of COF-5, COF-5/nanosupports, and pyrolysed COF-5 materials. Due to poor energy resolution and deconvolution effects, the presented values are not reliable.

7.5 Karl-Fischer Moisture Measurements

Solvent	Moisture (bench) / ppm	Moisture (dry) /ppm
Acetonitrile	788.9	79.31
1,4-Dioxane	501.8	88.24
Mesitylene	144.8	6.464

Table 27: Karl-Fischer moisture measurements using the procedure described in Chapter 4. Bench solvents were those available in the lab, dry solvents were purchased pre-dried under inert atmosphere with a puncture seal.

7.6 Scanning Electron Microscopy

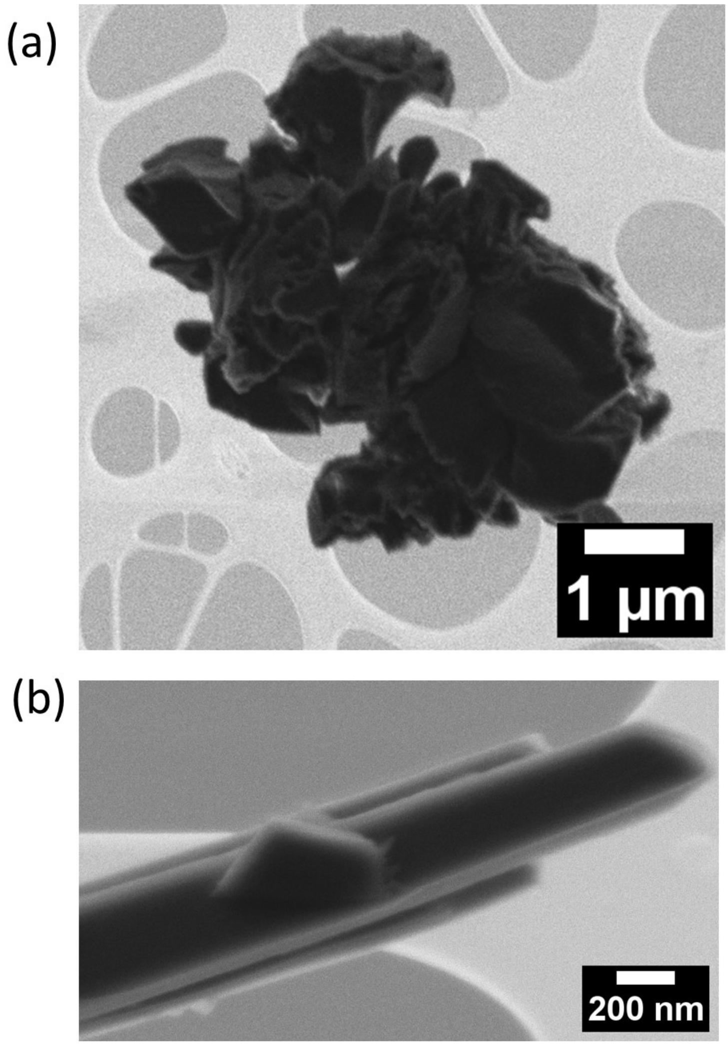

Figure 110: SEM images of: (a) Py-COF, in the form of irregular crystals; and (b) Bet-P-1, in the form of large needles.

7.7 Simulated EDX spectra

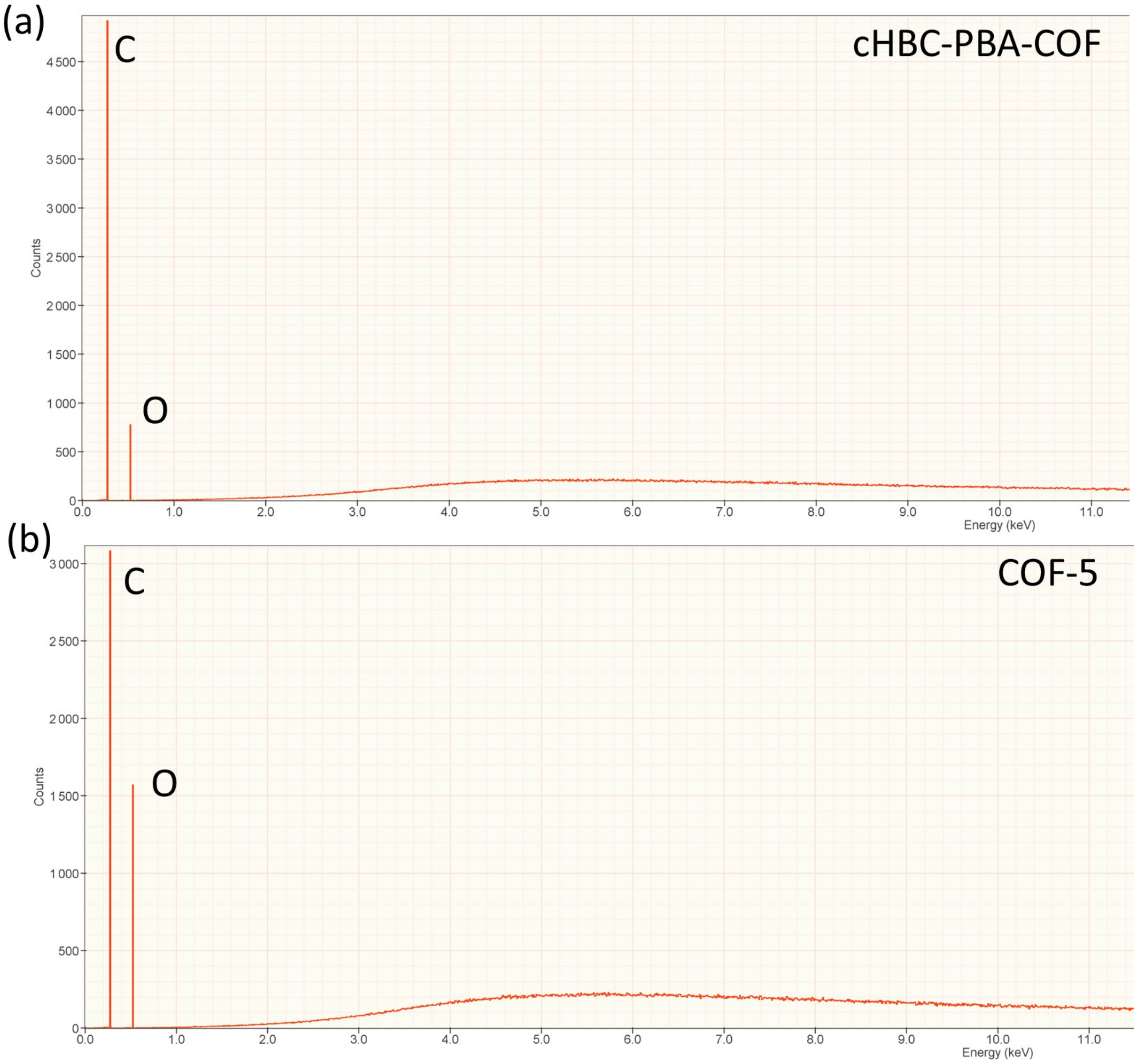

Figure 111: Simulated EDX spectra for (a) cHBC-BDA-COF and (b) COF-5. The spectra have carbon and oxygen peaks, and a broad noise contribution above 2.0 keV. Simulation details are in Chapters 2 and 3.

7.8 EDX Peaks

Element	Kα_1	Kβ_1	Lα_1	Lβ_1	Mα_1	Mα_1
B	0.183					
C	0.277					
N	0.392					
O	0.525					
F	0.677					
Na	1.04					
Al	1.486	1.557				
Si	1.74	1.837				
S	2.309	2.465				
Cl	2.622	2.812				
K	3.314	3.59				
Ca	3.692	4.013	0.341	0.345		
Cr	5.5414	5.415	0.572	0.5852		
Fe	6.405	7.059	0.705	0.718		
Ni	7.48	8.267	0.849	0.866		
Cu	8.046	8.904	0.928	0.947		
Br	11.924	13.292	1.481	1.526		
Au	68.806	77.982	9.713	11.443	2.123	2.203

Table 28: Literature values for EDX peaks of elements seen in this thesis.[1]

7.9 Infrared Spectra

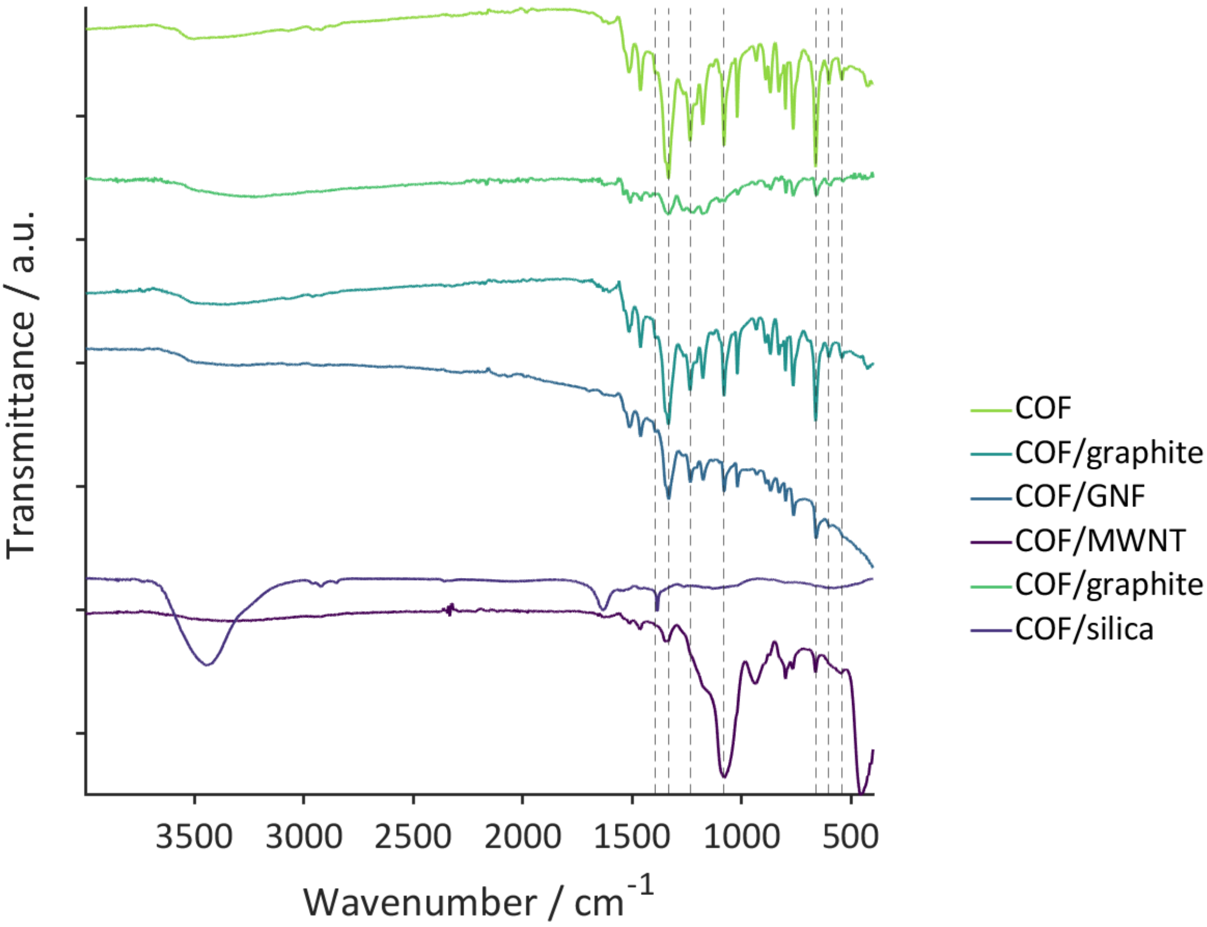

Figure 112: Full IR spectra of cHBC-BDA-COF and cHBC-BDA-COF/nanosupports seen in Chapter 2. Dotted lines indicate boronic acid vibrations. This version shows the full spectrum above 1600 cm^{-1}.

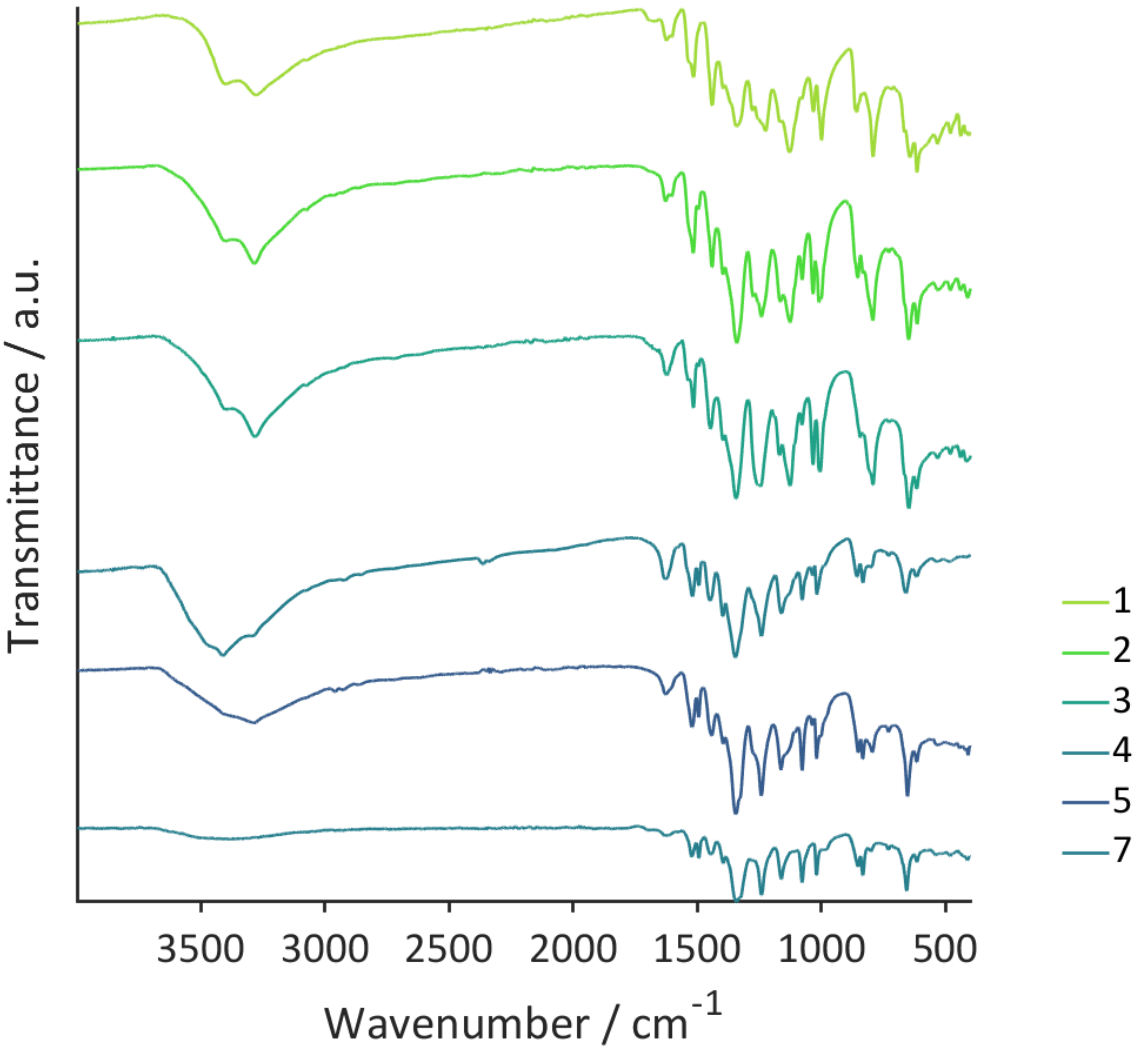

Figure 113: Full IR spectra of amorphous COF-5 samples; a truncated version is seen in Chapter 3. The key indicates the syntheses described in Chapter 3. This version shows the full spectrum above 1600 cm^{-1}.

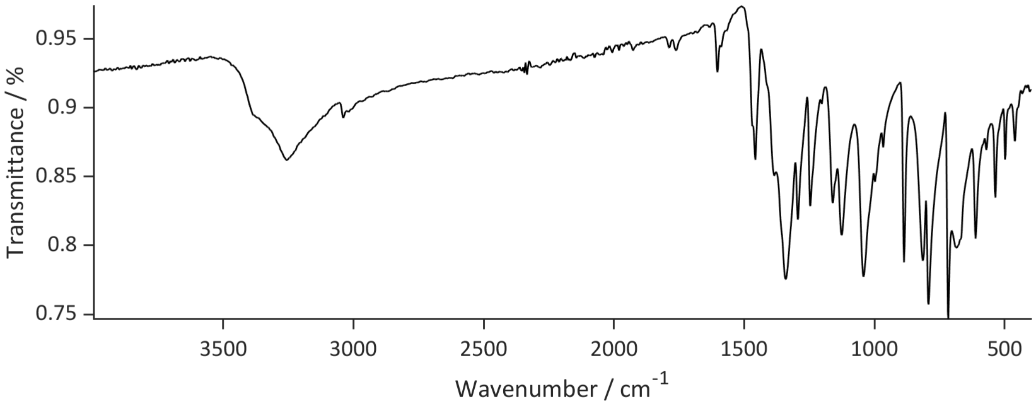

Figure 114: Full ATR transmission IR spectrum of Py-COF; a truncated version is seen in Chapter 5. This version shows the full spectrum above 1600 cm^{-1}.

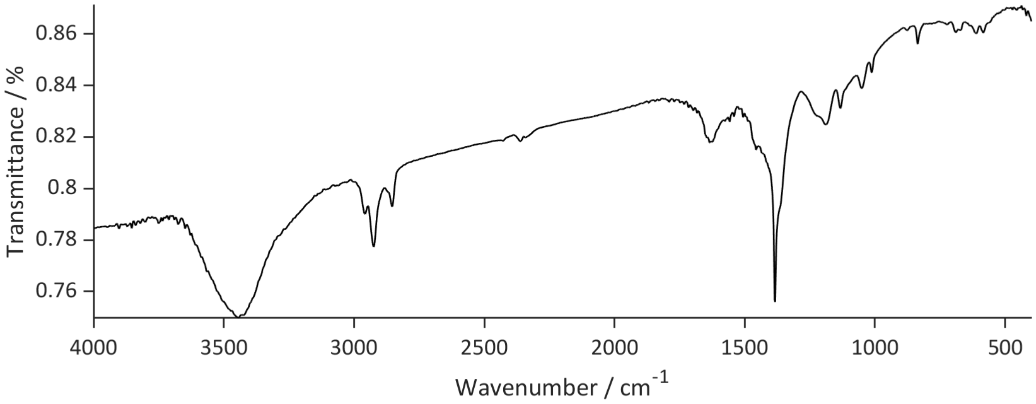

Figure 115: Potassium bromide pellet transmission spectrum of graphitised nanofibres (GNFs). The sloping baseline is due to Mié scattering from the GNFs. Key features are the C-H stretches at 2800 cm^{-1} and the radial breathing motion at 1400 $^{-1}$.

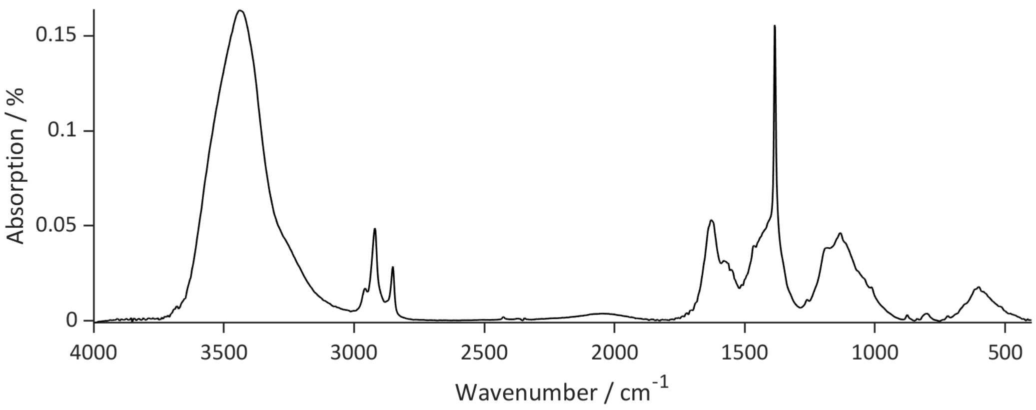

Figure 116: Potassium bromide pellet absorption spectrum of single-walled carbon nanotubes (SWNTs). Key features are the C-H stretches at 2800 cm^{-1} and the radial breathing motion at 1400 $^{-1}$.

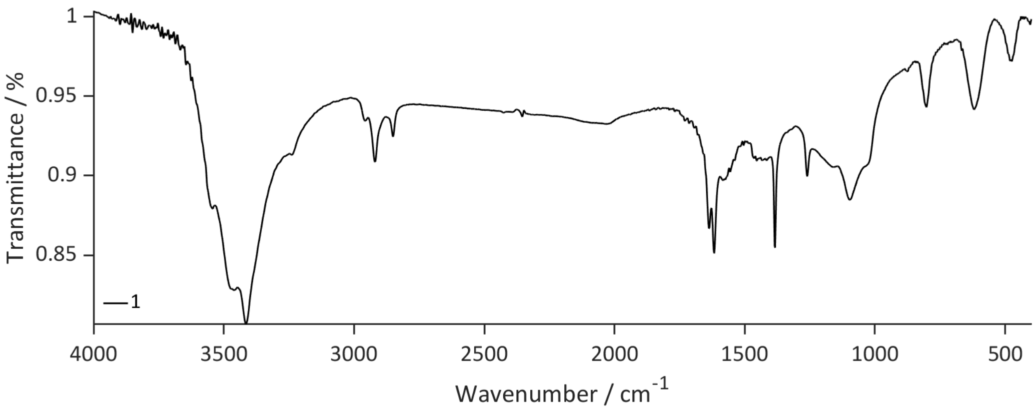

Figure 117: Potassium bromide pellet transmission spectrum of multi-walled carbon nanotube (MWNTs). Key features are the C-H stretches at 2800 cm^{-1} and the radial breathing motion at 1400 $^{-1}$.

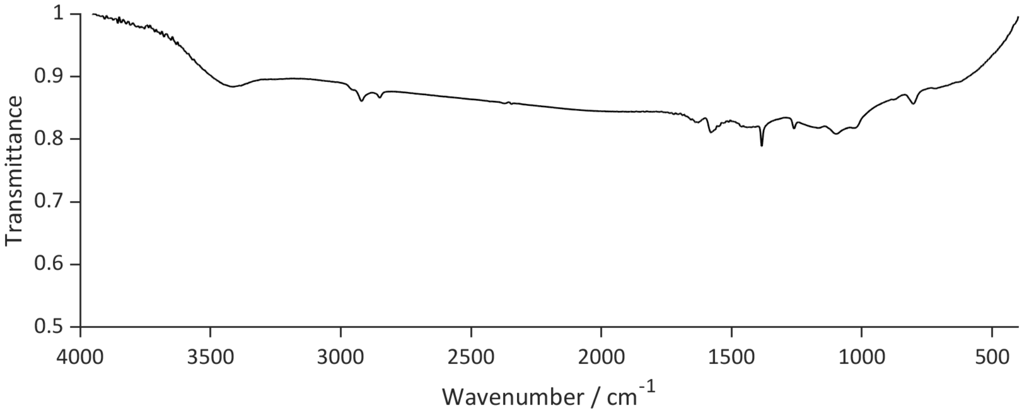

Figure 118: Potassium bromide pellet transmission spectrum of graphite. Low intensity is due to the strong IR absorption of graphite.

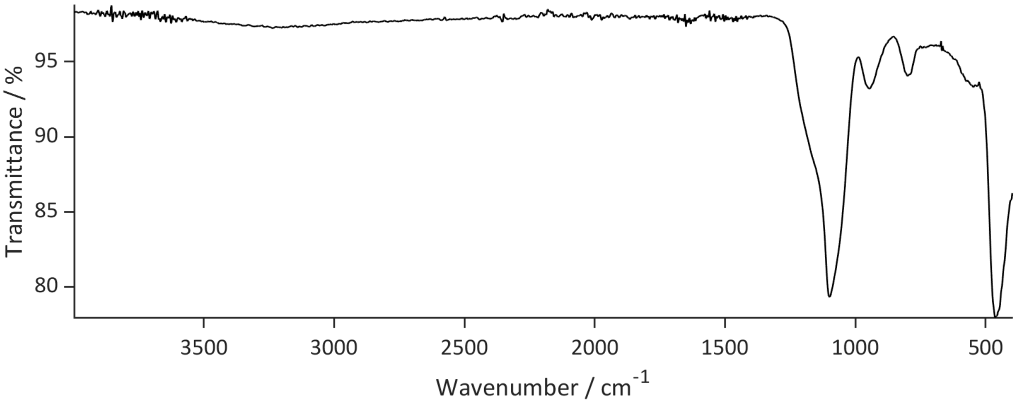

Figure 119: Attenuated total reflectance transmission spectrum of silica nanoparticles (SiONPs). Silica has relatively few IR stretches in the measured region, which can overlap with boronate ester COF vibrations.

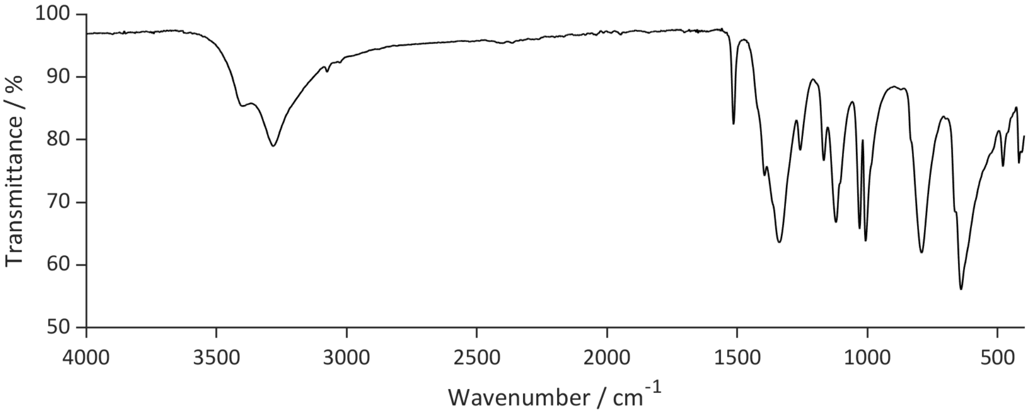

Figure 120: Attenuated total reflectance transmission spectrum of benzenediboronic acid (BDA), used to make COF-5 and cHBC-BDA-COF.

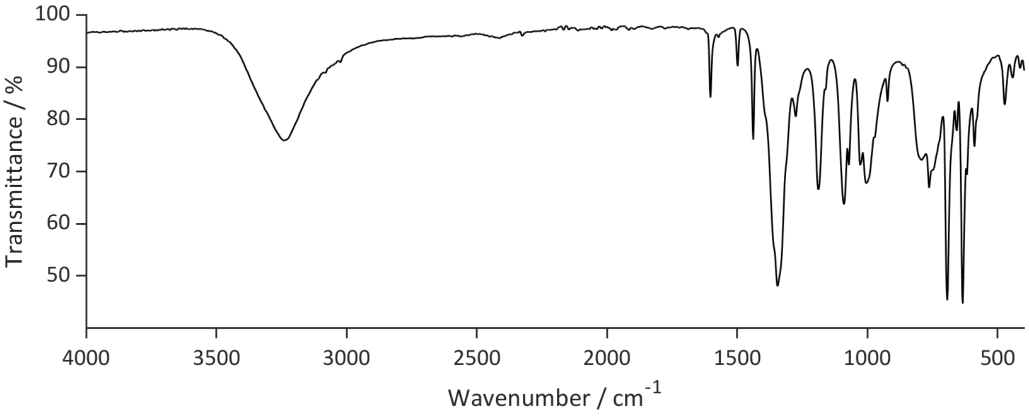

Figure 121: Attenuated total reflectance transmission spectrum of phenylboronic acid (PBA), used as a modulator for cHBC-BDA-COF synthesis.

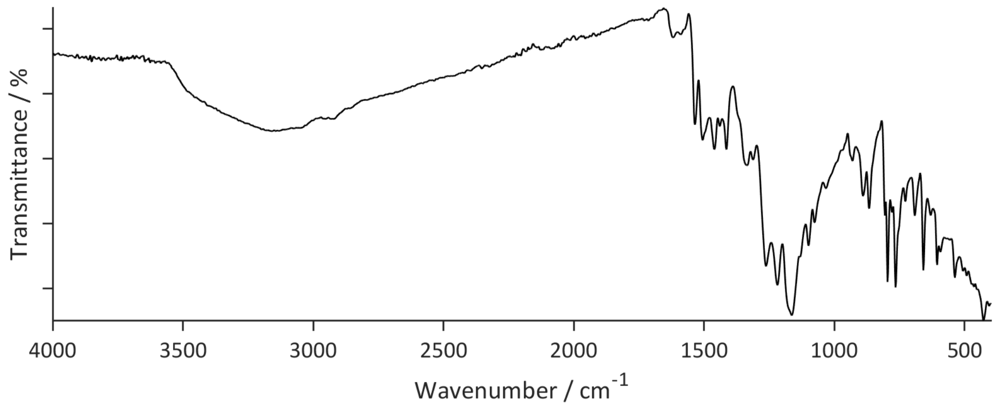

Figure 122: Attenuated total reflectance transmission spectrum of cata-hexabenzocoronene (cHBC), used to make cHBC-BDA-COF.

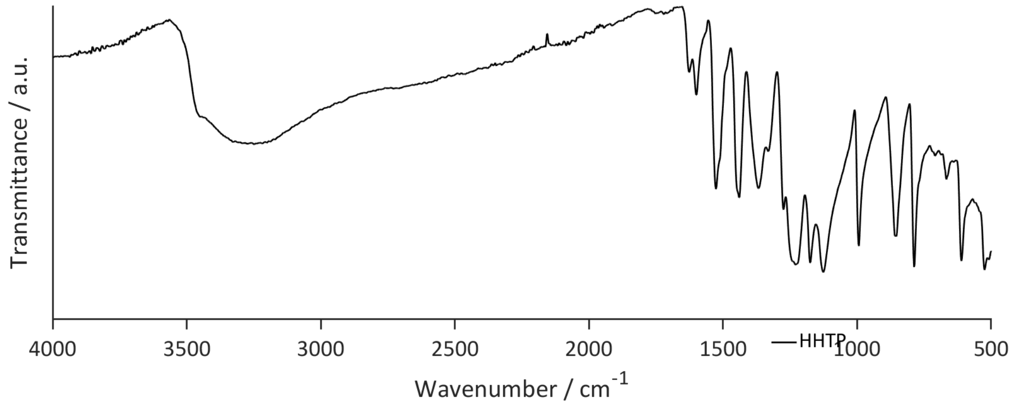

Figure 123: Attenuated total reflectance transmission spectrum of hexahydroxytriphenylene (HHTP), used to make COF-5.

7.10 Thermogravimetric Analysis

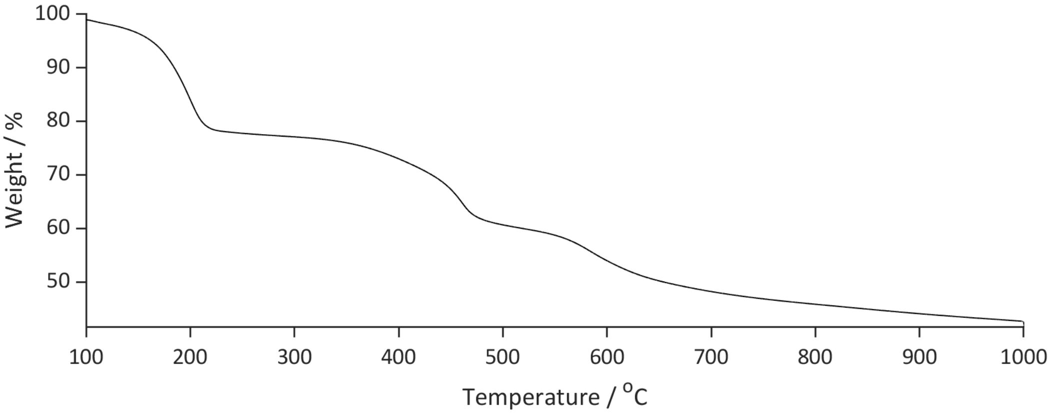

Figure 124: TGA thermogram of benzenediboronic acid (BDA), used to make COF-5 and cHBC-BDA-COF.

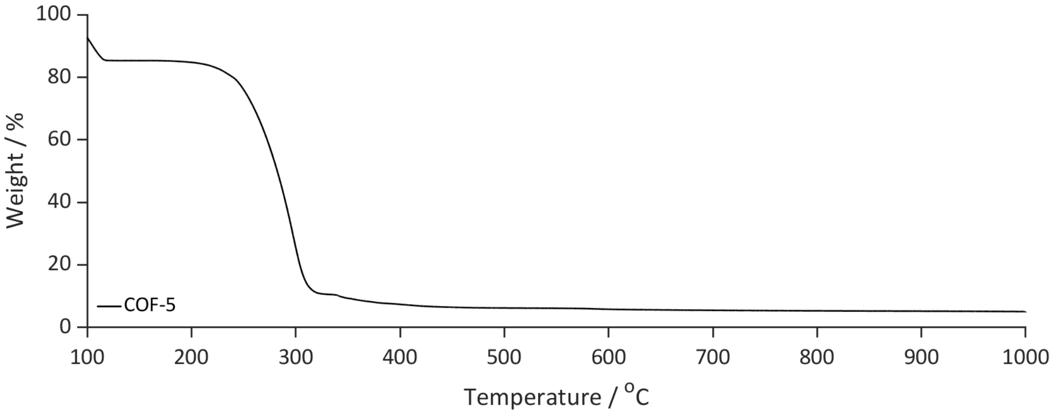

Figure 125: TGA thermogram of phenylboronic acid (PBA), used as a modulator in cHBC-BDA-COF synthesis.

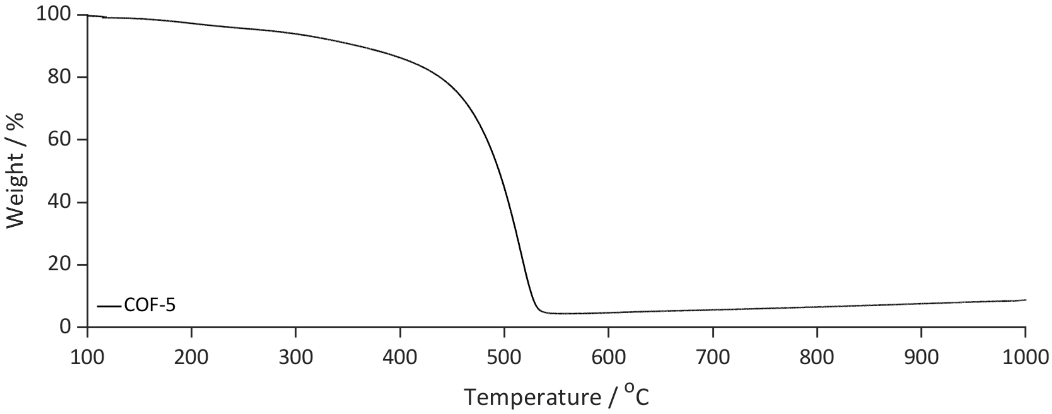

Figure 126: TGA thermogram of catahexabenzocoronene (cHBC), used in cHBC-BDA-COF synthesis.

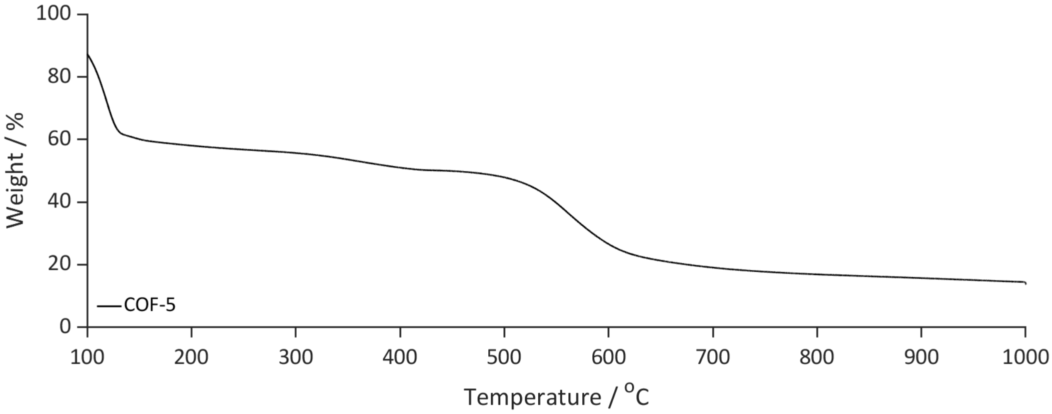

Figure 127: TGA thermogram of pyrene-2,7-diboronic acid (PDBA), the monomer used to make Py-COF.

7.11 Nuclear Magnetic Resonance Spectra

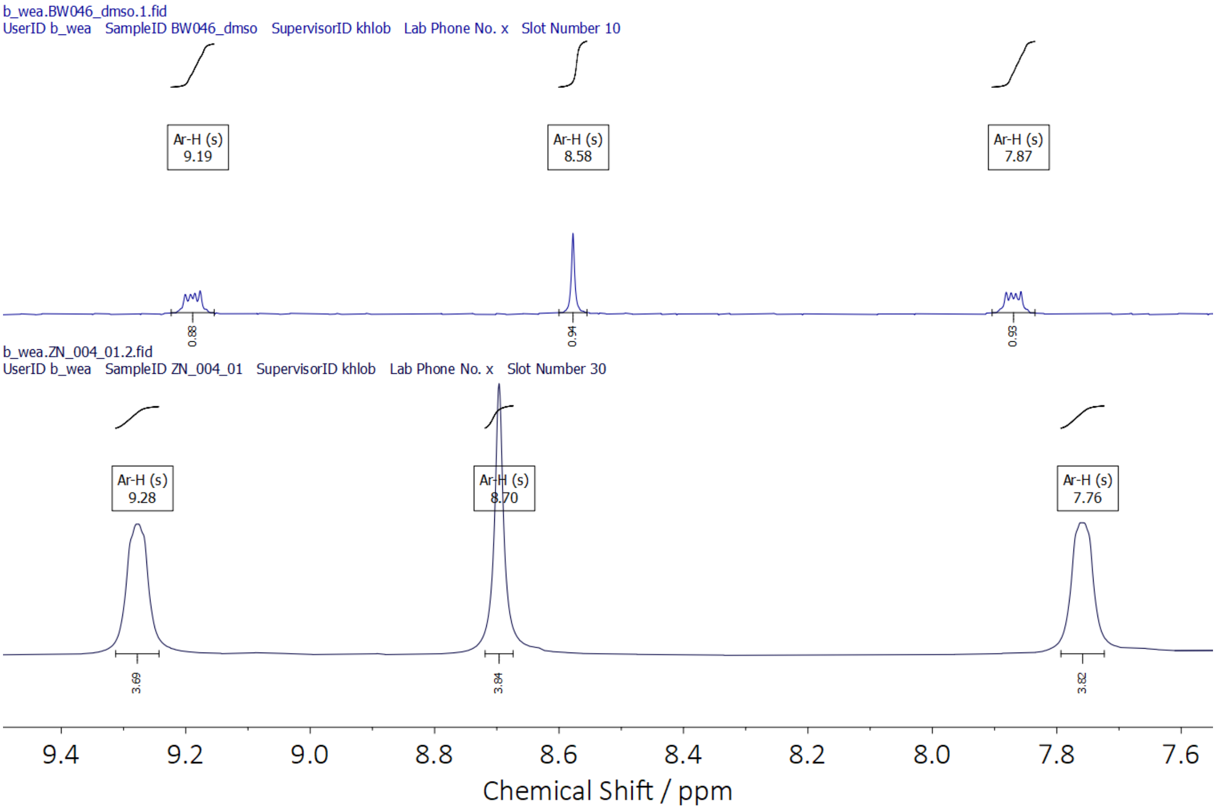

Figure 128: Proton NMR spectra. Top: cHBC-OMe, the as-synthesised product. Bottom: cHBC-OH, after de-protection. cHBC-OH was then used to make cHBC-BDA-COF in Chapter 2. Spectra have been cropped to the aromatic region.

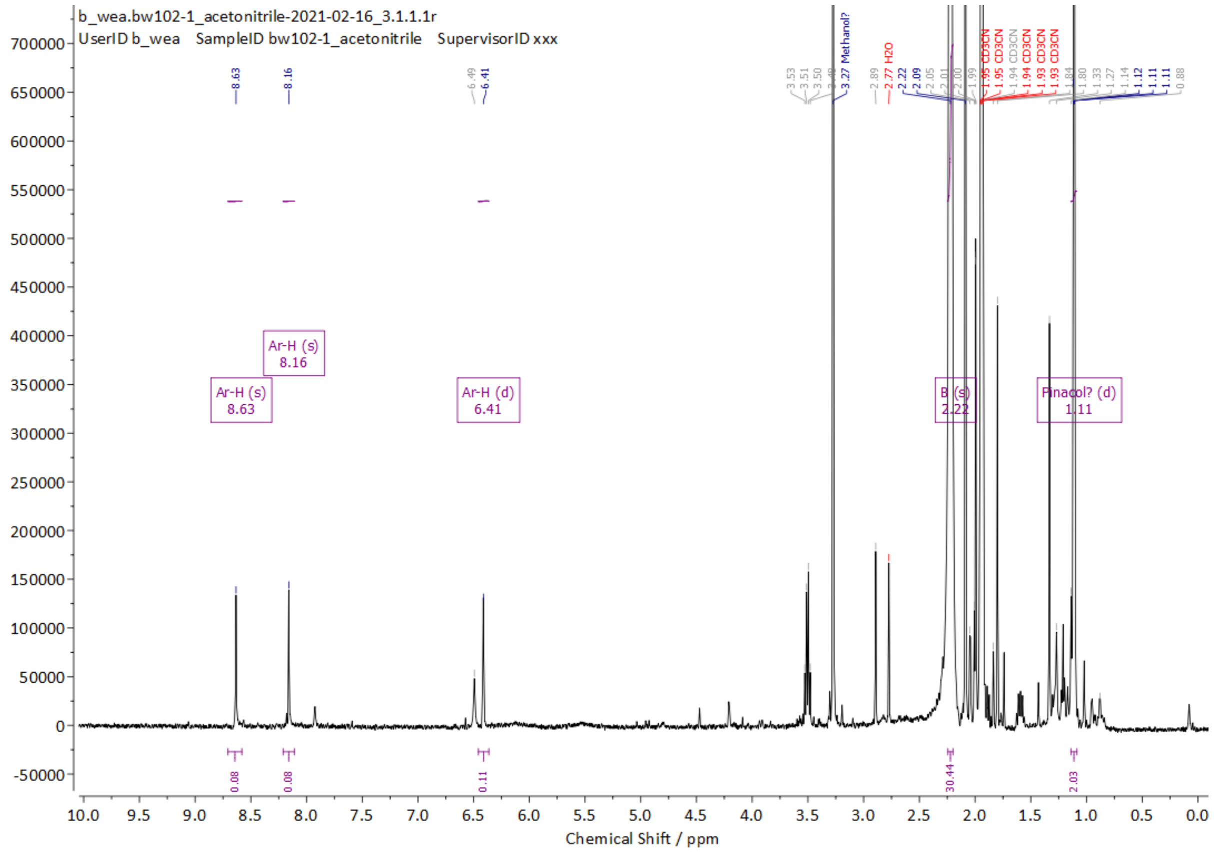

Figure 129: Proton NMR spectrum of pyrene-2,7-diboronic acid, used to make Py-COF in Chapter 5.

7.12 Dynamic Light Scattering

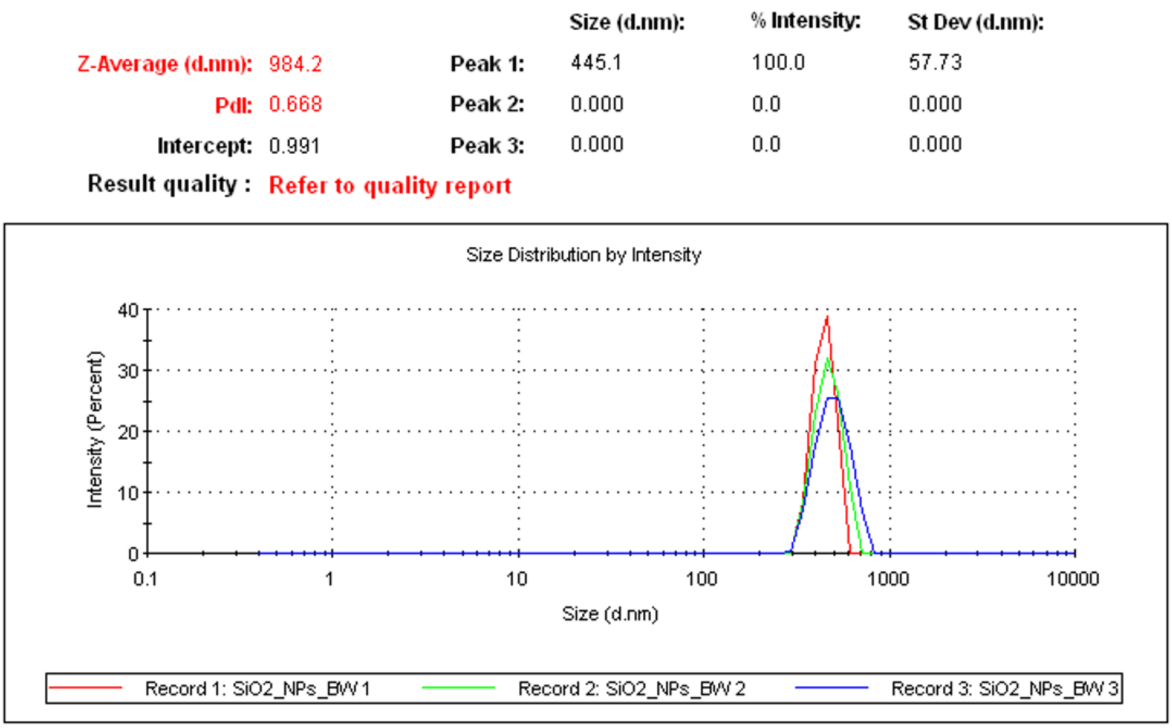

			Size (d.nm):	% Intensity:	St Dev (d.nm):
Z-Average (d.nm):	984.2	Peak 1:	445.1	100.0	57.73
PdI:	0.668	Peak 2:	0.000	0.0	0.000
Intercept:	0.991	Peak 3:	0.000	0.0	0.000

Result quality : Refer to quality report

Figure 130: Dynamic light scattering results for silica nanoparticles made via the Stöber process. These results show that the nanoparticles have an average diameter of 445 ± 57 nm.

7.13 Energy and Wavelength Conversions

To change from flux or fluence to energy (E) or current (I) is straightforward as long as the voltage (V) and irradiation time (t) is known:

$$E = \frac{IV}{t} \tag{43}$$

$$I = \frac{Et}{V} \tag{44}$$

This may be more accessible for readers from other pedagogical backgrounds. The conversions between wavelength, electron volts, Joules, and wavenumbers are also straightforward, with some comparisons presented in Table 29.

Energy / eV	**Wavelength / nm**	**Wavenumbers / cm^{-1}**
0.01	120168.8	83.21631
0.1	12016.88	832.1631
1	1201.688	8321.631
10	120.1688	83216.31
100	12.01688	832163.1
1000	1.201688	8321631

Table 29: Comparison between values in electron volts (eV), wavelength in nanometres, and wavenumbers.

7.14 Electron Beam Relativity

As an aside, the origin of e-beam contrast can also be considered from the perspective of relativity. As electron kinetic energy increases, a greater relativistic length contraction is observed in the direction of electron travel (Table 30). This means that an electron with 200 keV kinetic energy passes through a thinner sample than an electron with 80 keV kinetic energy, so has a lower probability of scattering than the 80 keV electron. This may be a more intuitive way of considering electron beam contrast than scattering cross-sections for some readers. The Lorentz factor γ is calculated by the usual equation:

$$\gamma = \frac{1}{(1-\frac{v}{c})^2)^{0.5}} \tag{45}$$

Where v is the velocity of the electron and c is the speed of light. The electron velocity is calculated via:

$$v = c(1 - \frac{m_e c^2}{Q_e V + m_e c^2}) \tag{46}$$

Where m_e is the mass of the electron, Q_e is elementary charge, and V is the accelerating voltage.

Kinetic Energy / keV	Velocity / ms^{-1}	Contracted Length	Lorentz Factor
80	1.5×10^8	86.5	1.15
100	1.64×10^8	83.6	1.20
200	2.08×10^8	71.9	1.39

Table 30: Contracted length for a resting distance of 100 nm, for electrons of typical TEM kinetic energies. Lorentz factors (γ) are indicated.

7.15 Nanotube Specific Surface Area and Specific Volume Calculation

A method for calculating the specific volume and surface areas of nanotubes was developed, but wasn't needed in the main text. If you consider a nanotube as a perfect cylinder it has an interior diameter (d_i), an external diameter (d_e), and a side wall thickness (c). Taking into account the Van der Waals radius of carbon (W_C), the interior and total radius of the nanotube are:

$$r_e = (d_e + W_C) \div 2$$

$$r_i = (d_i - W_C) \div 2$$

From this, the total side-wall volume (V_s) of a single nanotube of known length (L) can be calculated using the equations for volume of a cylinder:

$$V_s = V_e - V_i = (\pi r_e^2 L) - (\pi r_i^2 L)$$

Where V_e is the total volume of the nanotube and V_i is the volume of the nanotube cavity. Similarly for the surface area:

$$A_t = A_e + A_i + A_c = (2\pi r_e L) + (2\pi r_i L) + (2\pi r_e^2 - 2\pi r_i^2)$$

Where A_e is the surface area of the outside of the nanotube, A_i the the surface area of the inside surface of the nanotube cavity, and A_c is the surface area of the end faces of the nanotube. The mass of a single nanotube (m_t) is then estimated using the density of graphite (ρ) and the volume of the side walls:

$$m_t = V_s \rho$$

Then dividing surface area or volume of a nanotube gives the specific volume or specific surface area. The mass of a nanotube can also be used to calculate the number of nanotubes in a sample of known mass. The drawback to this method is that it relies on knowing the mean length and diameter of nanotubes in a sample.

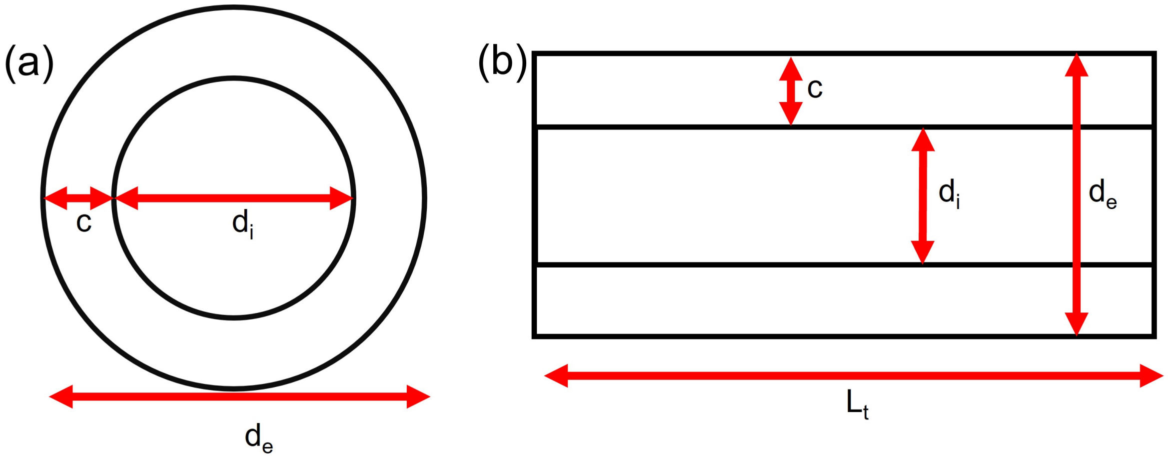

Figure 131: Schematic diagrams of nanotubes, (a) front view, and (b) side view. The following quantities are indicated: side wall thickness C; internal diameter d_i; external diameter d_e; and tube length L_t.

7.16 COF-TEM Review Accelerating Voltage Citations List

Due to some of the citations being called on in multiple sections of Chapter 1, the formatting for the citations for the reported accelerating voltage became very messy. As such here is the full list of citations divided by accelerating voltage:

- Publications not reporting accelerating voltage.[2–77]
- 300 kV accelerating voltage.[78–94]
- 200 kV accelerating voltage.[94–132]
- 120 kV accelerating voltage.[108,133–139]
- 100 kV accelerating voltage.[96,112,140–142]
- 80 kV accelerating voltage.[96,143–145]

References

(1) D. B. Williams and C. B. Carter, *Transmission electron microscopy: a textbook for materials science*, Springer, New York, 2nd ed, 2008.

(2) X. Zhang, Z. Wang, L. Yao, Y. Mai, J. Liu, X. Hua and H. Wei, *Materials Letters*, 2018, **213**, 143–147.

(3) L. Wang, Y. Xie, Y. Yang, H. Liang, L. Wang and Y. Song, *ACS Applied Nano Materials*, 2020, **3**, 1412–1419.

(4) Y. Sun, G. I. Waterhouse, L. Xu, X. Qiao and Z. Xu, *Sensors and Actuators B: Chemical*, 2020, **321**, 128501.

(5) F. Zhang, S. Wei, W. Wei, J. Zou, G. Gu, D. Wu, S. Bi and F. Zhang, *Science Bulletin*, 2020, **65**, 1659–1666.

(6) J. Liu, T. Cheng, L. Jiang, H. Zhang, Y. Shan and A. Kong, *Electrochimica Acta*, 2020, **363**, 137280.

(7) F. Xu, S. Jin, H. Zhong, D. Wu, X. Yang, X. Chen, H. Wei, R. Fu and D. Jiang, *Scientific Reports*, 2015, **5**, 8225.

(8) H. Guo, N. Song, D. Wang, J. Ma and Q. Jia, *Talanta*, 2019, **198**, 277–283.

(9) Z. Li, Z.-W. Liu, Z. Li, T.-X. Wang, F. Zhao, X. Ding, W. Feng and B.-H. Han, *Advanced Functional Materials*, 2020, **30**, 1909267.

(10) Y. Xiao, C. Ma, Z. Jin, C. Wang, J. Wang, H. Wang, X. Mu, L. Song and Y. Hu, *Separation and Purification Technology*, 2021, **259**, 118119.

(11) R.-R. Liang, R.-H. A, S.-Q. Xu, Q.-Y. Qi and X. Zhao, *Journal of the American Chemical Society*, 2020, **142**, 70–74.

(12) S. Kim and H. C. Choi, *Communications Chemistry*, 2019, **2**, 60.

(13) Z. Xiao, D. Kong, Q. Song, S. Zhou, Y. Zhang, A. Badshah, J. Liang and L. Zhi, *Nano Energy*, 2018, **46**, 365–371.

(14) W. Song, Y. Zhang, A. Varyambath and I. Kim, *ACS Nano*, 2019, **13**, 11753–11769.

(15) R. L. Li, N. C. Flanders, A. M. Evans, W. Ji, I. Castano, L. X. Chen, N. C. Gianneschi and W. R. Dichtel, *Chemical Science*, 2019, **10**, 3796–3801.

(16) M. R. Rao, Y. Fang, S. De Feyter and D. F. Perepichka, *Journal of the American Chemical Society*, 2017, **139**, 2421–2427.

(17) Y.-B. Huang, P. Pachfule, J.-K. Sun and Q. Xu, *Journal of Materials Chemistry A*, 2016, **4**, 4273–4279.

(18) Z. Xiang, Y. Xue, D. Cao, L. Huang, J.-F. Chen and L. Dai, *Angewandte Chemie International Edition*, 2014, **53**, 2433–2437.

(19) Y.-B. Zhang, J. Su, H. Furukawa, Y. Yun, F. Glándara, A. Duong, X. Zou and O. M. Yaghi, *Journal of the American Chemical Society*, 2013, **135**, 16336–16339.

(20) J. Guo, Y. Xu, S. Jin, L. Chen, T. Kaji, Y. Honsho, M. A. Addicoat, J. Kim, A. Saeki, H. Ihee, S. Seki, S. Irle, M. Hiramoto, J. Gao and D. Jiang, *Nature Communications*, 2013, **4**, 2736.

(21) Y. Cheng, S. K. Ravi, Y. Wang, J. Tao, Y. Gu, S. C. Tan and D. Zhao, *Chinese Chemical Letters*, 2018, **29**, 869–872.

(22) S. Wan, J. Guo, J. Kim, H. Ihee and D. Jiang, *Angewandte Chemie International Edition*, 2009, **48**, 5439–5442.

(23) S. Wan, J. Guo, J. Kim, H. Ihee and D. Jiang, *Angewandte Chemie International Edition*, 2008, **47**, 8826–8830.

(24) Y. Han, Q. Zhang, N. Hu, X. Zhang, Y. Mai, J. Liu, X. Hua and H. Wei, *Chinese Chemical Letters*, 2017, **28**, 2269–2273.

(25) E. Jin, J. Li, K. Geng, Q. Jiang, H. Xu, Q. Xu and D. Jiang, *Nature Communications*, 2018, **9**, 4143.

(26) Y. Meng, G. Lin, H. Ding, H. Liao and C. Wang, *Journal of Materials Chemistry A*, 2018, **6**, 17186–17191.

(27) J. Zhang, Z. Chen, S. Tang, X. Luo, J. Xi, Z. He, J. Yu and F. Wu, *Analytica Chimica Acta*, 2019, **1089**, 66–77.

(28) X. Ma, C. Pang, S. Li, Y. Xiong, J. Li, J. Luo and Y. Yang, *Biosensors and Bioelectronics*, 2019, **146**, 111734.

(29) M. Wang, M. Ballabio, M. Wang, H.-H. Lin, B. P. Biswal, X. Han, S. Paasch, E. Brunner, P. Liu, M. Chen, M. Bonn, T. Heine, S. Zhou, E. Cánovas, R. Dong and X. Feng, *Journal of the American Chemical Society*, 2019, **141**, 16810–16816.

(30) Z. Meng, R. M. Stolz and K. A. Mirica, *Journal of the American Chemical Society*, 2019, **141**, 11929–11937.

(31) P. Asadi, M. Falsafin and M. Dinari, *Journal of Molecular Structure*, 2021, **1227**, 129546.

(32) S. Xu, Z. Li, L. Zhang, W. Zhang and D. Li, *Talanta*, 2021, **221**, 121612.

(33) Y. Han, N. Hu, S. Liu, Z. Hou, J. Liu, X. Hua, Z. Yang, L. Wei, L. Wang and H. Wei, *Nanotechnology*, 2017, **28**, 33LT01.

(34) S. Kim and H. C. Choi, *ACS Omega*, 2020, **5**, 948–958.

(35) Z. Lei, Q. Yang, Y. Xu, S. Guo, W. Sun, H. Liu, L.-P. Lv, Y. Zhang and Y. Wang, *Nature Communications*, 2018, **9**, 576.

(36) L. Xu, F. Wang, X. Ge, R. Liu, M. Xu and J. Yang, *Microporous and Mesoporous Materials*, 2019, **287**, 65–70.

(37) Z. Lu, Z. Shi, S. Huang, R. Zhang, G. Li and Y. Hu, *Talanta*, 2020, **214**, 120864.

(38) Y. Li, X. Xu, S. Hou, J. Ma, T. Lu, J. Wang, Y. Yao and L. Pan, *Chemical Communications*, 2018, **54**, 14009–14012.

(39) K. Hu, Y. Lv, F. Ye, T. Chen and S. Zhao, *Analytical Chemistry*, 2019, **91**, 6353–6362.

(40) D. Ouyang, K. Luo, W. Ma, J. Wu, J. Li, Y. He, Z. Cai and Z. Lin, *The Analyst*, 2020, **145**, 3125–3130.

(41) Y. Zhang, J. Guo, G. Han, Y. Bai, Q. Ge, J. Ma, C. H. Lau and L. Shao, *Science Advances*, 2021, **7**, eabe8706.

(42) C. Jia, Y. Mi, Z. Liu, W. Zhou, H. Gao, S. Zhang and R. Lu, *Microchemical Journal*, 2020, **153**, 104522.

(43) X. Wang, R. Ma, L. Hao, Q. Wu, C. Wang and Z. Wang, *Journal of Chromatography A*, 2018, **1551**, 1–9.

(44) M. Gao, L. Deng, X. Kang, Q. Fu, K. Zhang, M. Wang, Z. Xia and D. Gao, *Journal of Chromatography A*, 2020, **1629**, 461476.

(45) Q.-B. Fu, H.-L. Jiang, L.-Q. Qiao, X. Sun, M.-L. Wang and R.-S. Zhao, *Journal of Chromatography A*, 2020, **1630**, 461534.

(46) X. Chen, Y. Xu, F.-H. Du and Y. Wang, *Small Methods*, 2019, **3**, 1900338.

(47) L. Guo, J. Liu, J. Li, L. Hao, W. Liu, C. Wang, Q. Wu and Z. Wang, *Journal of Chromatography A*, 2021, **1651**, 462301.

(48) Y. Li, B. Pei, J. Chen, S. Bing, L. Hou, Q. Sun, G. Xu, Z. Yao and L. Zhang, *Journal of Colloid and Interface Science*, 2021, **591**, 273–280.

(49) Y. Xie, Y. Chen, X. Sun, Y. Wang and Y. Wang, *Chinese Chemical Letters*, 2021, **32**, 2061–2065.

(50) K. Preet, G. Gupta, M. Kotal, S. K. Kansal, D. B. Salunke, H. K. Sharma, S. Chandra Sahoo, P. Van Der Voort and S. Roy, *Crystal Growth & Design*, 2019, **19**, 2525–2530.

(51) X. Shi, N. Li, D. Wu, N. Hu, J. Sun, X. Zhou, Y. Suo, G. Li and Y. Wu, *Analytical Methods*, 2018, **10**, 5014–5024.

(52) S. Thomas, H. Li, R. R. Dasari, A. M. Evans, I. Castano, T. G. Allen, O. G. Reid, G. Rumbles, W. R. Dichtel, N. C. Gianneschi, S. R. Marder, V. Coropceanu and J.-L. Brlédas, *Materials Horizons*, 2019, **6**, 1868–1876.

(53) M. L. Yola and N. Atar, *Nanoscale*, 2020, **12**, 19824–19832.

(54) W. Wang, Y. Zhang, L. Chen, H. Chen, S. Hu, Q. Li, H. Liu and S. Qiao, *Polymer Chemistry*, 2021, **12**, 650–659.

(55) H. Wu, D. Li, B. Zhao, S. Guan, X. Jing, Y. Ding and G. Fan, *Analytical Methods*, 2021, 10.1039.D1AY00496D.

(56) S. Guan, H. Wu, L. Yang, Z. Wang and J. Wu, *Journal of Separation Science*, 2020, **43**, 3775–3784.

(57) X. Chen, H. Zhang, C. Ci, W. Sun and Y. Wang, *ACS Nano*, 2019, **13**, 3600–3607.

(58) X. Li, Q. Su, Z. Liu, K. Luo, G. Li and Q. Wu, *Chemical Research in Chinese Universities*, 2020, **36**, 1017–1023.

(59) M. Wang, M. Gao, K. Zhang, L. Wang, W. Wang, Q. Fu, Z. Xia and D. Gao, *Microchimica Acta*, 2019, **186**, 827.

(60) O. Yildirim and B. Derkus, *Journal of Materials Science*, 2020, **55**, 3034–3044.

(61) C. Liu, Y. Jin, Z. Yu, L. Gong, H. Wang, B. Yu, W. Zhang and J. Jiang, *Journal of the American Chemical Society*, 2022, **144**, 12390–12399.

(62) J. Li, X. Xu, X. Wang, C. Li, X. Feng, Y. Zhang and F. Zhang, *Microchimica Acta*, 2022, **189**, 149.

(63) J. Yin, H. Zhai, Y. Wang, B. Wang, G. Chu, Q. Guo, Y. Zhang, X. Sun, Y. Guo and Y. Zhang, *Food Analytical Methods*, 2022, DOI: `10.1007/s12161-022-02369-1`.

(64) L. Yao, Z. Zhou, S. Wang, Q. Zou, H.-X. Wang, L.-X. Ma, S. Wang and X. Zhang, *Chemical Science*, 2022, **13**, 5902–5912.

(65) Ö. S. Bölükbaşi, B. B. Yola, C. Karaman, N. Atar and M. L. Yola, *Microchimica Acta*, 2022, **189**, 242.

(66) N. Keshmiri, P. Najmi, M. Ramezanzadeh, B. Ramezanzadeh and G. Bahlakeh, *ACS Applied Materials & Interfaces*, 2022, **14**, 19958–19974.

(67) L. Gao, Q. Dong, X. Zhao, X. Hu, H. Chu, R. Lv and S. Qin, *Processes*, 2022, **10**, 843.

(68) Y. Sun, L. Xu, G. I. Waterhouse, M. Wang, X. Qiao and Z. Xu, *Sensors and Actuators B: Chemical*, 2019, **281**, 107–114.

(69) S. Sarkar, S. Ghosh and S. M. Islam, *Organic & Biomolecular Chemistry*, 2022, **20**, 1707–1722.

(70) A. R. Abdellah, A.-B. A. El-Adasy, A. A. Atalla, K. I. Aly and H. N. Abdelhamid, *Microporous and Mesoporous Materials*, 2022, **339**, 111961.

(71) S. Xu, Z. Liao, A. Dianat, S.-W. Park, M. A. Addicoat, Y. Fu, D. L. Pastoetter, F. G. Fabozzi, Y. Liu, G. Cuniberti, M. Richter, S. Hecht and X. Feng, *Angewandte Chemie International Edition*, 2022, **61**, DOI: `10.1002/anie.202202492`.

(72) S. Ghosh, T. S. Khan, A. Ghosh, A. H. Chowdhury, M. A. Haider, A. Khan and S. M. Islam, *ACS Sustainable Chemistry & Engineering*, 2020, **8**, 5495–5513.

(73) I. Gadwal, G. Sheng, R. L. Thankamony, Y. Liu, H. Li and Z. Lai, *ACS Applied Materials & Interfaces*, 2018, **10**, 12295–12299.

(74) X. Hu, J. Jian, Z. Fang, L. Zhong, Z. Yuan, M. Yang, S. Ren, Q. Zhang, X. Chen and D. Yu, *Energy Storage Materials*, 2019, **22**, 40–47.

(75) S. Vargheese, D. Muthu, D. Pattappan, K. Kavya, R. R. Kumar and Y. Haldorai, *Electrochimica Acta*, 2020, **364**, 137291.

(76) J. Wang, W. Qin, X. Zhu and Y. Teng, *Energy*, 2020, **199**, 117372.

(77) T. Sun, J. Xie, W. Guo, D.-S. Li and Q. Zhang, *Advanced Energy Materials*, 2020, **10**, 1904199.

(78) I. Berlanga, M. L. Ruiz-González, J. M. González-Calbet, J. L. G. Fierro, R. Mas-Ballesté and F. Zamora, *Small*, 2011, **7**, 1207–1211.

(79) F. Lu, Y. Li, Q. Shi, C. Zhao, S. Li and S. Pang, *New Journal of Chemistry*, 2020, **44**, 15354–15361.

(80) Y. Peng, L. Li, C. Zhu, B. Chen, M. Zhao, Z. Zhang, Z. Lai, X. Zhang, C. Tan, Y. Han, Y. Zhu and H. Zhang, *Journal of the American Chemical Society*, 2020, **142**, 13162–13169.

(81) Y. Peng, Y. Huang, Y. Zhu, B. Chen, L. Wang, Z. Lai, Z. Zhang, M. Zhao, C. Tan, N. Yang, F. Shao, Y. Han and H. Zhang, *Journal of the American Chemical Society*, 2017, **139**, 8698–8704.

(82) G. Veber, C. S. Diercks, C. Rogers, W. S. Perkins, J. Ciston, K. Lee, J. P. Llinas, A. Liebman-Peláez, C. Zhu, J. Bokor and F. R. Fischer, *Chem*, 2020, **6**, 1125–1133.

(83) Y. Li, Z. Ou, B. Liang, J. Yang, R. Chen, H. Qi, U. Kaiser, W. Hong, X. Chen, L. Du, W. Liu and Z. Zheng, *Polymers*, 2021, **13**, 1561.

(84) B. P. Biswal, S. Chandra, S. Kandambeth, B. Lukose, T. Heine and R. Banerjee, *Journal of the American Chemical Society*, 2013, **135**, 5328–5331.

(85) C. Zhang, S. Wang, Z. Zhan, A. M. Amin and B. Tan, *ACS Macro Letters*, 2019, **8**, 403–408.

(86) D. Feng and Y. Xia, *Analytica Chimica Acta*, 2018, **1014**, 58–63.

(87) S. Vedachalam, P. Sekar, C. Nithya, N. Murugesh and R. Karvembu, *ACS Applied Energy Materials*, 2022, **5**, 557–566.

(88) M. Calik, T. Sick, M. Dogru, M. Döblinger, S. Datz, H. Budde, A. Hartschuh, F. Auras and T. Bein, *Journal of the American Chemical Society*, 2016, **138**, 1234–1239.

(89) I. Castano, A. M. Evans, H. Li, E. Vitaku, M. J. Strauss, J.-L. Brédas, N. C. Gianneschi and W. R. Dichtel, *ACS Central Science*, 2019, **5**, 1892–1899.

(90) S. Wang, Z. Zhang, H. Zhang, A. G. Rajan, N. Xu, Y. Yang, Y. Zeng, P. Liu, X. Zhang, Q. Mao, Y. He, J. Zhao, B.-G. Li, M. S. Strano and W.-J. Wang, *Matter*, 2019, **1**, 1592–1605.

(91) F. Haase, E. Troschke, G. Savasci, T. Banerjee, V. Duppel, S. Dörfler, M. M. J. Grundei, A. M. Burow, C. Ochsenfeld, S. Kaskel and B. V. Lotsch, *Nature Communications*, 2018, **9**, 2600.

(92) F. Auras, L. Ascherl, A. H. Hakimioun, J. T. Margraf, F. C. Hanusch, S. Reuter, D. Bessinger, M. Döblinger, C. Hettstedt, K. Karaghiosoff, S. Herbert, P. Knochel, T. Clark and T. Bein, *Journal of the American Chemical Society*, 2016, **138**, 16703–16710.

(93) I. Castano, A. M. Evans, R. d. Reis, V. P. Dravid, N. C. Gianneschi and W. R. Dichtel, *Chemistry of Materials*, 2021, **33**, 1341–1352.

(94) R. Nishiyabu, S. Teraoka, Y. Matsushima and Y. Kubo, *ChemPlusChem*, 2012, **77**, 201–209.

(95) A. M. Evans, I. Castano, A. Brumberg, L. R. Parent, A. R. Corcos, R. L. Li, N. C. Flanders, D. J. Gosztola, N. C. Gianneschi, R. D. Schaller and W. R. Dichtel, *Journal of the American Chemical Society*, 2019, **141**, 19728–19735.

(96) C. T. Stoppiello, H. Isla, M. Martínez-Abadía, M. W. Fay, C. D. J. Parmenter, M. J. Roe, B. Lerma-Berlanga, C. Martí-Gastaldo, A. Mateo-Alonso and A. N. Khlobystov, *Nanoscale*, 2019, **11**, 2848–2854.

(97) P. P. Ramees, P. K. Mondal and D. Chopra, *Journal of Chemical Sciences*, 2018, **130**, 51.

(98) S. Karak, S. Kandambeth, B. P. Biswal, H. S. Sasmal, S. Kumar, P. Pachfule and R. Banerjee, *Journal of the American Chemical Society*, 2017, **139**, 1856–1862.

(99) M. A. Khayum, S. Kandambeth, S. Mitra, S. B. Nair, A. Das, S. S. Nagane, R. Mukherjee and R. Banerjee, *Angewandte Chemie International Edition*, 2016, **55**, 15604–15608.

(100) S. Rager, A. C. Jakowetz, B. Gole, F. Beuerle, D. D. Medina and T. Bein, *Chemistry of Materials*, 2019, **31**, 2707–2712.

(101) A. Halder, S. Kandambeth, B. P. Biswal, G. Kaur, N. C. Roy, M. Addicoat, J. K. Salunke, S. Banerjee, K. Vanka, T. Heine, S. Verma and R. Banerjee, *Angewandte Chemie International Edition*, 2016, **55**, 7806–7810.

(102) S.-Y. Ding, J. Gao, Q. Wang, Y. Zhang, W.-G. Song, C.-Y. Su and W. Wang, *Journal of the American Chemical Society*, 2011, **133**, 19816–19822.

(103) M. Martínez-Abadía, C. T. Stoppiello, K. Strutynski, B. Lerma-Berlanga, C. Martí-Gastaldo, A. Saeki, M. Melle-Franco, A. N. Khlobystov and A. Mateo-Alonso, *Journal of the American Chemical Society*, 2019, **141**, 14403–14410.

(104) S.-J. Yin, C.-P. Zhao, H. Jiang, M. Lu, Y. Wang, H. Chen and F.-Q. Yang, *Microchemical Journal*, 2021, **164**, 105990.

(105) B. Sun, J. Liu, A. Cao, W. Song and D. Wang, *Chemical Communications*, 2017, **53**, 6303–6306.

(106) N. Bagherian, A. R. Karimi and A. Amini, *Colloids and Surfaces A: Physicochemical and Engineering Aspects*, 2021, **613**, 126078.

(107) A. R. Abdellah, H. N. Abdelhamid, A.-B. A. El-Adasy, A. A. Atalla and K. I. Aly, *Journal of Environmental Chemical Engineering*, 2020, **8**, 104054.

(108) Y. T. Guntern, J. Vávra, V. V. Karve, S. B. Varandili, O. Segura Lecina, C. Gadiyar and R. Buonsanti, *Chemistry of Materials*, 2021, **33**, 2646–2654.

(109) Y. Xing, L. Yin, Y. Zhao, Z. Du, H.-Q. Tan, X. Qin, W. Ho, T. Qiu and Y.-G. Li, *ACS Applied Materials & Interfaces*, 2020, **12**, 51555–51562.

(110) P. Wen, Y. Lei, Q. Yan, Y. Han and M. Fan, *ACS Applied Materials & Interfaces*, 2021, **13**, 11524–11534.

(111) Y. Zhao, H. Liu, C. Wu, Z. Zhang, Q. Pan, F. Hu, R. Wang, P. Li, X. Huang and Z. Li, *Angewandte Chemie International Edition*, 2019, **58**, 5376–5381.

(112) W. Liu, C. Wang, L. Zhang, H. Pan, W. Liu, J. Chen, D. Yang, Y. Xiang, K. Wang, J. Jiang and X. Yao, *Journal of Materials Chemistry A*, 2019, **7**, 3112–3119.

(113) X. Mu, J. Zhan, X. Feng, B. Yuan, S. Qiu, L. Song and Y. Hu, *ACS Applied Materials & Interfaces*, 2017, **9**, 23017–23026.

(114) T. Sun, W. Lei, Y. Ma and Y.-B. Zhang, *Chinese Journal of Chemistry*, 2020, **38**, 1153–1166.

(115) C. Feriante, A. M. Evans, S. Jhulki, I. Castano, M. J. Strauss, S. Barlow, W. R. Dichtel and S. R. Marder, *Journal of the American Chemical Society*, 2020, **142**, 18637–18644.

(116) J. Xu, Y. He, S. Bi, M. Wang, P. Yang, D. Wu, J. Wang and F. Zhang, *Angewandte Chemie - International Edition*, 2019, **58**, 12065–12069.

(117) J.-M. Seo, H.-J. Noh, H. Y. Jeong and J.-B. Baek, *Journal of the American Chemical Society*, 2019, **141**, 11786–11790.

(118) M. Martínez-Abadía, K. Strutyński, B. Lerma-Berlanga, C. T. Stoppiello, A. N. Khlobystov, C. Martí-Gastaldo, A. Saeki, M. Melle-Franco and A. Mateo-Alonso, *Angewandte Chemie International Edition*, 2021, **60**, 9941–9946.

(119) Z. Liu, B. Zhang, Y. Huang, Y. Song, N. Dong, J. Wang and Y. Chen, *iScience*, 2021, **24**, 102526.

(120) H.-S. Xu, Y. Luo, X. Li, P. Z. See, Z. Chen, T. Ma, L. Liang, K. Leng, I. Abdelwahab, L. Wang, R. Li, X. Shi, Y. Zhou, X. F. Lu, X. Zhao, C. Liu, J. Sun and K. P. Loh, *Nature Communications*, 2020, **11**, 1434.

(121) Z. Wang, X. Jia, P. Zhang, Y. Liu, H. Qi, P. Zhang, U. Kaiser, S. Reineke, R. Dong and X. Feng, *Advanced Materials*, 2021, **34**, 2106073.

(122) P. Arul, S.-T. Huang, V. Mani and C.-H. Huang, *ACS Applied Nano Materials*, 2022, **5**, 6340–6351.

(123) L. Niu, X. Zhao, Z. Tang, F. Wu, J. Wang, Q. Lei, W. Liang, X. Wang, M. Teng and X. Zhang, *Separation and Purification Technology*, 2022, **294**, 121145.

(124) Y. Deng, Y. Wang, J. Wang, Z. Wei, C. Xin, J. Liu, C. Zhao and Z. Zhang, *Materials Today Chemistry*, 2022, **26**, 101027.

(125) P. Guo, Y. Zhan, Y. Yang and T. Lu, *Catalysis Letters*, 2022, DOI: `10.1007/s10562-022-03941-4`.

(126) A. K. Mohammed, V. Vijayakumar, A. Halder, M. Ghosh, M. Addicoat, U. Bansode, S. Kurungot and R. Banerjee, *ACS Applied Materials & Interfaces*, 2019, **11**, 30828–30837.

(127) C. Li, W. Ju, S. Vijay, J. Timoshenko, K. Mou, D. A. Cullen, J. Yang, X. Wang, P. Pachfule, S. Brückner, H. S. Jeon, F. T. Haase, S.-C. Tsang, C. Rettenmaier, K. Chan, B. R. Cuenya, A. Thomas and P. Strasser, *Angewandte Chemie International Edition*, 2022, **61**, DOI: `10.1002/anie.202114707`.

(128) R. Gomes and A. J. Bhattacharyya, *ACS Sustainable Chemistry & Engineering*, 2020, **8**, 5946–5953.

(129) C. Zhang, M. Cui, J. Ren, Y. Xing, N. Li, H. Zhao, P. Liu, X. Ji and M. Li, *Chemical Engineering Journal*, 2020, **401**, 126025.

(130) A. M. Evans, L. R. Parent, N. C. Flanders, R. P. Bisbey, E. Vitaku, M. S. Kirschner, R. D. Schaller, L. X. Chen, N. C. Gianneschi and W. R. Dichtel, *Science*, 2018, **361**, 6.

(131) B. J. Smith, L. R. Parent, A. C. Overholts, P. A. Beaucage, R. P. Bisbey, A. D. Chavez, N. Hwang, C. Park, A. M. Evans, N. C. Gianneschi and W. R. Dichtel, *ACS Central Science*, 2017, **3**, 58–65.

(132) S. W. Park, Z. Liao, B. Ibarlucea, H. Qi, H. H. Lin, D. Becker, J. Melidonie, T. Zhang, H. Sahabudeen, L. Baraban, C. K. Baek, Z. Zheng, E. Zschech, A. Fery, T. Heine, U. Kaiser, G. Cuniberti, R. Dong and X. Feng, *Angewandte Chemie - International Edition*, 2020, **59**, 8218–8224.

(133) R. Liang, Y. Hu and G. Li, *Journal of Chromatography A*, 2020, **1618**, 460867.

(134) J. Sun, A. Klechikov, C. Moise, M. Prodana, M. Enachescu and A. V. Talyzin, *Angewandte Chemie International Edition*, 2018, **57**, 1034–1038.

(135) Y. Xie, T. Zhang, Y. Chen, Y. Wang and L. Wang, *Talanta*, 2020, **213**, 120843.

(136) G. Zhang, M. Tsujimoto, D. Packwood, N. T. Duong, Y. Nishiyama, K. Kadota, S. Kitagawa and S. Horike, *Journal of the American Chemical Society*, 2018, **140**, 2602–2609.

(137) B.-Q. Li, S.-Y. Zhang, B. Wang, Z.-J. Xia, C. Tang and Q. Zhang, *Energy & Environmental Science*, 2018, **11**, 1723–1729.

(138) H. Chu, X. Sun, X. Zha, Y. Zhang and Y. Wang, *Colloids and Surfaces A: Physicochemical and Engineering Aspects*, 2022, **648**, 129238.

(139) S. D. Diwakara, W. S. Y. Ong, Y. H. Wijesundara, R. L. Gearhart, F. C. Herbert, S. G. Fisher, G. T. McCandless, S. B. Alahakoon, J. J. Gassensmith, S. C. Dodani and R. A. Smaldone, *Journal of the American Chemical Society*, 2022, **144**, 2468–2473.

(140) C. Gao, J. Bai, Y. He, Q. Zheng, W. Ma and Z. Lin, *ACS Sustainable Chemistry & Engineering*, 2019, **7**, 18926–18934.

(141) Q. Sun, C. Gao, W. Ma, Y. He, J. Wu, K. Luo, D. Ouyang, Z. Lin and Z. Cai, *Microchimica Acta*, 2020, **187**, 370.

(142) W. A. Braunecker, K. E. Hurst, K. G. Ray, Z. R. Owczarczyk, M. B. Martinez, N. Leick, A. Keuhlen, A. Sellinger and J. C. Johnson, *Crystal Growth & Design*, 2018, **18**, 4160–4166.

(143) D. D. Medina, V. Werner, F. Auras, R. Tautz, M. Dogru, J. Schuster, S. Linke, M. Döblinger, J. Feldmann, P. Knochel and T. Bein, *ACS Nano*, 2014, **8**, 4042–4052.

(144) W. Huang, Y. Jiang, X. Li, X. Li, J. Wang, Q. Wu and X. Liu, *ACS Applied Materials & Interfaces*, 2013, **5**, 8845–8849.

(145) B. L. Weare, R. W. Lodge, N. Zyk, A. Weilhard, C. L. Housley, K. Strutyński, M. Melle-Franco, A. Mateo-Alonso and A. N. Khlobystov, *Nanoscale*, 2021, **13**, 6834–6845.